ΠΡΩΤΟΤΥΠΟ ΠΑΡΑΚΕΝΤΡΙΚΟ ΗΜΙΣΦΑΙΡΙΚΟ ΦΑΣΜΑΤΟΜΕΤΡΟ ΥΨΗΛΗΣ ΑΠΟΔΟΣΗΣ ΓΙΑ ΦΑΣΜΑΤΟΣΚΟΠΙΑ AUGER ΗΛΕΚΤΡΟΝΙΩΝ ΜΗΔΕΝ ΜΟΙΡΩΝ

ΕΜΜΑΝΟΥΗΛ Π. ΜΠΕΝΗΣ

ΔΙΔΑΚΤΟΡΙΚΗ ΔΙΑΤΡΙΒΗ

ΤΜΗΜΑ ΦΥΣΙΚΗΣ
ΠΑΝΕΠΙΣΤΗΜΙΟ ΚΡΗΤΗΣ
ΗΡΑΚΛΕΙΟ

2001

A NOVEL HIGH-EFFICIENCY PARACENTRIC HEMISPHERICAL SPECTROGRAPH FOR ZERO – DEGREE AUGER PROJECTILE SPECTROSCOPY

EMMANOUIL P. BENIS

A DOCTOR'S DISSERTATION

DEPARTMENT OF PHYSICS
UNIVERSITY OF CRETE
HERAKLION

2001

Approved by:

Prof. T.J.M. Zouros

Contents

1 Introduction **1**

2 The technique of Zero-degree Auger Projectile Spectroscopy (ZAPS) **8**
2.1 Introduction 8
2.2 Kinematic Effects 11
2.2.1 Frame Transformation Effects 12
2.2.2 Line Broadening Effects 18
2.3 Concluding remarks 22

3 Experimental Arrangement: Hardware and Electronics **24**
3.1 Experimental Setup 24
3.2 Vacuum 27
3.3 The spectrograph 29
3.4 The 2D-PSD 31
3.5 Electronics 33
3.6 Data Acquisition System 33
3.7 Dead Time 36

4 The paracentric HDA: I. Ideal 1/r potential - Theory **39**
4.1 Introduction 39
4.2 Motion of a charged particle in an ideal 1/r potential 40
4.2.1 Definitions 40
4.2.2 Derivation of the charged particle trajectory 42
4.2.3 Initial & boundary conditions 44
4.2.4 Focusing conditions of the ideal HDA 46
4.2.5 Spectrograph basic equation 48
4.3 Analyser Voltages 49
4.4 Properties of the hemispherical deflector analyser 51
4.4.1 Magnification, dispersion and angular aberration 52
4.4.2 Energy resolution 54
4.4.3 Energy calibration 58
4.4.4 Energy acceptance window 62
4.5 Conclusions 63

5 The paracentric HDA: II. Ion optics simulations using SIMION **65**
5.1 SIMION HDA study motivation 65
5.2 Spectrograph simulation under SIMION 66
5.3 Energy Resolution Optimization 68
5.4 Energy Resolution over the PSD area 70
5.5 Energy Window 72
5.6 Discussion - Conclusions 73

6 The paracentric HDA: III. The real spectrograph **76**
6.1 Spectrograph operation mode 76
6.2 HDA - Lens voltages parameterization 77
6.2.1 V_0 study 77
6.2.2 Lens focusing study 79
6.3 Spectrograph operation in low resolution mode 82
6.4 Spectrograph operation in high resolution mode 82
6.5 Performance comparison of the hemispherical spectrograph and the KSU tandem spectrometer 89
6.6 Discussion and Conclusions 91

7 Data Analysis: Determination of absolute DDCS **93**
7.1 Energy Calibration 93
7.2 Double Differential Cross-Section 95
7.3 Absolute MCP efficiency determination: Binary Encounter electron normalization 106
7.4 Error analysis 108

8 Binary Encounter electrons **111**
8.1 Background and motivation 111
8.2 Impulse Approximation 113
8.2.1 Rutherford Scattering Model 115
8.2.2 Elastic electron Scattering Model 115
8.3 BEe peak enhancement factors for collisions of 0.4–1.2 MeV/u $B^{(2-5)+}$ + H_2 117
8.3.1 Historical background 117
8.3.2 Results and discussion 120
8.4 Conclusions 124

9 Spectroscopy of $B^{(1-3)+}$ intermediate states **126**
9.1 Motivation 126
9.2 The Auger spectrum of B^{4+} + H_2: Production of He-like B^{3+} doubly excited states 126
9.3 The Auger spectrum of B^{3+} + H_2:
I. Production of Li-like B^{2+} and He-like B^{3+} doubly excited states . . . 132
9.4 The Auger spectrum of B^{3+} + H_2:
II. Production of Li-like B^{2+} triply excited states 138
9.5 The Auger spectrum of B^{3+} + H_2:
III. Determination of B^{3+} beam metastable fraction 142
9.6 The Auger spectrum of B^{2+} + H_2 147
9.7 Conclusions 156

10 Resonant transfer and excitation **157**
10.1 Background 157
10.2 IA - RTEA theoretical description 160
10.3 RTEA with B^{4+} ions 164
10.4 RTEA with B^{3+} ions 170
10.5 Conclusions 174

11 Summary and conclusions **175**

Appendices **177**

A Kinematic Broadening **177**

B Ion Beam Production and Manipulation **179**

C Vacuum considerations **182**

D Electronics Calibration **184**

E The paracentric HDA: I. Ideal 1/r potential - Theory **186**
E.1 Energy conservation across potential boundary 186
E.2 Particle refraction across potential boundary 188
E.3 General form of the elliptical trajectory 190
E.4 HDA dispersion 191
E.5 HDA resolution 193

F SIMION3D basics **199**

G Classification of He-like doubly excited states **201**

H The Auger selection rules **202**

I The boron energy level diagram **203**

J Laboratory frame $B^{(2-4)+} + H_2$ spectra **204**

List of Figures

1 Set-up for Zero-degree Auger spectroscopy. 9
2 Zero-degree spectrum obtained by the KSU Tandem spectrometer. . . . 10
3 Velocity addition diagram. 11
4 Two auto-ionizing states with energies 60meV and 100meV, respectively. 13
5 The stretching effect. 15
6 Stretching (compressing) $\Delta\epsilon/\Delta\epsilon'$ between two Auger lines. 16
7 Angular compression of electrons emitted from fast projectiles. 17
8 Geometrical interpretation of the broadening effect. 19
9 Broadening coefficients $\Delta B_{\theta}^{(1)}/\epsilon$ and $\Delta B^{(2)}/\epsilon$ as a function of the laboratory angle θ. 21
10 Top view of the J. R. Macdonald Laboratory. 24
11 The zero-degree experimental setup. 26
12 Chamber pressure as a function of the gas-cell pressure. 28
13 The hemispherical paracentric spectrograph for ZAPS. 29
14 The 4-element electrostatic focusing and decelerating lens. 30
15 Chevron arrangement microchannel plates. 31
16 PSD spatial resolution study. 33
17 The Electronics Diagram. 34
18 XSYS Data Acquisition System output. 35
19 Dead Time Correction as a function of the count rate. 37
20 Schematic diagram of the hemispherical deflector analyser geometry. . . 41
21 Detection plane of hemispherical analyser. 47
22 3-D orbit in HDA. 48
23 Reduced voltages V_1/W and V_2/W applied on the HDA. 50
24 3-D graph of the dispersion D. 53
25 Lens geometry and focusing parameters. 55
26 3-D graph of the overall base-resolution $\Re_b$. 56
27 Mean overall base resolution $\bar{\Re}_b$. 57
28 Theoretical energy calibration curves. 59
29 Constants A,B and C of the energy calibration relation. 60
30 Derivative of the energy calibration relation. 61
31 The energy acceptance window $\Delta\tau_{window}$. 63
32 SIMION simulation for central and paracentric entries. 66
33 SIMION simulation for six different analyser entries R_0. 67
34 SIMION study of base energy resolution. 69
35 SIMION study of trace widths over the PSD area. 70
36 SIMION study of energy resolution over the PSD area. 71
37 SIMION study of reduced acceptance energy window. 72
38 SIMION simulations, theoretical calculations and experimental results on the overall base energy resolution, the universal energy calibration curve, the energy window and the mean overall base energy resolution. 74

39 Energy resolution study as a function of potential parameter γ. 78
40 Experimental energy resolution at FWHM study for different deceleration factors F. 80
41 Comparison of the DDCS $(2p^2)^1D$ spectra at decel factors of F = 1, 4 and 8. 81
42 Absolute DDCS ZAPS spectrum for collisions of 7.79 MeV B^{3+} + H_2, obtained by overlapping ten different energy slices. 83
43 High resolution spectra in the energy region of the $F^{7+}(2p^2)^1D$ RTE peak obtained in collisions of 21.78MeV F^{8+} + H_2. 85
44 DDCS spectra of the $(2p^2)^1D$ formed in collisions of 21.78 MeV F^{8+} + H_2, obtained at deceleration factors of 1,2,4,6 and 8. 87
45 DDCS spectra of the $(2p^2)^1D$ RTE line obtained at deceleration factors of 1,2,4,6 and 8, corrected for the "extra-background". 88
46 SDCS of the $(2p^2)^1D$ RTE line measured at different deceleration factors. 89
47 Performance comparison of the hemispherical spectrograph utilizing a PSD and the KSU tandem slit parallel plate spectrometer. 90
48 Plot of the A, B and C factors of the experimental universal energy calibration relation $\tau_i = A + B\,i + C\,i^2$. 95
49 BEe peak obtained in collisions of 21.7MeV F^{8+} + H_2, recorded at different count rates. 96
50 BEe peak obtained in collisions of 21.78MeV F^{9+} + He, recorded at different target pressures. 98
51 4.4 MeV B^{3+} + Ar spectra recorded in target pressures of 5, 10 and 20 mTorr. 99
52 Artificial raw data (counts vs energy) for a Gaussian electron distribution over energy is obtained from the simulation of the ideal field HDA at three slices of different tuning energies. 101
53 Artificial raw data (counts vs energy) for a Gaussian energy electron distribution obtained from the simulation of the ideal field HDA at deceleration factors of F = 1 and F = 4. 102
54 Artificial spectra of electron energy distribution, consisting of two Gaussian peaks G_1 and G_2, of mean energies 1000eV and 1020eV, and FWHM of 25eV and 1eV, respectively are "recorded" at tuning energies of 1000eV and 1050eV and a deceleration factor F = 1. 103
55 SIMION study of transmission of the hemispherical spectrograph for the case of $\xi = 1.23$ and $\gamma = 1.5$. 104
56 Experimental relative MCP efficiency η as a function of the electron energy detection. 106
57 Absolute MCP efficiency η obtained by the normalization of the experimental data obtained in collisions of 21.5MeV F^{9+} + H_2. 107
58 Absolute MCP efficiency η as a function of the PSD position - channel number. 108
59 Calculated IA–Rutherford BEe DDCSs. 116

60 Compton profiles for H_2, He and Li. 117
61 Experimentally measured BEe DDCSs for the collisional system of 13 MeV$B^{(2-5)+} + H_2$. 122
62 Experimentally measured BEe DDCSs for the collisional system of 4.9 MeV$B^{(2-5)+} + H_2$. 123
63 Experimentally measured BEe DDCS enhancement factors for the collision system of $B^{(2-5)+} + H_2$. 124
64 Absolute Auger electron DDCS spectra showing the KLn (n=2-5) series of doubly excited states of He-like $B^{3+}(2lnl')$. 128
65 Energy level diagram of He-like $B^{3+}(2lnl')$ doubly excited states. 129
66 Absolute Auger electron DDCS spectra for the collisions of 4–8 MeV B^{3+} with H_2 targets. 134
67 Energy level diagram with the dominant production mechanisms for the $(1s2l2l')\,^{(2S+1)}L$ doubly excited states formed in collisions of $B^{3+}(1s^2\,^1S)$ and $B^{3+}(1s2s\,^3S)$ ions with H_2 targets. 136
68 Experimental data for collisions of 3.80 MeV B^{3+} ground state $(1s^2)^1S$ and 4.11 MeV B^{3+} mixed state $(1s^2\,^1S, 1s2s\,^3S)$ ions with H_2 targets. . 139
69 Formation of the $(1s2s2p)^4P$ state in collisions of 4.11 MeV $B^{3+} + H_2$ indicating the existence of a significant metastable $B^{3+}(1s2s\,^3S)$ beam component. 144
70 Lifetimes of the $(1s2s)^3S$ and $(1s2s)^1S$ metastable states as a function of the atomic number Z_p. 146
71 Experimental $B^{3+}(1s2s\,^3S)$ and estimated $B^{3+}(1s2s\,^3S)$ metastable beam fractions as a function of the projectile stripping energy. 147
72 Absolute Auger electron DDCS spectra for the collisions of 4–8 MeV $B^{2+}(1s^22s)$ with H_2 targets. 149
73 Simplified schematic diagram of the DR, RES, RTEX, RTEA. 159
74 SDCS of the $B^{3+}(2p^2\,^1D)$ RTE state as a function of the projectile energy. 167
75 Quadratic fits on the theoretical data of the Auger and X-ray rates A_α and A_r, respectively, of the $(2p^2)^1D$ state of He-like doubly excited ions. 168
76 Resonant Excitation strengths Ω_{RE} of the $(2p^2)^1D$ RTE state as a function of the atomic number Z_p. 168
77 SDCSs of the $2l3l'$ and $2l4l'$ intermediate states formed in collisions of 4–8 MeV $B^{4+} + H_2$. 170
78 SDCS of the $B^{2+}(1s2p^2\,^1D)$ RTE state as a function of the projectile energy. 171
79 Second order broadening coefficient $\Delta B^{(2)}$ as function of the Auger electron energy ϵ' for $\theta' = 0°$ and $\theta = 0°$. 177
80 Second order broadening coefficient $\Delta B^{(2)}$ as function of the Auger electron energy ϵ' for $\theta' = 180°$ and $\theta = 0°$. 178
81 Electronics Calibration Diagram. 185

82 Integration path (bold line) $abcdefa$ used to show energy conservation across the potential step at $\theta_0 = 0$. 187
83 Relation between the entry angle $\alpha^\star$ prior to refraction (angle of incidence) and angle α after refraction (angle of refraction). 189
84 Plot of the semi-major axis as a function of γ and ξ. 192
85 Mean overall base-resolution $\overline{\Re_b} = \overline{\Delta T}/T$ plotted as a function of the lens linear magnification $|M_L|$ for different deceleration factors F. . . . 194
86 Plot of the optimum overall base-resolution as a function of the reduced pass-energy τ for different deceleration factors and of the mean overall base-resolution as a function of the deceleration factor. 195
87 Plot of the image distance d_i (left y-axis) and the lens optimal linear magnification factor $|M_{Lopt}|$ (right y-axis) as a function of the deceleration factor F. 196
88 Average ratio $\overline{\chi} \equiv \chi(\tau = 1)$ for different magnifications $|M_L|$. 197
89 Overall base-resolution $\Re_b = \frac{\Delta T}{T}$ as a function of the reduced pass-energy τ. 198

List of Tables

1 Doubling, shifting, stretching and enhancing frame transformation kinematic effects for $\theta = 0°$ detection. 18
2 Basic geometrical parameters of the ZAPS setup. 38
3 Optimum lens voltages V_{L4} and V_{L5} and mean energy resolution at FWHM for different deceleration factors 81
4 A, B and C constants for the universal energy calibration relation: $\tau_i = A + B\,i + C\,i^2$. 94
5 Experimental quantities related in the determination of the absolute DDCS spectra. 110
6 Classification of the $B^{3+}(2lnl')$ (n = 2–5) doubly excited states ordered by their binding energies. 130
7 KLL Auger electron energies of B^{2+} excited states produced in collisions of $B^{3+}(1s^2\,{}^1S, 1s2s\,{}^3S) + H_2$. 137
8 Binding energies of boron Li-like triply excited states and Auger decay electron energies to the Helium-like B^{3+} $(1s2s)^1S$, $(1s2s)^3S$, $(1s2p)^1P$ and $(1s2p)^3P$ states. 140
9 Auger electron energies of boron Li-like triply excited states de-exciting to the Helium-like B^{3+} $(1s2s)^1S$, $(1s2s)^3S$, $(1s2p)^1P$ and $(1s2p)^3P$ arranged in increasing order. 141
10 Binding energies of the He-like $B^{3+}(1s2l\,{}^{(2S+1)}L)$ states. 142
11 Lifetimes of the $(1s2s)^3S$ and $(1s2s)^1S$ metastable states for different atomic numbers Z_p. 146
12 Auger electron energies of B^{2+} and B^+ excited states produced in collisions of of $B^{2+}(1s^2 2s\,{}^2S) + H_2$. 150
13 $B^{3+}(1s2ln'l'\,{}^{(2S+1)}L_J)$ intermediate states Auger decaying to the $B^{3+}(1s^2)$ ground state. 151
14 Tentative assignments of the unidentified b_i and c_j lines observed in the spectra of $B^{3+} + H_2$ and $B^{2+} + H_2$ according to calculations of the COWAN code. 153
15 Auger energies E_R, Auger rates A_α, x-ray rates A_r, Resonant Excitation strengths Ω_{RE} and the angular distribution term $\hat{W}(\theta = 0°)/4\pi$ for the KLL intermediate states. 165
16 Resonance parameters for the $(2p^2)^1D$ doubly excited state resulting from the collisions of H-like ions with H_2 targets. 169
17 Resonance Excitation strengths Ω_{RE} along with the the corresponding Auger energies E_R and the Auger decay rates A_α. 172
18 Summary of RTEA SDCS and Ω_{RE} measred in this work. 173
19 Table of measured B^{q+} electrical currents at the target. 181

Acknowledgments

Having reached the end of this work, I would like to express my deep thanks to the people who supported and inspired me throughout this period of my life. First of all I thank my supervisor Prof. Theo Zouros, not only for trusting me and assigning me this project, but also for helping and guiding me through the numerous details of the experimental physics. Maybe the greatest lesson I have learnt from him is that usually the most interesting physics lies in the "not so well understood" details. The final form of this dissertation is largely affected by his comments on numerous fine - though essential details on technical and/or physical concepts. I also express my gratefulness to him for giving me the chance to participate in many international conferences and to visit many laboratories in Europe. Thus, I had the privilege to work with pioneer researchers in the field of ion–atom collisions such as Niko Stolterfoht, Bela Sulik and Reinhold Schuch, who I acknowledge at this point for their encouraging interest in my first steps as an experimenter. Furthermore, I acknowledge the Human Capital and Mobility European network program for the financial support of the above activities and the PENED91 (ΠΕΝΕΔ91) and PENED95 (ΠΕΝΕΔ95) programs of the Greek Ministry of Research for the partial financial support of this work. In particular, I express my thanks to Niko Stolterfoht and the Hanh-Meitner Institute, Berlin, for loaning the chamber with the turbomolecular pump and the μ-metal, through the collaboration via the Human Capital and Mobility European network program.

My thanks are extended to the director of the J. R. Macdonald laboratory (JRML) Prof. Patrick Richard, who strongly supported the development of the new experimental setup in JRML. Throughout my stay in Kansas State University (KSU) he always guided and encouraged me to face many persisting problems concerning the mastering of the experimental setup operation. His remarks on the interpretation of the experimental data and the understanding of different physical properties involved with these, were always a guiding path for further investigations. At this point, I acknowledge the financial support of the Chemical Sciences, Geosciences and Biosciences Division, Office of Basic Energy Sciences, Office of Science and the U. S. Department of Energy.

I am greatly indebted to Prof. Chander Bhalla for providing me his codes on the Elastic Scattering Model in order to include theoretical calculations on Binary Encounter electrons for my experimental data. I am also indebted to Prof. Martin Stöckli for his "private lectures" on vacuum and machine shop designing, and to Prof. Tom Gray for teaching me to operate the tandem Van de Graaff accelerator "without solving the Dirac equation". Moreover, I thank Profs. Siegbert Hagmann and Itzik Ben-Itzhak for their help with the electronics and Prof. Chii-Dong Lee for fruitful discussions on the physics of two electron ions.

It is a pleasure to acknowledge at this point Dave Dahl, the creator of SIMION, for his immediate help on certain SIMION design details, through e-mail. I would also like to acknowledge useful communications from Profs. Nick Martin, Jim Erskine, Denis Roy and Bela Sulik about the hemispherical deflector analyser and the lens system, and also Dr. Steffan Schippers for providing his COWAN utilities program. In addition, I thank Dr. Lars Madsen for providing an independent calculation of the binding energies for the triply excited states.

I would like also to express my thanks to the personnel of JRML and the Machine Shop for their politeness and willingness to help, which provided a very friendly and at the same time productive work environment. I especially acknowledge Prof. Kevin Carnes and Vince Needham for their help with the computers, Bob Krause for providing the ion beams even on the weekends, Paul Gibson, Bob Geering, Steve Kelly, Mike Wells and Al Rankin for their generous help on various daily problems.

I also express my gratefulness to Dea Richard for reading and commenting on my English for a large part of my thesis manuscript, and Peggy Mathews for dealing with all the bureaucracy during my stay in KSU.

My gratefulness along with my admiration are extended to my professors in the Department of Physics at the University of Crete, for their high quality lectures during my graduate studies. Furthermore, I express my deep thanks to my colleagues at the University of Crete, Drs. Lambros Nikolopoulos and Zaharias Fthenakis for their true friendship and support throughout the graduate years and mostly through my "army" years. My thanks for this peculiar period of my life are extended to my good friends Christos, Giorgos, Dimitris, Nellie, Aspasia and Sofia. I also thank my colleges at KSU Habib Aliabadi and Michael Zamkov for sharing with me the long beamtime periods. In addition, I would like to thank my roommate this year in Manhattan KS, George and also Brenda, for putting up with me during the writting period of this dissertation. Their belief in me along with their great sense of humor made this period one of the most productive and joyful of my life.

Finally, I would like to express my deep and most sincere thanks along with my true love to my parents for their support all these years. This work is dedicated to them.

Abstract

The basic aim of this work is to describe in detail the implementation of a state of the art hemispherical spectrograph into the zero-degree Auger projectile spectroscopy technique and to provide new absolute differential cross section measurements utilizing very weak intensity beams and/or low cross section processes. A secondary task is the investigation of the spectrograph focusing and dispersive properties independently of the experimental technique, due to the non-conventional *paracentric* entry in combination with the PSD and the focusing/decelerating lens system in use. Binary encounter electrons along with the $(2p^2)^1D$ RTE state, both produced in collisions of 21.6 MeV F^{8+} with H_2 targets were utilized for the study of the spectrograph operational properties. The study was completed with simulations using the ion optics simulation package SIMION and with the theoretical investigation of the ideal 1/r electrostatic potential of a paracentric hemispherical deflector analyser. It is explicitly shown that the paracentric entry improves the analyser focusing properties. An efficiency factor of about 300 - 1,000 compared to the KSU tandem parallel plate analyser slit spectrometer has been established for low intensity beams. Using the ZAPS technique with the new high-efficiency spectrograph the BEe peak enhancement factors for the collision system $B^{(2-5)+} + H_2$, at impact energies of 0.4–1.2 MeV/u were studied. Impulse Approximation Elastic Scattering Model calculations are shown to be in very good agreement with the measurements. These results were used for the *in situ* calibration of the electron detection efficiency. In addition, utilizing the low intensity boron beams available at the tandem Van de Graaff accelerator, first systematic measurements on the B^{q+} (q = 1,2,3) spectroscopy, obtained from collisions of 4–8 MeV $B^{(2-4)+}$ ions with H_2 targets was accomplished. These results showed the formation of the $(2s2p^2)^2D$ Li-like B^{2+} triply excited state in a single ion–atom collision. Furthermore, the metastable $(1s2s)^3S$ component of the B^{3+} beam was determined, a result of potential importance for the determination of absolute cross sections in ion–atom collisions involving the B^{3+} ions. Finally, first measurements on the single differential cross sections (SDCSs) and Resonance Excitation collision strengths (Ω_{RE}) of the $B^{3+}(2p^2)^1D$ and $B^{3+}(1s2p^2)^2D$ Resonance Transfer and Excitation (RTE) states were obtained. Impulse Approximation calculations for RTE followed by Auger decay (RTEA) are seen to be in good agreement with the measurements.

ΟΥ ΜΗΝ ΟΥΔ ΑΜΑ ΚΑΤΑ ΤΟΥΣ ΔΙΑ ΛΟΓΟΥ ΘΕΩΡΗΤΟΥΣ ΧΡΟΝΟΥΣ ΑΥΤΟ ΤΟ ΦΕΡΟΜΕΝΟΝ ΣΩΜΑ ΕΠΙ ΤΟΥΣ ΠΛΕΙΟΥΣ ΤΟΠΟΥΣ ΑΦΙΚΝΕΙΤΑΙ – ΑΔΙΑΝΟΗΤΟΝ ΓΑΡ – ΚΑΙ ΤΟΥΤΟ ΣΥΝΑΦΙΚΝΟΥΜΕΝΟΝ ΕΝ ΑΙΣΘΗΤΩ ΧΡΟΝΩ ΟΘΕΝ ΔΗΠΟΘΕΝ ΤΟΥ ΑΠΕΙΡΟΥ ΟΥΚ ΕΞ ΟΥ ΑΝ ΠΕΡΙΛΑΒΩΜΕΝ ΤΗΝ ΦΟΡΑΝ ΤΟΠΟΥ ΕΣΤΑΙ ΑΦΙΣΤΑΜΕΝΟΝ

Not that, if we consider the minute times perceptible by reason alone, the moving body itself arrives at more than one place simultaneously (for this too is inconceivable), although in time perceptible to sense it does arrive simultaneously, however different the point of departure from that conceived by us.

Letter to Herodotus

Epicurus

(around 300 B.C.)

1 Introduction

"It is indeed fascinating that ion-atom collisions in the 20–30 MeV energy region provide a detailed test of delicate quantum mechanics in the few hundred eV region" Knut Taulbjerg [1]. The previous statement made by Knut Taulbjerg[1] in his Journal of Physics Letter in 1990 on the interpretation of the "anomalous" enhanced binary encounter electron peak yield at zero-degree observation [2], shows most clearly the unexpected and sometimes astonishing physical processes underlying ion-atom collisions. The "scattering experiment", initiated in 1911 by Rutherford in his famous experiment of bombarding thin gold films with α-particles [3], has long been known to provide valuable information both on the structure and on the interaction potential of the collision partners involved. The fundamental aspects of atomic collision theory were already formulated by Mott and Massey in their monumental work first published in 1933 [4]. However, interest remained focused solely on nuclear physics for the next 30 years.

It wasn't until the early 1960's when the tandem Van de Graaff ion accelerators, popular in nuclear physics by that time, were implemented in atomic physics, primarily due to the fact that projectile-ions can excite atomic states inaccessible by photon and electron impact. Shortly, the use of light ions, available in most of the charge states and in a wide band of collision energies, became a unique tool in atomic physics studies. At the same time, the increasing interest in the investigation of the Auger and autoionization effects made the use of electrostatic spectrometers wide spread. Today, tandem Van de Graaff accelerators, Linear Accelerators, Electron Cyclotron Resonance (ECR) ion sources, Electron Beam Ion sources (EBIS) and Storage Rings, can provide atomic ions from hydrogen to uranium in all charge states and in energies varying from a few eV/u to hundreds of MeV/u, depending on the atomic species, the charge state and the source in use. A large variety of energy dispersive spectrometers like the parallel plate spectrometer, the cylindrical plate spectrometer, the toroidal spectrometer, the hemispherical analyser and spherical plate spectrometer are also extremely popular, indicating the continuous interest in the physics of ion-atom collisions, as also the wide development of different experimental techniques, as for example the most modern COLd Target Recoil Ion Momentum Spectroscopy (COLTRIMS) experiments.

Aside from the possibility to improve theories of ion-atom interactions through comparisons with experimental data, ion-atom collisions results play an essential role in developing and providing important cross section data to other scientific branches of physics, such as plasma physics, astrophysics, nuclear physics and solid state physics, as well as in other sciences such as chemistry, biophysics and medicine. For example, the properties and behavior of magnetically confined thermonuclear plasmas strongly depend on energy-loss mechanisms. The accurate knowledge of the cross section of such processes is of vital importance for an adequate kinetic modeling of plasma. Similar arguments can be stated also for the domains of the controlled nuclear fusion and the

[1]Sadly, Knut Taulbjerg passed away after a short and courageous battle with cancer in March 2001.

modeling of astrophysical plasmas. Furthermore, interest in electron emission cross sections is especially widespread in applied particle physics such as radiobiology since about 2/3 of the energy loss of the ion is transferred into kinetic energy of δ electrons. [5]

In this dissertation, the interest is focused on the Auger electrons emitted from the projectiles during energetic collisions between highly charged ions and atoms. The Auger electrons carry the signature of the processes that occurred during the collision time, providing thus invaluable information about the structure of the charged particles and the collision mechanisms. Most important, projectile Auger spectroscopy has direct access to investigate free atomic ions. [6–10] Atoms are provided in a large variety of charge states and a wide spread of kinetic energies from the ion sources and accelerators, allowing thus, for the detailed study of most of the atomic species under ionized conditions.

Foils were initially used as targets in Auger projectile spectroscopy. The beam-foil technique [11] has the advantage of a localized target region with respect to the beam direction thus favoring coincidence measurements. The major disadvantage of this method, however, is that single collision conditions are not satisfied as the ions may suffer multiple charge-changing collisions during their passage through the foil. The Auger line-blending due to numerous Auger lines, combined with the different projectile charge states emerging from the beam-foil collision, is also a major difficulty in the analysis of the Auger spectra.

The problems of line-blending and multiple charge-changing collisions in the beam foil technique are simplified when gas targets are used instead of solid state ones. Gas density is many orders of magnitude smaller than the foil target and thus single collision conditions can be readily satisfied and controlled. Furthermore, the use of light atoms (H_2,He) as targets may simplify even more the Auger spectrum by reducing substantially the amount of states produced in violent ion-atom collisions. It is well known that light atoms act like a "needle", selectively ionizing or exciting the inner shell, without disturbing the outer shell. [8, 10] Thus the study of Auger electrons from various selected projectile charge states is possible.[2] Furthermore, light projectiles have small fluorescence yields but much larger Auger electron yields, thus favoring Auger spectroscopy for investigating low-Z projectile autoionizing states formed in the collision.

Projectile ions are mostly moving at relatively high velocities. Consequently, the Auger lines suffer considerable kinematic effects. [8] A very popular method to improve the intrinsic analyser resolution, is to perform electron deceleration prior to their analysis in the spectrometer. However, the tremendous decrease of the electron transmission, present in all spectrographs utilizing slits, sets a practical limit on the applied deceleration and therefore on the achieved energy resolution. To improve the energy resolution the Auger electrons are detected at 0° or 180° with respect to the beam direction, as in this way substantial reduction of the kinematic broadening can be achieved. [6]

[2] The phenomenon of one or at most two electrons being ionized, excited or captured in the projectile ion without affecting the other electrons has been referred to as "ion surgery", and in the case of ionization (excitation) as "needle" ionization (excitation). [9]

The technique of detecting Auger electrons emitted from projectiles at 0° with respect to the beam direction, is known as Zero-degree Auger Projectile Spectroscopy (ZAPS) and has received considerable attention the past two decades. [10, 12] The potential advantage of the technique is that it is the *only* efficient method which can provide *state-selective* cross section information about collision mechanisms. X-ray crystal spectrometry, while having similar resolutions, suffer from very low efficiency. [13] COLTRIMS, even though it enjoys similar resolutions but with tremendous efficiency, it only works for relatively low energy electrons (<300eV). [14] ZAPS is the experimental method this dissertation is involved with. The advantages as also the limitations of the method along with specific aspects of the technique, are examined in detail in chapter 2.

Dissertation Goals

Over the past two decades, Zero-degree Auger Projectile electron Spectroscopy has provided unique information on KLL state-selective double differential and single differential cross sections measurements for the ionization, excitation and capture mechanisms of few-electron highly-charged ions in collisions with light targets. In particular, combinations of these processes such as transfer and excitation, transfer loss, electron-electron excitation, etc., have been successfully measured and interpreted providing important insights into correlation mechanisms. The tandem parallel plate analyser (PPA) slit spectrometers was favorably utilized for the all these measurements due to its basic simplicity.

However, certain experimental aspects of the implementation of the tandem PPA in ZAPS set insuperable limits on the attainable cross-section measurements. KLL state selective measurements require high energy resolution ($\simeq$1 eV), which primarily depends on the geometrical characteristics of the analyser. The instrumental resolution is proportional to the width of the analyser apertures and inversely proportional to the distance between them. Apertures cannot be made too small (1mm diameter is a typical circular aperture dimension) as the intensity lessens quadratically with the aperture width. Besides, analyser dimensions cannot be enlarged at will. Thus a certain limit on the energy resolution is set by the spectrometer, which is about 1–3%. In addition, the high resolution operation (under deceleration mode) has the side effect of the tremendous intensity loss, resulting in a rather long acquisition time for a decent statistics spectrum. Furthermore, relatively high beam currents are needed (50–200 nA is a typical value) which are not available for certain species or charge states in the ion sources and accelerators in use.

In this dissertation, a novel high-efficiency hemispherical spectrograph is proposed as an alternative solution for future ZAPS measurements. The spectrograph, quite common in fields such as electron spectroscopy for chemical analysis (ESCA) [15], and time-resolved electron energy loss spectroscopy (TREELS) [16], is implemented for the first time in the ZAPS technique. A novel feature of the hemispherical spectrograph

is its *paracentric* entry, i.e., an entry R_0 smaller than the conventional central entry $\bar{R} \equiv (R_1 + R_2)/2$, where R_1 and R_2 are the inner and outer radii of the analyser, respectively. It has been explicitly shown in this work that the paracentric entry improves the analyser focusing properties. [17] Furthermore, it is the first time that a *single-stage* spectrometer is successfully implemented in ZAPS, as previous attempts, using a 30° PPA [18] failed primarily due to the extremely high production of secondary electrons which dominated the spectra especially in the deceleration operation mode.

The spectrograph described here, consists of a 4-element focusing lens, a hemispherical analyser and a large 40mm diameter 2-dimensional position sensitive detector (2D-PSD). The four-element lens, mounted at the entrance of the spectrometer, provides a virtual slit for the incoming electrons, by focusing while at the same time decelerating them, to improve their energy resolution. The potential advantage of the lens is that the electron intensity remains almost unaffected in the deceleration mode of operation ($\sim$ 100% transmission through the lens) - a fact that was the primary source of low transmission in tandem PPA slit spectrometers. The large size of the hemispherical analyser (101.6mm mean radius) is important both for the the reduction of the background electron signal and for the initial energy resolution (non-decelerating operation mode). The *paracentric* entry of the analyser also improves the energy resolution relative to the central entry case, thus being a correction scheme for the large fringing field effects. The analyser is run at fixed voltages so that a whole energy spectrum slice ($\simeq$20% of the tuning energy) can be collected at once with substantial savings in collection time, over the voltage stepped mode used in the tandem PPA analysers. The double focusing properties of the hemispherical analyser together with the time saved in data collection, greatly improves the overall efficiency for the electron detection and the analysis. Therefore, the huge gain (> 300) in spectra acquisition time is expected to allow for including low intensity beams in ion-atom studies as well as much lower cross section processes.

It is the primary purpose of this work to describe in detail the implementation of such a state of the art device into the ZAPS technique as well as to provide new measurements utilizing weak intensity beams and/or low cross section processes. Moreover, the *paracentric* entry of the hemispherical spectrograph implies an investigation of the spectrograph focusing and dispersive properties independent of the experimental technique in use, which is the secondary purpose of this work. It is expected that the successful implementation of the high-efficiency hemispherical spectrograph into the ZAPS technique will make the method even more applicable as a standard investigation tool.

Dissertation Outline

In chapter 2, the ZAPS technique is examined in detail. Its application in ion-atom collisions utilizing tandem parallel plate slit spectrometers is reviewed along with the most important results on state selective cross section measurements available to

date. The kinematics frame transformation effects of peak doubling, energy shifting, line stretching, angular compression and peak height enhancement, in addition to line broadening effects are theoretically investigated and further commented. Limitations of the method arising from the low electron detection efficiency of the tandem parallel plate slit spectrometers, are explicitly pointed out, proposing at the same time the new high-efficiency hemispherical spectrograph as an alternative solution for the future of ZAPS measurements.

In chapter 3, the ZAPS experimental station setup at the J. R. Macdonald laboratory at Kansas State University is described. The hardware components utilized, the spectrograph consisting of the hemispherical detector analyser (HDA), the focusing/decelerating lens and the two-dimensional position sensitive detector (2D-PSD), the vacuum conditions, the electronics and the data acquisition system are described in fine detail. In addition, the geometrical parameters of the spectrograph in relation to the experimental setup are also provided.

Chapters 4, 5 and 6 can be seen as a trilogy in investigating the new spectrograph optimum operation in relation to its focusing and dispersive properties, theoretically, with simulations and experimentally, respectively. Specifically, in chapter 4 the problem of the electron trajectories followed inside the ideal electrostatic potential 1/r of a hemispherical deflector analyser is solved for the first time for the most general case of arbitrary charged particle entry R_0 and arbitrary entry potential $V(R_0) \equiv V_0$. In the literature, this problem was only partially solved for central entry $R_0 = \bar{R} \equiv (R_1 + R_2)/2$, where R_1 and R_2 are the two hemispheres radii, and $V_0 = 0$ V entry potential. The problem of particle refraction across a potential boundary, present in all analysers but not well treated in the literature, was also elucidated, establishing a refraction law, analogous to Snell's law in light optics. The paracentric HDA operation voltages, the focusing conditions and the properties of magnification, dispersion, angular aberration, energy resolution, energy calibration and energy acceptance window are investigated using the previously obtained general charged particle trajectory equation as the starting point. Results on the previous properties from simulations using the SIMION simulation package and from experimental measurements are shown in comparison to the theoretical calculations for the ideal 1/r potential HDA. In this way the fringing field effects, due to the departures from the ideal 1/r field, are identified and qualitatively treated.

In chapter 5, the electron trajectories followed inside the hemispherical spectrograph are simulated using the SIMION ion optics simulation package. A more realistic study using simulated non-ideal HDA potentials is performed for investigating in more detail the spectrograph focusing and dispersive properties as a function of the entry R_0 and the potential V_0. It is explicitly shown that for the non-ideal field, the paracentric entry significantly improves the energy resolution over that of the conventional central entry. Although SIMION does not reproduce quantitatively the experimental results, a general qualitative agreement between SIMION and experiment, which deviates from the theory of the ideal 1/r potential, is observed. Furthermore, it is indicated that the paracentric entry along with the non-zero entry potential is seen to compensate for

the the fringing field effects, in the sense that improved quality focusing conditions are achieved despite the presence of large fringing fields. The paracentric entry along with the non-zero entry potential is proposed as an alternative correction scheme over the cumbersome implementation of fringing field correctors.

In chapter 6, the *real* spectrograph performance is tested through certain measurements. First, the experimental lens and analyser voltages parameterization, complete the studies of the focusing properties. Then the performance of the spectrograph in low resolution mode is presented with a new measurement of a zero-degree double differential cross section (DDCS) obtained in collisions of 7.79 MeV B^{3+} with molecular hydrogen targets. The low resolution spectrum is shown to be obtained after successfully matching ten different energy slices of the same spectrum. The performance in high resolution mode, on the other hand, is depicted by comparing DDCS measurements of the 21.6 MeV F^{8+} + H_2 collisional system, recorded at different energy resolutions. The obtained single differential cross section (SDCS) results for the $(2p^2)^1D$ RTE line, present in the DDCS spectrum, are shown to be similar independent of the resolution attained, which is the strongest indication of the proper performance of the spectrograph. Special considerations on the reliability of the absolute cross-section results are further discussed. Finally, an overall efficiency comparison of the new hemispherical spectrograph and the KSU tandem parallel plate spectrometer is made, showing that the new spectrograph is about 300 times faster when low intensity ion beams are utilized. This huge gain in spectra acquisition time is actually expected to make the ZAPS technique even more applicable as a standard investigation tool, opening up new possibilities.

In chapter 7, the method for determining the absolute DDCSs from the experimental raw data, obtained with the new spectrograph, is presented in detail. The energy calibration of the spectra along with the determination of all the geometrical and other experimental factors which may affect the final absolute DDCS results, are discussed and further commented. The binary encounter electron peak normalization is used for the absolute determination of the electron detection efficiency, which essentially provides the absolute results on the DDCS spectra. In addition, an artificial model of the HDA operation, simulating the experimental electron detection was developed in FORTRAN code, the results of which, not only illustrated the correctness of the data analysis method, but also pointed out significant details on the process of spectra overlapping. Finally, the error analysis is also included in this chapter.

In chapter 8, first new data on the Binary Encounter electron (BEe) peak enhancement factors for the collision system of 4–8 MeV $B^{(2-5)+}$ + H_2 are reported. The boron ion beam is one of the weakest beams available and its use in ZAPS with the conventional tandem PPA slit spectrometers was practically impossible. Experimental results clearly show the well known BEe DDCS increase with decreasing ion charge state observed in the past for similar collisional systems. Calculations with the Elastic Scattering Model (ESM) utilized within the Impulse Approximation (IA) show a very good agreement with the experimental data. Therefore, the ESM model is proposed as a benchmark for the *in situ* determination of the absolute electron detection efficiency

by normalizing the experimental BEe spectra of $B^{(2-4)+}$ ions impinging on H_2 targets, to the ESM calculations on BEe DDCSs. In addition, it is shown that the information on the BEe DDCS enhancement factors can be used with the Rutherford BEe DDCS instead of the ESM calculations for conveniently obtaining quick and at the same time reliable results.

In chapter 9, the first systematic measurements on the B^{q+} (q = 1,2,3) spectroscopy, obtained from collisions of 4–8 MeV $B^{(2-4)+}$ ions with H_2 targets is presented and compared to previous works. As already mentioned, the implementation of the high-efficiency hemispherical spectrograph at the J.R. Macdonald laboratory facilities, allowed for including boron ions in ion–atom collision studies, as the boron ion beam is one of the lower intensity beams. The observed Auger spectra are presented in absolute DDCSs, utilizing results from the previous study in BEe enhancement factors for partially stripped boron ions. The Auger line identification energy and energy determination is seen to be in very good agreement with previous available measurements or calculations. Two very interesting results are pointed out from this study. The first is the observation of the $(2s2p^2)^2\bar{D}$ and $(2s2p^2)^2D$ Li-like B^{2+} triply excited states, i.e. the formation of *hollow* boron ions, in collisions of 4–8 MeV B^{3+}+ H_2. The second is the observation and the quite accurate determination of the metastable $(1s2s)^3S$ component of the B^{3+} beam. This result is of potential importance for the determination of absolute cross sections in ion–atom collisions involving the B^{3+} ions.

In chapter 10, the experimental data of the Auger spectra of the 4–8 MeV B^{4+} + H_2 and 4–8 MeV B^{3+} + H_2 collision systems are used to obtain the first measurements on the SDCS of the $(2p^2)^1D$ and $(1s2p^2)^2D$ RTE states, respectively. IA - RTEA calculations are seen to be in good agreement with the measurements.

Finally, in chapter 11 a summary of the new results is made and future prospects in the use of this highly efficient spectrograph are discussed. The fine details of different theoretical or experimental aspects of this work have been placed in the appendices, in order not to tire the reader. Also, all the publications to date and contributions to different international conferences involving this work are listed at the end of this dissertation.

2 The technique of Zero-degree Auger Projectile Spectroscopy (ZAPS)

2.1 Introduction

The past two decades, fundamental atomic collision processes such as excitation, ionization and capture, were successfully investigated, both experimentally and theoretically, by using simplified ion-atom collision systems. *Projectile* electron spectroscopy of few–electron *highly–charged* ions in collisions with simple targets, such as H_2 and He, provided unique experimental conditions for studying basic interaction mechanisms. The large variety of highly charged ions available at a wide range of energies and charge states, is the main advantage of the method. The main disadvantage though, is the kinematic line broadening effects, which limits the Auger spectra resolution and therefore its usefulness. Broadening effects strongly depend on the detection angle. However, as it will become clear in this chapter, electron detection at 0° or 180° with respect to the beam direction, substantially reduces the broadening effects. The first measurements at these favorable angles were reported at 180° for low keV/u collisions [19–21], at 0° for high (1-5MeV/u) [6, 7] and intermediate (15-150keV/u) [22–24] collision energies. Ever since, only zero-degree measurements have been reported, mainly due to the fact that, for high energy collisions, electron detection at 180° is not possible. The method of projectile Auger electron detection at zero-degrees is known as Zero-degree Auger electron Projectile Spectroscopy (ZAPS). [10]

ZAPS utilization has provided unique information on *state-selective* differential cross sections, for basic collision mechanisms such as transfer and excitation [22, 25], resonance transfer and excitation [26–32] electron-electron excitation [33, 34], electron-electron ionization [35–37] and double electron capture [23, 38–41]. Furthermore, electron production mechanisms such as cusp electrons [42, 43] and binary encounter electrons ([44] and references therein) were also successfully investigated.

Today, ZAPS is used by more than 15 laboratories in Europe, US, Japan and South America to investigate the interaction mechanisms of highly charged ions with atoms, at collision energies ranging from a few keV to hundreds of MeV. ZAPS is the only efficient known method that can provide information on *state-selective* cross sections for basic ion-atom collision processes. Its results are used in practical applications as in plasma physics, in thermonuclear fusion research, in astrophysics and in biophysics. On the other hand, theoretical ion-atom collision models, largely successful up to now in total and single differential cross-section predictions, are more stringely tested using state-selective double differential cross section measurements. Furthermore, few electron collision systems, mostly utilized with ZAPS, provide a simple ground for studying the many-body problem, with emphasis on electron-electron interactions.

Until recently, all ZAPS measurements used the tandem parallel plate electrostatic spectrometer, in which two parallel plate analysers are joined together in series. The tandem spectrometer was preferred instead of the single stage parallel spectrometer, as it was proved to substantially improve the signal to noise ratio, by reducing the

background. [6] In general, an experiment in ion–atom collisions utilizing a tandem spectrometer in the ZAPS technique is performed in the following way:

The ion beam is driven through a gas target where the collisions take place. Only the electrons which are emitted at zero-degrees with respect to the beam direction reach the entrance of the first analyser. Large apertures are used at the front and back plate of the first analyser, for preventing the ion beam from hitting the plates, during its passage through the analyser. Its trajectory remains unaffected by the analyser voltages due to its very high kinetic energy. The second analyser has much narrower apertures providing the desired high energy resolution. Further resolution improvement is obtained by applying electron deceleration between the two analysers.[3] The spectrum is obtained by scanning the analyser voltages in a stepping mode and recording the electron intensity for each step. A typical ZAPS experiment using tandem parallel plate analyser is shown in Fig. 1.

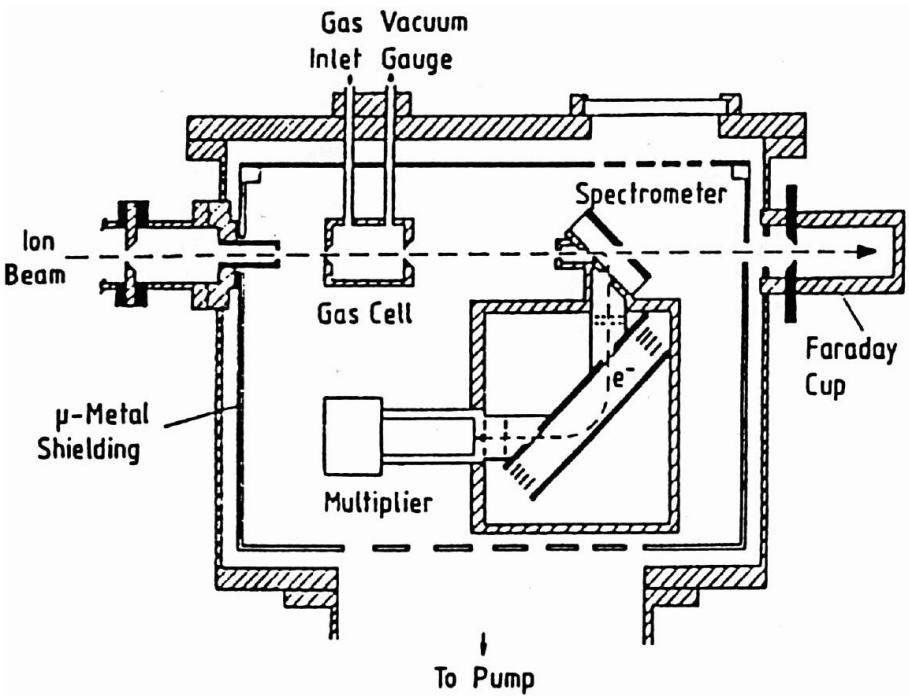

Figure 1: Typical experimental set-up for Zero-degree Auger spectroscopy utilizing a tandem parallel plate analyser. From Itoh and co-workers [6]

Typical zero-degree low resolution spectra of 30MeV $O^{5+} + H_2$ are shown in Fig. 2. The intense sharp peak at the left part of the spectrum, centered at energy t=1028eV, is known as the *cusp* peak. The processes involved with the cusp peak are the electron capture to the continuum (ECC) and the electron loss to the continuum (ELC). [42] During the ECC process, electrons from the target are captured to the continuum

[3]Pre-deceleration is typically used to improve the overall resolution of any electrostatic spectrometer whose resolution $\Delta T/T$ is constant, since reducing energy T must necessarily also reduce ΔT. [10]

spectrum of the projectile, while during the ELC process, electrons from the projectile are excited to the continuum spectrum of the projectile. The cusp peak, present only at zero-degree measurements, plays an important role in the determination of the beam kinetic energy, since cusp electrons are moving at the same velocity as the projectiles [12, 43, 45].

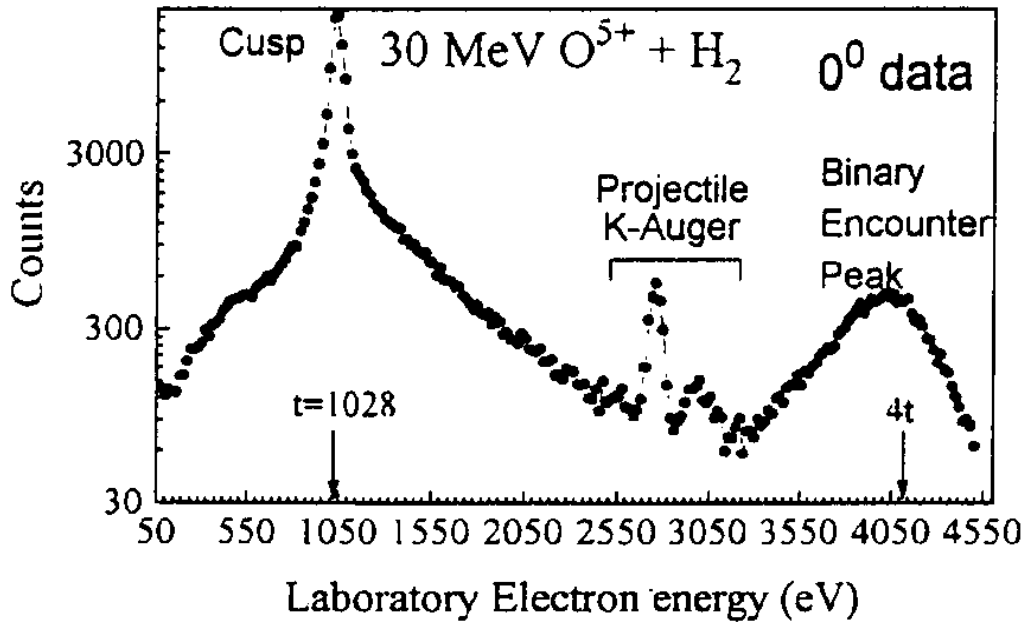

Figure 2: A typical Zero-degree spectrum obtained by the KSU Tandem spectrometer. (from Ref. [10])

The broad peak at the right part of the spectrum, centered at energy $\simeq$ 4t, is known as the Binary Encounter electron (BEe) peak. [44] Binary-encounter electrons are target electrons ionized through direct, hard collisions with energetic projectiles. BEe double differential cross-sections (DDCS) of bare ions colliding with H_2 or He targets, were used in the past for determining the electron detection efficiency, thus obtaining absolute DDCSs on electron spectra. [46] The method is utilized on data normalization in this dissertation. Details on the physics of the BEe and their utilization in ZAPS will be presented in chapters 7 and 8.

The peaks located between the cusp peak and the BEe peak in Fig. 2 are the projectile K–Auger lines. K–Auger peaks spectral location depends on the beam energy. In a zero-degree spectrum L–Auger lines can also be detected and are located symmetrically at the shoulders of the cusp peak. Target Auger lines may also be present in a ZAPS spectrum. The continuum character of the leftmost part of the spectrum is due to "soft" electrons, which are target electrons ionized by the projectile in soft, small momentum transfer, collisions. [47]

2.2 Kinematic Effects

Auger electrons emitted from scattered projectiles are kinematically influenced. A detailed analysis of the general electron kinematic effects can be quite complicated [8]. However, for the case of energetic collisions of a few MeV/amu or larger, studied in this dissertation, projectile ions are scattered through very small angles ($\sim$ mrads), resulting in negligible effects both on the energy loss and on the projectile electron trajectories.

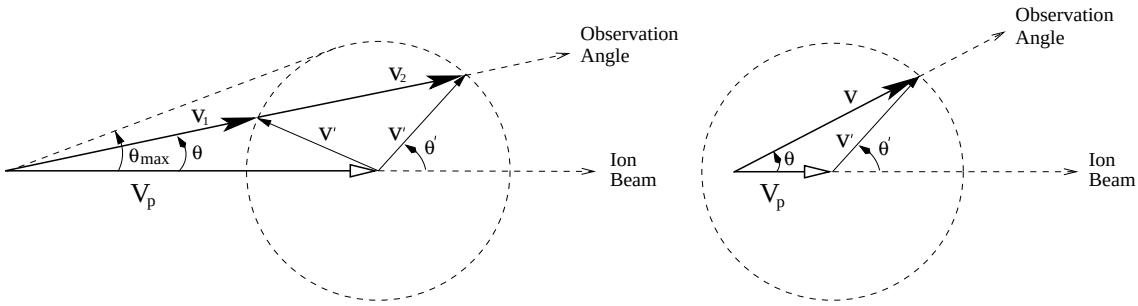

Figure 3: Velocity addition diagram. The electron velocity $\mathbf{v}'$ in the projectile rest frame is transformed in the laboratory frame according to the vector addition rule as $\mathbf{v} = \mathbf{V_p} + \mathbf{v}'$ [*Left*] Emitter velocity is larger than the electron velocity $V_p > v'$. [*Right*] Emitter velocity is smaller than the electron velocity $V_p < v'$

Thus, for simplicity, the projectile ion scattering angle in swift collisions can be safely assumed to be zero. With this consideration, a simple velocity vector addition model is sufficient for determining the projectile-to-laboratory frame transformation and related kinematic effects, as the ion-recoil effects can be overlooked. The velocity $\mathbf{v}$ of the Auger electron in the laboratory frame is obtained by adding the projectile velocity $\mathbf{V}_p$ to the velocity $\mathbf{v}'$ of the electron in the projectile rest frame as shown in Fig. 3. Denoting by primed symbols the quantities in the projectile rest frame, the electron kinetic energy $\epsilon = \frac{1}{2}mv^2$ in the laboratory frame can be related to the corresponding rest frame electron kinetic energy $\epsilon' = \frac{1}{2}mv'^2$ as:

$$\epsilon = \epsilon' + t + 2\sqrt{\epsilon' t}\ cos\theta' \tag{1}$$

or equivalently

$$\epsilon' = \epsilon + t - 2\sqrt{\epsilon t}\ cos\theta \tag{2}$$

where

$$t = \frac{1}{2}mV_p^2 = \frac{m}{M}\ E_p\ =\ 548.58\ \frac{E_p(MeV)}{M(amu)}\ (eV) \tag{3}$$

is the reduced projectile energy known also as the *cusp* energy. E_p and M are the kinetic energy and mass of the projectile respectively, while m is the electron mass.

2.2.1 Frame Transformation Effects

In order to systematically study the kinematic transformation properties of the experimentally measurable physical quantities, it is convenient to adopt the universal dimensionless parameter ζ [10]

$$\zeta \equiv \sqrt{\frac{t}{\epsilon'}} = \frac{V_p}{v'} \tag{4}$$

Also, it is experimentally convenient to express the relation between the energies in rest and laboratory frame as a function of the *laboratory* observation angle θ. Using simple trigonometric rules in Fig. 3 geometry and the introduced parameter ζ, the energy in the laboratory frame can be written as

$$\epsilon_{\pm}(\theta) = \epsilon'(\zeta \cos\theta \pm \sqrt{1-\zeta^2 \sin^2\theta}\ )^2 \qquad (\zeta > 1,\ \ 0 < \theta < \arcsin\frac{1}{\zeta}) \tag{5}$$

$$\epsilon(\theta) = \epsilon'(\zeta \cos\theta + \sqrt{1-\zeta^2 \sin^2\theta}\ )^2 \qquad (\zeta < 1,\ \ 0 < \theta < 180^\circ) \tag{6}$$

As illustrated in Fig. 3, for fast emitters ($V_p > v'$ or $\zeta > 1$) there can be two possible solutions for the laboratory electron energy ϵ as a function of the laboratory detection angle θ, while for slow emitters ($V_p < v'$ or $\zeta < 1$) there is only one solution. For fast emitters ($\zeta > 1$) the constraint $\zeta^2 \sin\theta^2 \leq 1$ results in a restriction in the observation angle θ with a maximum value

$$\theta_{max} = \arcsin\frac{1}{\zeta} \tag{7}$$

This is a crucial limitation for non-zero degree Auger Projectile Spectroscopy since different electron energies correspond to different maximum detection angles, applying a lower limit on the electron energies accessible to the spectrometer. However, for $\theta = 0^\circ$ (i.e. ZAPS technique) the whole projectile electron energy range is accessible. This is one of the most important advantages for measuring electron spectra at zero degrees. Eqs. 5, 6 result for zero-degree observation [4]

$$\epsilon_+ = (\sqrt{\epsilon'} + \sqrt{t}\ )^2 = \epsilon'(1+\zeta)^2 \qquad (\ All\ \ \zeta,\ \theta' = 0^\circ,\ \theta = 0^\circ\ ) \tag{8}$$

$$\epsilon_- = (\sqrt{\epsilon'} - \sqrt{t}\ )^2 = \epsilon'(1-\zeta)^2 \qquad (\ \zeta > 1,\ \theta' = 180^\circ,\ \theta = 0^\circ\ ) \tag{9}$$

Kinematic effects change the position, energy width and intensity of an Auger line and are referred to in the literature as *shifting, stretching* and *enhancing*, respectively. Also the possible occurrence of the same Auger line at two different electron energies in the spectrum is referred as *doubling*. [8] In Table 1 all the results of the kinematic transformation analysis are summarized for the case of zero degree laboratory detection angle. A detailed presentation of each case follows.

- Doubling: It has already been shown (see Fig. 3 and Eq. 5), that there can be two possible solutions for the laboratory electron energy ϵ, resulting in the observation

[4] For 180° observation Eqs. 5, 6 result in $\epsilon = \epsilon'(1-\zeta)^2 \qquad (\zeta < 1,\ \theta' = 180^\circ,\ \theta = 180^\circ\ )$

of two peaks in the laboratory frame which correspond to the same Auger line. The phenomenon is known as *doubling* and an example of it is given in Fig. 4. The two Auger peaks appear symmetrically around the cusp peak as predicted by Eqs. (8) and (9). In this way, forward-backward asymmetries of inelastically scattered quasi-free target electrons from ions were successfully studied. [48] Doubling find practical application in the accurate determination of the beam energy [8].

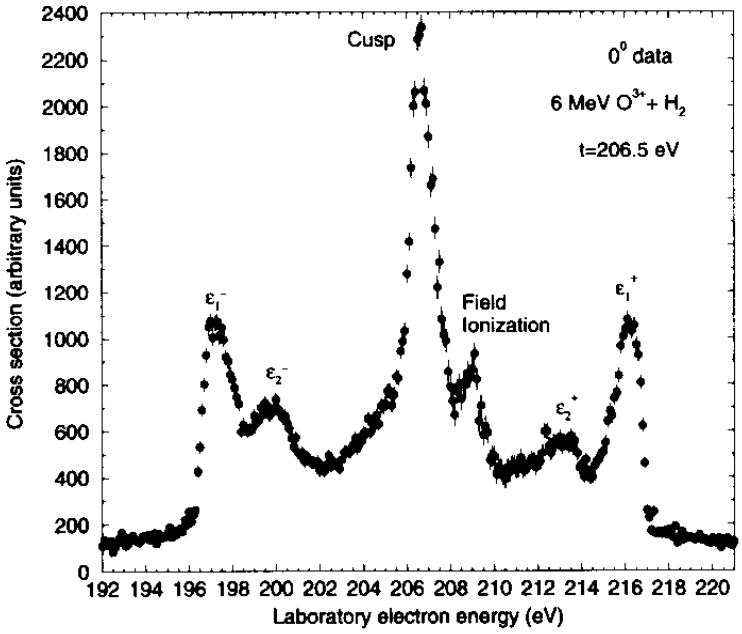

Figure 4: Example of detection of two auto-ionizing states with energies 60meV and 100meV, respectively, at laboratory energies around 200eV, in collisions of 6MeV O^{3+} + H_2. Each peak appears symmetrically around the cusp peak due to the doubling effect. The small peak at the right shoulder of the cusp peak, is due to the field ionization of projectile Rydberg states inside the analyser. From Ref. [10]

- Shifting: Eq. 1 shows that an electron emitted at energy ϵ' in the projectile rest frame, will be detected in the laboratory frame at a different energy ϵ. Forward electron emission in the projectile rest frame, ($\theta' = 0°$) yields a larger laboratory energy, while backward electron emission ($\theta' = 180°$) yields larger or smaller laboratory energy values depending on the ζ value. The fact of detecting an Auger line at energy larger than the physical value is very important in ZAPS, as it allows the detection of very low energy electrons. For example, in the spectrum of Fig. 4, the two auto-ionizing states shown, have rest energies of 60meV and 100meV, respectively. They are detected though at laboratory energies around 200 eV. It should be emphasized at this point, that detection of electrons with energies less than 10eV becomes an increasingly difficult task, since low energy electrons can be readily affected by very small stray magnetic and electric

fields such as the earth's magnetic field or the contact potentials fields developed at the interface between two different metal surfaces.

- Stretching: The energy width $\Delta\epsilon$ of an Auger line observed in the laboratory frame differs from the corresponding width $\Delta\epsilon'$ in the projectile rest frame. Differentiating Eq. 1 with respect to ϵ' results for zero-degree observation angle in:

$$\frac{\Delta\epsilon}{\Delta\epsilon'} \simeq \frac{d\epsilon}{d\epsilon'} = \sqrt{\frac{\epsilon}{\epsilon'}} = |1 \pm \zeta| \qquad (\theta = 0^\circ) \tag{10}$$

It is clearly seen that for the case of (+) solution (forward electron emission in the projectile rest frame, i.e. $\theta' = 0$) line stretching is established, while for the case of (-) solution (backward electron emission in the projectile rest frame, i.e. $\theta' = \pi$) a line stretching or compression is established depending on the ζ value (see Table 1). It is very important to note that the energy stretching (or compressing) does not increase the overlap of two closely neighboring Auger lines. Therefore it does not wash out intrinsic structures of the spectrum. That is due to the stretching (compressing) of the mean values of the Auger lines by practically the same amount as their widths. An example of this stretching effect is given in Fig. 5, where the Auger decaying states of $(1s2s2p)^2P_+$ and $(1s2p^2)^2D$ of F^{6+} formed during collisions of 21.78MeV $F^{7+} + H_2$, are plotted in the laboratory (top) and projectile (bottom) rest frames, respectively. The ratios of the energy widths and energy difference of the two lines, measured in the laboratory and projectile frames, are identical: $\Delta\epsilon/\Delta\epsilon' = \Delta\epsilon_{p-p}/\Delta\epsilon'_{p-p} = 2.08$. Although the line overlap is not affected by the stretching effect, the energy resolution $\Delta\epsilon/\epsilon$ *does* change. This can easily be derived from Eq. 10:

$$\frac{\Delta\epsilon}{\epsilon} = \sqrt{\frac{\epsilon'}{\epsilon}}\,\frac{\Delta\epsilon'}{\epsilon'} \tag{11}$$

However, for two peaks located within a certain energy interval, one should be careful in calculating the peak stretching (compressing). Eq. 10 is not valid for relatively large energy intervals. In order to calculate the correct formula in this case, two lines at energies ϵ'_1 and ϵ'_2 differing by the energy interval $\Delta\epsilon'$ are considered and subtracted mutually according to Eq. 1 yielding

$$\frac{\Delta\epsilon}{\Delta\epsilon'} = 1 \pm 2\,(\frac{t}{\epsilon'_1})\,(\frac{\epsilon'_1}{\Delta\epsilon'})(\sqrt{\frac{1+(\Delta\epsilon'/\epsilon'_1)}{t/\epsilon'_1}} - \sqrt{\frac{\epsilon'_1}{t}}\,) \qquad (\theta = 0^\circ) \tag{12}$$

For $\Delta\epsilon'/\epsilon'_1 << 1$, Eq.10 is obtained. In Fig. 6 a plot of the quantity $\Delta\epsilon/\Delta\epsilon'$ as a function of the dimensionless variable $\Delta\epsilon'/\epsilon'_1$ is shown for different values of cusp energies t according to Eq. 12.

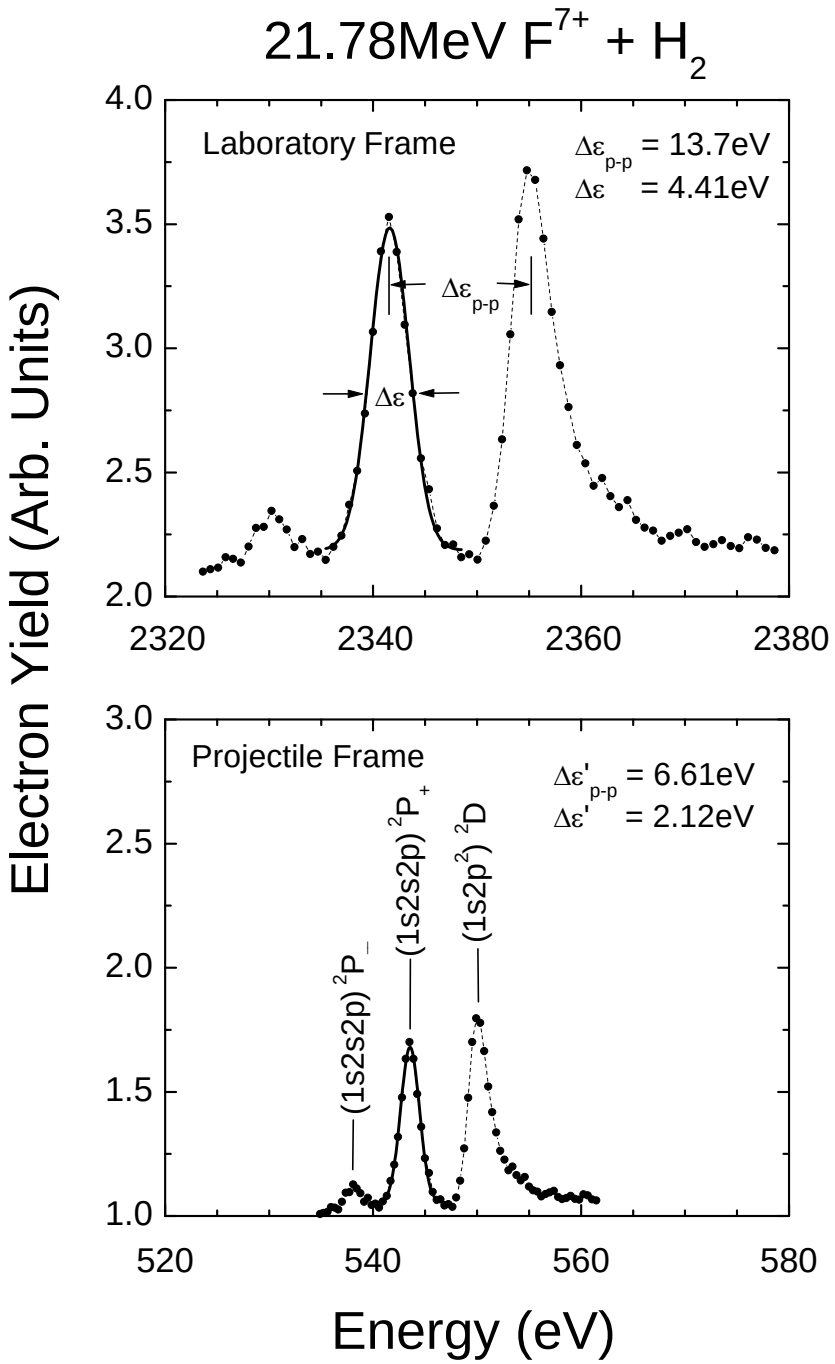

Figure 5: Example of the stretching effect. The Auger decaying states of $1s(2s2p\,^3P)^2P_-$, $1s(2s2p\,^1P)^2P_+$ and $1s2p^2\ ^2D$ of F^{6+} formed during collisions of 21.78MeV $F^{7+}+H_2$, are detected in the laboratory [*top*], and then they are transformed to the projectile [*bottom*] rest frame, respectively. Note that $\Delta\epsilon/\Delta\epsilon' = \Delta\epsilon_{p-p}/\Delta\epsilon'_{p-p}$ = 2.08.

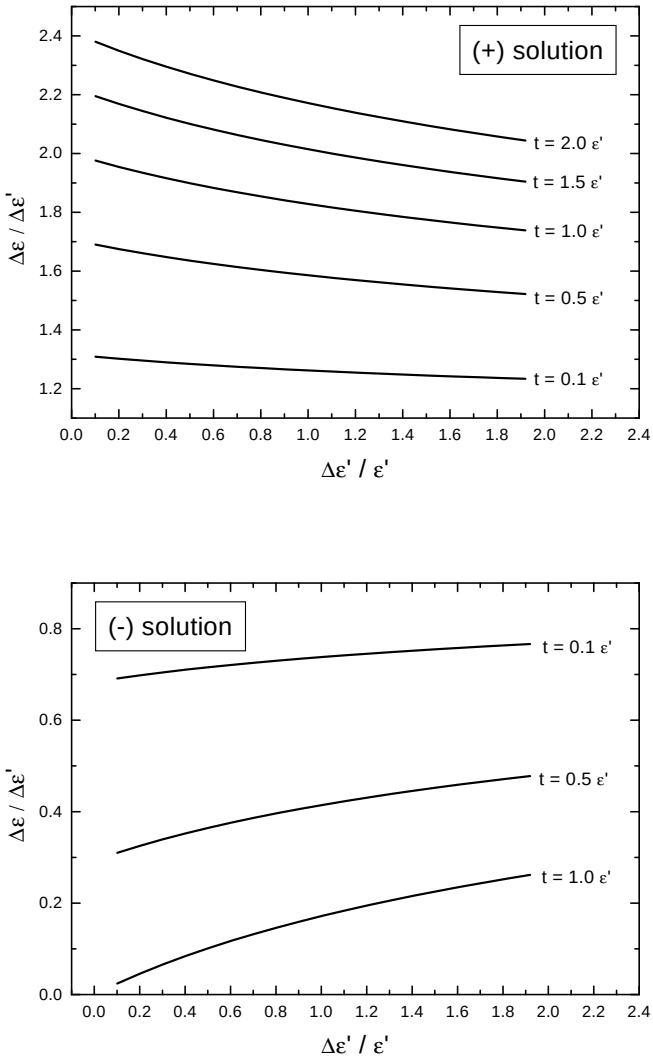

Figure 6: The amount of stretching (compressing) $\Delta\epsilon/\Delta\epsilon'$ between two Auger lines detected at the laboratory frame, is plotted as a function of their reduced rest frame energy interval $\Delta\epsilon'/\epsilon'_1$. Shown cases refer to different values of cusp energies t. [*Top*] (+) solution of Eq. 12 [*Bottom*] (-) solution of Eq. 12.

- Angular Compression: Electrons ejected from fast projectiles suffer the well known *beaming* effect observed in X-rays emitted from relativistic emitters. Electrons emitted isotropically in the projectile rest frame are detected in a narrow solid angle in the forward direction in the laboratory frame for fast projectile ions. The phenomenon is dominant for forward emission in the projectile frame, while for backward emission it happens only for $\zeta > 2$. In Fig. 7 it is geometrically explained (in a two-dimensional

projection) that for fast emitters the projectile frame solid angle $\Delta\Omega'$, denoted as $\Delta\Omega_-$ and $\Delta\Omega_+$, is always larger than the laboratory frame solid angle $\Delta\Omega$, defined by the distance between the source and the spectrometer opening. For zero-degree laboratory observation angle ($\theta = 0°$), it is proved [8] that

$$\frac{\Delta\Omega}{\Delta\Omega'} \simeq \frac{d\Omega}{d\Omega'} = \frac{\epsilon'}{\epsilon} = \frac{1}{(1 \pm \zeta)^2} \qquad (\theta = 0,^\circ) \tag{13}$$

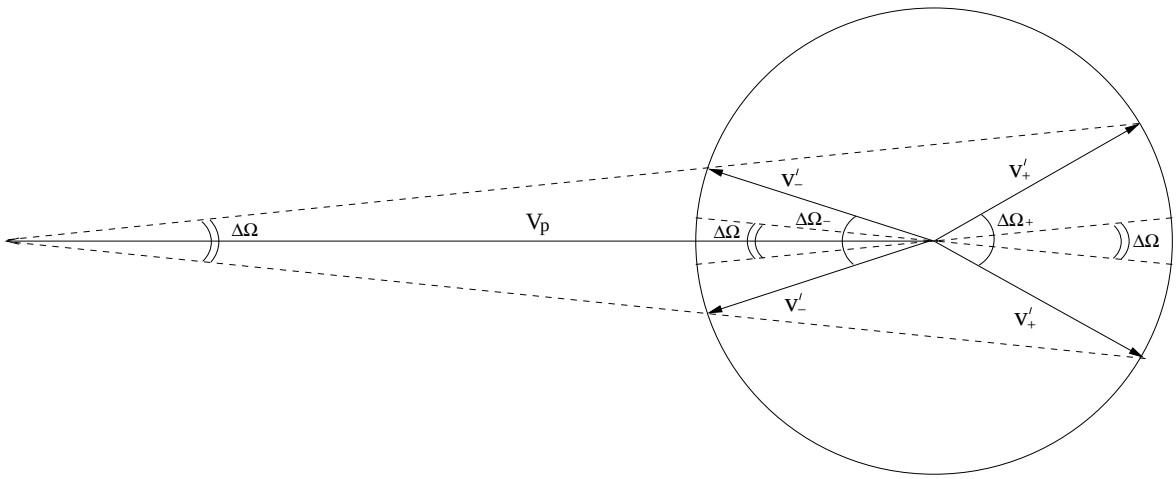

Figure 7: Angular compression of electrons emitted from fast projectiles.

- Enhancement: The height of an Auger peak recorded at the laboratory frame differs from the hypothetical height recorded at the projectile rest frame. The situation is illustrated in Fig. 5. The effect of the enhancement or diminishment of the Auger line intensity - mostly called *enhancement* - can be understood through the transformation of the double differential cross-section (DDCS) from projectile to laboratory frame at zero degrees. Combining Eqs. 10 - 13 results in:

$$\frac{d^2\sigma}{d\Omega d\epsilon} = \sqrt{\frac{\epsilon}{\epsilon'}}\,\frac{d^2\sigma}{d\Omega' d\epsilon'} = |1 \pm \zeta|\,\frac{d^2\sigma}{d\Omega' d\epsilon'} \qquad (\theta = 0°) \tag{14}$$

In the cases of forward angles (+ solution – all ζ) and backward angles (- solution and $\zeta > 2$) an enhancement of the laboratory peak heights is established, while in the case of backward angles (- solution and $1 < \zeta < 2$) the situation is reversed.

Finally, the projectile-to-laboratory transformation for the single differential cross-section (SDCS) results in:

$$\frac{d\sigma}{d\Omega} = \frac{\epsilon}{\epsilon'}\,\frac{d\sigma}{d\Omega'} = (1 \pm \zeta)^2\,\frac{d\sigma}{d\Omega'} \qquad (\theta = 0°) \tag{15}$$

Table 1: The doubling, shifting, stretching and enhancing frame transformation kinematic effects of an Auger peak are summarized for $\theta = 0°$ detection. All the possible cases are determined by the projectile rest frame emission angle θ' and the relation between the projectile velocity V_p and the electron velocity at the projectile rest frame v'.

θ'	v'	t	ζ	Doubling	Shifting	Stretching	Enhancement
		$\frac{1}{2}mV_p^2$	$\sqrt{\frac{t}{\epsilon'}}$		$\frac{\epsilon}{\epsilon'} = (1 \pm \zeta)^2$	$\frac{\Delta\epsilon}{\Delta\epsilon'} = \lvert 1 \pm \zeta \rvert$	$\frac{\frac{d^2\sigma}{d\Omega d\epsilon}}{\frac{d^2\sigma}{d\Omega' d\epsilon'}} = \lvert 1 \pm \zeta \rvert$
0	$v' \geq V_p$	$\epsilon' \geq t$	$\zeta \leq 1$	NO	> 1	> 1	> 1
0	$v' < V_p$	$\epsilon' < t$	$\zeta > 1$	YES	> 1	> 1	> 1
π	$v' < \frac{V_p}{2}$	$\epsilon' < \frac{t}{4}$	$\zeta > 2$	YES	> 1	> 1	> 1
π	$v' = \frac{V_p}{2}$	$\epsilon' = \frac{t}{4}$	$\zeta = 2$	YES	1	1	1
π	$\frac{V_p}{2} < v' < V_p$	$\frac{t}{4} < \epsilon' < t$	$1 < \zeta < 2$	YES	< 1	< 1	< 1
π	$v' \geq V_p$	$\epsilon' \geq t$	$\zeta \leq 1$	NO ELECTRON DETECTION AT $\theta = 0°$			

2.2.2 Line Broadening Effects

It has already been pointed out that, electrons ejected in the projectile rest frame with the same velocity v' will be detected in the laboratory frame with velocity v, the value of which depends on the observation angle θ (Eqs. 5 and 6). Therefore, two electrons with the *same* energy in the projectile frame, but emitted at two different angles θ'_1 and θ'_2 respectively, will be detected in the laboratory frame at two *different* energies $\epsilon_1(\theta_1) \neq \epsilon_2(\theta_2)$. Assuming that the emission angles of the two electrons of the former example, correspond to the angular width $\Delta\theta$ of the spectrometer acceptance angle, i.e. $\Delta\theta = \theta_2 - \theta_1$, the observed energy width ΔE, is then written as: $\Delta E = \epsilon_1(\theta_1) - \epsilon_2(\theta_2)$. As clearly seen from Eqs. 5 and 6, the observed energy width ΔE is not a linear function of $\Delta\theta$ but rather depends on the average observation angle $\theta \equiv (\theta_1 + \theta_2)/2$. The situation is geometrically illustrated in Fig. 8, where it is indicated that the observation at zero-degrees ($\theta = 0°$) reduces substantially the observed energy width ΔE. As a rule, the finite spectrometer solid angle results in the overlap between two neighboring peaks, degrading in this way the energy resolution of the spectra. The effect is referred to as kinematic *broadening* effect. [8]

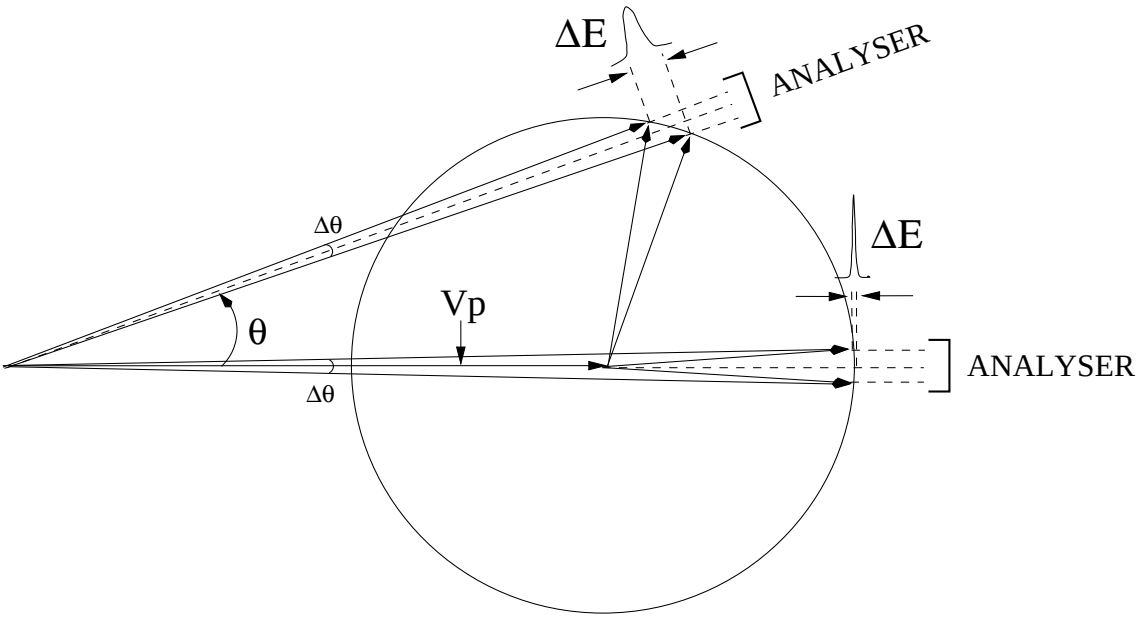

Figure 8: Geometrical interpretation of the broadening effect due to the laboratory observation angle. It is clearly seen how observation at zero-degrees ($\theta = 0°$) reduces substantially the line energy broadening.

The broadening can be understood algebraically as the uncertainty of the two variables, the laboratory observation angle θ and the cusp energy t in Eq. 1 or 2. A systematic way to estimate the uncertainties of these variables is to expand Eq. 1 or 2 in a Taylor series in powers of $\Delta\theta$ and Δt:

$$\Delta B_\theta = |\sum_n \frac{\partial^n \epsilon(\theta)}{\partial \theta^n} \frac{(\Delta\theta)^n}{n!}| = |\sum_n \Delta B_\theta^{(n)}| \tag{16}$$

$$\Delta B_t = |\sum_n \frac{\partial^n \epsilon(t)}{\partial t^n} \frac{(\Delta t)^n}{n!}| = |\sum_n \Delta B_t^{(n)}| \tag{17}$$

The broadening ΔB_θ due to observation angle θ can be calculated exactly for each experimental setup since the observation angle is defined geometrically by the dimension of the effective spectrometer acceptance aperture and the distance between this aperture and the target. Even though an easy broadening calculation is feasible for every spectrometer, the algebraic treatment of the problem provides further insight into the broadening effect. By differentiating Eq. 2 with respect to θ the first order broadening coefficient in terms of θ and ϵ is obtained. Thus

$$\Delta B_\theta^{(1)} = -2\sin\theta\Delta\theta \left(\frac{\sqrt{\epsilon t}}{1-\sqrt{\frac{t}{\epsilon}}\cos\theta}\right) \tag{18}$$

For 0° or 180° observations this term vanishes, as can be seen also in Fig. 9, where the first order broadening coefficient $\Delta B_\theta^{(1)}$ is plotted as a function of the laboratory angle

θ. In these cases, the second order coefficient must be calculated giving (replacing $\Delta\theta$ with $\Delta\theta/2$)

$$\Delta B_0^{(2)} = \frac{\epsilon}{|1-\sqrt{\frac{\epsilon}{t}}|}\left(\frac{\Delta\theta}{2}\right)^2 \tag{19}$$

$$\Delta B_\pi^{(2)} = \frac{\epsilon}{1+\sqrt{\frac{\epsilon}{t}}}\left(\frac{\Delta\theta}{2}\right)^2 \tag{20}$$

The relative broadening $\Delta B^{(2)}/\epsilon$ for both 0° and 180° is thus given by the following simple result: [10]

$$\frac{\Delta B_{0,\pi}^{(2)}}{\epsilon} = \zeta\left(\frac{\Delta\theta}{2}\right)^2 \tag{21}$$

while the absolute broadening can be expressed as a function of ϵ':

$$\Delta B_{0\pm}^{(2)} = \epsilon'(1\pm\zeta)^2\zeta\left(\frac{\Delta\theta}{2}\right)^2 \tag{22}$$

$$\Delta B_\pi^{(2)} = \epsilon'(1-\zeta)^2\zeta\left(\frac{\Delta\theta}{2}\right)^2 \tag{23}$$

It is important to notice that observation at zero-degrees *substantially* reduces the broadening due to the observation angle θ. In Fig. 8 the geometrical interpretation of this phenomenon is explained. In Fig. 9 (left), where the first order coefficient $\Delta B_{0,\pi}^{(2)}/\epsilon$ is plot as a function of the detection angle θ, it is clearly seen that broadening is maximized for the detection angle of 60°, while it diminishes for the detection angles of 0° and 180°. In Fig. 9 (right) the second order reduced broadening coefficient $\Delta B^{(2)}/\epsilon$ is plot as a function of the rest frame electron energy ϵ' for various projectile energies, at forward and backward angles. It is clearly seen that for high energy electrons (KLL-Auger) the broadening is negligible, but for low energy electrons (Coster-Krönig, Rydberg) it becomes significant. The spectrograph's full acceptance angle is $\Delta\theta$=0.868° (i.e. the full acceptance angle of the hemispherical spectrograph studied in this dissertation).

In Figs. 79 and 80, in appendix A, the second order broadening coefficients $\Delta B_{0+}^{(2)}$ and $\Delta B_{0-}^{(2)}$, respectively, are plotted as a function of the Auger electron energy for different projectile energies. It is worth mentioning that even though the absolute value of the broadening for the (-) solution (emission angle $\theta' = 180°$) is much smaller than the value of the broadening for the (+) solution (emission angle $\theta' = 0°$), the energy resolution due to broadening $\Delta B^{(2)}/\epsilon$ is the same in both cases, as it can be clearly seen from Eq. 21.

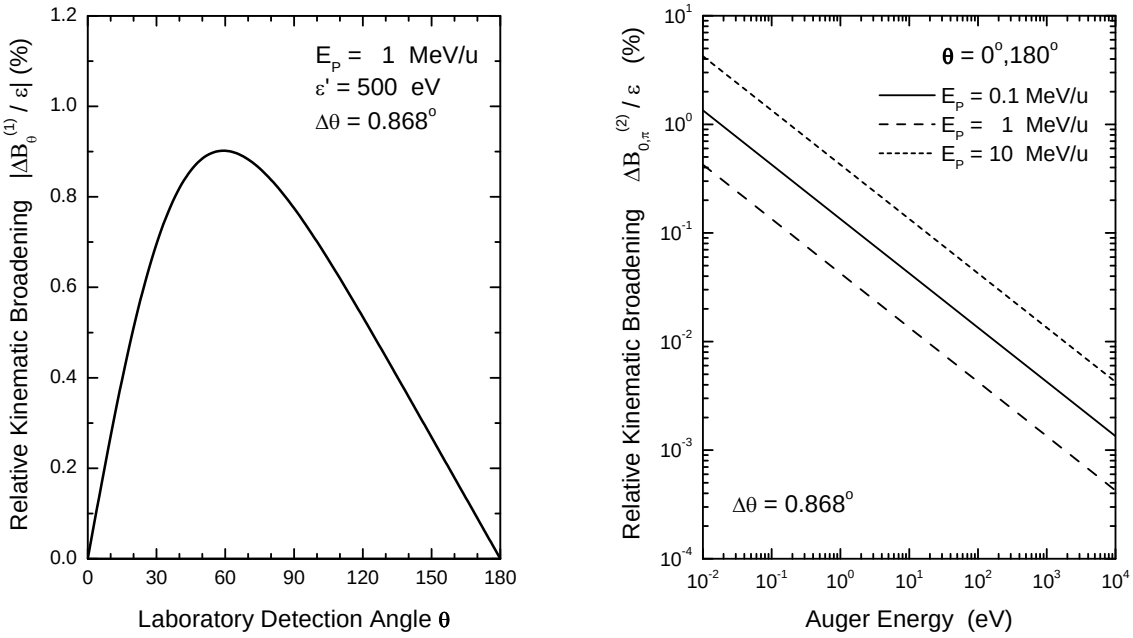

Figure 9: [*Left*] First order relative broadening coefficient $\Delta B_\theta^{(1)}/\epsilon$ as a function of the laboratory angle θ. [*Right*] Second order relative broadening coefficient $\Delta B^{(2)}/\epsilon$ as function of the Auger electron energy ϵ' for laboratory observation angles $\theta = 0°$ and $180°$. In all cases the acceptance angle is $\Delta\theta = 0.868°$.

The uncertainty in the beam energy is another factor which leads to line broadening. Expanding Eq. 1 to first order in Δt for $\theta = 0$ gives:

$$\Delta\epsilon_t \;=\; |1 \pm \frac{1}{\zeta}|\;\Delta t \qquad\qquad (\theta = 0°) \tag{24}$$

A beam energy spread of $\Delta t/t = 7\times10^{-4}$ is characteristic to the J. R. Macdonald laboratory tandem Van de Graaff (prior to the installation of the new pelletron chain in 2000) and typical for tandem Van de Graaff accelerators. However, when the post-stripping method is used to obtain a certain charge state of a ion (see §3.1), an additional beam energy spread should be considered due to the beam straggling in the post-stripper foil. [49, 50]

A broadening, maybe considered also from the uncertainty of the variable ϵ' in Eq. 1. $\Delta\epsilon'$ in this case will be the intrinsic width of the Auger line and will be transformed to $\Delta\epsilon$ in the laboratory frame according to Eq. 10. This kind of broadening though is actually a stretching and therefore the kinematic transformation of the intrinsic width $\Delta\epsilon'$ cannot be considered as a broadening. However, in order to estimate the width of a peak in the laboratory frame this factor should also be considered.

Adding in quadrature all the kinematic broadening factors discussed previously, the energy width of an Auger line can be estimated in first order non-vanishing terms at zero-degrees observation angle as:

$$\Delta\epsilon = \sqrt{[\epsilon'(1 \pm \zeta)^2\zeta]^2 \left(\frac{\Delta\theta}{2}\right)^4 + \left[1 \pm \frac{1}{\zeta}\right]^2 (\Delta t)^2 + [1 \pm \zeta]^2 (\Delta\epsilon')^2} \tag{25}$$

This energy width constitutes the lowest permissible limit to the measured resolution. It defines the limit of the experimental energy resolution. The quantity $\Delta\epsilon/\epsilon$ should always be compared to the smallest attainable instrumental energy resolution $\Delta\epsilon_I/\epsilon$, in order to have an estimate on the possible spectral identification of closely neighboring Auger lines. The major component of the broadening at 0° is usually due to instrumental effects and usually not due to the beam energy spread. However, in the case where the beam is obtained by post-stripping in a foil, the effect of increased beam spread is observable.

2.3 Concluding remarks

In conclusion, the ZAPS technique has been shown to be a very powerful tool for high resolution studies of projectile electrons and related phenomena. The strength of ZAPS lies on the kinematic advantages of the minimization of broadenings at 0°, the access to the whole electron energy spectrum and the ability of detecting very low energy electrons. To date, ZAPS technique has utilized two-stage (tandem) slit spectrometers providing unique information on state-selective differential cross-sections for basic collision mechanisms. However, tandem slit spectrometers greatest disadvantage is the large time consumed for collecting a single spectrum. The use of very small apertures (1–2 mm for the second stage analyser) along with the dramatic transmission reduction in the deceleration mode of operation, necessitates the use of relatively large beam currents (typically 50–100 nA) to maintain experimental acquisition times at the 12–24 hr level. A typical high resolution spectrum needs at least a day of data recording. Therefore, experiments utilizing low beam currents (< 10 nA) or attempting to measure very low cross section processes (DDCS $< 10^{-22}$ cm^2 / eV sr) are practically forbidden for the parallel plate tandem spectrometers.

In this dissertation, a position sensitive detector instead of an exit slit is incorporated into a single stage hemispherical deflector analyser (HDA) to increase by more than a factor of 100 the data collection efficiency. Even though such a spectrometer is typical in today's modern electron spectroscopy for chemical analysis (ESCA) [15] experiments, its utilization at zero-degrees entailed special considerations, since small slits could not be used at the entrance. Instead, a focusing/decelerating lens system is incorporated providing thus a virtual slit entrance by focusing while at the same time decelerating the electrons for improved energy resolution. The spectrograph study,

operation and performance is a major part of this thesis and will be presented in detail in the following chapters.

3 Experimental Arrangement: Hardware and Electronics

3.1 Experimental Setup

The experimental setup was developed at the J. R. Macdonald laboratory at Kansas State University (KSU). A top view of the laboratory is shown in Fig. 10.[5] The ion beam is obtained at the desired energy from the tandem Van de Graaff accelerator and transferred to the experimental area in the way described in appendix B.

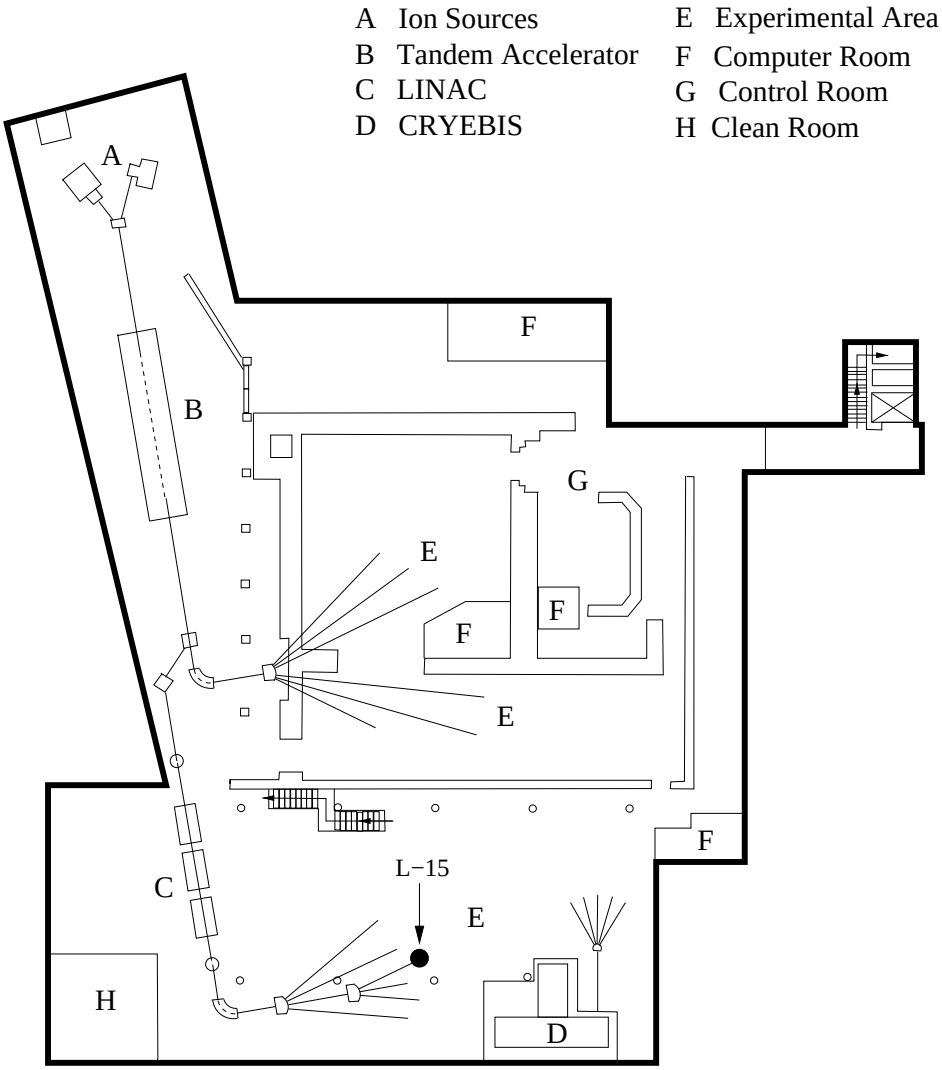

Figure 10: Top view of the J. R. Macdonald Laboratory. The ZAPS experimental station is shown at L-15

[5] A virtual tour in J. R. Macdonald laboratory is available at the address http://www.phys.ksu.edu/area/jrm/tour.html

Numerous changes took place to the beamline manifold in the continuing effort to improve the experimental conditions until the final arrangement was reached. All the physical dimensions referred to, are those used in the arrangement of the experimental apparatus as of December 1999, unless otherwise stated. In the effort to make this thesis more readable, many technical but important details have been shifted to the appendix.

The beamline was located at 15° left (L-15) of the second switching magnet with respect to the beam direction (see Fig. 10). Two pairs of 4-jaw slits, separated by a distance of 1m, were used to collimate the beam down to 1×1 mm^2 cross-section. Due to the focusing properties of the switching magnet, the upstream slits were set wider open than the downstream ones. Typical collimation values are 3×3 mm^2 and 1×1 mm^2 for the upstream and the downstream slits, respectively. Between the two pair of slits, a Beam Profile Monitor (BPM) was located. This device proved extremely useful for fine tuning the beam transport, since the spatial beam distribution could be monitored on an oscilloscope. Also, in cases of extremely low currents (e.g. 20pA for the beam of 3.7 MeV B^{4+}), monitoring the beam profile through the BPM, proved very helpful. The beam current was maximized at the Faraday Cup (FC) after the second pair of 4-jaw slits and then was driven through the apertures of the gas-cell and the spectrograph to the last FC (see Fig. 10), using the switching magnet, the quadrupole and the magnetic deflectors further upstream.

For Zero-degree Auger Projectile Spectroscopy it is extremely important for the ion beam *not* to hit any of the spectrograph apertures, since in this case the secondary electron production will dominate and destroy the spectra (especially for a single stage spectrometer). For this reason large apertures with diameters of 4 mm for the lens entrance, 6 mm for the analyser entrance and 9 mm for the analyser beam exit were used (see Fig. 11), so that after a tight beam collimation, the current measured at any of the spectrograph apertures resulted in zero. It was found that the spectrum was not affected much by the secondary electron emission produced at the surface of the gas-cell apertures.

Another important issue is that when the beam is obtained with the post-stripping method, the current in the last FC decreases with time. This is due to the change in the stripping foil thickness, due to carbon build up, resulting in a slightly lower beam energy and therefore a different beam trajectory through the second switching magnet. It would be a mistake in this case to re-tune the magnet in order to maximize the beam current at the last FC. The different beam energy would result in a shift in the projectile electron spectrum (see chapter 2.1). Instead, the foil was moved so that the beam collided with an unused part of it or even it was replaced with a new one. The movable rod, used for replacing the foils, had 12 different foils which were more than enough for an experiment. In the later case, a beam re-tuning was usually needed. In most of the cases the foils lasted many hours which was enough time to collect all of the data with the new spectrograph. Although, in some cases, where beam re-tuning was unavoidable, the spectra, recorded in between the beam re-tuning, were added together after small energy shift alignments were made.

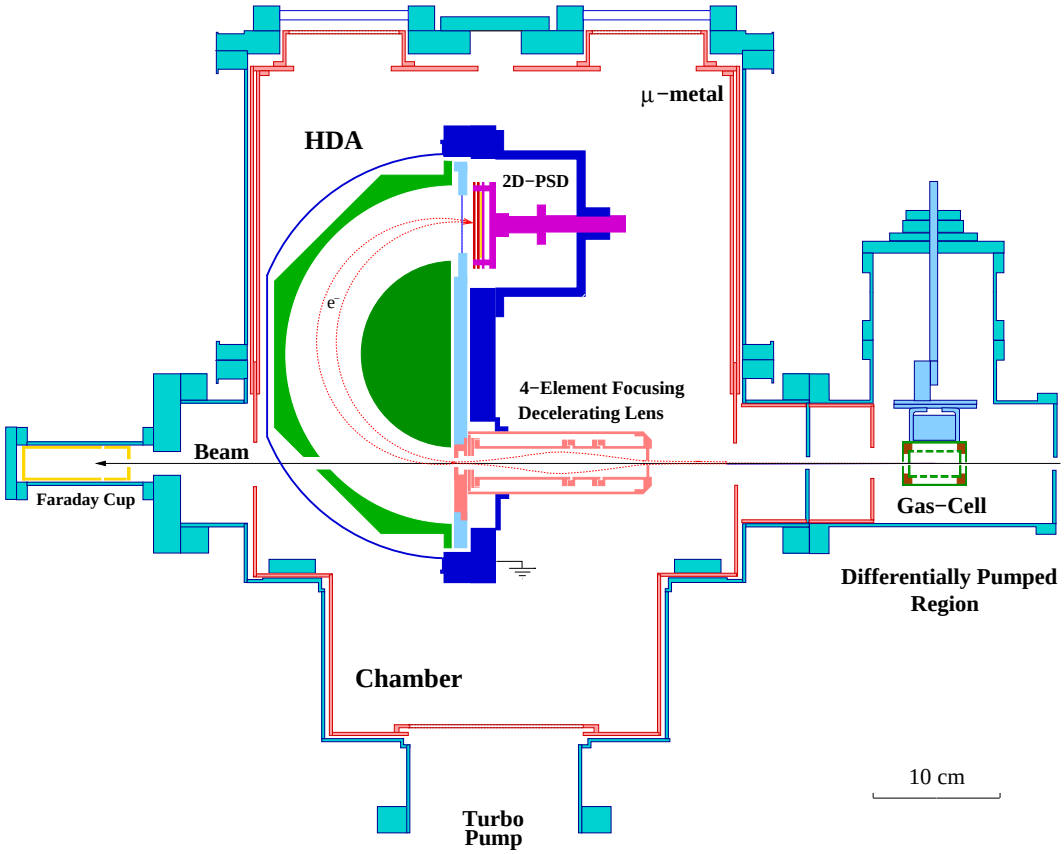

Figure 11: The zero-degree experimental setup: The ion beam interacts with a gaseous target in a cell and exits through a hole at the back of the spectrograph. Electrons ejected from the collision in the gas-cell are focused into the hemispherical analyser and detected at the 2D-PSD.

In Fig. 11 a side view of the zero-degree experimental setup is shown in detail. The chamber [6] consists of two cylindrical parts of 400 mm diameter. The lower part of the chamber supports the hemispherical spectrograph and is mounted on a specially designed base, so that it can be moved upwards, sideways or tilted across the beam direction. A connection of the chamber and the beamline pipe via a bellow, allows for an easy alignment of the spectrograph along the beam axis. The J.R.M. laboratory

[6]The lower part of the vacuum chamber with the mounting base, the lower part of the μ-metal shield, the gas cell and the turbomolecular pump with its controller were loaned by the Hahn-Meitner Institute (HMI). The upper part of the chamber was built in the machine shop of the Foundation of Research and Technology (FORTH). The upper part of the μ-metal shield was bought from Magnetic Shields Limited, (Kent, GB). The spectrograph (hemispherical analyser and focusing lens) was bought to order from Comstock Inc., (Oak Ridge, Tennessee), while the position sensitive detector was bought from Quantar Technology, (Santa Cruz, California). All these components along with the pressure measuring system which was bought from Kurt J. Lesker (Clairton, PA), were gathered in the atomic physics laboratory of the University of Crete and transfered to KSU. The rest of the hardware, target turbomolecular pumps, roughing pumps and all the electronics were supplied by the JRM Laboratory.

beamlines are fixed at 1.74 m (68.5″)in height and all the alignments were done with the use of a special telescope. The upper part of the chamber is removable for greater accessibility and manipulation of the components inside the chamber.

Both lower and upper parts have an inner cylinder made of μ-metal for the reduction of the earth's magnetic field to a few mGauss. μ-metal cylinders were also used between the collision region and the chamber. Measurements of the magnetic field inside the chamber, using a magnetic probe, showed that even when the switching magnet – which is located 2 m away from the chamber – was operated at its highest experimentally allowed values, it didn't exceed the value of 10 mGauss at any direction. Care was taken to replace any nuts or bolts magnetized through contact with any magnetized wrenches or screwdrivers.

The gas-cell consisted of two coaxial cylinders. The inner cylinder was 36mm long with a diameter of 20 mm while the outer cylinder was 50 mm long with a diameter of 34mm. The two cylinders were made of brass and were electrically isolated. Each cylinder had removable entrance and exit circular apertures. The apertures of the outer cylinder were also electrically isolated from the main part of the cylinder, so that the beam current could be monitored at the entrance, middle and exit of the gas-cell. This information was quite helpful in transporting the ion beam through the cell. Also the electrical isolation of the inner cell from the outer, was used for biasing the inner cell to negative voltage values, in order to accelerate and distinguish between electrons generated inside the gas-cell from those generated outside the gas-cell (as for example in metastable Auger decays). The inner cylinder openings of the apertures were 2.5mm diameter, while the entrance and exit openings of the outer cylinder apertures, used in most of the experiments, were 1.5mm and 3mm, respectively. The gas-cell was placed at the top of a 101.6mm (4″) diameter 5-way cross, in front of the chamber. It was mounted on a specially designed movable base so that it could be moved upwards and sideways for easy alignment of the whole apparatus. The distance between the center of the gas-cell and the entrance of the lens was 264mm.

3.2 Vacuum

The chamber was pumped by a 450 l/s turbomolecular pump while the target area was differentially pumped through a 250 l/s turbomolecular pump also. Two cylindrical baffles were placed on either side of the gas-cell to further improve the differential pumping. The chamber pressure was measured with a thermocouple and an ion gauge, controlled automatically by the Ion Gauge Controller (Kurt J. Lesker model 4400). The gas pressure was measured by a baratron manometer (MKS model 390HA) connected to a feedback system (MKS: needle valve model 248A, controller model 250B, signal controller model 270) so that the measured pressure remained at a predetermined fixed value during the measurement. The rest of the beamline up to the switching magnet (about 2 m long) was pumped by a 170 l/s turbomolecular pump. Viton O-rings were used in all joints. After pumping, while heating the system using fiber lines up to 70 °C for many weeks, a base chamber pressure of 1.5×10^{-7} Torr was achieved. A study

of the chamber pressure as a function of the gas-cell pressure was performed for the gases of H_2 and He. The results are shown in fig. 12.

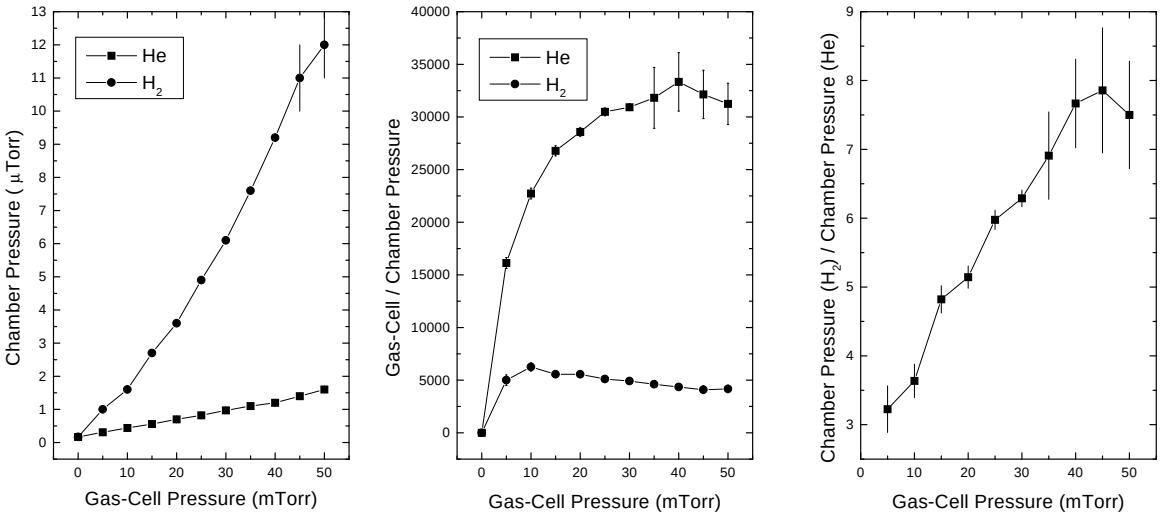

Figure 12: [*Left*] Chamber pressure as a function of the gas-cell pressure for the gases of H_2 and He. [*Middle*] Ratio of gas-cell pressure to chamber pressure as a function of the gas-cell pressure. An average ratio of about 30,000 for He targets is established at gas-cell pressures between 15 and 50 mTorr, while an average ratio of about 5,000 for H_2 targets is established at gas-cell pressures between 5 and 50 mTorr. [*Right*] Ratio of the chamber pressure with H_2 gas in use to the chamber pressure with He gas in use as a function of the gas-cell pressure.

The reason for higher chamber pressures in the case of H_2 compared to He can be understood qualitatively according to the following arguments. The effective pumping speed of H_2 is higher than the effective pumping speed of He. This means that the pressure measured at a point x will be higher for H_2. Actually, it can be shown that $P_{H_2} \simeq (\frac{C_{H_2}}{C_{He}})^2 \, P_{He}$ with $C_{H_2} > C_{He}$, where C_{H_2} and C_{He} are the conductances for H_2 and He, respectively, (see appendix C for the proof of these statements). Therefore, part of the difference is due to the different effective pumping speeds. Also the sensitivity of the ion gauges to these two gases are different. The sensitivity for H_2 is about 3 times higher than He. This means that the pressure reading for H_2 will be about 3 times higher than for He. It should be mentioned here that the baratron used for measuring the gas-cell pressure reads the actual pressure independent of the gas. Though Fig. 12 (right), where the ratio of the chamber pressure with H_2 gas in use to the chamber pressure with He gas in use as a function of the gas-cell pressure is plotted, indicates that the two previous arguments do not justify the ratio behavior. Instead they predict a fixed difference between the two gas cases but not a gas-cell pressure dependent one. This gas-cell pressure dependence can be understood if a back-streaming is established in the turbomolecular pump of the differentially pumped region. Unfortunately there

were not any gauge meters used in the differentially pumped region for measuring the foreline pressure, therefore there is no direct way to justify this statement.

In conclusion, an average gas-cell pressure to chamber pressure ratio of about 30,000 for the case of He and 5,000 for the case of H_2, was established, for gas-cell pressures ranging form 15 to 50 mTorr and 5 to 50, respectively, as can be clearly seen in Fig. 12 (middle).

3.3 The spectrograph

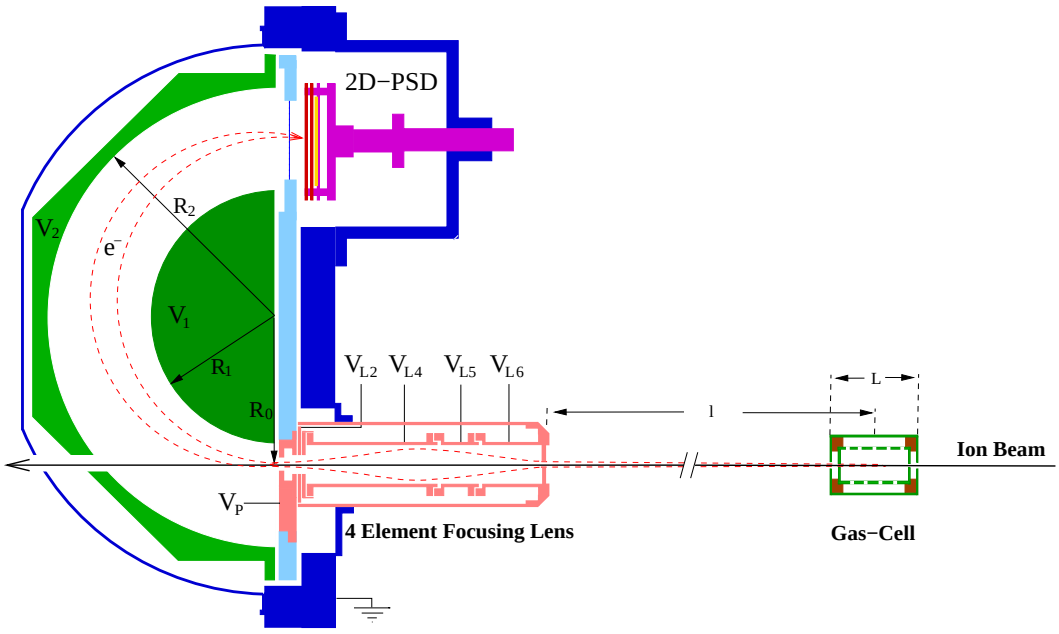

Figure 13: The hemispherical paracentric spectrograph for ZAPS. Note the asymmetric position of the entrance aperture on the analyser. The voltage notation corresponds to the different electrodes. Existing sapphire ball insulation between the different electrodes is not shown. The most important distances of the experimental setup are given in Table 3.7.

The spectrograph is shown in detail in Fig. 13. It is composed of commercially available components including a hemispherical analyser, a 4-element focusing lens and a two-dimensional position sensitive detector (2D-PSD). Both analyser and lens were made of aluminum with their inner surfaces coated by soot to reduce secondary electron emission. [51] An additional shield placed around the outer hemisphere was found to be necessary, substantially reducing background electrons. The four-element focusing lens, which is illustrated in detail in Fig. 14, provides a virtual slit for the incoming electrons by focusing them at the entrance of the analyser. The lens can also be used to decelerate the electrons (high resolution or deceleration mode) while focusing them for improved energy resolution. The entrance lens element V_{L6} is always

grounded, while the exit lens element is on potential $V_{L2} = V_P$, which is also grounded when running in the low resolution (non-deceleration) mode. The 2D-PSD consists of a pair of 40 mm active area multichannel plates (MCP) and a resistive anode encoder (RAE). The entire detection system is mounted in its own cylindrical casing and further shielded from background electrons.

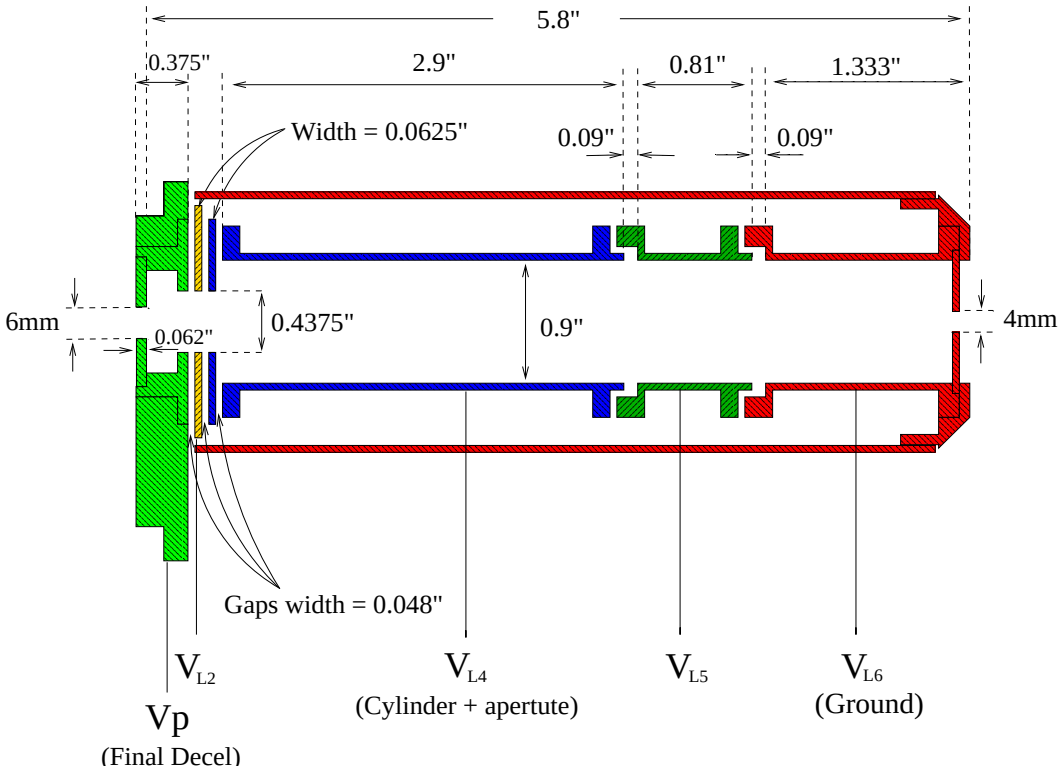

Figure 14: The 4-element electrostatic focusing and decelerating lens.

The analyser consists of two hemispherical shells with outer R_2 and inner R_1 radii of 130.8 mm (5.15″) and 72.4 mm (2.85″), respectively. The two shells are supported on a cylindrical base plate from which they are electrically isolated with carefully positioned sapphire ball insulators. The base plate constitutes the relative ground of the analyser and can be independently biased with a plate voltage V_p, when deceleration of electrons prior to analysis is required. The four-element lens is also supported from this plate with the exit lens element and base plate being on the same potential V_p. Apertures of 4 mm and 6 mm were used at the entrance and exit of the lens respectively. In the exit part of the analyser there is a 60 mm circular opening where the detector is mounted. The basic geometrical parameters of the ZAPS setup are given in Table 14 at the end of this chapter.

On the exit side of the analyser a 90% transmission nikel grid was stretched over the large exit aperture to shield the inside of the analyser from external fields. This is typically done in all electrostatic spectrometers incorporating a large area PSD. This grid was also on potential V_p. Another 90% transmission grid was also placed on the

PSD cylindrical casing about 9 mm from the front of the first MCP. Initialy, this grid was placed for controlling the detection energy of the electrons, but along the way, it proved an indispensable component when the spectrograph is run in high resolution mode. That grid was set at slightly more negative voltages than V_p (usually at V_p - 48 V). The two hemispheres with the common base plate are supported on a second plate which constitutes the absolute ground of the spectrograph. Sapphire ball insulators were used for electrical isolation of the various components of the spectrograph.

3.4 The 2D-PSD

The two-dimensional position sensitive detector (2D-PSD or just PSD) in use, consists of two microchannel plates (MCP) of 40mm diameter and a resistive anode encoder (RAE). The use of two MCP at the orientation shown in Fig. 15 is known in the literature as the *Chevron* arrangement. [52] The PSD is mounted on a ceramic base along with the four 1nF capacitors needed for the signal decoupling (see Fig. 17).

An MCP is an array of $10^4 - 10^7$ channel multipliers (microdynodes) oriented parallel to one another. Typical channel diameters are in the range 10 - 100 μm and have length to diameter ratios between 40 and 100. A typical distance between microdynode centers is 50 - 150 μm. The theory of channel multiplication has been adequately investigated. [53] For an overview of the multiplication mechanism in different type microchannel plates see [54] and references therein. A brief summary of the mechanism will be given here.

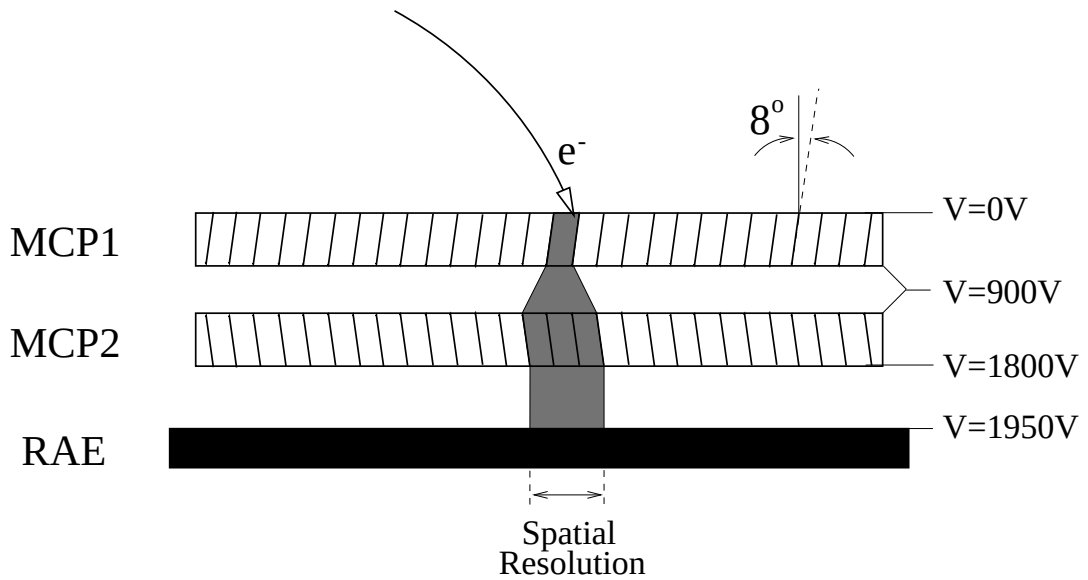

Figure 15: The operation of a chevron arrangement microchannel plates (MCP) of use in the HDA Position Sensitive Detector (PSD).

An electron entering a channel of the first microchannel plate produces an average of δ^n electrons at its exit, where δ is the average production of secondary electrons per

collision with the channel wall, and n is the number of collisions. The procedure is repeated for the second microchannel plate, resulting in an overall amplification factor of $10^6 - 10^7$. Electrons are then collected through an extraction voltage of ~150V on the RAE surface. RAE's resistance is of the order of 1 GΩ. The spot size of the electrons on the RAE determines the spatial resolution of the PSD (see Fig. 15).

Secondary electron yield (known as MCP gain) depends on the overall MCP voltages and is limited by the space charge saturation effects at the rear of the second MCP. In the saturated operation the output signal does not vary in amplitude with respect to input events, which is the basic assumption for particle detection independent of their energy. Normally, voltages are set at values where maximum gain is established, i.e. where saturation effects appear. The Chevron MCP is a common method for producing space charge saturated output pulses. PSD voltages given in Fig. 15 were typically used.

In the Chevron type MCP, the orientation of the channel axis is tilted at a small angle (±8°) with respect to the MCP normal. This geometry inhibits positive ions produced at the output of the rear plate (by electron collisions with the residual gas molecules) to drift back into the channel input, producing additional secondary electrons ("ion after pulses"). The Chevron MCP geometry also forces electrons entering the MCP parallel to the channel axis, to hit the channel wall early enough, leading to the production of space charge saturated pulses.

An upper limit to the spatial resolution was determined experimentally. A mask made of brass, filled with 0.5mm diameter holes, was made as shown in Fig. 16. [7] The non-symmetric hole distribution on the mask area accounted for the PSD center and orientation identification. The mask was placed in front of the PSD and the whole detection system was mounted on a 4″ port inside the collision chamber. An unfocused electron gun was used to illuminate the whole surface of the PSD. As shown in Fig. 16, although the illumination was not uniform over the PSD surface, the results presented below were obtained.

a. The PSD orientation was determined.

b. The active MCP area was found to be ~38 mm, while the actual area was 40 mm.

c. The center of the PSD was found at channels X=Y=128 (The total number of channels in use was X=Y=256, see §3.6).

d. A single channel corresponds to 0.2 mm.

e. An upper limit on the PSD spatial resolution was measured at the value of the hole diameter i.e. 0.5mm. The MCP manufacturer [8] gives a spatial resolution of 0.15mm. However, for the HDA spectrograph as a whole, the spatial resolution

[7] The hole diameter dimension was the smallest available at the machine shop.
[8] Gallileo Electro-Optics Corporation (now Burle Electro-Optical Inc.).

is solely defined by the analyser resolution which was determined (by measuring the FWHM of K-Auger lines) to be 0.7 ± 0.06 mm (i.e. 3.5 ± 0.3 channels).

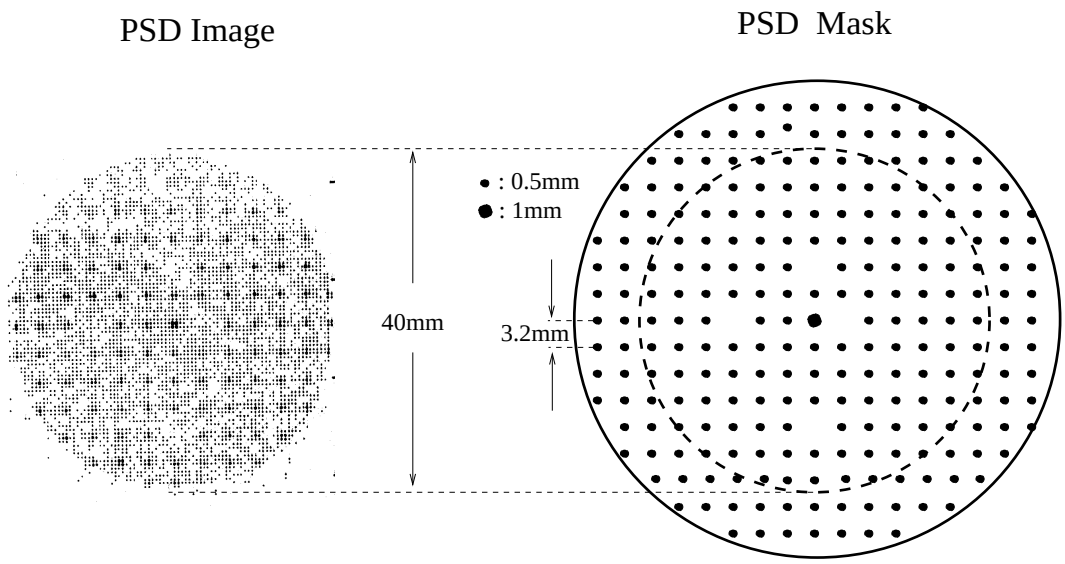

Figure 16: PSD spatial resolution study. [*Right*] The designed mask with oriented small openings allows the illumination of the PSD surface only through these holes, the dimension of which are an upper limit to the PSD spatial resolution. [*Left*] The 2-dimensional spectra showing the PSD area after illuminating it through the mask openings using electron gun.

3.5 Electronics

In Fig. 17 the electronics diagram is shown. Approximately 1pC signals were decoupled by the 1nF capacitors giving rise to small negative pulses of the order of 1mV. [9] The four capacitors, used for the four corner signals, were mounted on the same stand as the MCP inside the vacuum, minimizing in this way any electrical noise that could be picked up by the wires, in case the signal decoupling had taken place outside the chamber. The mV signals were driven to the preamplifiers via coaxial cables. Preamplifiers (model PC142IH ORTEC) and dual main amplifiers (model TC247 TENNELEC) were used to produce the final bipolar pulses at the desired amplification, which depended on the input signals of the ADC in use. For example, the AD811 ORTEC model accepted up to 4 Volts peak-to-peak signals while the 7164 PHILLIPS model up to 10 Volts.

3.6 Data Acquisition System

The data-acquisition system used at the J. R. Macdonald laboratory is a VME-based system. Its main hardware components are the CAMAC subsystem, the VME front-

[9] Note that $\sim 10^7$ electrons which is the output saturated pulses of the MCP equals $\sim$1pC.

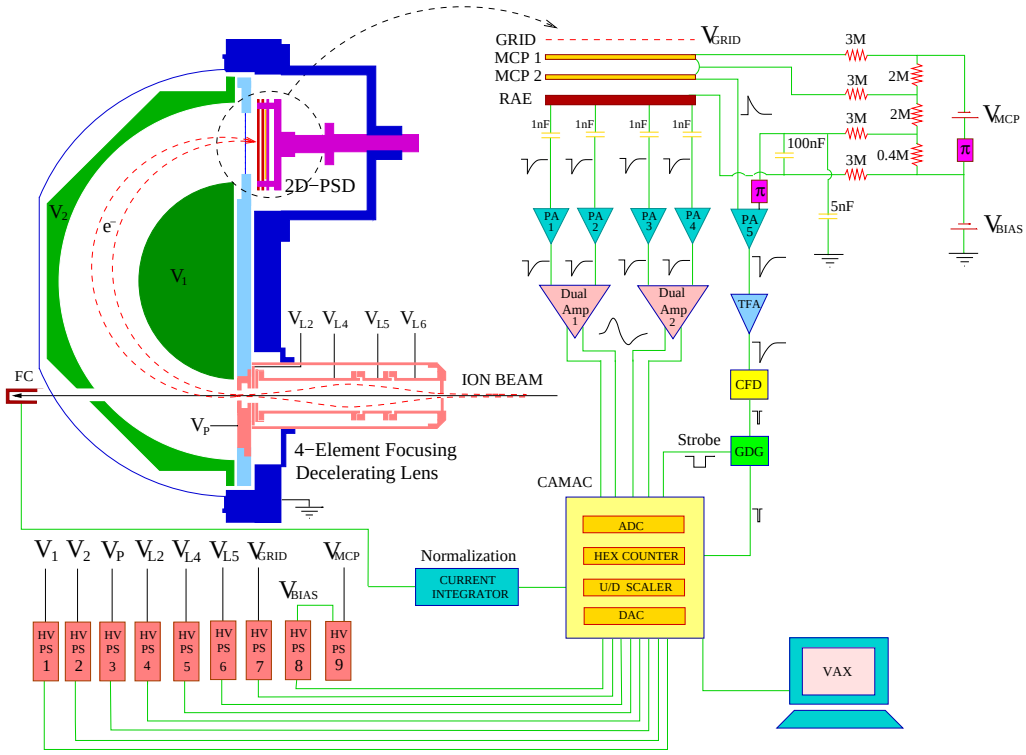

Figure 17: The Electronics Diagram. PG: Pulse Generator, PA: PreAmplifier, Dual Amp: Dual Amplifiers, TFA: Timing Filter Amplifier, CFD: Constant Fraction Discriminator, GDC: Gate and Delay Generator, ADC Analog to Digital Converter, π: π-filter for electronic noise reduction.

end and the back-end host computer. The basic VME front-end consists of a VME crate with one Motorola MVME167 68040 CPU module and one CES CBD-8210 CAMAC branch driver module. The back-end host computer is a VAX station 4000/96 running the XSYS data acquisition software package (Indiana University Cyclotron Facility). Event data may be recorded on a tape or a disk drive attached to the back-end host computer.

The signals from the four corners of the PSD were digitized at the ADC and their pulse height distribution was obtained. The pulses heights were digitized and distributed in 2048 channels as shown in Fig. 18(a)-(d). It is essential to produce good quality pulse height distributions. Typical electron distributions show a very sharp rise and a long tail (i.e. most electrons give rise to small height pulses, since electrons have lower ionization ability on the MCP dynode surfaces than the ions). The good quality of the PSD image depends primarily on the amplification at the MCPs (i.e. saturated operation mode). Noise elimination and proper thresholds (Constant Fraction) set in the electronics are of considerable importance too.

The position information (X,Y) is derived from the four corner signals (X_1, X_2, Y_1

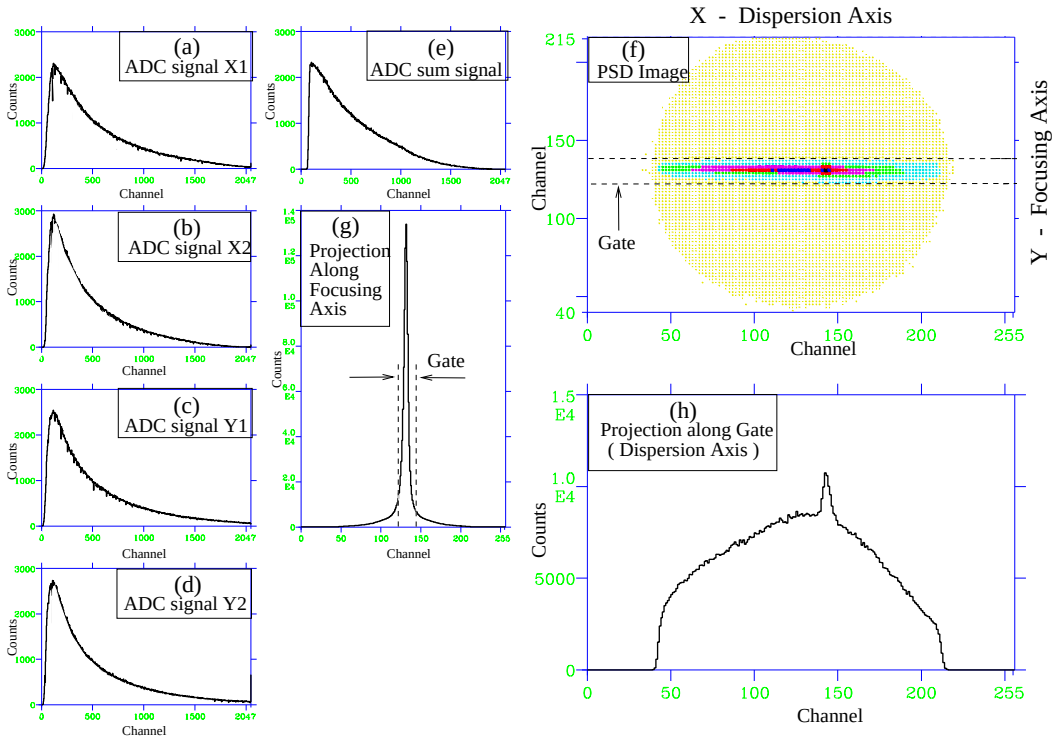

Figure 18: XSYS Data Acquisition System output. (a) – (d) The four PSD corners pulse height distribution signals. (e) The pulse height distribution of the sum of the four signals. (f) The PSD image constructed from the four PSD corner signals. (g) Projection of the PSD image along the focusing axis. (h) Projection of the PSD image confined by the gate along the dispersion axis.

and Y_2) according to the formulas: [55]

$$X = \frac{X_1 + Y_1}{X_1 + X_2 + Y_1 + Y_2}, \qquad Y = \frac{X_2 + Y_1}{X_1 + X_2 + Y_1 + Y_2} \tag{26}$$

Therefore a two dimensional image is constructed from the four corner signals, showing the information of the electron position detection of Fig. 18(f). The dimension of this 2D array was chosen to be 256×256, which was found adequate without taking up too much disk space. [10]

As it will be shown in §4.2.4, due to the double focusing properties of the HDA, the electrons are detected along a narrow strip on the PSD surface as shown in Fig. 18(f). One could argue that the use of a 2D-PSD instead of a 1D-PSD – since electrons are

[10] It has been mentioned that the FWHM resolution was measured to be 3.5 channels when an array of 256×256 channels was in use. The use of an array of 128×128 channels would result in a FWHM of 1.75 channels, degrading in this way the energy resolution, as the whole peak would be detected only in three channels, which is not adequate. On the other hand a choice of an array of 512×512 would result in much larger space consumption both in hard disk and memory.

focused on a narrow strip – is not really essential. However, during the development and mastering of the detection system, the two dimensional information was very helpful in understanding the origin of the background spurious electrons, detected all over the PSD area, especially in high resolution mode. Methods of background minimization and background corrections on the raw data, are described in chapter 6. A one dimensional detector would give very poor information on facing the secondary electron emission problem. In addition, the correct circular image of the 2D-PSD is considered as a sensitive test for checking proper setup operation.

The length of the strip is the dispersion (energy) axis while the width depends solely on the focusing quality of the analyser. Assuming that the magnification of the hemispherical analyser is one, the width would be equal to the focusing trace of the electron beam image at the exit of the lens (entrance of the analyser). A projection of the whole spectrum along the Y-axis (focusing axis) gives a distribution of the FWHM which can be viewed as the parameter needed to be minimized in order to achieve good focusing conditions. As it will be explicitly shown in chapter 6.2.1, more parameters are needed to be studied for optimum focusing conditions.

The spectrum is obtained by setting a gate around the upper and lower ends of the strip width, and projecting the points summed along the y-channels per x-channel, onto the dispersion axis as seen in Fig. 18(h). The strip width limits shown in Fig.18(g), corresponds to less than $\sim$5% of the maximum height of the distribution projected along the focusing axis, when the spectrograph is run in the low resolution mode. In high resolution operation mode the situation is more complicated and is described in detail in chapter 6.4.

All the above data manipulation was done using the XSYS software data acquisition package. Basic data acquisition codes specialized for the 2D detection were built, in addition to FORTRAN codes, which helped with the software control of the power supply voltages and the general manipulation of the measurement. The "raw" data were seen on the computer screen the way they are presented in Fig. 18. All the information needed for the proper operation of the system is available in this figure, while most of the changes that can take place during the experiment are computer controlled. Thus, the detecting system is largely automated and the experiment can be run easily even by only one experimenter.

3.7 Dead Time

Every ADC requires a certain time to digitize the analog input signal in order to send it to the next level of acquisition, i.e. the front-end computer. The time needed for this conversion process, which is independent of the input signal amplitude and proceeds in parallel for all the ADC channels (inputs), is called "dead time", due to the fact that, a pulse will not be counted if it arrives during the conversion time interval. For example the digitization time of the AD811 ORTEC is 80μs, while the PHILLIPS 7164 is 7.8μs. In addition, the data acquisition system itself also has dead time. The dead times involved in the measurement are the following:

- Front end processor overhead: 29μs
- Time per CAMAC command: 2.5μs
- Transfer time for word to VAX: 1.6μs

Four parameters are read from the ADC (the signals of the four corners of the resistive anode) and thus the dead time of the data acquisition system is: 29 + 4×(2.5 + 1.6) = 45.4μs. Use of the AD811 ORTEC ADC would increase the dead time up to 125.4μs, while the 7164 PHILLIPS ADC up to 53.2μs. The maximum count rates arising from the previous cases are 8kHZ and 19kHz respectively, assuming that the events are regular. However, the random nature of the real events reduces substantially the maximum count rate. In the case of the 7164 PHILLIPS ADC in real experimental conditions, the count rate was limited down to 2kHz in order to have a dead time of less than 30%. In Fig. 19 the experimentally measured DTC (see §7.2 for details) is plotted as a function of the count rate.

In order to measure absolute cross sections the knowledge of the total dead time of the data acquisition system is needed. For this an output NIM signal from the Discriminator was used to monitor the real count rate through a CAMAC scaler, which counts up to several MHz without any dead time. (The scaler is reading each pulse and every 5sec it provides the data to the computer while it is still accumulating new data). The ratio of the total counts of the scaler to the total counts of the ADC gives the dead time correction (DTC) that can be used to correct the data (see §7.2) .

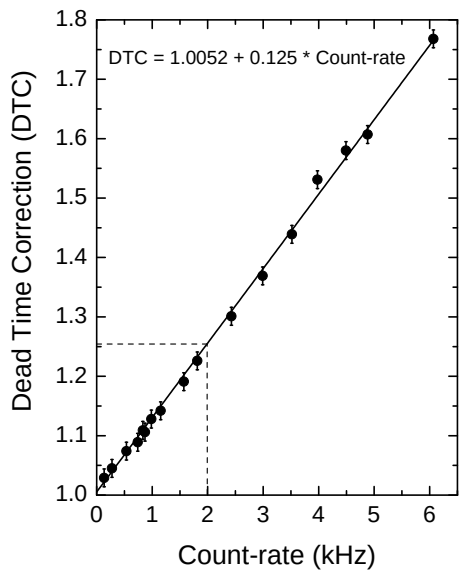

Figure 19: Dead Time Correction (DTC) as a function of the count rate. PHILLIPS 7164 ADC in use. The count rates used in most of the measurements are noted (dashed line).

Table 2: Basic geometrical parameters of the ZAPS setup (see Fig. 13).

Quantity	Symbol	Value
Outer radius	R_1	72.4 mm
Inner radius	R_2	130.8 mm
Paracentric entry	R_0	82.6 mm
PSD diameter	d_{PSD}	40 mm
Gas-cell length	L	50 mm
Gas-cell apertures diameters (Ion beam entry-to-exit)		1.5, 2.5, 2.5, 3 mm
Gas-cell to lens entry distance	l	264 mm
Lens entry aperture diameter	d_{LE}	4 mm
Lens exit aperture diameter		6 mm
Analyser beam exit aperture diameter		9 mm
Full angular acceptance $\left[= \arctan\left(\frac{d_{LE}}{l}\right)\right]$	$\Delta\theta$	0.868°
Full acceptance solid angle $\left[= \frac{\pi d_{LE}^2}{4l^2}\right]$	$\Delta\Omega$	$1.8 \cdot 10^{-4}$ sr

4 The paracentric HDA: I. Ideal 1/r potential - Theory

4.1 Introduction

A brief overview of the hemispherical deflector analyser (HDA) will be given below. The citation to references below is only indicative since HDAs became common experimental utility in the last forty years and a full description of the subject is beyond the purpose of this chapter.

Purcell [56] first studied the paths of charged particles traversing a portion of an ideal (no fringing fields or perfect 1/r potential) spherical condenser. The velocity dispersion properties along with the relativistic approach of the problem are discussed in his paper. Ever since, the hemispherical version of the condenser became very popular - due to its advantageous focusing properties and rugged construction - in electron spectroscopy, and many hemispherical spectrometers were studied and utilized in experiments.

Kuyatt and Simpson [57] developed an electron monochromator design based on a hemispherical analyser. The choice of the slit width and electron energy at a given energy resolution for maximum current were investigated in their paper. Their choice of equal size entrance and exit round entrance apertures instead of slits, with dimensions satisfying the restriction $\alpha^2 = w/2\bar{R}$ (where α is the pencil angle, w the aperture diameter and $\bar{R}$ the analyser radius) became the standard criteria for HDA designs.

Paolini and Theodoridis [58], and Kemeny et. al. [59] reported on the transmission properties of spherical plate electrostatic analysers. Roy and Carette [60], [61] included the hemispherical spectrometer in their method of calculating the energy distribution of electrons selected electrostatically. Heddle [62] reported on the comparison of the étendue (the product of the entrance area and solid angle) of electron spectrometers including spherical plate analysers. Polaschegg [63] reported on the features of the spherical analysers with and without pre-retardation. He also reported on the study of the energy resolution and the intensity behavior of the spherical analysers as a function of the entrance parameters. [64] Imhof et. al. [65] studied the energy resolution and transit time spread in the hemispherical analysers involved in coincidence experiments. Kevan [66] also reported on design criteria for a high-resolution angle-resolving HDA.

Hadjarab and Erskine [67] reported on the image properties of the HDA used with a position sensitive detector (PSD), replacing in this way the commonly used exit slit with a large area detector. A double-stage spectrograph consisting of two HDAs has been reported by Mann and Linder [68], and Baraldi and Dhanak [69]. Page and Read [70] investigated the energy non-linearity of HDA when used with a multi-detector anode or PSD.

For a general overview on dispersive electron spectrometers, the reader is referred to the reviews in references [71–73].

In the previous references, the HDA was studied as if the electrostatic field was ideal, i.e. fringing field effects, primarily present at the HDA entry and exit, were not

taken into account. However, for HDAs used with large PSDs, fringing field effects become important, resulting in departures from the spectrograph properties predicted for ideal fields theoretically. In the literature different schemes for treating the fringing field effects are reported. See for example references [67, 74–79].

All studies to date, have basically treated the specific case of a hemispherical spectrometer constructed with the entry and exit apertures placed at the mean radius of the analyser opening (i.e. for radii R_1 and R_2 the entry R_0 is placed at the position $R_0 = \bar{R} = (R_1 + R_2)/2$). In all these cases the potential value V_0 for the circular equipotential line is assumed to be zero, while the orbit followed by the particles inside the HDA is circular. Analysers whose exit due to geometry limitations could not be placed at $\bar{R}$ have recently been reported in the literature [80].

In this work the more general case of an HDA in use with a large PSD with *paracentric* entry (i.e. $R_0 \neq \bar{R}$) and non-zero ($V_0 \neq 0$) entry potential value is studied in detail. The paracentric entry and non-zero entry potential value are considered as free parameters which can be varied, in order to investigate the general focusing and dispersive properties of the HDA. Results are tested on well-known formulas from the literature, which arise as special solutions of the new generalized case. Search for favorable values of the free parameters which optimize the focusing properties are also included in the study, indicating improved focusing properties of the paracentric HDA over the conventional. Theoretical calculations are also accompanied by results on SIMION simulations and experiment (whenever available), for comparison.

The model spectrograph investigated consists primarily of an HDA, a system of electrostatic lenses and a large (40-50 mm diameter) PSD. The use of such a PSD allows for the detection of a whole energy range of particles simultaneously, reducing substantially the acquisition time of the spectrum. The electrostatic lenses are used to focus the charged particle beam at the entrance of the analyser, while at the same time decelerating (or accelerating) the particles from an initial energy T to a final energy t, prior to entering the analyser. The use of such spectrographs is quite common in fields such as electron spectroscopy for chemical analysis (ESCA) [15], time-resolved electron energy loss spectroscopy (TREELS) [16]. Its use, however, in ZAPS requires some special considerations, which are studied here. The spectrograph performance to date for ZAPS use has been reported in various conference proceedings [81–83].

4.2 Motion of a charged particle in an ideal 1/r potential

4.2.1 Definitions

The HDA model under study is shown in Fig. 20. The analyser consists of two cocentric hemispherical plates of inner and outer radii R_1 and R_2, respectively. The center of the hemispheres is set as the origin of the coordinate system. A paracentric entry is located at distance R_0, while a PSD is placed at the HDA exit centered at distance $R_\pi \equiv \bar{R} = (R_1 + R_2)/2$. A cylindrical lens system is mounted with its optical axis centered at the paracentric entry for focusing and deceleration purposes. A particle of

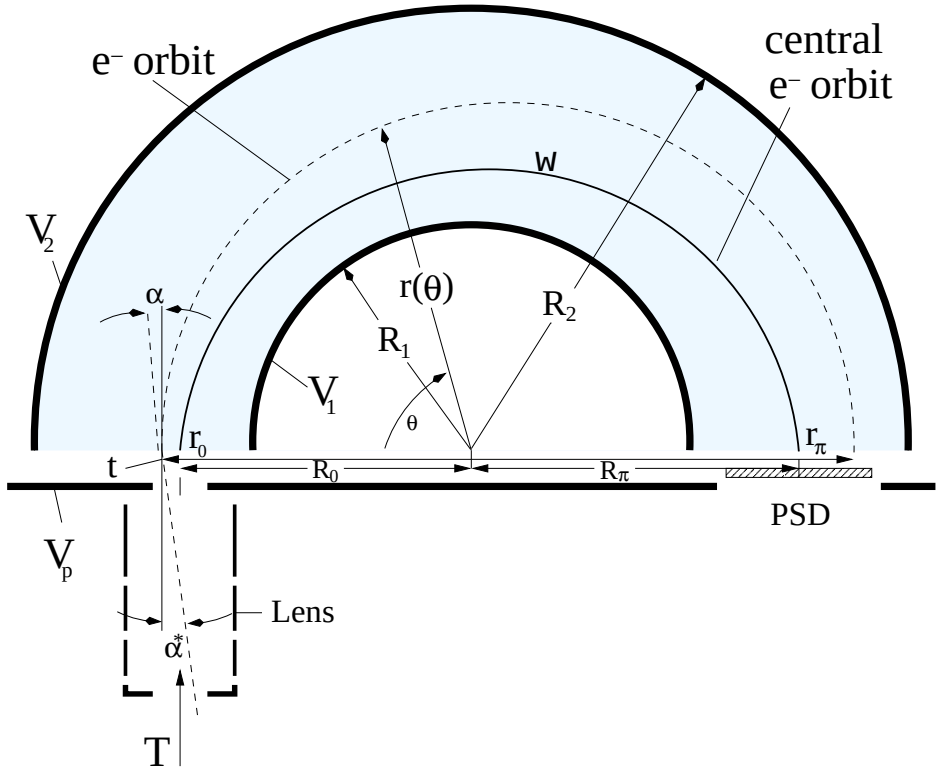

Figure 20: Schematic diagram of the hemispherical deflector analyser geometry.

charge q, mass m and initial kinetic energy T is ejected at *zero* potential far from the spectrograph. Prior to entering the analyser it passes through a deceleration/focusing stage (e.g. lens system) which can change its kinetic energy to t such that:

$$t = T - q\,V_p \tag{27}$$

by applying a potential V_p on the last electrode of the deceleration stage. When deceleration is not required, V_p is set to zero ($V_p = 0$). However, when deceleration is used V_p is the voltage upon which all analyser potentials are referenced to.

The particle enters the HDA at a point r_0 (in the vicinity of R_0) with kinetic energy t and polar angle α. Actually, since the particle is ejected in three-dimensional space, it enters the analyser at an azimuthal angle β also. However, as it will be shown in §4.2.4, β just rotates the motion plane around the axis defined by the entrance point r_0 and the center of the analyser (see §4.2.4). This is the reason why it is not included in Fig. 20 which shows the motion in the orbit plane only. The particle follows a trajectory specified by $r(\theta)$ and exits at r_π after being deflected through an angle $\Delta\theta = \pi$.

A set of parameters, variables and formulas will be introduced here for convenience and will be used in the next sections.

The analyser potential $V(r)$ is ideally given by:

$$V(r) = \tilde{V}(r) + V_p \tag{28}$$

where the symbol $\tilde{V}(r)$ is used as a shorthand for the frequently appearing quantity:

$$\tilde{V}(r) = -\frac{k}{r} + c \tag{29}$$

The symbols $V_1 \equiv V(R_1)$, $V_2 \equiv V(R_2)$ and the corresponding $\tilde{V}_1$, $\tilde{V}_2$ are reserved for the inner and outer hemispheres, respectively. Also the symbol $V_0 \equiv V(R_0)$ and the corresponding $\tilde{V}_0$ is reserved for the value of the potential at the entry R_0. Finally the quantities $\Delta V \equiv V_2 - V_1 = \tilde{V}_2 - \tilde{V}_1$ and $\Delta R \equiv R_2 - R_1$ are defined.

When the analyser is "tuned" to the energy w, an electron with kinetic energy $t = w$ can be made to follow a particular reference trajectory known as the *central trajectory*, in which case the particle is also referred to as the central ray.

For analysing systems with deceleration, as in the present system, one may define an "undecelerated tuning energy" W (using Eq. 27):

$$W \equiv w + q\,V_p \tag{30}$$

and the deceleration ratio F:

$$F \equiv \frac{W}{w} \tag{31}$$

so that a central ray with kinetic energy W far from the spectrometer (at "infinity") undergoing deceleration with factor F will have the energy w just prior to entering the hemispherical analyser. The "reduced" pass energy τ is also defined as:

$$\tau \equiv \frac{t}{w} = F(\frac{T}{W} - 1) + 1 \tag{32}$$

which may also be expressed in terms of the undecelerated quantities, T, W and the deceleration factor F. Finally, the independent parameter γ by which the potential set on the analyser is controlled:

$$q\,(V_0 - V_p) = q\,\tilde{V}_0 \equiv (1 - \gamma)\,w \tag{33}$$

and the parameter

$$\xi \equiv \frac{R_\pi}{R_0} \tag{34}$$

are also defined.

4.2.2 Derivation of the charged particle trajectory

The motion of a charged particle of mass m and charge q in a central potential V(r), is always motion in a plane. The problem is equivalent to the extensively studied "two body" problem. The general solution along with its properties can be found in most of the undergraduate textbooks of classical mechanics. Here, following the formalism of Goldstein's textbook [84], the solution of the orbital motion will be derived in brief

steps. The fixed center of force, which corresponds to the potential, will be taken as the origin of the coordinate system.

Expressed in plane polar coordinates the Lagrangian is:

$$\mathcal{L} = \frac{1}{2}m\,(\dot{r}^2 + r^2\,\dot{\theta}^2) - q\,V(r) \tag{35}$$

The Euler - Lagrange equations of motion are:

$$\frac{d}{dt}\left(\frac{\partial\mathcal{L}}{\partial\dot{\theta}}\right) - \frac{\partial\mathcal{L}}{\partial\theta} = 0 \Rightarrow \frac{d}{dt}(mr^2\dot{\theta}) = 0 \tag{36}$$

$$\frac{d}{dt}\left(\frac{\partial\mathcal{L}}{\partial\dot{r}}\right) - \frac{\partial\mathcal{L}}{\partial r} = 0 \Rightarrow m\ddot{r} - mr\dot{\theta}^2 = -q\frac{\partial V(r)}{\partial r} \tag{37}$$

Integrating the equations of motion (36) and (37), the first integrals of motion (conserved quantities) are obtained:

$$(36) \quad \Rightarrow mr^2\dot{\theta} = const. = L \tag{38}$$

$$(37) \quad \Rightarrow \frac{1}{2}m\dot{r}^2 + \frac{1}{2}\frac{L^2}{mr^2} + qV(r) = E \tag{39}$$

L is the magnitude of the angular momentum of the system [11] while E is the total energy. Two more integrations are needed to solve the equations of motion, since there are two variables, r and θ. It can be shown ([84] pp 75-87) that the equations (38) and (39) can be integrated, giving:

$$\theta = \int_{r_0}^{r} \frac{dr}{r^2\sqrt{\frac{2mE}{L^2} - \frac{2mqV(r)}{L^2} - \frac{1}{r^2}}} + \theta_\epsilon \tag{40}$$

where r_0 and θ_ϵ are defined by the initial conditions. This is the most general solution of the equation of motion. Replacing in Eq. 40 the general central potential V(r), with the electrostatic potential of a spherical capacitor of the form of Eq. 28, the final solution of the particle orbit inside a spherical analyser is obtained ([84] pp 94-98).

$$r(\theta) = \frac{\frac{L^2}{mqk}}{1 + \sqrt{1 + \frac{2E'L^2}{mqk^2}}\cos(\theta - \theta_\epsilon)} = \frac{p}{1 + \epsilon\cos(\theta - \theta_\epsilon)} \tag{41}$$

Eq. 41 is the general solution of a conic section with one focus at the origin. Latus rectum p and eccentricity ϵ are given by the Eqs. 42 and 43, respectively.

$$p = \frac{L^2}{mqk} \tag{42}$$

$$\epsilon = \sqrt{1 + \frac{2E'L^2}{mqk^2}} \tag{43}$$

[11] The spherical symmetry of the system implies the total angular momentum of the system $\mathbf{L} = m\mathbf{r} \times \dot{\mathbf{r}}$ to be conserved. Therefore $\mathbf{L}$ is always perpendicular to the plane of motion.

E′ is a quantity with dimensions of energy which defines the nature of the orbit by defining the magnitude of ϵ (i.e. for $E' < 0 \Rightarrow \epsilon < 1$, and the orbit reduces to an ellipse). E′ is defined from Eqs. 28 and 39 as

$$\frac{1}{2}m\dot{r}^2 + \frac{1}{2}\frac{L^2}{mr^2} - q\frac{k}{r} = E - qc - qV_p \equiv E' \tag{44}$$

In the case of the elliptical orbit - which is the case of a charged particle orbit inside the spherical analyser - Eq. 41 reduces to

$$r(\theta) = \frac{a(1-\epsilon^2)}{1+\epsilon\cos(\theta-\theta_\epsilon)} \tag{45}$$

where a is the semi-major axis given by:

$$a = -\frac{qk}{2E'} \tag{46}$$

4.2.3 Initial & boundary conditions

To further define the elliptical trajectory, the four constants, resulting from the two integrations of the initial equations of motion (36) and (37), must be related to experimentally controlled ones. These are the initial kinetic energy T, the polar angle α (defined by the spectrograph acceptance solid angle) and the entry point r_0. As it will be shown in this chapter, the forth constant θ_ϵ simply defines the orientation of the orbit relative to the analyser coordinate system and it is the only one that explicitly appears in Eq. 45. The initial kinetic energy T is related to the constant E' (see Eq. 182) and therefore to the semi-major axis a. The polar angle α and the entry point r_0, are related to the angular momentum L and therefore the eccentricity ϵ. Therefore, only the θ_ϵ constant needs to be determined explicitly.

Using the initial position and velocity specification: [12]

$$r_0 \equiv r(\theta_0) = \frac{p}{1+\epsilon\cos(\theta_0-\theta_\epsilon)} \tag{47}$$

$$\dot{r}_0 \equiv \dot{r}(\theta_0) = \frac{q\,k\,\epsilon}{L}\sin(\theta_0-\theta_\epsilon) \tag{48}$$

the following relations for the $\sin(\theta_0-\theta_\epsilon)$, $\cos(\theta_0-\theta_\epsilon)$ and $\tan(\theta_0-\theta_\epsilon)$ can be obtained: [85]

$$\sin(\theta_0-\theta_\epsilon) = \frac{L\,\dot{r}_0}{q\,k\,\epsilon} \tag{49}$$

$$\cos(\theta_0-\theta_\epsilon) = \frac{\frac{p}{r_0}-1}{\epsilon} \tag{50}$$

$$\tan(\theta_0-\theta_\epsilon) = \frac{L\dot{r}_0}{qk(\frac{p}{r_0}-1)} \tag{51}$$

[12] Eq.48 is proved using the relation $\dot{r}_0 = \dot{\theta}_0 \frac{\partial r}{\partial \theta}\big|_{r=r_0,\theta=\theta_0}$ and the identity $\frac{\partial}{\partial\theta}\left(\frac{1}{r}\right) = -\frac{1}{r^2}\frac{\partial r}{\partial\theta}$

Keeping in mind that $\mathbf{v} = v_r\hat{r} + v_\theta\hat{\theta}$, it is clearly seen from Fig. 20 that the radial velocity component v_r may be written as:

$$\dot{r}_0 \equiv v_r = v_0 \sin\alpha \tag{52}$$

Also the magnitude of the angular momentum can be written as:

$$L = |\mathbf{L}| = |m\mathbf{r}_0 \times \mathbf{v}_0| = |mr_0v_0 \sin(\frac{\pi}{2} \pm \alpha)| = mr_0v_0 \cos\alpha \tag{53}$$

Using Eqs. 49, 50 and 51 in combination with Eqs. 52, 53 and 42, the elliptical trajectory of Eq. 45 can be written as:

$$\frac{r_0}{r_\theta} = \frac{r_0}{p}[1 + \epsilon\cos(\theta - \theta_\epsilon)] \tag{54}$$

$$= \frac{r_0}{p} + \frac{\tan\alpha}{\sin(\theta_0 - \theta_\epsilon)}\cos(\theta - \theta_\epsilon) \tag{55}$$

Both θ_0 and θ_ϵ are functions of the entrance angle α. However, since only the difference $\theta_0 - \theta_\epsilon$ is important their values can be set for convenience. $\theta_0 = 0$ is a convenient choice for the hemispherical analyser under study, since it implies the starting point of measuring the angle θ, to be the entrance of the analyser. With this choice and using Eqs. 49, 51, 52 and 53, Eq. 55 is finally written as:

$$\frac{r_0}{r_\theta} = \frac{r_0}{p}(1 - \cos\theta) + \cos\theta - \tan\alpha\sin\theta \tag{56}$$

Eq. 56 is the well-known form introduced by Purcel [56] and discussed in more detail by Rudd [86], Hadjarab & Erskine [67] and Louette *et al.* [87].

Taking into account the boundary conditions on the plane separating the analyser from the lens, forming in this way a potential step, it may easily be proven (see appendix E.1) that the energy is conserved in going across the boundary, resulting in the following relation:

$$E' = t - qc = T - qc - qV_p \tag{57}$$

where E' is the total energy inside the analyser found to be conserved in Eq. 44 and is negative for bound motion. It is seen from Eq. 57 that the two total energies T and E' just differ by a constant. Energy T is referred to zero potential, while E' is referred to the potential $q(c + V_p)$ as seen from the definition of the potential $V(r)$ in Eq. 28.

However, the angular momentum is proven (see appendix E.2) *not* to be conserved across the boundary. The two angular momenta $L^{\star 2}$ outside the analyser[13] and L^2 inside the analyser are related as follows:

$$L^2 - L^{\star 2} = -2\,m\,r_0^2\,q\,\tilde{V}(r_0) \tag{58}$$

[13]The symbol $\star$ is reserved for marking quantities inside region of potential V_p to distinguish from quantities inside region of potential V(r).

As it is shown in appendix E.2, a refraction law for charged particles, analogous to Snell's law for light, exists. The discontinuity effects across the sharp potential boundary at $\theta = 0°$, with the exceptions of some references (e.g. [56, 65, 67, 88]), where they are briefly mentioned, have not been well treated in the literature and have contributed to some errors.[14] However, in most cases using *conventional* HDAs, the entry voltage is zero ($\tilde{V}_0 = 0$ or $\gamma = 1$), the entry slits are very narrow and thus, $\alpha^\star$ is rather small making the effect of refraction negligible.

Using the previous results the most general form for the charged particle trajectory inside a non-conventional hemispherical analyser is written as: (see appendix E.3)

$$\frac{r_0}{r_\theta} = \frac{q\,k}{2\,t\,r_0}\frac{(1-\cos\theta)}{(1-\frac{q\,\tilde{V}(r_0)}{t\,\cos^2\alpha^\star})\cos^2\alpha^\star} + \cos\theta - \frac{\tan\alpha^\star\,\sin\theta}{\sqrt{1-\frac{q\,\tilde{V}(r_0)}{t\,\cos^2\alpha^\star}}} \tag{59}$$

This new result was published in a recent paper. [85]

4.2.4 Focusing conditions of the ideal HDA

The focusing conditions of the ideal hemispherical analyser are directly obtained by expanding the elliptical orbit equation (Eq. 56) to second order in α around $\alpha = 0$. [15]

$$\frac{r_0}{r_\theta} = \frac{q\,k + (2\,t\,r_0 - q\,k)\,\cos\theta}{2\,t\,r_0} - (\sin\theta)\,\alpha + \frac{q\,k\,(1-\cos\theta)}{2\,t\,r_0}\,\alpha^2 \tag{60}$$

The first order term in α is readily seen to be zero for $\theta = \pi$ and thus the hemispherical deflector analyser (HDA) is said to focus to first order for a deflection angle of 180°. Particles that enter the HDA with the same radius $r = r_0$ and the same energy but different angles α, after a deflection of 180°, will all lie on radii $r_\pi = r(\theta = \pi, \alpha)$, which will only differ to second order in α.

The most important feature of the HDA is its all order focusing at $\theta = \pi$ for the azimuthal angle β. A simple explanation of this statement is the following: The plane of the elliptical orbit is defined by the origin of the central potential - which is actually one of the foci of the orbit - and the particle position vector $\mathbf{r}_0$. Therefore the ellipse must lie on a plane which intercepts the plane defined by the detector surface across a line which connects the entrance and exit points r_0 and r_π, respectively (see Fig. 21). This should be true for all angles β. Consequently, particles initiated at the same energy t, the same polar angle α but different angles β, will reach the analyser exit at exactly the same point.

The image of the particles on the detection plane is visualized in Fig. 21, while a 3-D plot [85] of a charged particle orbit inside the HDA is shown in Fig. 22. Since

[14] See for example the erroneous result obtained by ignoring refraction for the angular momentum in Eq. 7 in Ref. [58] compared to our Eq. 187 in appendix E.

[15] Alternatively, one may use Eq. 59, written in terms of the incident (unrefracted) angle $\alpha^\star$, to show that the focusing condition still remains the same, i.e. first order focusing (in $\alpha^\star$) takes place for a deflection of 180°.

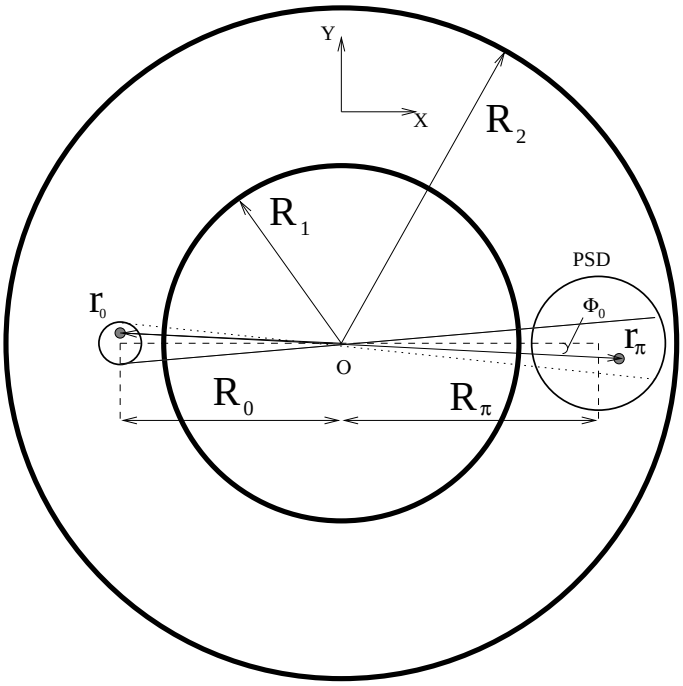

Figure 21: Detection plane of hemispherical analyser.

the entrance point r_0, the center of the analyser at O (one of the foci of the elliptical motion) and the exit point r_π must lie along the same line, the trace along the PSD can be constructed by extending the line r_0 - O to the point r_π, where the range of the trajectory $r_0 + r_\pi$ is determined by the initial kinetic energy t and the azimuthal entrance angle α. Therefore, a beam of particles entering the analyser with a wide spread in kinetic energies will be detected at the PSD along a strip, as shown in Fig. 21 (see also the experimentally obtained image in Fig. 18).

Choosing the XY coordinate system for the detection plane as shown in Fig. 21, the following relations are derived between the x and y coordinates of the entry and exit particle positions:

$$r_0 = \sqrt{x_0^2 + y_0^2} \tag{61}$$

$$\tan \Phi_0 = -\frac{y_0}{x_0} \tag{62}$$

$$x_\pi = r_\pi \cos \Phi_0 \tag{63}$$

$$y_\pi = -r_\pi \sin \Phi_0 \tag{64}$$

from which it becomes clear that the hemispherical analyser inverts the image.

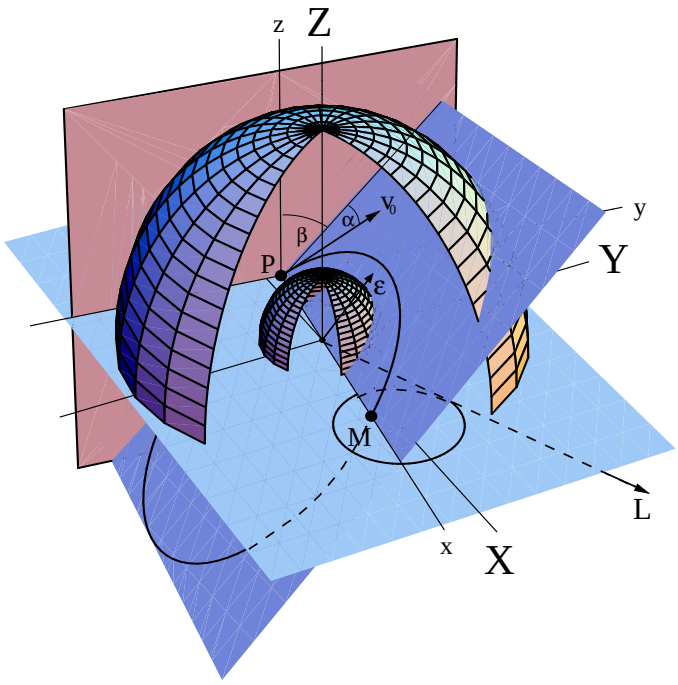

Figure 22: 3-D orbit in HDA: Charged particle enters at P and exits at M with $\alpha = -30°$, $\beta = -50°$, $\gamma = 1.5$, $\tau = 1.16$ and $w = 1000$ eV. **XYZ** is the fixed laboratory frame, while xyz is the relative reference frame traditionally used to describe the orbit in terms of angles α and β. The entry velocity $\mathbf{v}_0$ and eccentricity $\boldsymbol{\epsilon}$ are also shown. From Zouros *et al* [85].

4.2.5 Spectrograph basic equation

Since the HDA focusing properties can be studied only from the ray trace on the exit plane, an expression which gives the position of the particle at the image (exit), as a function of its position and direction at the object (entrance) and its pass energy τ would be very useful. This equation can be derived from Eq. 202 (appendix E) by setting $\theta = \pi$ after some straightforward algebra as follows: [85]

$$r_\pi = -r_0 + \frac{R_0\,(1+\xi)}{1 + \frac{\xi}{\gamma}\,(1 - \tau\,\cos^2\alpha^\star)} \tag{65}$$

This kind of equation is known as the *basic equation* of the spectrograph. The equation can also be written (in terms of potential constants k and c) in the form

$$r_\pi = -r_0 + \frac{q\,k}{q\,c - t\,\cos^2\alpha^\star} \tag{66}$$

or may be rearranged into the usual form:

$$\frac{(r_\pi - R_\pi)}{R_\pi} = -\frac{(r_0 - R_0)}{\xi R_0} - (1 + \frac{1}{\xi}) \frac{1}{1 + \frac{\xi}{\gamma}\sin^2\alpha^\star - (\tau - 1)\frac{\xi}{\gamma}(1 - \sin^2\alpha^\star)} \tag{67}$$

The form of Eq. 67 is the extension of Eq. (8) of Hadjarab and Erskine [67] to the more general paracentric case.[16]

Eq. 65 shows that the range of the electron trajectory inside the analyser (i.e. the sum $r_\pi + r_0$) is a universal function of the "reduced" pass-energy τ and the incident angle α. This, universal scaling with τ is particularly useful during the energy calibration of the spectrometer since different energies T and deceleration factors F must all fall on one universal curve dependent on τ, avoiding the tedious task of calibrating the spectrometer for all combinations of F, T and W used.

4.3 Analyser Voltages

The voltage scheme V_1 and V_2 applied on the inner and outer spherical shells of the analyser, respectively, is actually a function of the tuning energy of the spectrometer. The determination of the voltages is based on the concept of "central" ray, in a straightforward way. The entry and exit points are specified. For these points, a central or reference ray with $\alpha = 0$ and pass energy t, set to the analyser tuning energy w, i.e. $t = w$, is decided. [71]. These conditions are adequate to define the proper potential applied on the analyser. In this study, the central ray is defined such that a charged particle enters at $r = R_0$ (i.e. $r_0 = R_0$) and exits after a deflection by 180° at $r = \bar{R} \equiv (R_1 + R_2)/2$.

Applying voltages V_1 and V_2 on the inner and outer spherical shells of the analyser, respectively, the expressions for k and c are obtained:

$$c = \frac{R_2 V_2 - R_1 V_1}{\Delta R} - V_p = \frac{R_2 \tilde{V}_2 - R_1 \tilde{V}_1}{\Delta R} \tag{68}$$

$$k = \frac{\Delta V}{\Delta R} R_1 R_2 = \frac{\Delta \tilde{V}}{\Delta R} R_1 R_2 \tag{69}$$

Substituting k and c from the expressions above into the spectrograph basic equation Eq. 66, the central ray case reduces to:

$$R_\pi = -R_0 - \frac{q\,\Delta V\, R_1\, R_2}{q\,\tilde{V}_1\, R_1 - q\,\tilde{V}_2\, R_2 + w\,\Delta R} \tag{70}$$

Furthermore, for a pre-specified entrance potential V_0 (see Eq. 28), after substitution of k and c in terms of V_1 and V_2 from Eqs. 68 and 69, V_0 is written in terms of V_1 and V_2:

$$V_0 = \frac{(R_2 - R_0)R_1 V_1 + (R_0 - R_1)R_2 V_2}{\Delta R\, R_0} \tag{71}$$

[16] Clearly, with the identification of $\zeta_\pi = (r_\pi - R_\pi)/R_\pi$, $\zeta_0 = (r_0 - R_0)/R_0$, $\Delta E/E_0 = \tau - 1$ and $\xi = \gamma = 1$ applicable in the case of a conventional hemispherical analyser their result is obtained.

and

$$\tilde{V}_0 = \frac{(R_2 - R_0)R_1\tilde{V}_1 + (R_0 - R_1)R_2\tilde{V}_2}{\Delta R\, R_0} + V_p \tag{72}$$

Finally, solving Eqs. 70 and 71 for V_1 and V_2 the voltage equations are obtained: [17,81]

$$qV_i = qV_p + w + [q(V_0 - V_p) - w]\frac{R_0(R_\pi + R_0 - R_i)}{R_\pi R_i} \qquad i = 1, 2 \tag{73}$$

or expressed in terms of the $\tilde{V}$ potentials:

$$q\tilde{V}_i = w + (q\tilde{V}_0 - w)\frac{R_0(R_\pi + R_0 - R_i)}{R_\pi R_i} \qquad i = 1, 2 \tag{74}$$

which uniquely determine V_1 and V_2 in terms of potentials V_0, V_p, the tuning energy w and the "central ray" positions of the entrance R_0 and the exit R_π, respectively. This is the most general formula for the voltages from which all specific cases can be derived.

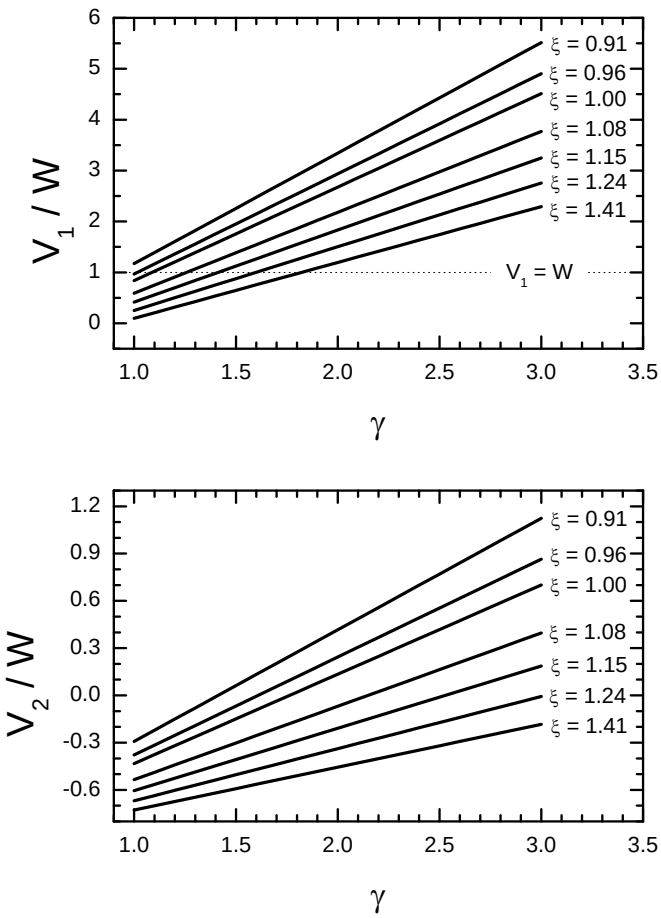

Figure 23: Reduced voltages V_1/W (top) and V_2/W (bottom) applied on the HDA, plotted as a function of parameter γ for different ξ values.(q = -1, $V_p = 0V$)

The potential energy difference $q\Delta V$ is:

$$q\Delta V = \left(\frac{\gamma}{\xi}\right) \frac{(1+\xi)}{\xi} \frac{R_\pi \, \Delta R}{R_2 R_1} w \tag{75}$$

from which a spectrometer constant f can be defined to be:

$$f \equiv q\frac{\Delta V}{w} = \frac{1}{2}\left(\frac{\gamma}{\xi}\right) \frac{(1+\xi)}{\xi} \frac{R_\pi}{\bar{R}} f_0 \tag{76}$$

where f_0 is just the spectrometer constant of the conventional hemispherical analyser, i.e. $R_0 = \bar{R} = R_\pi$ with $V_0 = V_p$ ($\gamma = 1$):

$$f_0 = \frac{\Delta R}{R_2 R_1} 2\bar{R} \tag{77}$$

The constant of the analyser f is actually a number which determines the gradient voltage value applied on the plates, for tuning the spectrometer at a given energy $t = w$. This number was introduced in the past for convenience, since in most spectrometers it uniquely defines the voltages set on the analyser as a function of w (see for example [89]). However, in the paracentric HDA case, f does not determine the voltage values V_1 and V_2 uniquely, since the information on V_0 (or γ) value is also needed. Therefore f is only a qualitative number describing the actual potential gradient between the hemispheres. [17]

In Fig. 23, the reduced voltages V_1/W and V_2/W applied on the HDA are plotted as a function of parameter γ for different ξ values. The proper choice of analyser voltages will be discussed in §6.2. It is worth mentioning at this point, however, that an experimentally desirable feature is the detection of the charged particle of energy $T = W$ at the lowest possible voltage[18].This is the reason for showing in Fig. 23 the case of $V_1 = W$ (for q = -1).

4.4 Properties of the hemispherical deflector analyser

Next, the basic properties of a hemispherical spectrograph are studied through the theoretical predictions based on the previous analysis. In most cases, the predictions are compared to the results obtained by the SIMION ion-optics simulation program, and the experimental data obtained from the use of the paracentric hemispherical spectrograph, studied in this report. The treatment of an ion-optics problem in SIMION

[17] Instead, two analysers constants f_1 and f_2 referring to voltages V_1 and V_2 respectively, could be defined, which, to my opinion should be avoided since it does not simplify the problem of voltage application on the plates.

[18] It is important to use as small as possible voltage values on the analyser electrodes (relative to a certain tuning energy W), as higher energy regions become accessible in this way for the same HV power supply. Furthermore the avoidance of voltage breakdown along with the lower cost of smaller voltage output power supplies, contribute to this argument.

would unnecessarily complicate the presentation at this point, and therefore is not treated here. The same holds for the recording experimental procedure and further analysis of the "raw" data. Therefore, only the final results will be presented in this chapter, in order to be compared to the theoretically obtained ones and be commented further. The reader is referred to chapters 5 and 7 for further insight on either SIMION or experimental techniques, respectively.

4.4.1 Magnification, dispersion and angular aberration

All the spectrograph properties may be obtained from the radial exit equation given in either of the forms of Eqs. 65 or 66. For the sake of simplicity the symbol of $\alpha^\star$ will be replaced with plain α from here on. Thus, Eq. 66 is re-written as:

$$r_\pi = -r_0 + \frac{q\,k}{q\,c - t\cos^2\alpha} \tag{78}$$

In general, the Taylor expansion of the exit position Δr_{exit} up to first order in energy and up to the second order in the angular terms takes the unique form for electrostatic spectrometers: [71, 73, 90]

$$\Delta r_{exit} \equiv \mathcal{M}\Delta r_{entry} + D\frac{\Delta t}{t} + P_1\alpha + P_2\alpha^2 + \ldots \tag{79}$$

In particular, for the HDA, a Taylor expansion of r_π in Eq. 78 to first order in Δr_π, Δr_0, Δt and to second order in α gives:

$$\Delta r_\pi \equiv r(\theta = \pi, R_0 + \Delta r_0, \alpha, t + \Delta t) - r(\theta = \pi, R_0, \alpha = 0, t) \tag{80}$$

$$= \mathcal{M}\Delta r_0 + D\frac{\Delta t}{t} + P_1\alpha + P_2\alpha^2 \tag{81}$$

where

$$\mathcal{M} = -1 \tag{82}$$

$$D = \frac{q\,k\,t}{(q\,c - t)^2} \tag{83}$$

$$P_1 = 0 \tag{84}$$

$$P_2 = -D \tag{85}$$

Here $\mathcal{M}$ is the HDA linear magnification, D the dispersion and P_2 the polar angular aberration or trace width [73] of the hemispherical analyser. It is seen that the magnification $\mathcal{M}$ is always a constant, inverting the image, while the polar aberration term P_2 is always equal and opposite to the dispersion D. These properties are thus seen to be generic properties of any HDA independent of the type of central trajectory chosen.

The dispersion definition in the case of spectrographs with fixed voltages differs from the one valid for spectrometers, where the spectrum is obtained by scanning the

analyser voltages. According to Afanas'ev [71], "the dispersion is the magnitude of the image displacement caused by a slight change in the tuning energy, divided by the relative energy change, for a monoenergetic source". Following Afanas'ev notation: $D = E\,(dx/dW)|_{0,E}$

In cases where the spectrum is obtained at constant tuning energy (a part of the spectrum is recorded simultaneously over the PSD area) the dispersion can be redefined as the magnitude of the image displacement caused by a slight change in the initial pass-energy, divided by the relative energy change, for the initial pass-energy. According to this notation, D is written as:

$$D = t\left[\frac{dr_\pi}{dt}\right]_{r_\pi,t} \tag{86}$$

Substituting in Eq. 83 the expressions for k and c from Eqs. 198 and 199, dispersion D takes the following form:

$$D(\tau) = \frac{\tau\,(1+\xi)}{\gamma[1+\frac{\xi}{\gamma}\,(1-\tau)]^2}\,R_\pi \tag{87}$$

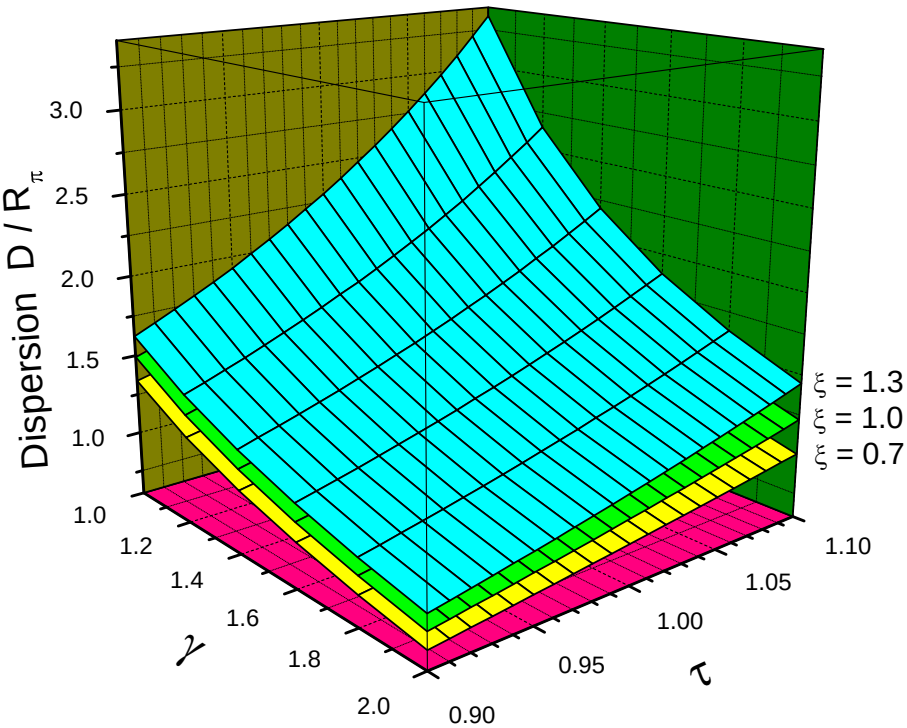

Figure 24: 3-D graph of the dispersion D as a function of the reduced pass-energy τ and the parameter γ for different values of ξ.

The dispersion D in Eq. 87 is seen to be a universal function of the "reduced" pass-energy τ and thus will vary across the length of the PSD with energy. In Fig. 24,

the dispersion is plotted as a function of the reduced pass-energy τ and the parameter γ for different values of ξ. It is seen that the dispersion increases with increasing initial kinetic energy, as expected, through the dispersion definition (Eq. 86). The dispersion, which is the most important parameter in the energy resolution definition, is seen to depend on the electrostatic field and geometry parameters γ and ξ respectively, and therefore can be manipulated through them, for achieving the optimum energy resolution. For a more detailed analysis and discussion on the dependence of the dispersion properties on γ and ξ, see appendix E.4.

4.4.2 Energy resolution

A hemispherical spectrograph with a PSD will have a minimum *position* resolution Δr_π along the dispersion direction. For a slit spectrometer, Δr_π is the exit slit width along the dispersion direction. Thus, the spectrometer base energy resolution R_b will be the maximum energy spread, in the energy of the analysed particles that make it into Δr_π, centered at r_π, from anywhere within Δr_0, at any permissible angle α. The base resolution R_b is written according to the basic equation of the spectrometer, Eq. 81:

$$R_b = \frac{\Delta t}{t} = \frac{\Delta \tau}{\tau} = \frac{\Delta r_\pi + \Delta r_0}{D} + \alpha^2 \tag{88}$$

Depending on analyser parameters, the analysed line shape very often has a long tail to it, and thus the resolution at FWHM is usually smaller or equal to half the base width [61], i.e.

$$R_{FWHM} \leq \frac{1}{2} R_b \tag{89}$$

In systems with a deceleration stage, it is the overall resolution $\Re_b = \frac{\Delta T}{T}$ of the spectrometer plus lens system that is of primary importance. Using Eq. 32 $\Re_b$ is written:

$$\Re_b \equiv \frac{\Delta T}{T} \quad = \quad \frac{\Delta \tau}{\tau} \left(\frac{\tau}{\tau + F - 1} \right) \tag{90}$$

A focusing and decelerating system of lenses is usually implemented into the spectrograph, to provide control over the optical properties of the charged particle beam, prior to energy analysis. The particle beam emanates from the target area of diameter d_o at maximum half-angle α_o (the "pencil" angle) and energy T. The beam is focused at the entrance of the analyser illuminating a disk of diameter d_i, entering at maximum half-angle α_i and energy t (see Fig. 25). In this case, the law of Helmholtz and Lagrange requires: [91, 92]

$$\alpha_o d_o \sqrt{T} = \alpha_i d_i \sqrt{t} \tag{91}$$

This equation can also be written as

$$|M_L| \cdot |M_\alpha| = \sqrt{\frac{T}{t}} \tag{92}$$

where $|M_L| = \frac{d_i}{d_o}$ and $|M_\alpha| = \frac{\alpha_i}{\alpha_o}$ are the linear and angular lens magnification terms, respectively.

Identifying, the HDA entrance angle α with α_i, Δr_0 with the electron beam radius $\frac{d_i}{2}$ at the image and setting $\alpha_o = \frac{d_{LE}}{2l}$, where l is the mean distance of the object (target) to the entrance of the lens and d_{LE} is the diameter of the lens entrance aperture (see Fig. 25), then the entrance angle α is written as:

$$\alpha^2 = \frac{1}{4}\left(\frac{d_{LE}}{M_L\, l}\right)^2 \frac{T}{t} \tag{93}$$

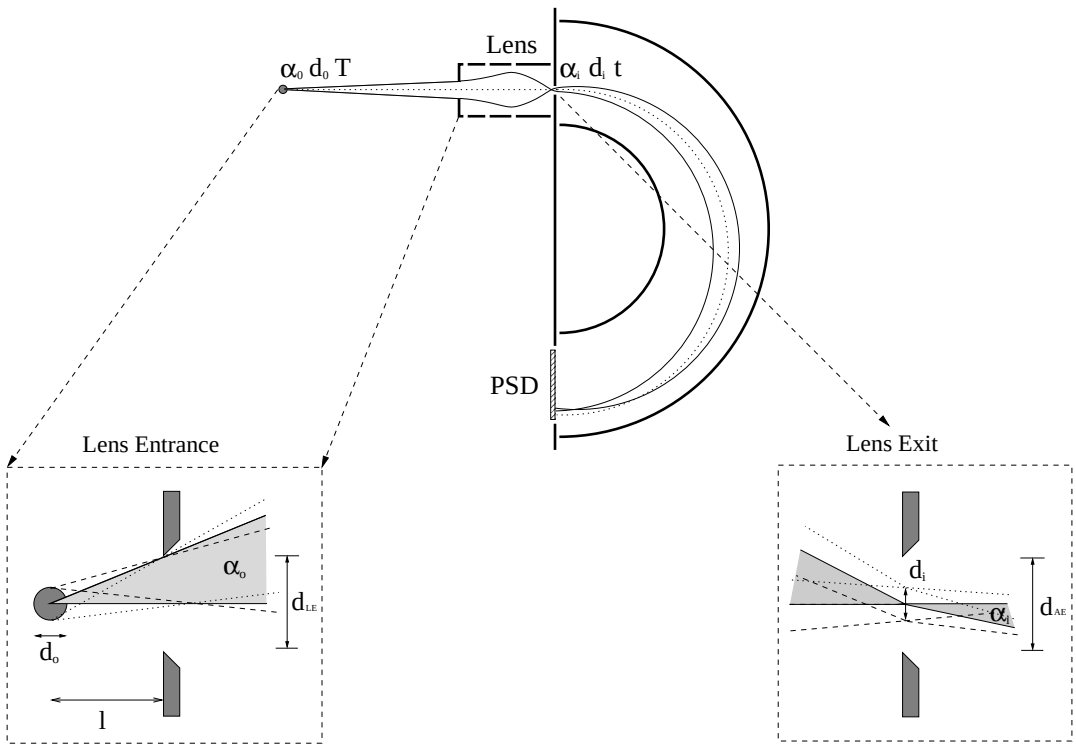

Figure 25: Lens geometry and focusing parameters: α_o and d_o are the object half-angle and diameter respectively, of the electron bundle, originating from the target area (object) at energy T. Following focusing and deceleration in the lens, the electrons exit the lens and enter the analyser at energy t, half-angle α_i covering a disk area of diameter d_i (image).

Upon replacing α^2 from Eq. 93 into Eqs. 88 and 90 it gives:

$$\Re_b = \frac{(\frac{1}{2}|M_L|d_o + \Delta r_\pi)}{D}\left(\frac{t}{T}\right) + \frac{1}{4}(\frac{d_{LE}}{M_L\, l})^2 \tag{94}$$

$$= \frac{(\frac{1}{2}|M_L|d_o + \Delta r_\pi)}{(1+\xi)R_\pi} \cdot \frac{\gamma[1+\frac{\xi}{\gamma}(1-\tau)]^2}{(\tau + F - 1)} + \frac{1}{4}(\frac{d_{LE}}{M_L\, l})^2 \tag{95}$$

Eq. 94 shows that the resolution for *fixed* lens magnification M_L cannot be improved infinitely by increasing the deceleration factor F, but is eventually limited by the term $\frac{1}{4}(\frac{d}{M_L\, l})^2$ which is directly traced to the angular term α^2 in the resolution expression (Eq. 90).

In Fig. 26, a 3-D graph of the overall base-resolution as a function of the reduced pass-energy τ and γ, for different values of ξ, reveals the improvement of the resolution for paracentric entries with $\xi > 1$. This graph, as the rest presented in this chapter (or related appendices), refers to the resolution properties of the particular geometrical conditions of the paracentric spectrograph with $d_0 = 2.5$ mm, $d_{LE} = 4$ mm, $l = 264$ mm and $\Delta r_\pi = 0.2$ mm[19] studied in this thesis.

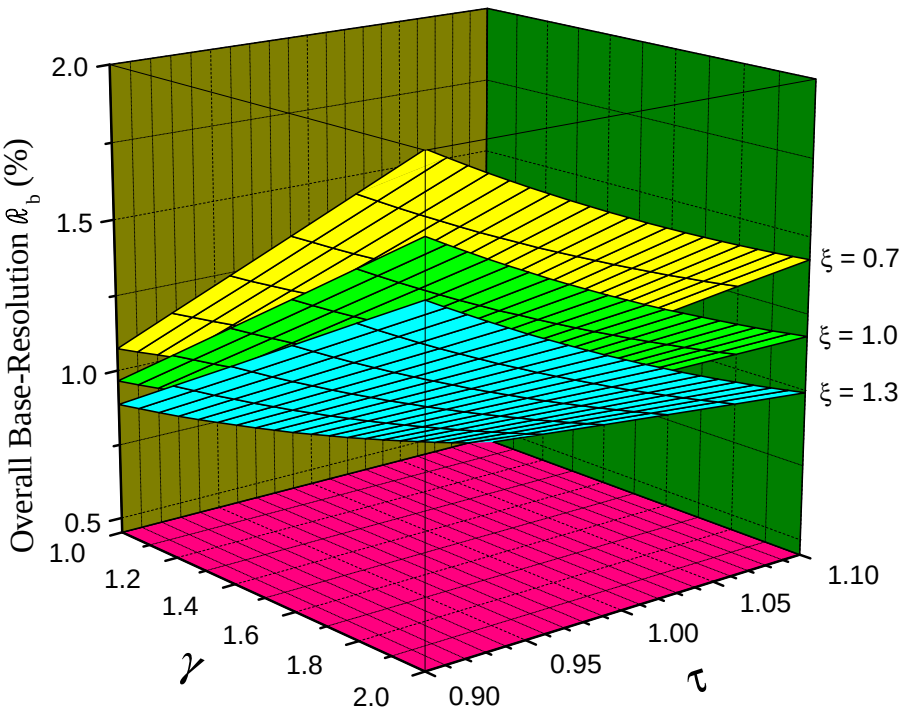

Figure 26: Overall base-resolution as a function of the reduced pass-energy τ and γ, for different ξ values. In all three plots, the lens linear magnification and the deceleration factor were set to unity, i.e. $|M_L| = 1$, $F = 1$ respectively. Note that paracentric entry $\xi > 1$ improves the energy resolution.

It is seen that the resolution decreases with increasing reduced pass energy τ (i.e. increasing the initial kinetic energy T), decreases with increasing ξ and increases with increasing γ. These can readily be interpreted noting that resolution and dispersion are quantities inversely proportional. Therefore, the interpretation for the dispersion

[19]For PSD detectors using MCP's with resistive anode, Δr_π is close to $\sim$ 0.15 mm(see §3.4). However, in this analysis Δr_π should be chosen as the distance occupied by one data acquisition channel, and that should be close to the manufacturer's specifications.

behavior presented in appendix E.4, works also for the interpretation of the resolution behavior.

In appendix E.5 a detailed study of the energy resolution properties is presented. Here, theoretical along with experimental results on the mean overall base resolution $\overline{\Re_b} = \Re_b(\tau = 1)$ as a function of the deceleration factor, are illustrated in Fig. 27 (left). It is seen that achieving small magnification factors $|M_L|$ at small deceleration factors F is very important, as in this case high resolution modes can be avoided. Also, it is seen that the experimental data, obtained according to the way described in §6.2.2, show an improvement for the energy resolution for deceleration factors up to F = 8. The agreement to the theory can be stated as satisfactory due to the presence of fringing field in the real spectrograph, which seems to be the reason for the limited deceleration up to F = 8.

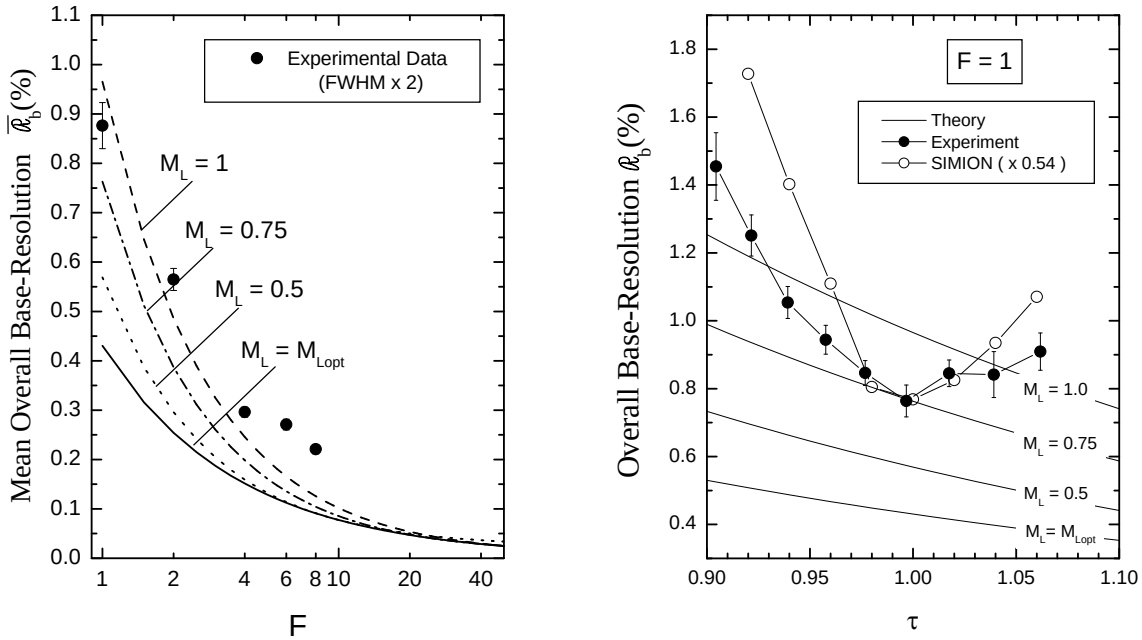

Figure 27: [*Left*] Plot of the mean overall base resolution as a function of the deceleration factor for $|M_L| = 1$, $|M_L| = 0.5$, $|M_L| = 0.75$ and $|M_L| = |M_{Lopt}| = 0.24\,F^{\frac{1}{3}}$. The importance of achieving small magnification factors $|M_L|$ at small deceleration factors F is obvious. [*Right*] Overall base resolution $\Re_b = \frac{\Delta T}{T}$ as a function of the reduced pass energy τ. Comparison between theory (ideal $1/r$ potential), SIMION simulation and experiment. Deceleration factor was set to unity (F=1).

A comparison between theory, SIMION and experiment on the overall base resolution $\Re_b = \Delta T/T$ as a function of the reduced pass energy τ, is illustrated in Fig. 27 (right). Qualitative agreement between SIMION and experiment seems to be reason-

able. SIMION results were scaled by a factor of 0.54. Theoretical results for different magnification factors were plotted in order to have an estimation of the value of this quantity, as the experimental value of M_L can only be indirectly inferred, from the width of the image on the PSD (see §6.2).

The deviation from the theoretical curves behavior is assumed to be due to effects from the fringing fields. It should be noted though, that another factor which contributes to the deviation is the use of the same lens voltages for the whole detected energy range. The lens voltages are set so as to minimize the energy resolution of the rays at energy i.e. $T = W$. This means that other energies, $T < W$ or $T > W$, will be focused either before or after the lens exit, respectively, producing images corresponding to $|M_L| > |M_L|_W$, in general, where $|M_L|_W$ is the magnification factor for the rays at $T = W$. This fact degrades the energy resolution at the edges of the PSD area.

4.4.3 Energy calibration

The energy calibration of the spectrograph is indispensable for the connection between exit particle position and its initial kinetic energy. In the laboratory, the particle position is known from the channel number i of the PSD where the particle left its trace. Therefore a relation between the initial kinetic energy and the channel number i, rather than the exit position, should be established. Here the above relationship is derived theoretically, for a paracentric spectrograph. Initialy, it is assumed that the position along the PSD depends linearly on the channel number i

$$r_{out_i} = G + H\, i \tag{96}$$

Constants G and H will in general depend on the electronic setup. Assuming, n to be the total number of channels available, there will always be an i_{min} and i_{max} which will correspond to the limiting positions along the PSD of diameter d_{PSD} of $r_\pi(min) = R_\pi - d_{PSD}/2$ and $r_\pi(max) = R_\pi + d_{PSD}/2$ such that

$$R_\pi - \frac{1}{2} d_{PSD} = G + H\, i_{min} \tag{97}$$

$$R_\pi + \frac{1}{2} d_{PSD} = G + H\, i_{max} \tag{98}$$

where the diameter of active PSD is d_{PSD}. In the experimental setup 40mm MCP's were used, so nominally $d_{PSD} = 40$ mm with $n = 256$ channels. As directly inferred from the PSD spectrum: $i_{min} = 32$ and $i_{max} = 226$ (see for example Fig. 18(h)).

Eqs. 97 and 98 are solved for the parameters G and H and upon substituting them back into Eq. 96, the position calibration equation reads

$$r_{out_i} = R_\pi - \left(\frac{1}{2} + \frac{i_{min}}{\Delta n}\right) d_{PSD} + \frac{i}{\Delta n}\, d_{PSD} \tag{99}$$

where it was assumed that the center of the PSD at R_π corresponds to the center of the channel range (e.g. $n/2$) with the lowermost edge at channel i_{min} and the

highermost edge at channel i_{max} so that $\Delta n = i_{max} - i_{min} = 194$. Then, assuming uniform illumination of the entrance aperture of the analyser, (i.e. averages $< \alpha >= 0$, $< r_0 >= R_0$) the averaged reduced pass-energy $< \tau >$ of the analysed particles can be related to the channel number via Eq. 65 to obtain the relationship

$$< \tau >= \frac{\gamma \frac{<r_\pi>}{R_0} + (1 - \gamma + \frac{<r_\pi>}{R_0})\xi}{(1 + \frac{<r_\pi>}{R_0})\xi} \tag{100}$$

which upon substitution of r_{out_i} for $< r_\pi >$ from Eq. 99 and τ_i with $< \tau >$ gives the sought exact energy versus channel number calibration relation

$$\tau_i = \frac{1 + \xi + \frac{s}{R_\pi}(\gamma + \xi)(i - i_0)}{1 + \left[1 + \frac{s}{R_\pi}(i - i_0)\right]\xi} \tag{101}$$

where $i_0 = \frac{1}{2}(i_{max} + i_{min})$ is the center channel and $s = \frac{d_{PSD}}{\Delta n}$ is the effective "slit" width of a single channel.

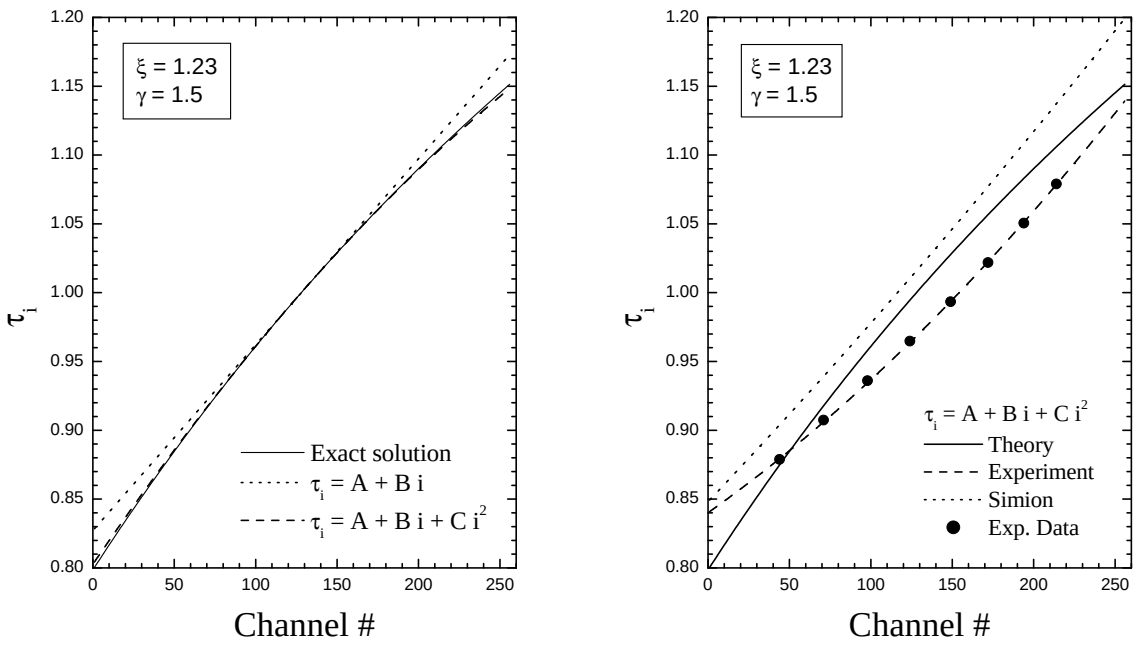

Figure 28: *[Left]* Theoretical energy calibration curves (τ_i) for the cases of the exact calibration (continuous line), first order approximation (dotted line) and second order approximation (dashed line). *[Right]* Comparison of the second order reduced pass-energy approximation in the case of ($\xi = 1.23$, $\gamma = 1.5$) as predicted by theory, SIMION and experimentally measured.

It is seen that the relationship between the reduced pass energy τ and the channel number i is in general not linear. However, when the quantity $\delta \equiv \frac{s}{R_\pi}(i - i_0)$ is smaller than 1, as in most cases (for example with $d_{PSD} = 40$ mm, $R_\pi = 101.6$ mm, $i_0 = 129$ and $\Delta n = 194$, the maximum value of $\delta = 0.255$), a power expansion of the denominator of Eq. 101 is justified yielding

$$\tau_i \approx 1 + \left(\frac{\gamma}{1+\xi}\right)\delta_i - \left[\frac{\xi\,\gamma}{(1+\xi)^2}\right]\delta_i^2 \tag{102}$$

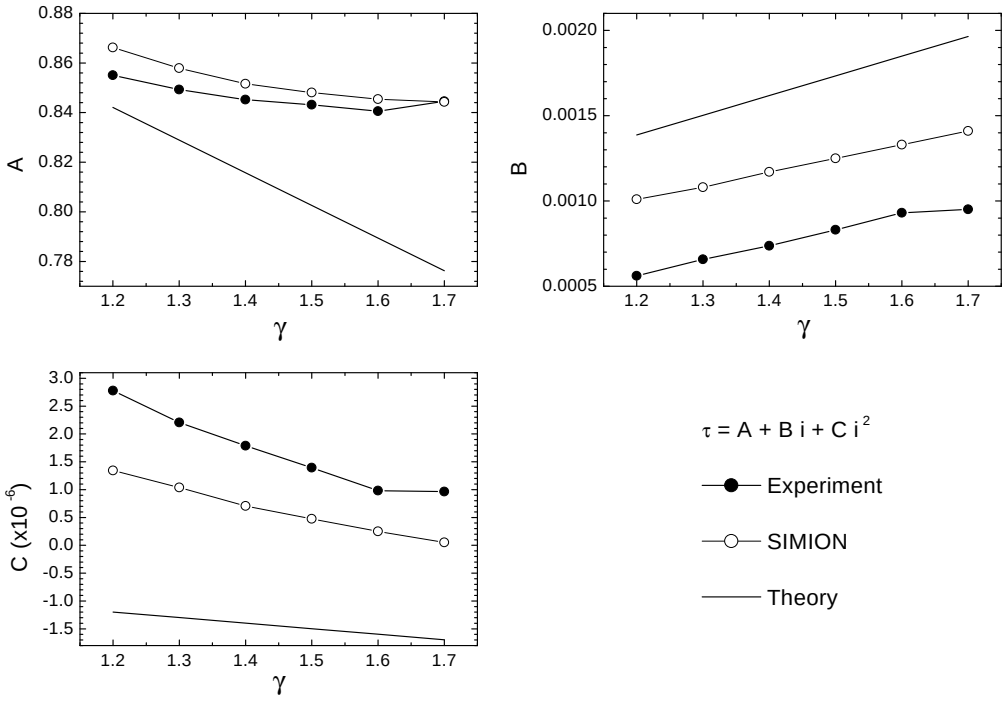

Figure 29: Constants A,B and C of the energy calibration relation: $\tau_i = A + B\,i + C\,i^2$, as a function of γ. Comparison between theory, SIMION and experimental results.

In most experimental cases the relation between the reduced pass energy τ and the channel number i is better fitted by a quadratic function of the form

$$\tau_i = A + B\,i + C\,i^2 \tag{103}$$

When Eq. 102 is put in the form of Eq. 103, it gives for A, B and C:

$$A = 1 - \frac{s\,i_0\,\gamma\,[s\,i_0\,\xi + R_\pi(1+\xi)]}{[R_\pi(1+\xi)]^2} \tag{104}$$

$$B = \frac{s\,\gamma\,[2s\,i_0\,\xi + R_\pi(1+\xi)]}{[R_\pi(1+\xi)]^2} \tag{105}$$

$$C = -\frac{s^2\gamma\,\xi}{[R_\pi(1+\xi)]^2} \tag{106}$$

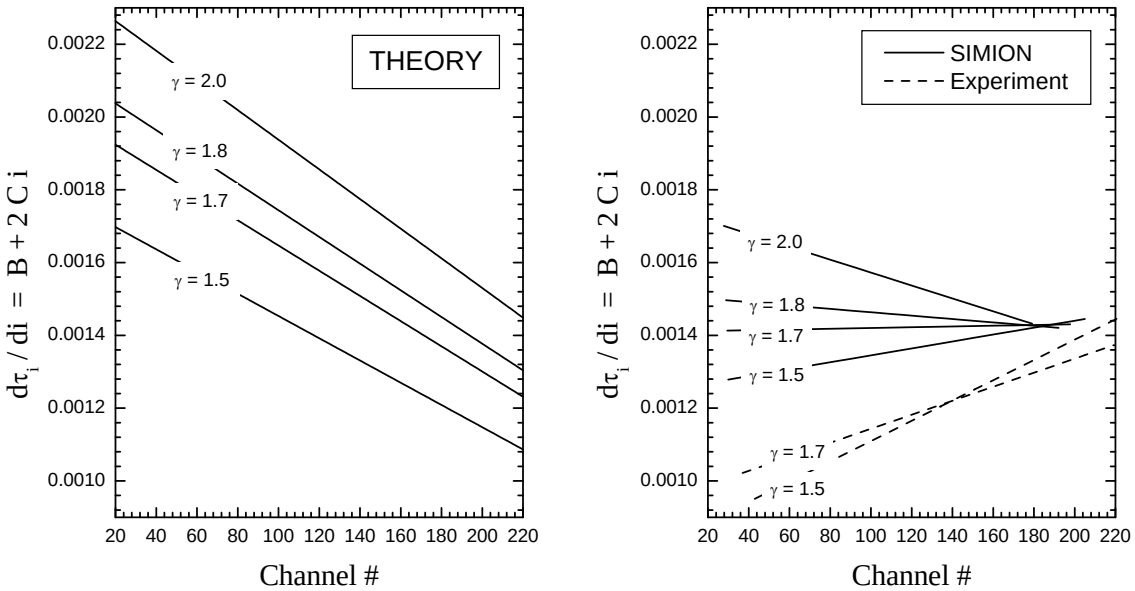

Figure 30: Plot of $\frac{d\tau_i}{di} = B + 2Ci$ theoretical calculations (left) and, SIMION and experimental results (right). SIMION show that for some particular γ value (between 1.7 and 1.8) $C = 0$, and thus the energy calibration relation becomes linear. Experiment seems to indicate to this behavior.

As can can be seen from Fig. 28(Left), where the exact reduced pass-energy calibration is compared to the first and second order approximation respectively, a quadratic function in i does an excellent job in representing $< \tau >$, being very close to the exact theoretical result. In Fig. 28 (right) the theoretical second order reduced pass-energy approximation (in the case of $\xi = 1.23$, $\gamma = 1.5$) is compared to the SIMION prediction and experimental measurement. In Fig. 29 the constants A,B and C of the quadratic reduced pass energy calibration relation Eq. 103 are plotted as a function of γ, for comparison between theory, SIMION and experimental results. The results of SIMION and experiment show similar behavior, contrary to theory. It is a quite unexpected result that the curvature of the quadratic curve has an opposite sign in SIMION and experimental cases, compared to the theoretical one. This can be seen much clearer in Fig. 30 where the derivative function $\Delta\tau$/channel of Eq. 103 is plotted for theoretical, SIMION and experimental results. Note that for some particular γ value (between 1.7 and 1.8) SIMION predicts $C = 0$, and thus the energy calibration relation becomes linear. Experiment seems to be in qualitatively agreement with this behavior. The above result is of great interest in pointing out the side effects caused by the fringing fields on the non-ideal field spectrograph operation.

4.4.4 Energy acceptance window

For a slit spectrometer the energy acceptance window is just the base energy width. For the case of a spectrograph with a PSD of effective diameter d_{PSD} the energy window $\Delta\tau_{window}$ is defined [67] as the energy range which can be simultaneously detected on the PSD.

Using Eq. 65 and assuming the averaged entrance angle $< \alpha >= 0$ and $< r_0 >= R_0$, then the basic reduced pass energy is related to position relation via:

$$\tau = \frac{r_\pi(\gamma + \xi) - R_\pi(\gamma - 1)}{R_\pi + r_\pi\,\xi} \tag{107}$$

Assuming that the end points of the PSD are at $R_\pi \pm \frac{1}{2}d_{PSD}$ achieved at the energy acceptance limits τ_{max} and τ_{min}, then through Eq. 107 it is obtained:

$$\tau_{max} = \frac{(R_\pi + \frac{1}{2}d_{PSD})(\gamma + \xi) - R_\pi(\gamma - 1)}{R_\pi + (R_\pi + \frac{1}{2}d_{PSD})\,\xi} \tag{108}$$

$$\tau_{min} = \frac{(R_\pi - \frac{1}{2}d_{PSD})(\gamma + \xi) - R_\pi(\gamma - 1)}{R_\pi + (R_\pi - \frac{1}{2}d_{PSD})\,\xi} \tag{109}$$

Thus, the effective energy acceptance window $\Delta\tau_{window} = \tau_{max} - \tau_{min}$ is given by:

$$\Delta\tau_{window} = \frac{\left[\frac{d_{PSD}}{R_\pi\,(1+\xi)}\right]\gamma}{1 - (\frac{\xi}{2})^2\left[\frac{d_{PSD}}{R_\pi\,(1+\xi)}\right]^2} \approx \gamma\,\frac{d_{PSD}}{R_\pi\,(1+\xi)} \tag{110}$$

The energy window is seen to increase with increasing γ and decrease with increasing ξ. This can be clearly seen in Fig. 31[Left], where the energy acceptance window $\Delta\tau_{window}$, given by Eq. 110, is plotted as a function of γ for different values of ξ.

The dependence of $\Delta\tau_{window}$ on γ may be explained directly from the fact that γ can be seen to be a kind of acceleration factor. From conservation of energy the central ray must have a new energy w' at R_0 such that:

$$w' + qV_0 = w + qV_p \tag{111}$$

Using the definition of γ from Eq. 33 in Eq. 111

$$\frac{w'}{w} = \gamma \tag{112}$$

Thus, for $\gamma > 1$, the particle is further accelerated, so that a central ray with initial energy W ends up having a pass energy w' at R_0 such that

$$\frac{w'}{W} = \frac{w}{W}\frac{w'}{w} = \frac{\gamma}{F} \tag{113}$$

The ratio γ/F is thus seen to be the overall deceleration/acceleration factor.

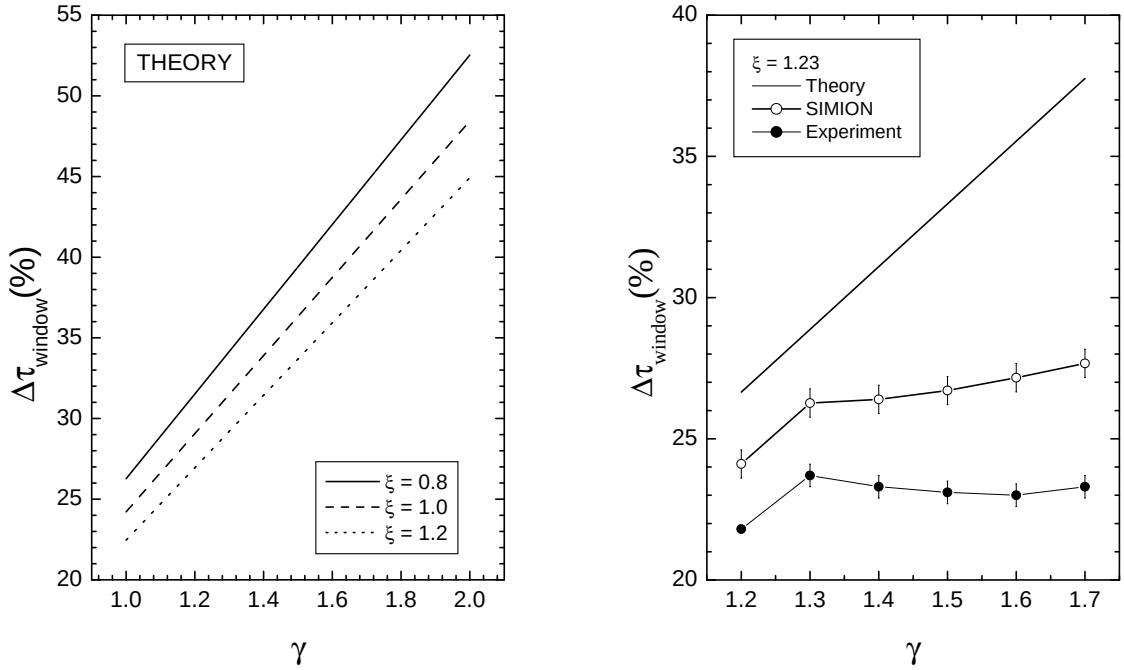

Figure 31: *[Left]* The energy acceptance window $\Delta\tau_{window}$ predicted theoretically as a function of γ for different ξ. *[Right]* Comparison of the energy acceptance window $\Delta\tau_{window}$ predicted by theory and SIMION, and experimentally measured for the HDA under study.

The dependence of $\Delta\tau_{window}$ on ξ may be explained directly from the fact that, an increase in ξ is identical to a decrease in the entrance point distance R_0. Therefore the charged particle enters the analyser at higher potential value and is more accelerated. Therefore, ξ as well as γ, can also be seen to contribute to the overall acceleration/deceleration factor.

In Fig. 31(right) the energy acceptance window $\Delta\tau_{window}$ is plotted as a function of γ for $\xi = 1.23$, (i.e. the analyser under study), using data from theory, SIMION simulations and experiment. SIMION and experimental results are much alike showing a much lower increase of the energy window with increasing γ. Thus, fringing field effects indicate a much smoother acceleration (or deceleration) at the analyser entry and exit, establishing a lower overall acceleration/deceleration factor compared to theory.

4.5 Conclusions

In this chapter, a new, more general approach to the focusing and dispersive properties of the ideal field hemispherical deflector analyser was attempted. The paracentric

analyser entry ξ, and the non-zero entry potential value γ, were considered as variable parameters allowing for a further insight into the HDA focusing and dispersive properties. In addition, the use of a large PSD at the HDA exit, resulted in a more complete information, including, the dependence of the focusing properties also on the detection position. Finally, the incorporation of the focusing/decelerating lens system at the entrance of the HDA, accounted for the control over the focusing of the charged particle beam, prior to energy analysis. Thus, the linear magnification factor was reserved as an extra variable parameter, for improving the focusing properties and therefore the energy resolution.

In this way, the more general forms of the trajectory of a charged particle inside an non-conventional HDA, the basic equation of the HDA and the voltages applied on the HDA hemispheres were obtained, which reduce to the well-known formulas in the literature, depending on the choice of entry and potential parameters. It is worth mentioning at this point that, the problem of particle refraction across a potential boundary, present in all analysers but not well treated in the literature, was also solved, establishing a refraction law, analogous to Snell's law in light optics.

Results on the HDA dispersion and resolution properties, indicate that an HDA operated with a paracentric entry $\xi > 1$ has improved energy resolution over the conventional HDA, although the energy acceptance window for the paracentric HDA is seen to be reduced in this case. The energy resolution of the HDA was also studied as a function of the lens linear magnification factor $|M_L|$, showing that there is an optimum value $|M_{Lopt}|$, depending on geometrical factors and the deceleration factor F, which minimizes the energy resolution.

Experimental and SIMION simulation results, on the energy resolution as a function of the deceleration factor and the PSD exit position, on the energy window and on the energy calibration, were also included in this chapter for comparison to the theory. These results indicate a general agreement between SIMION and the experiment which deviate from the theory, though. The explanation is the presence of the fringing fields, resulting in large departures from the ideal 1/r field, especially at the HDA entry and exit. The fringing field effects will be better understood after the SIMION analysis presented in chapter 5. The lens parameterization was excluded from the study at this point. It was performed empirically and is presented in chapter 6.

5 The paracentric HDA: II. Ion optics simulations using SIMION

5.1 SIMION HDA study motivation

SIMION is a very powerful user-friendly ion-optics package that can simulate the trajectories of charged particles flying in a setup consisting of electrostatic and/or magnetostatic elements. In SIMION the space is transformed to a 3-dimensional grid, and the potential at each grid point of the volume is calculated for every element, using a relaxation method. [93] The relaxation method, which actually approximates the Laplace Equation solutions, uses the 6 nearest neighbor points in the 3-dimensional space, to obtain the average new estimates for each point. Ions are flying in the 3-dimensional space by experiencing the electrostatic and/or magnetostatic forces of the estimated potential at each grid point. Relativistic and space charge effects are also included in the ion-optics treatment. It is not the intention of this dissertation to explain in detail SIMION's operational features, but a few remarks on how one may build and solve a problem in SIMION have been summarized in the appendix F. The reader is referred to the SIMION manual for further information [93]

The idea of simulating the spectrograph using SIMION arose due to the two possible lens mounting positions available on the analyser, placed at $R_0 = 82.55mm$ (paracentric entry) and $R_0 = \bar{R} = (R_1 + R_2)/2 = 101.6mm$ (central or conventional entry) respectively.

Two identical spectrograph models were built in SIMION differing only at the location of the analyser entry, ($R_0 = 82mm$ for paracentric entry and $R_0 = 102mm$ for central entry, respectively) as shown in Fig. 32. Electrons with initial kinetic energy W = 1000eV were flown from a point source located at a distance of 30mm from the lens entrance, within an emittance cone angle of 6 degrees. These were focused at the entrance of the analyser by the lens and further energy analysed inside the HDA to be detected at the exit plate, which simulated the PSD electron detector. In both cases, all voltages applied on the lens and hemispheres were the same. The HDA voltages used were those known from the theory of the conventional (central entry) ideal spherical condenser with asymmetric voltages ([94] - table II).

The improved focusing conditions on the exit plane area achieved for the paracentric over the central entrance are shown in Fig. 32, where the two cases are compared. The V = 0 equipotential is emphasized. The result of the fringing fields on the potential near the entrance and exit of the analyser are clearly visible. For the case $\theta = 180°$, to smaller deflection angles is clearly seen to result in a badly focused trace Δr. In the paracentric case, good focusing conditions on the detector plane are restored. The improvement of Δr is about a factor of 3.

This interesting SIMION result prompted a more detailed study of the spectrograph focusing properties, and their dependence on the electron entrance position and possibly the analyser electrode voltages. This was also the reason for the theoretical study of the paracentric HDA, presented in chapter 4, along with the ray tracing calculations

performed with the SIMION package to be presented in this chapter.

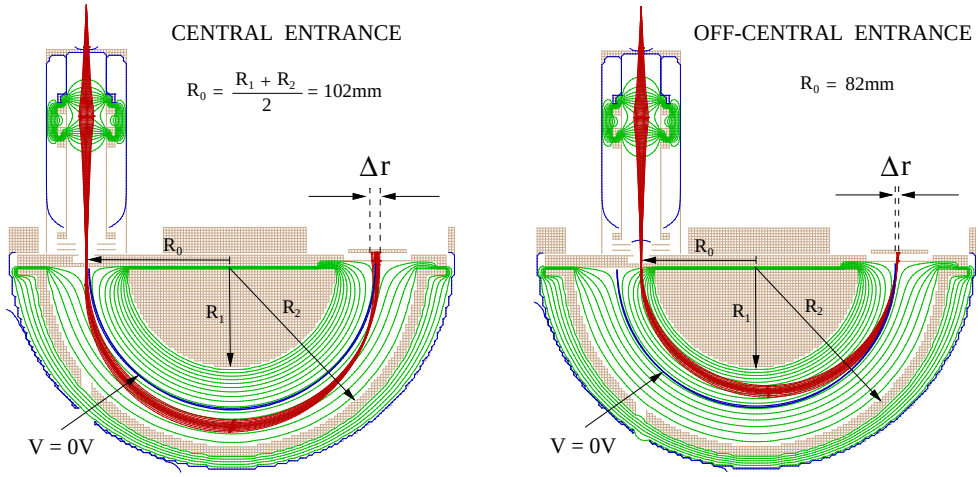

Figure 32: SIMION simulation. Left: central entrance with $R_0 = \bar{R} = 102$mm. Right: paracentric (off-central) entrance with $R_0 = 82$ mm. In both cases all voltages are the same. Clearly observable are the improved (by about a factor of 3) focusing conditions on the position sensitive detector achieved for the paracentric entrance. From Benis & Zouros [17].

5.2 Spectrograph simulation under SIMION

The primary point in designing a focusing-dispersive system in SIMION is to retain the focusing properties unaffected by the design scaling. The cylindrical lens focusing properties depend solely on the ratio λ = d/D, where d is the spacing between the neighboring elements and D is the cylinder lens diameter. A convenient and popular ratio is $\lambda = 1/10$, [91] which is also the case of the lens in use. The spectrograph scaling design therefore depended primarily on the lens scaling design, since the smaller distances were the ones between the lens elements.

In order to maintain the value of $\lambda = 1/10$ in the scaling design, the spectrograph should be designed, in such a way that, the spacing d, between the neighboring lens elements, would correspond to the values of 1, 2, 3,...,etc grid units (gu), and therefore D = 10gu, 20gu, 30gu, ..., etc. Despite the cylindrical spectrograph symmetry, the relatively large spectrograph dimensions along with the limited (64MB) RAM memory allowed by SIMION version 6.0 in use, did not permit the construction with d > 1 gu. For example, with d = 2 gu, SIMION would require about 150MB of RAM memory per electrode, which SIMION6.0 could not handle.[20] The remaining choice of d = 1 gu

[20]SIMION allows for the use of unlimited *virtual* memory when running under DOS, but at the price of becoming extremely slow. SIMION7.0 though version for WindowsNT allows the use of unlimited virtual memory.

resulted in the scaling of 1 gu to 2.286mm, and 19MB RAM memory for each electrode element. Seven electrodes were utilized, 3 for the lens, 3 for the HDA and 1 for the PSD.

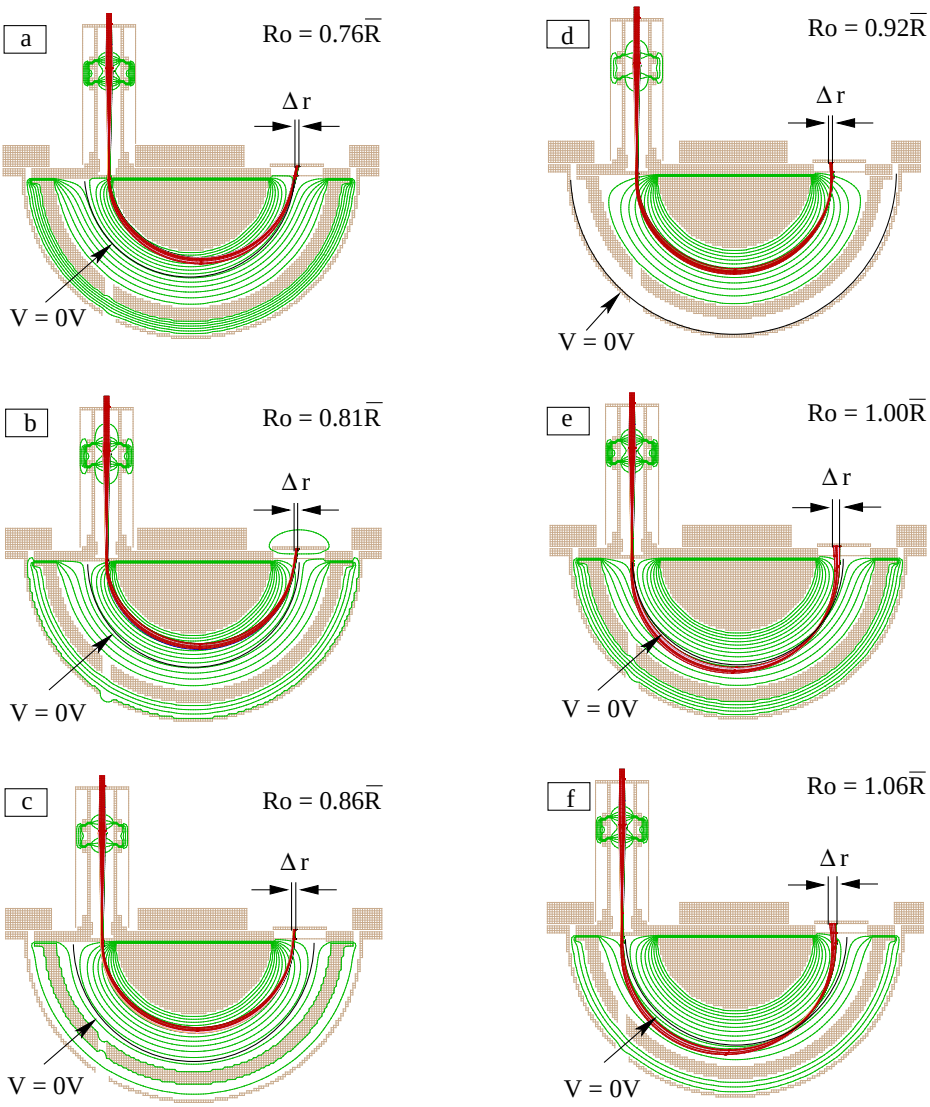

Figure 33: SIMION simulation for six different analyser entries R_0. Electrons at initial kinetic energy T=W are flown from the gas-cell area and focused under the same lens voltages at different R_0. The analyser voltages were set, according to Eqs. 73, for the optimized γ values obtained from the energy resolution study, at each case. The electron trajectories followed inside the spectrograph for along with the equipotential lines and location of the zero equipotential are shown. It is seen that there is an improvement in focusing trace width Δr for the cases of $R_0 < \overline{R} = \frac{R_1+R_2}{2}$ [(a)-(d)] compared to the conventional central entrance case $\overline{R}$ (e).

Electrons were generated to be flown from the distance where the gas-cell was actually placed at the experimental setup, i.e. 264mm from the lens entrance aperture. The study took place with two kind of electron sources. A point source where 9 electrons were flown from the center of the gas-cell and an extended source where 63 electrons were generated all over the gas-cell volume. In both cases electrons were emitted within the allowed solid angle defined by the electron emitting point and the lens entrance aperture.

In order to study the focusing properties as a function of the entrance position R_0 (i.e. the parameter ξ in Eq. 34) and the potential value V_0 (i.e. the parameter γ in Eq. 33) at this point, six identical models of the spectrograph were designed, differing only at the position of the analyser entrance aperture.

In the following study, which includes the central entry case ($R_0 = \overline{R} = \frac{R_1+R_2}{2}$) and the paracentric entry used in the experiments (R_0 = 82.55mm), only the non-decelerating operation mode is considered (F = 1 or V_p=0). For this mode, one lens element was enough to focus the mono-energetic electrons at the analyser entrance. It was found that using element V_{L5} at a voltage of V_{L5} = -0.695T, where T was the kinetic energy of the electrons, the smallest focusing trace width at the entrance of the analyser was achieved. The analyser was tuned to the electron energy T (W = T), according to the voltages predicted by the theory of paracentric HDA in Eq. 73. Thus, for a given set of (R_0,V_0) or (ξ, γ) parameters, a set of V_1, V_2 electrode voltages were defined, according to Eq. 73. Then, for each one of the six spectrograph models (i.e. for a set of ξ), parameter γ was scanned and the focusing trace width Δr across the PSD area was recorded. An energy calibration was used to convert the width Δr to a base energy width ΔE. The energy calibration was accomplished by flying electrons at different known energies along the lens axis (zero azimuthal angles) and recording their position across the PSD area (see §4.4.3 and §7.1).

5.3 Energy Resolution Optimization

The results on the base energy resolution for point and extended sources are shown in Fig. 34. As it can be clearly seen, there is no entrance position which is best. Rather specific combination of R_0 and V_0 (or ξ and γ respectively) parameters lead to the best focusing condition. In general, for entrance positions R_0 smaller than the central one $\overline{R}$, there is an improvement of the energy resolution while for larger ones, resolution becomes worse. Results using a point electron source indicate the combination of $R_0 = 0.86\overline{R}$, ($\xi = 1.16$) and $\gamma = 1.9$ as the best values for the energy resolution. However, the more realistic case, i.e. the extended electron source, predicts the values of $R_0 = 0.81\overline{R}$, ($\xi = 1.23$), $\gamma = 1.7$ as the best combination. This fact fully justifies the choice of $R_0 = 0.81\overline{R} \simeq 82.6mm$ for the analyser entrance in the new-built spectrometer. It should be pointed out that for an experiment using a gas-nozzle as a target instead of a gas-cell, the point source results should be followed in order to have the best focusing conditions.

A qualitative explanation of the energy resolution improvement for the cases of

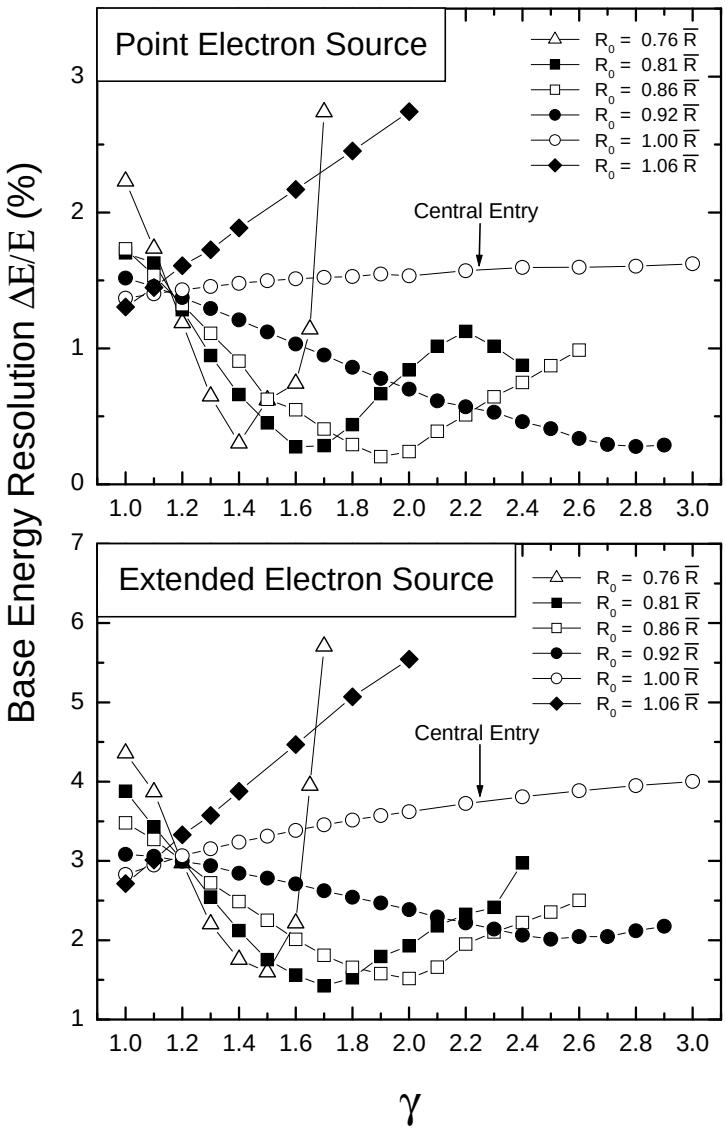

Figure 34: SIMION study of base energy resolution for point and extended electron sources for different (γ , ξ) cases.

smaller entrance aperture distance than the conventional one ($R_0 < \overline{R}$) can be viewed in Fig. 33. The electron trajectories followed inside the spectrograph for the optimum focusing cases of the six different entrance aperture positions along with the equipotential lines, are shown.

For the case of $R_0 = \overline{R}$ (see Fig. 33(e)) it is noticed that the electron trajectories do not lie in the neighborhood of the V=0 circular equipotential line as theory predicts. Instead they deviate to negative potential values resulting in a longer path inside the analyser. This behavior is attributed solely to the large fringing fields at the entrance

and exit of the analyser and may be qualitatively understood in the following way. The orbit deviation towards negative potentials results in smaller values of the total conserved energy E' inside the analyser, relative to the one corresponding to the central ray. This leads to an increase in the value of the semi-major axis of the elliptical orbit ($a = -qk/2E'$) or in other words in a longer path. Then, as it is clearly seen in Fig. 33(e), the focusing point takes place at angles much smaller than the theoretically predicted 180°, where the detector lies. Consequently, the focusing trace width becomes larger than the theory prediction.

The same explanation stands for the improvement of the focusing trace width when $R_0 < \overline{R}$ (see Fig. 33(a-d)). Electrons are flown towards positive potentials, increasing in this way the total conserved energy E', relatively to the one corresponding to the central ray of the conventional entry. The semi-major axis a of the elliptical orbits decreases, the path inside the analyser becomes smaller and the focusing point "moves" closer to the analyser exit at 180°.

5.4 Energy Resolution over the PSD area

The energy resolution study presented in §5.3 refers to trajectories for which the kinetic energy T is equal to the tuning energy W of the analyser. A more complete study, on the variation of the energy resolution over the detection (PSD) area, as a function of the initial electron kinetic energy, for different ξ, γ cases was also performed.

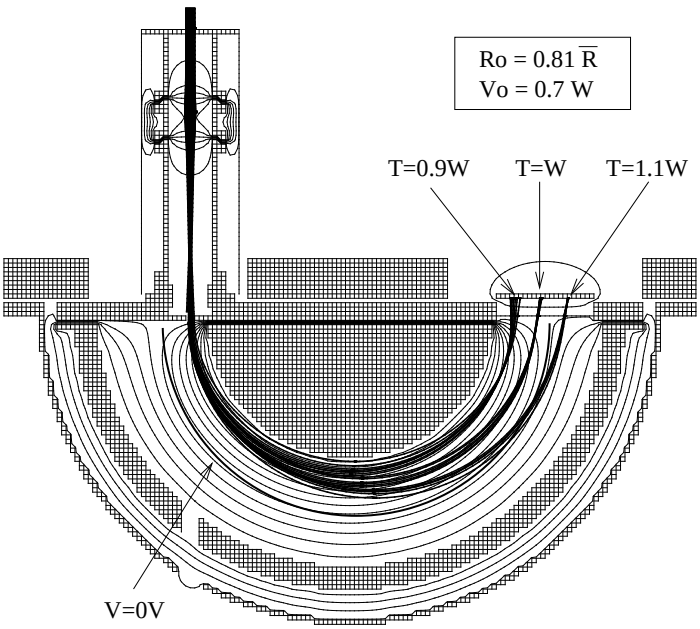

Figure 35: SIMION study of trace widths over the PSD area of three electron groups at kinetic energies of 0.9W, W and 1.1W. Electrons were flown from the gas-cell area to the spectrometer under the same focusing conditions. Here, $R_0 = 0.81\overline{R}$ and $\gamma = 1.7$

The electron elliptical orbits at smaller or larger kinetic energies than W, lie at different potential value areas. Therefore the paths inside the analyser are different for each of these energies resulting in a variation of the focusing trace width, compared to the case of T = W. This case is graphically illustrated in Fig. 35. Three electron groups of kinetic energies T=0.9W, T=W and T=1.1W were flown from the gas-cell area to the spectrometer under the same spectrograph voltages for the case of $R_0 = 0.81\overline{R}$ and $\gamma = 1.7$.

Note that even though in Fig. 35, it seems that the focusing trace width is the smallest for the case of T = 1.1 W, the energy resolution $\Delta T/T$ is worse than the case of T = W. This is clearly seen in Fig. 36 where the quantitative results on the energy resolution over the PSD area are shown. The voltages applied on the HDA for each case were the ones which provided the best energy resolution for T = W (see Fig. 34). Electrons were flown from all over the gas-cell area in groups of different kinetic energies. All the groups were focused by the same lens voltages, since the spectrometer (and therefore the lens) is run at fixed voltages for each tuning energy W.

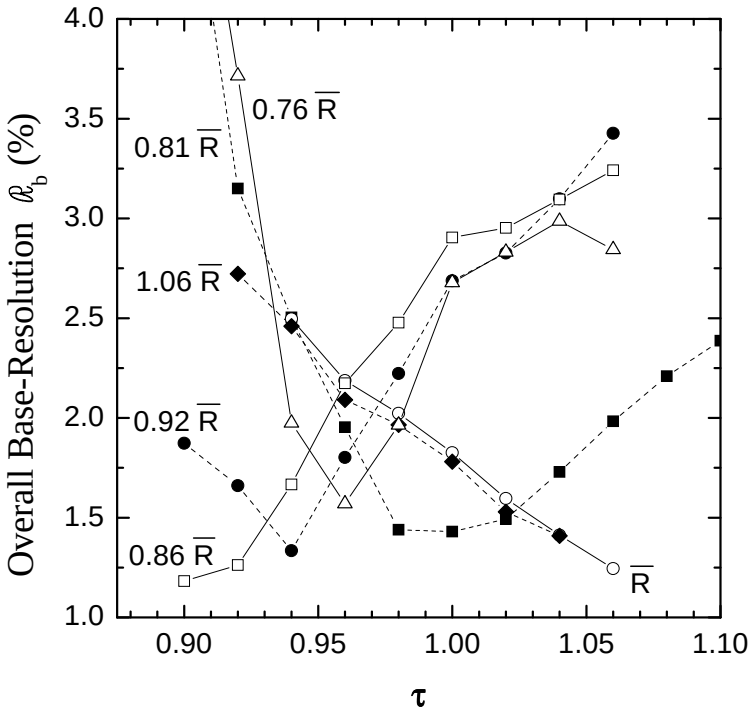

Figure 36: SIMION study of energy resolution over the PSD area for different entries R_0. The HDA voltages for each case were the ones which provided the best (optimum γ) energy resolution for T = W.

5.5 Energy Window

A more general study, on the HDA energy window, for different ξ, γ cases was also performed. Results for the case of $\xi = 1.23$ and $\gamma = 1.5$ have already been shown in §4.4.4 Fig. 31. In Fig. 37 the reduced energy window $\Delta\tau_{window}$ of the spectrograph is shown for each one of the six different ξ cases and for all γ values. The energy window was obtained by flying groups of extended source electrons at all possible energies that can be detected at the exit within the PSD limits used in the experiments (i.e. 40mm diameter). Only cases of 100% transmission (i.e. all initial electrons detected finally at the exit area) are considered. Cases where extreme non-linearities of the energy calibration at the edges of the exit area were excluded.

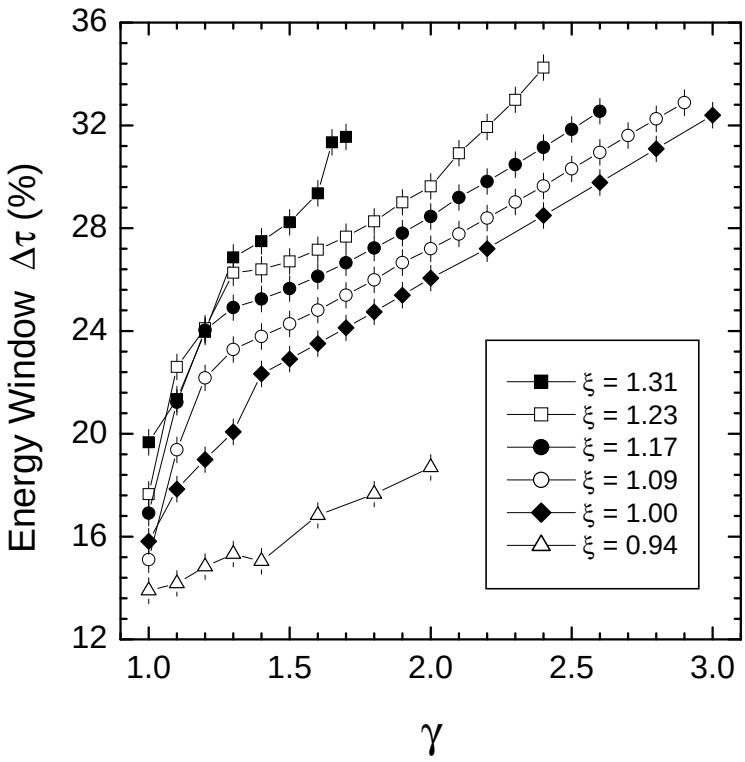

Figure 37: SIMION study of reduced acceptance energy window for the hemispherical spectrograph with different locations of the entrance point ξ and entrance potential parameter γ. Energy window is defined by the PSD limits. Cases where transmission through the analyser was 100% were only considered.

It is seen that the smaller the distance of the entrance aperture from the analyser center, the larger the energy window. This fact is also understood within the concept of the increase of the total conserved energy E', compared to the conventional entry one, that has already been mentioned in §5.3. Thus, for the case of $R_0 = 82.6mm$

and $\gamma = 1.7W$, decided by energy resolution requirements, the reduced energy window reaches the value of $\Delta\tau_{window} = 0.27$, while in the central entrance case this value is only $\Delta\tau_{window} = 0.16$. Therefore proper combination of entry R_0 and potential V_0 not only improves the energy resolution, but also enhances substantially the spectrograph energy acceptance window. This is an important result of interest to the greater spectrograph community.

5.6 Discussion - Conclusions

The previous study of the spectrograph using the SIMION ion-optics package showed that SIMION can be a very useful tool in designing and studying a charged-particle detection system. A primary question though, on how well SIMION simulates reality has to be commented. For this reason, the SIMION simulation results on the overall base energy resolution as a function of the reduced energy τ, the universal energy calibration curve, the energy window and the mean overall base energy resolution as a function of γ, presented in other chapters, are shown together in Fig. 38, for convenience.

It is clearly seen from Fig. 38 that, although SIMION does not reproduce quantitative the experimental results, a general agreement between SIMION and experiment, which deviates from the theory of the ideal 1/r potential, is observed. Indeed, the functional form of the overall base energy resolution over the PSD area is not identical to the experimental but satisfactorily alike (Fig. 38(top-left)). The energy calibration curve differs substantially from the experimental one, but the sign of its derivative is the same, contrary to the theoretical prediction (Fig. 38(top-right)). The energy window is predicted higher than the experimental but the behavior as a function of γ is the same and again different from the theoretical prediction (Fig. 38(bottom-left)). Finally, although the mean overall base energy resolution as a function of γ do not coincide, both SIMION and experiment, predict the same γ value as the optimum for energy resolution minimization.

The above remarks, clearly shows that SIMION can simulate the behavior of a focusing/dispersive system (when properly designed as mentioned in §5.2), quite safely. This study showed that quantitative experimental results could not be reproduced by SIMION but qualitative results, which elucidate the behavior of the focusing and dispersive properties of the system, were very well predicted. This is a quite strong indication for the correctness of SIMION general predictions.

In this chapter, it has explicitly been shown that for a hemispherical spectrograph, the combination of entry $\xi > 1$ ($R_0 > \bar{R}$) and an entry potential with $\gamma > 1$ ($V_0 > 0$)) results in improved focusing properties (energy resolution and energy window) over the conventional case of $\xi = 1$ and $\gamma = 1$. Unfortunately, this result could not directly demonstrated experimentally, as explained in §6.2.1. However, the available experimental results for the case of $\xi = 1.23$ and $\gamma = 1.5$ strongly supports the correctness of the SIMION results presented in this chapter.

The deviation of SIMION simulations and experimental results from the theory is

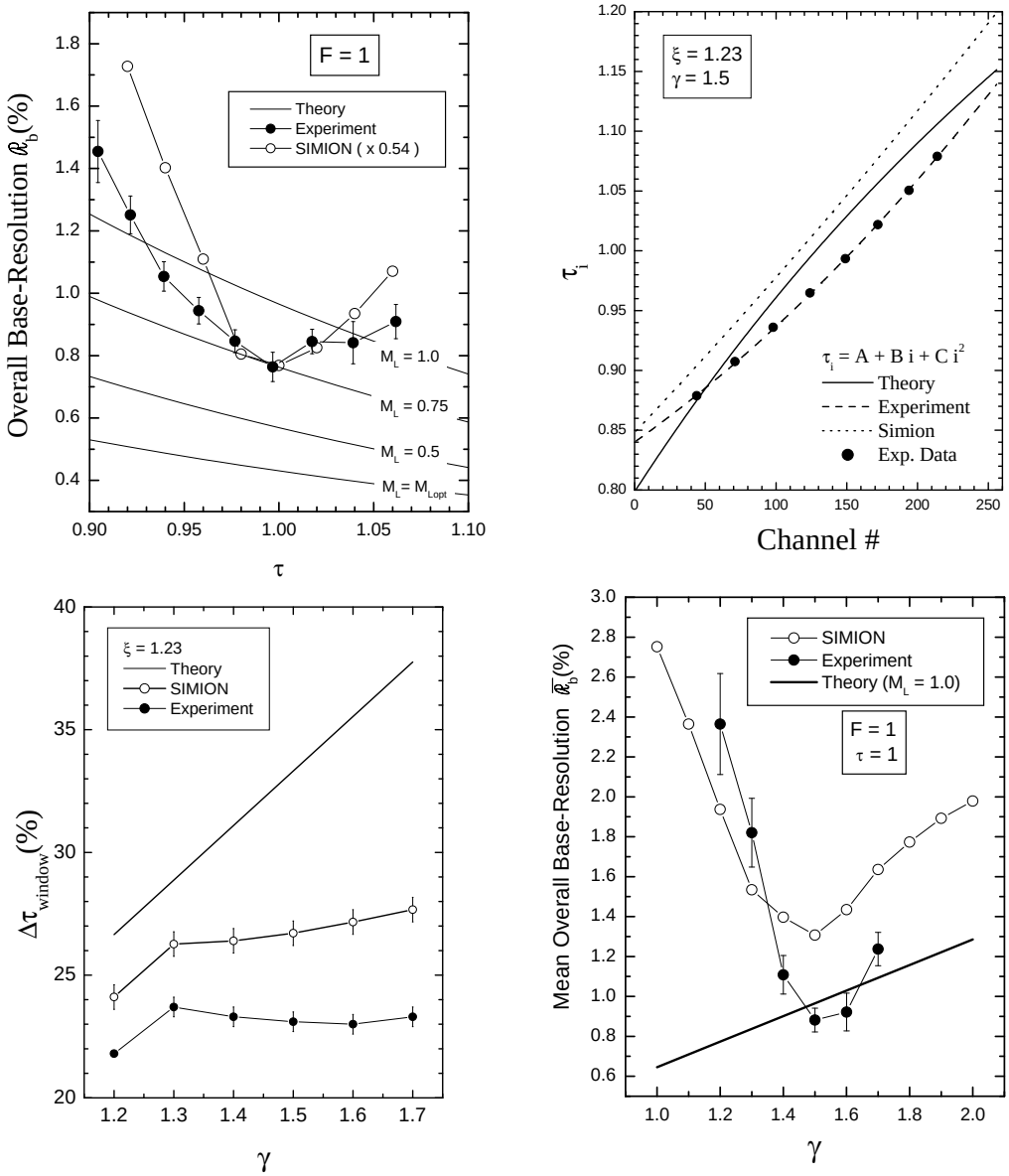

Figure 38: SIMION simulations, theoretical calculations and experimental results on (top-left) the overall base energy resolution as a function of the reduced energy τ, (top-right) the universal energy calibration curve, (bottom-left) the energy window and (bottom right) the mean overall base energy resolution as a function of γ, are shown for comparison.

attributed to the fringing fields, present in both SIMION and experiment. Actually, the paracentric entry along with the non-zero entry potential is seen to compensate for the the fringing field effects, in the sense that improved quality focusing conditions are achieved despite the presence of large fringing fields. This is pointed out in our recent NIMA Letter [17]. Therefore improvements in energy resolution can be expected

to be attained without the use of fringing field correctors, simplifying in this way the implementation of large PSD area as a detector. It should be reminded, that the complicated nature of the fringing field problem does not permit any straightforward analytical solutions. Then, SIMION becomes a powerful tool for obtaining an insight into ion-optical problems involving stray fringing fields. As Dahl mentions in the SIMION manual [93] "SIMION's capabilities are designed to develop intuition and promote understanding".

6 The paracentric HDA: III. The real spectrograph

The experimental studies of the HDA energy resolution, energy window and energy calibration have already been included in chapters 4 and 5, for comparison to the theory and SIMION simulations. In this chapter, the results on the analyser and lens voltages parameterization, complete the HDA study, initiated in chapter 4. The performance of the paracentric HDA in low and high resolution modes is also presented here, while special considerations on the reliability of the absolute cross-section results are discussed in detail. Finally, an efficiency comparison of the new hemispherical spectrograph and the KSU tandem parallel plate spectrometer is presented. The data presented in this chapter were analysed using the method discussed in chapter 7.

6.1 Spectrograph operation mode

Spectrographs using a PSD can be run in two modes. The first mode is with *fixed voltages*, where the voltage values remain constant during the measurement, while a portion of the spectrum is recorded. Then, the next spectrum portion is recorded at the new fixed voltages and finally the whole spectrum is obtained by overlapping all the different portions (see chapter 7). The second mode is with *scanned voltages*, where the spectrograph voltages are scanned between their minimum and maximum values (i.e. minimum and maximum energy values of the spectrum, respectively) at constant rate. The data are recorded on a tape and analysed by "replaying" the tape. The *scanned voltages* mode has the advantage that the same peak is detected at all different possible positions on the PSD area, evening out in this way small differences in PSD efficiency establishing an average efficiency for the whole spectrum. [21] In addition an average energy resolution is established contrary to the position dependent resolution of the *fixed voltages* mode. However, the complexity of the *scanned voltages* mode when the analyser is combined with a focusing lens system (which in principle could be scanned too) in relation to the quadratic energy dependence on the channel number, lead to a rather complicated data analysis. Therefore the *fixed voltages* mode is preferable due to its simplicity. Moreover, an aesthetic advantage of the *fixed voltages* mode is that the spectrum is monitored continually on the computer screen, contrary to the *scanned voltages* mode where the spectrum is revealed only after all the data have been replayed. In many cases it is very important for the experimenter to watch the spectrum development, since this can lead to crucial decisions on the proper operation of the system or on possible changes to the experimental planning.

In this dissertation, the *fixed voltages* mode was used in the spectrograph operation. The analyser and lens voltage values were determined by considerations presented in §6.2.

[21] However, for a new pair of MCP's the efficiency variation is not more than 2%, which is well within the statistical error bar in a typical ZAPS measurement.

6.2 HDA - Lens voltages parameterization

6.2.1 V_0 study

The analyser voltages are given by Eq. 73. In this equation the optimum values of the parameters R_0 and V_0 (or ξ and γ, respectively) have yet to be decided. A study of the above parameters should precede the lens voltages study, as it defines the HDA properties independent of the focusing conditions applied by the lens at the HDA entrance. Unfortunately, the spectrograph was not designed for this kind of studies, since the lens can be mounted only in two positions on the analyser plate V_p (i.e. $R_0 = \frac{R_1+R_2}{2} = 101.6mm$ and $R_0 = 82.6mm$). A SIMION treatment of this problem is presented in §5, where favorable focusing properties for the position of $R_0 = 82.6mm$ are predicted (see Fig. 34).

Initially an electron gun was used to study the focusing quality in the two experimentally available positions. However, electron gun instabilities, due to both temperature and negative bias voltage changes, led to non-reproducible results and thus the idea of doing the study using the electron gun as the electron source was abandoned.

The idea of using ion-atom collisions to produce a single Auger peak on the Binary Encounter electron (BEe) peak (see §2.1) was preferred instead. In this way, the minimization of the FWHM of the Auger line at different voltage settings, could be safely studied. The price that had to be paid though, was that the only available position for the focusing lens was the $R_0 = 82.6mm$,[22] since these measurements, due to present hardware constraints, could only be done at 0°. Therefore, a systematic study like the one achieved with SIMION was not possible. Instead, a study of V_0 for the position of $R_0 = 82.6mm$ was performed and the results were compared to SIMION predictions.

Collisions of 21.7MeV F^{8+} + H_2 were used in order to obtain a spectrum of a single Auger peak (the $(2p^2)^1D$) lying on the top of the BEe peak. The Auger peak was used in order to study the energy resolution while, the BEe peak was used as a supplementary study for the energy window and the transmission function of the spectrometer. This line had already been measured with a tandem parallel plate spectrometer [29], so comparison of the two spectrometers could also be directly made (see §6.5).

The analyser voltages were set for the tuning energy of W = 2500eV and deceleration factor F = 1. The lens voltages were set at the empirical values $V_{L4} = -0.45W$ and $V_{L2} = V_p = 0$, while V_{L5} was reserved as a variable parameter.[23] In this way, for each V_{L5} value, V_0 was varied in order to achieve the optimum focusing conditions. The observed Auger peaks were fitted with Gaussians and the FWHM was obtained. The results are plotted in Fig. 39, where it is seen that there is no unique γ value for which the best energy resolution is attained, but rather a combination of V_0 and V_{L5}. A further study of the energy acceptance width, the energy calibration, the efficiency

[22] At 0°, the ion-beam exits the analyser from the exit aperture, available only for the position of $R_0 = 82.6mm$.

[23] All voltages are referred to tuning energy $W(\text{Volt}) = W(\text{eV})/|e|$, where e is the electron charge in atomic units.

and the HDA voltages, is needed, in order to decide on the optimum V_0 value to be used.

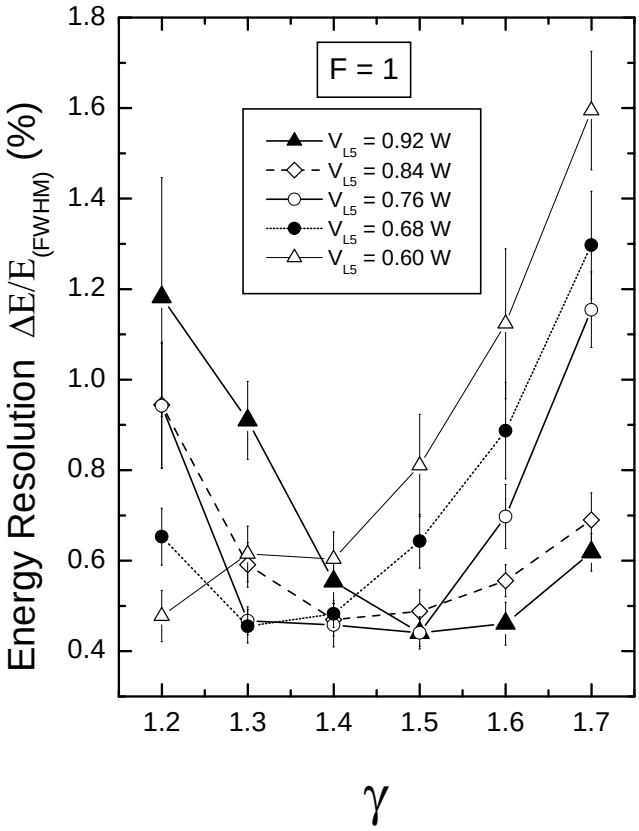

Figure 39: Energy resolution study as a function of potential parameter γ, at deceleration factor F = 1, using the $(2p^2)^1D$ Auger peak obtained in collisions of 21.7MeV $F^{8+} + H_2$.

It is very important to have a constant spectrograph transmission for the whole attainable energy window, otherwise it would be a function of the PSD position and should also be studied as an extra experimental parameter. The spectrograph transmission was monitored, by comparing the experimentally obtained BEe peak to the theory. In this way the energy window was obtained for each case of V_0 value. The results were already presented in Fig. 31(right) along with the theoretical and SIMION predictions. The extreme non-linear energy-to-channel relation for $V_0 < 0.2W$ should be mentioned at this point. These cases were excluded from the study.

A parameter that cannot be excluded from the analysis is the maximum applied voltage values as mentioned already in §4.3. Therefore, the lowest possible voltage values should be preferred for accessing higher energy values with lower probability of

high voltage breakdown.

Keeping in mind the results of the above study shown in Figs. 31(right) and 39, along with the fact that the energy of the electrons in this dissertation do not exceed the value of 4keV and the fact that 3kV power supplies were readily available, the value of $V_0 = 0.5W$ or $\gamma = 1.5$ was decided on. In this way, the optimum energy resolution was achieved at an energy window of $\Delta E/W = 22.5\%$ for a maximum permissible electron energy of 3.8keV in the low resolution mode of operation.

6.2.2 Lens focusing study

So far, it was assumed that the lens magnification factor $|M_L|$ is a perfectly controllable feature which can take any value down to $|M_{Lopt}|$. Actually, the value of $|M_L|$ depends both on the number of focusing elements and the voltage values applied on them. The general rules applied to lens systems, when the distance of the electron source from the lens entrance is kept constant, are the following: [92]

- for a three-element lens system with variable acceleration/retardation, $|M_L|$ and $|M_\alpha|$ both change.
- for a four-element lens system with variable acceleration/retardation, one of the magnifications can be kept constant ($|M_L|$ or $|M_\alpha|$), while the other changes ($|M_\alpha|$ or $|M_L|$, respectively).

Lenses with more than four elements may have other advantages, such as lower aberrations or a more extended operation range. [92]

The actual values of M_L could only be indirectly inferred from the width of the image on the PSD. A theoretical paraxial-ray lens focusing study, including extended electron sources (i.e. gas-cell) and focusing conditions for rays covering a wide energy window at different deceleration factors is in general quite complicated. Instead, SIMION simulations were used, in order to understand the lens behavior under the previously referred conditions. Lens voltages V_{L5} and V_{L4} were scanned in a very wide range appropriate for minimizing the trace width of rays at energies $T = W$ at the HDA exit.

The same study took place under experimental conditions, and the actual lens voltages were empirically set to minimize $\overline{\Re_{FWHM}}$ at different deceleration factors F. The $(2p^2)^1D$ Auger line produced in collisions of 21.7MeV F^{8+} + H_2 was used again in the same way as in §6.2.1. The results are shown in Fig. 40.

In Fig. 41(left) a comparison of the DDCS $(2p^2)^1D$ spectra at decel factors of 1, 4 and 8 can be seen. Note that, while the energy resolution is improving, the area under the peak, which is the single differential cross-section for the formation and Auger decay of the RTE $2p^2\ ^1D$ line, remains the same (see also §6.4 and Fig. 46) as it should. In Fig. 41(right) the spectrograph energy resolution at FWHM is shown as a function of the deceleration factor. The data are the same as the ones presented in Fig. 27 for the mean overall base resolution.

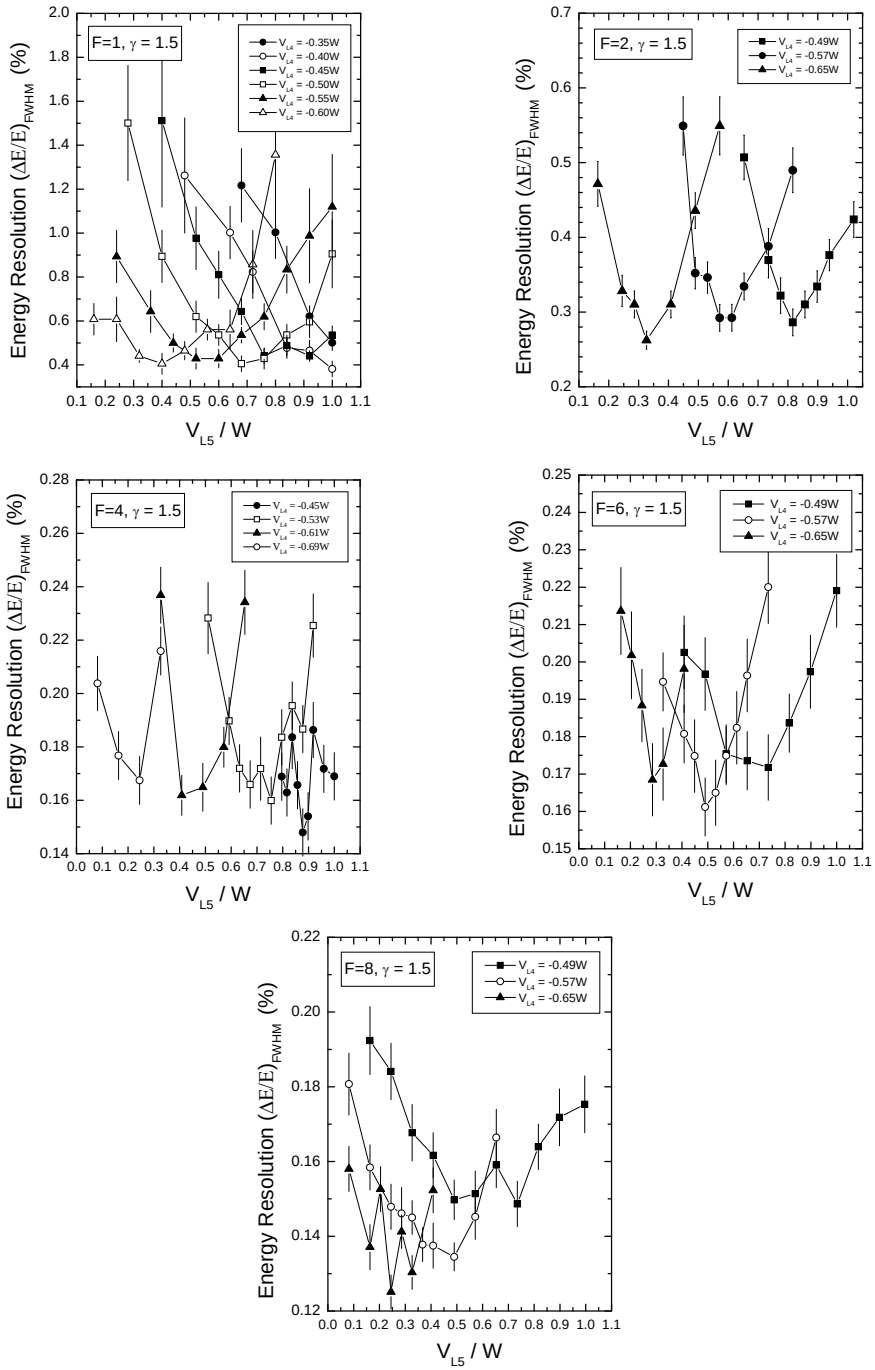

Figure 40: Experimental energy resolution at FWHM study for different deceleration factors F. Lens voltages V_{L5} and V_{L4} were scanned in very wide range appropriate for minimizing the FWHM of the $2p^2\ ^1D$ Auger line, used for the study, which was produced in collisions of 21.7 MeV F^{8+} + H_2.

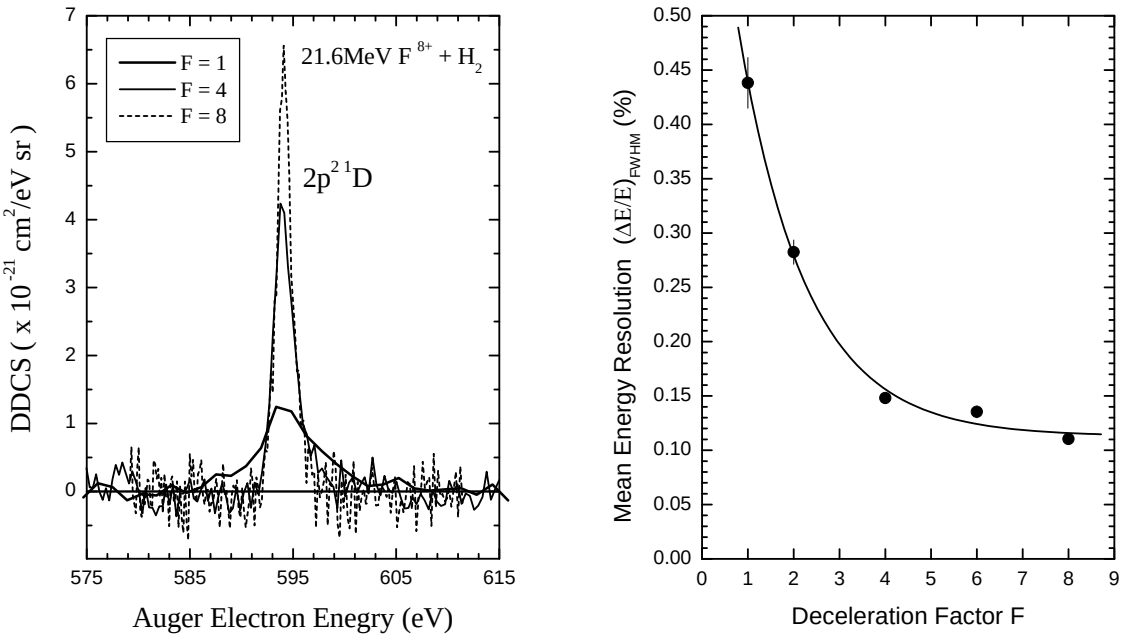

Figure 41: (*Left*) Comparison of the DDCS $(2p^2)^1D$ spectra at decel factors of F = 1, 4 and 8. (*Right*) The spectrograph mean energy resolution at FWHM as a function of the deceleration factor. Line was fitted to the data to guide the eye.

Table 3: Optimum lens voltages V_{L4} and V_{L5} and mean energy resolution at FWHM for different deceleration factors

F	$\frac{V_{L4}}{W}$	$\frac{V_{L5}}{W}$	$\left(\frac{\Delta E}{E}\right)_{FWHM}$ (%)
1	-0.45	0.92	0.44 ± 0.02
2	-0.49	0.82	0.28 ± 0.01
4	-0.45	0.88	0.149 ± 0.005
6	-0.57	0.49	0.135 ± 0.005
8	-0.24	0.65	0.110 ± 0.005

It is seen that a minimum FWHM energy resolution of 0.11% and 0.149% is established, for deceleration factors F = 8 and F = 4, the last case mostly used in the measurements of this work, respectively. Deceleration up to F = 8 seemed to be the limit, as tests for higher factors, not only did not show any improvement in the energy resolution but, on the contrary, showed an increase. Data were fitted to an exponential decay line resulting in the following relation: $(\Delta E/E)_{FWHM}(\%) = 0.113 + 0.64e^{-F/1.48}$. These data were obtained according to the method presented in §6.4.

In table 3, the lens voltages V_{L4} and V_{L5} decided for every deceleration factor (the choice included also some side effects like the secondary electron background minimization at the PSD edges) are shown, along with the attainable mean energy resolution at FWHM for every case.

6.3 Spectrograph operation in low resolution mode

The spectrograph operation in low resolution mode was quite successful, in the sense that a wide energy spectrum could be obtained by overlapping and matching different energy slices spectra together, according to the way described in chapter 7. In Fig. 57, an example is shown where different energy slices overlap to cover the binary encounter electron peak, recorded in collisions of 21.5MeV $F^{9+} + H_2$. The spectrograph operation in low resolution mode was one of the first tests performed on the spectrograph, and the results on measurements of projectile Auger electrons have been reported, [81] showing a satisfactorily good agreement with theory and other known experimental results.

Here, new unpublished results on a whole DDCS ZAPS spectrum obtained in collisions of 7.79 MeV $B^{3+} + H_2$ are presented. Different energy slices were recorded and overlapped according to the method of chapter 7. Overall absolute electron efficiency detection was determined from the binary encounter peak recorded in collisions of bare Boron ions with H_2 targets (see §7.3). Results are shown in Fig. 42. Different symbols on the data (i.e. open and filled circles alternately) indicate the different energy slices. BEe calculations using the electron scattering model (ESM) are also presented, showing a very good agreement with the data.

6.4 Spectrograph operation in high resolution mode

Initially, the operation in high resolution mode was problematic. First attempts to run the spectrograph in high resolution mode, were only partially successful due to a spurious background that dominated the spectra even at very small deceleration factors.

A first test of the spectrograph in deceleration mode, was the determination of the DDCS of the well-known $F^{7+}(2p^2)^1D$ Auger line produced by RTE in collisions of 21.78MeV $F^{8+} + H_2$. [29, 95] In this way, the BEe peak has only a single Auger line on it. A typical PSD image and associated energy spectrum is shown in Fig. 43. On the left, in (a) and (b) the spectrum is seen to be problematic with many spurious peaks, while in (c) and (d) a clean image and energy spectrum with a well-shaped peak are

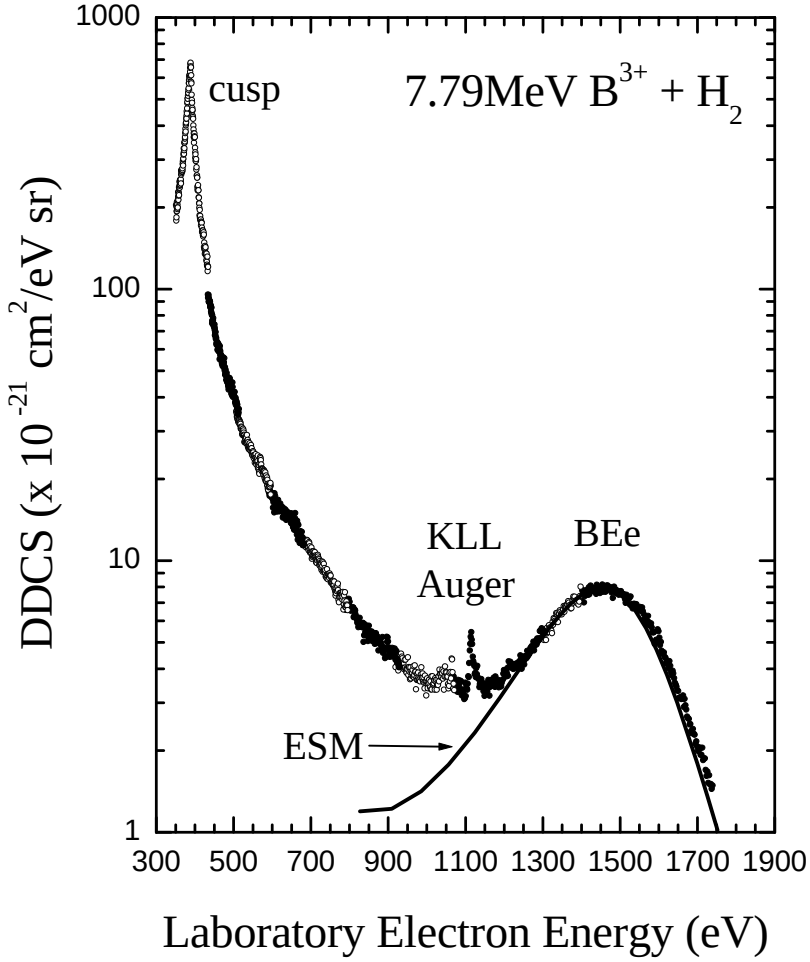

Figure 42: Absolute DDCS ZAPS spectrum for collisions of 7.79 MeV B^{3+} + H_2, obtained by overlapping ten different energy slices, indicated by the different symbols (i.e. open and filled circles alternately). The cusp peak, the BEe peak and the Boron Auger–KLL lines are explicitly shown. BEe calculations using the electron scattering model (ESM) are also shown.

shown. In each case, the energy spectra are the projections of the images within the 2-D gate drawn on the PSD and shown in the figure. The analyser voltages were set to pass electrons of nominal energy $w = 612.5$ eV, following deceleration from an initial energy of $W = 2450$ eV, i.e. deceleration factor F = 4.

In Fig. 43(a) the image of the PSD area is seen to be dominated by the spurious electrons. These electrons are distributed over the entire PSD area including the focus-

ing strip thus essentially destroying the spectrum. The spurious electrons giving rise to the "bagel"-like shape on the PSD were seen in all spectra collected in deceleration mode. The target gas did not seem to matter as the spurious electrons appeared when either H_2, He or Ne targets were used. The "bagel" image became progressively more intense as the deceleration factor F was increased. However, the "bagel"-effect was absent in the non-decel mode, i.e. when $W = w$ (F = 1). It was also absent when a mono-energetic electron beam from an electron-gun was used to test the spectrograph in deceleration mode.

The solution to the problem came from the second 90% transmission grid, placed in front of MCP1 (see Fig. 17). That grid was Initially set on a slightly negative potential $V_{GRID} = -20$V to repel spurious low energy electrons. It did not seem, however, to have any effect on the "bagel" structure. A careful study of the effect of varying V_{GRID}, showed that the bagel structure disappeared only when V_{GRID} was set to a *more* negative voltage than V_p. Typically, $V_{GRID} = V_p - 50$V was sufficient to produce a clean spectrum, as the one shown in Fig. 43 (c) and (d).

The spurious electrons which are distributed over the entire PSD area, clearly could not enter the analyser through the lens - since in this case they would be focused only along the strip - but must therefore be produced inside the analyser. The inner surfaces of the hemispheres were coated with soot, known for its good properties in suppressing secondary electron emission. [51] A possible explanation would be, that electrons entering the spectrograph properly, but having energies outside the acceptance window of the detector, hit the inner surfaces of the analyser close to the exit grid, producing spurious secondary electrons at energies up to $e|V_p|$. These electrons, when not repelled by a correctly biased V_{GRID} are accelerated to the detector since this is at a more positive potential.

A more systematic study of the background electrons produced inside the analyser took place for different deceleration factors. The $F^{7+}(2p^2)^1D$ peak was recorded at decel factors F = 1, 2, 4, 6 and 8. The grid voltage value of $V_{GRID} = V_p - 50$V was applied in all cases. Data were corrected according to the method described in chapter 7. The PSD efficiency was determined by the spectrum in no decel mode (F = 1) and was found to be $\eta = 0.5$. The efficiency number obtained from the F = 1 spectrum was used as a correction to the deceleration spectra. The result of this operation is shown in Fig. 44. The spectra recorded in deceleration mode are seen to lie higher than the theoretically predicted BEe peak. Actually, the higher the deceleration the higher the divergence (with an exception for the case of F = 4).

The only reasonable explanation is that despite the $V_{GRID} = V_p - 50$V repulsive voltage, "background" electrons still make it to the detector. Experimental tests on reducing the background contribution to the spectra by increasing V_{GRID} value did not seem to improve the situation.

In principle, the energy of the secondary electrons emanating from the HDA inner surfaces could roughly be estimated as $(V_2 + 50)$eV when F = 1, assuming an average emission energy of 50eV. The inner surface is at positive voltage $V_2 > 0$ and therefore is not expected to contribute to secondary electron emission, since it attracts them

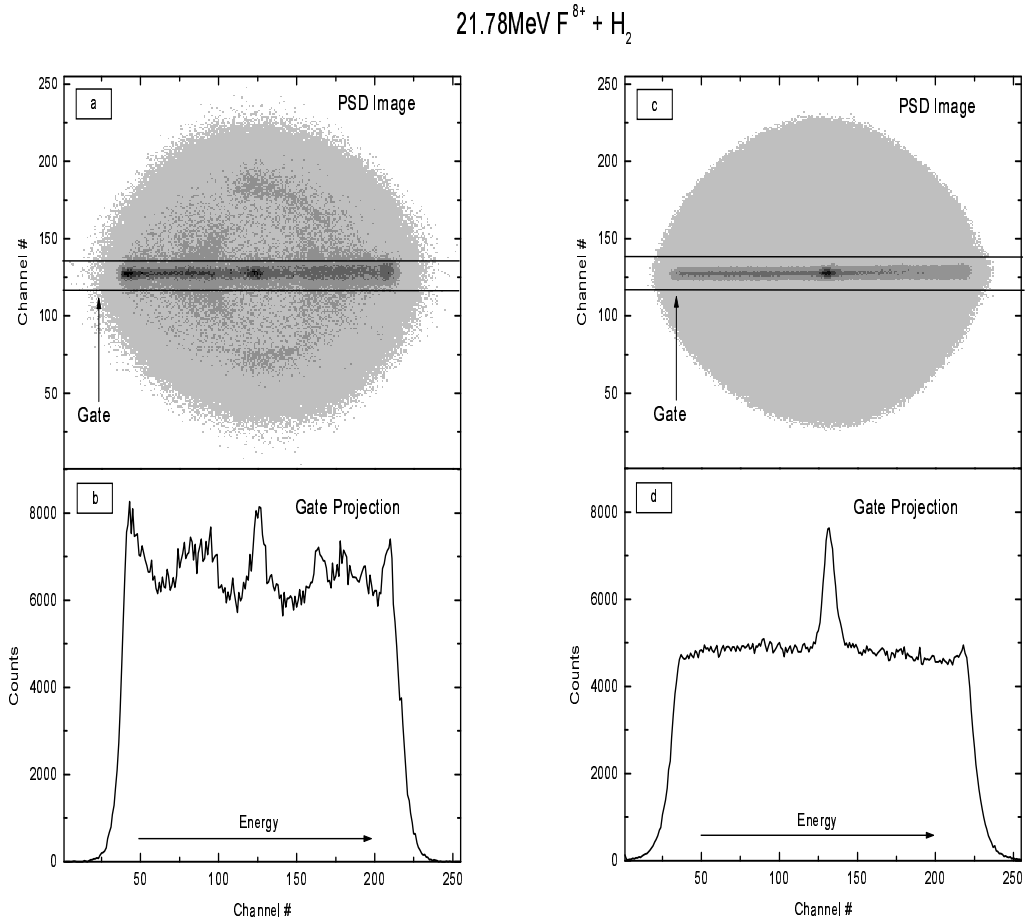

Figure 43: High resolution spectra in the energy region of the $F^{7+}(2p^2)^1D$ RTE peak obtained in collisions of 21.78MeV F^{8+} + H_2. The deceleration factor is $F = 4$. Top (a) and (c): Images of the PSD area, Bottom (b) and (d): projections of the PSD images in (a) and (c), respectively, lying in the 2-dimensional gate also shown in the figures. Measurement in (a) were taken with $V_{GRID} = -50$V, while in (c) with $V_{GRID} = V_p - 50$V$= -1887.5$V. The clean narrow strip of counts lies along the dispersion axis of the analyser showing its nice double focusing features. The spurious electrons seen in (a) and (b) lie mostly off this strip and therefore must be produced inside the analyser where they cannot be focused. The counts are normalized to the same pressure and beam current. From Ref. [82].

back to the inner hemisphere surface. The fact that, for F = 1, a grid voltage of $V_{GRID} = -50$V, was adequate to practically eliminate all the background electrons, indicates that the secondary electron production on the HDA inner surfaces is indeed very small.

Therefore, the main stream of the observed background electrons in deceleration

operating mode cannot be secondary electrons. Any secondary electrons produced inside the analyser surfaces should be repelled by the biased grid voltage $V_{GRID} = V_p - 50$V. Therefore the only explanation left, is that these are electrons from the energy spectrum, at higher or lower energies than the energy acceptance window, scattered at the analyser inner surfaces in such a way that they can be detected on the PSD surface finally.

The reason of the increased background electrons at higher decel factors can be understood if the previous argument about the scattered electrons is valid. In deceleration mode, a much narrower energy window is recorded. Usually the electron spectrum has a quite constant yield around the narrow energy window, allowing for more high energy electrons to be scattered on the surfaces, since the focusing lens cannot repel electrons of energies higher than the analyser window. In the low resolution mode the spectrum yield varies significantly around the energy window. For example, when measuring the high energy shoulder of BEe peak there are almost no electrons at energies higher than the energy window to be scattered. When recording the low energy shoulder though many electrons from the high energy side can contribute to the background. This could be the explanation for the enhanced left BEe shoulder in Fig. 44 for the case of F = 1.

Such a background behavior at the PSD edges has been observed to be depended on the lens voltages, and was one of the parameters taken into consideration, during the lens voltages parameterization (see §6.2.2).

According to the previous argument, the extra background should be subtracted from the data. This was achieved by subtracting an appropriate number from the experimental spectra of Fig. 44, in order to normalize them to the BEe peak. Actually a tilt of the spectra around the central channel (i.e. channel 128) was also necessary. After these operations the theoretical BEe peak was subtracted from the normalized experimental data and the DDCS were transformed to the projectile rest frame. The results are seen in Fig. 45.

The $F^{7+}[(2p^2)^1D]$ peaks were integrated for each case and the SDCS results were compared to the RTE theory. Fig. 46 shows not only a very good agreement between theory and experiment, but also proves that the SDCS measurements are not affected by the deceleration mode of operation, at least up to deceleration factors of F = 8.

In conclusion, the absolute cross section information when the spectrograph is run in deceleration mode should be obtained according to the following steps:

- Record the energy region in interest first in low resolution mode. If more than one energy slices are needed then record the slices so that an overlapping of 50% is established.

- Measure the efficiency η, of the MCP at the high energy wing of the BEe peak and use this to correct both the decelerated and undecelerated data.

- Normalize the decelerated data to the undecelerated (by subtracting a constant amount and even tilting the spectrum).

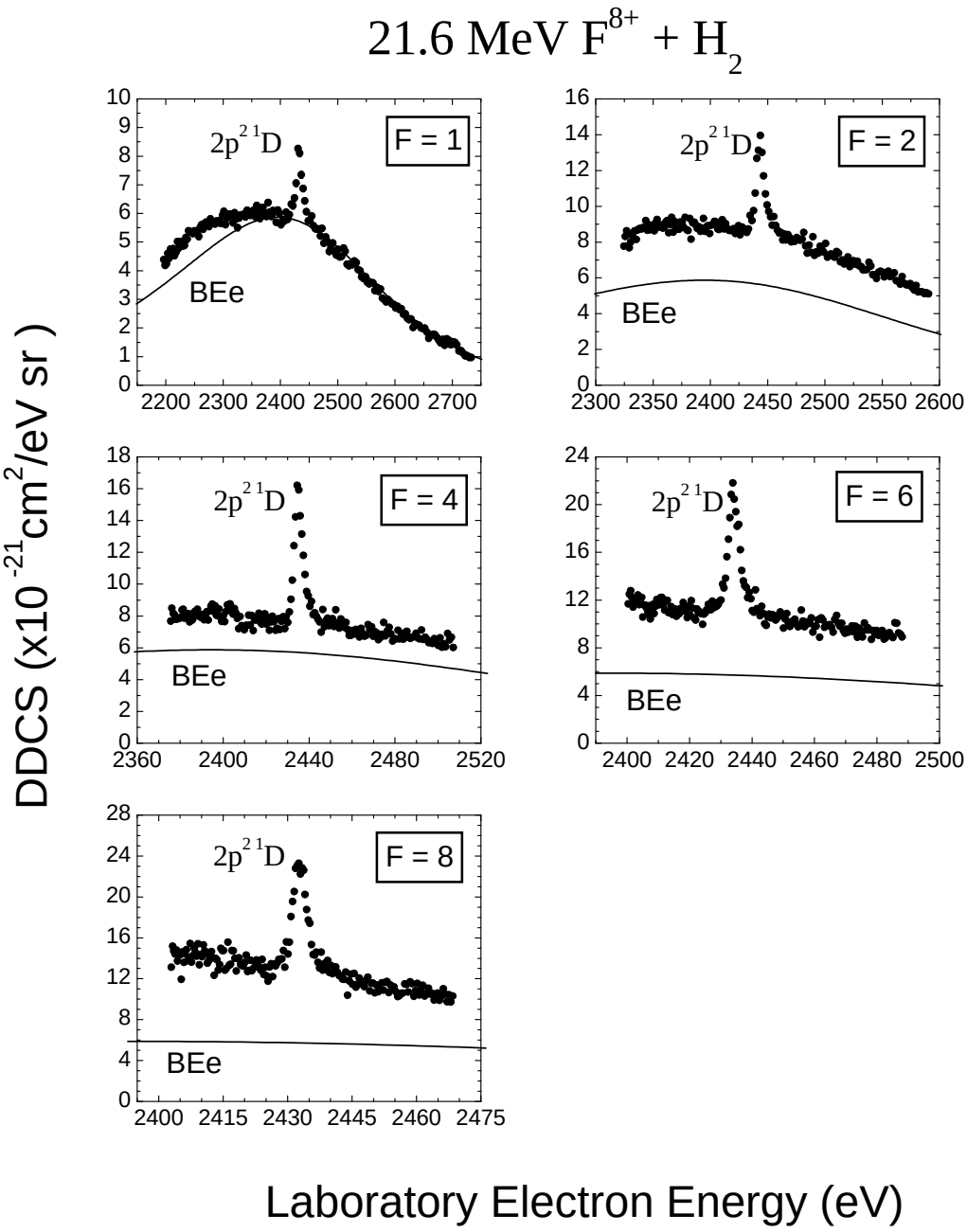

Figure 44: DDCS spectra of the $(2p^2)^1D$ formed in collisions of 21.78 MeV F^{8+} + H_2, obtained at deceleration factors of 1,2,4,6 and 8. High resolution data (F> 1)were converted to DDCS using the efficiency obtained by the low resolution (F=1) measurement. The DDCS spectra in deceleration mode are seen to be higher than the BEe DDCS calculations.

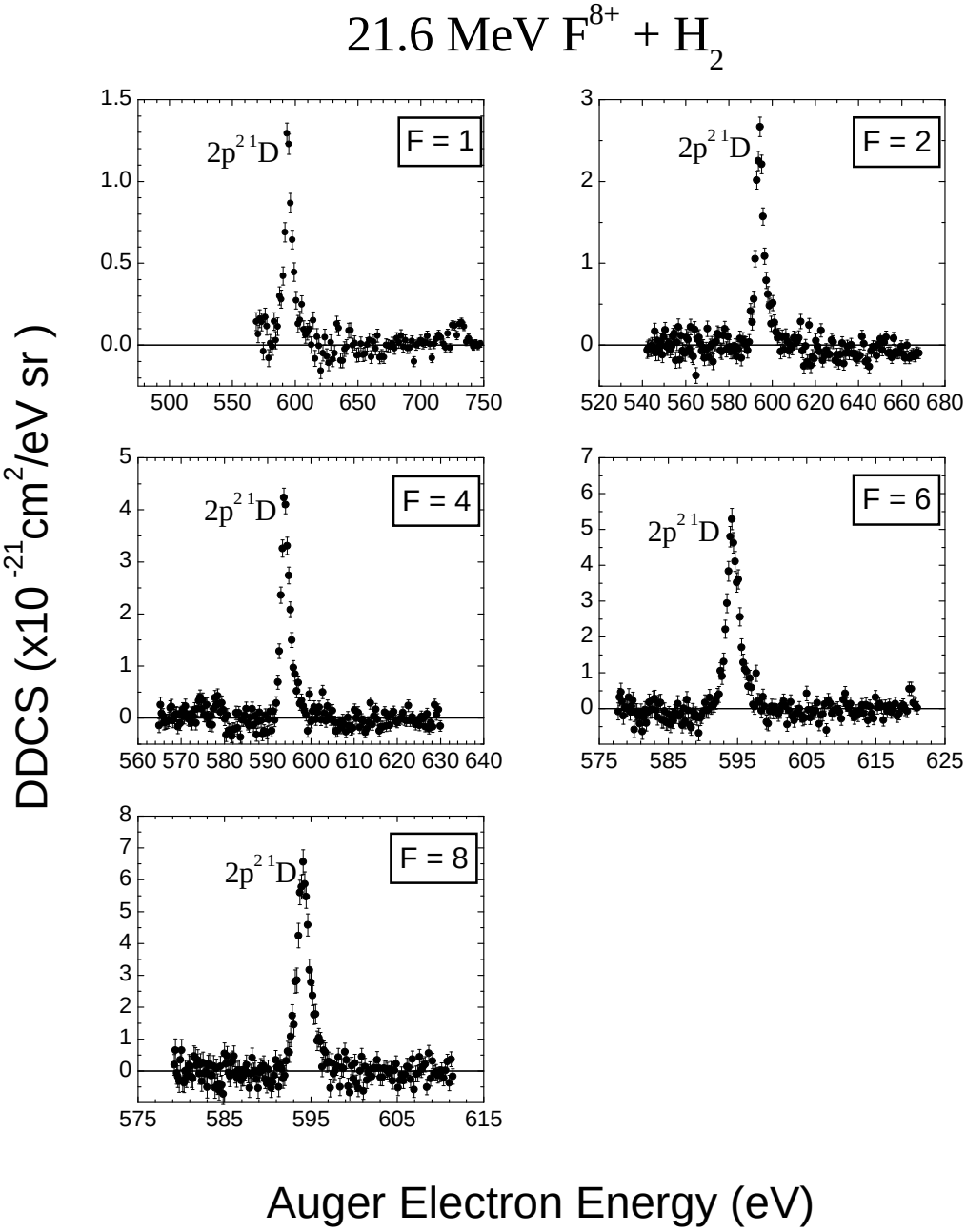

Figure 45: DDCS spectra of the $(2p^2)^1D$ RTE line obtained at deceleration factors of 1,2,4,6 and 8. Data were corrected for the "extra-background".

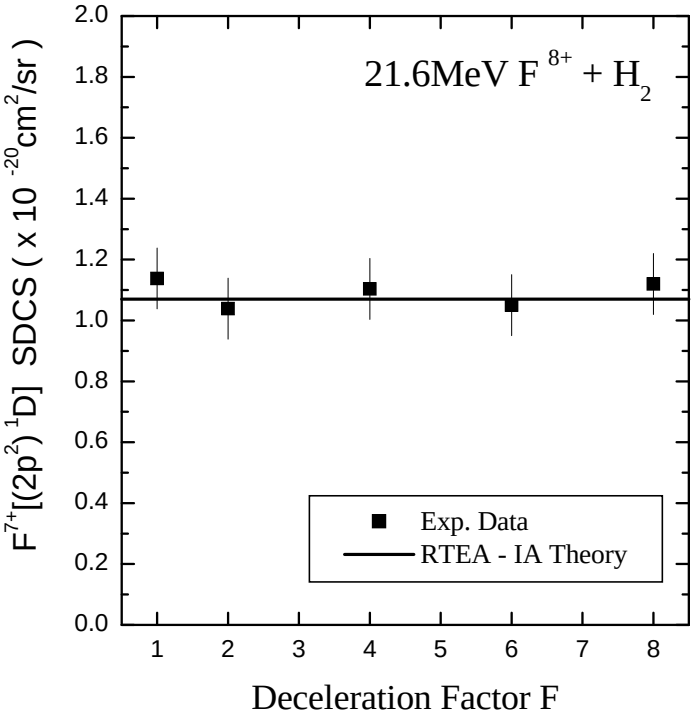

Figure 46: SDCS of the $(2p^2)^1D$ RTE line measured at different deceleration factors.

6.5 Performance comparison of the hemispherical spectrograph and the KSU tandem spectrometer

The high resolution spectra of the $F^{7+}(2p^2)^1D$ peak in collisions of 21.78 MeV F^{8+} + H_2 were also used for testing the performance of the new high efficiency hemispherical spectrograph. This was done by comparing the obtained spectra to the same spectra recorded with the KSU tandem spectrometer. The KSU tandem spectrometer has an energy resolution of 2.8% in the low resolution mode. [89] A deceleration factor of $F = 4$ was used with the spectrograph, while constant pass energy of 400 eV was used with the tandem to obtain comparable resolution. Both spectra were collected in 400s and were normalized to the same pressure and target areal density. A beam current of 120nA was used with the tandem spectrometer, while only 5nA was possible with the spectrograph to avoid excessive dead-time.

In Fig. 47 the performance of the KSU tandem analyser [89] is compared to that of the new spectrograph. The spectrograph is presently [*Left*] seen to be about 9 times faster with about 3 times more data points in the same energy interval, while used at the much lower beam current of 5nA. Background spectra (no target gas) are also compared. In both cases the ratio of signal to background is seen to be about the same with a value of 6 for the collision under study.

The present data acquisition system (CAMAC) did not have an intermediate data

storage buffer (histogramming memory) and therefore singles count rates were limited to a few kHz to avoid excessive dead-time. An improvement by factor of 10 in the count rate is well within the capabilities of present day systems and will be implemented in the near future. This would give an improved gain of at least 350 as it can be seen in Fig. 47 [*Right*] where the data were also normalized to the same beam current. Actually, an improved gain of about 300 is gained for the Boron beams, used mostly in this dissertation, where the maximum current at the target region did not exceed the value of 10nA.

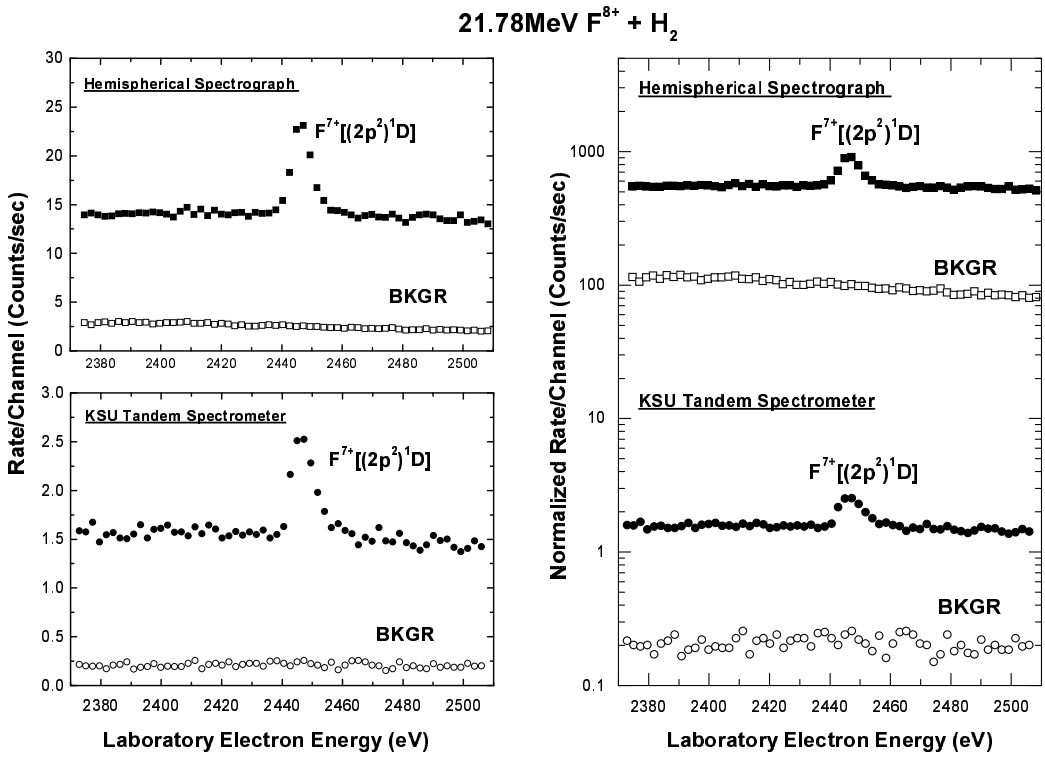

Figure 47: Performance comparison of the hemispherical spectrograph utilizing a PSD and the KSU tandem slit parallel plate spectrometer. High resolution spectra (deceleration mode) of the $F^{7+}(2p^2)^1D$ peak in the laboratory frame in collisions of 21.78 MeV $F^{8+} + H_2$ are compared after normalization to the same experimental conditions. (*Left*) The spectrograph is seen to be about 9 times more efficient than the tandem slit spectrometer. (*Right*) When also normalized to the same beam intensity the spectrograph was found to be about 300 times more efficient. Adapted from [82].

Furthermore, as already shown, for measurements with F = 1–8, no loss of transmission or detection efficiency is observed, as opposed to the tandem spectrometer, whose overall transmission is known to decrease roughly proportional to F. Thus at F $\geq$ 8, the spectrograph is expected to be more than 600 times faster than the equivalent

resolution tandem slit spectrometer.

Finally, the full acceptance angle $\Delta\theta$ for the hemispherical spectrograph is $\Delta\theta = 0.868°$, while for the tandem spectrometer $\Delta\theta = 1.17°$ (in the non-focusing direction). [10] Thus, the spectrograph is expected to have about half the kinematic broadening, allowing in principle for even higher resolution measurements.

6.6 Discussion and Conclusions

This chapter was the third part of a trilogy (chapters 4, 5 and 6), in which the performance of the *real* paracentric spectrograph was investigated. The experimental results of the HDA properties of the energy resolution, energy window and energy calibration have been reported in chapters 4 and 5, for comparison to the theory and SIMION simulations. The results on the analyser and lens voltages parameterization, presented in this chapter can be seen as a completion to the HDA properties.

The spectrograph operation in low resolution mode was successfully tested on the grounds of obtaining a full range ZAPS DDCS spectrum from collisions of 7.79 MeV B^{3+} ions with H_2 targets, by overlapping ten energy slices recorded at different tuning energies. The operation of the spectrograph in low resolution mode was satisfactorily reliable, at least for the energy region of the BEe peak, where the results could be accurately compared to previously measured data and also to theoretical calculations known to be in good agreement to the data (i.e. ESM, IA–RTE). The reason for this success is mainly due to the practical elimination of background electron contributions which allowed for the correct data analysis and reduction of the DDCS and SDCS results, as described in the next chapter. Consequently, the low resolution spectra were decided to be used for the normalization of the high resolution spectra, due to problems with background increase when deceleration was applied.

The enhanced background contributions to the electron spectra was the persisting problem for the high resolution data. The nature of these background electrons has been explicitly pointed out not to be only secondary electron emission but rather primary scattered electrons with energies higher or lower than the energy acceptance window in use. The normalization of the decelerated data to the data obtained in low resolution mode, was proposed as a method for obtaining absolute DDCSs as well as SDCSs. The method has also been used in the past in a similar mode in the tandem parallel plate slit spectrometers. [96] The correctness of the method was proven from the successful SDCS RTE measurement of the $F^{7+}[(2p^2)^1D]$ RTE line for deceleration factors ranging from 1 to 8.

Finally, an efficiency comparison of the new hemispherical spectrograph and the KSU tandem parallel plate spectrometer, normalized for the same experimental conditions, show that the spectrograph is presently seen to be about 9 times faster with about 3 times more data points in the same energy interval, while using only 1/24 of the beam current used by the KSU tandem spectrometer. Accounting also for the beam current either by implementing a much faster data acquisition system (which actually is under progress) or by utilizing really weak ion beams like Boron the spectrograph is

proved to be faster by a factor of 300 at deceleration factor of F = 4.

In cases where the data acquisition is not limited by the dead time, as for example in the case of very weak ion beams, the full power of the hemispherical spectrograph shows that, in fact, gain factors of 300 or larger maybe attained in experimental conditions. Thus, a typical high resolution spectrum taken with a tandem parallel plate analyser requiring about 600 min, could now be taken in 2 min. This huge gain in spectra acquisition time is expected to make the ZAPS technique even more applicable as a standard investigation tool and open new roads for investigations.

7 Data Analysis: Determination of absolute DDCS

The primary task of the data analysis is to convert the measured electron spectra to absolute double differential cross-section (DDCS). The base for this analysis is the raw data of Fig. 18(h), showing the number of electron counts as a function of the channel number. In this chapter, the data analysis for obtaining the absolute ZAPS DDCS spectra is developed.

7.1 Energy Calibration

To convert a spectrum recorded as a function of channel number to electron energy, an energy calibration of the spectra has to be performed as described in §4.4.3. The principle of doing this is by detecting, under the same experimental conditions as the measurement under study, electrons at known energies. Electrons can be supplied either by an electron-gun, or by ion-atom collision producing well-known target Auger lines. An electron-gun can provide electrons at any favorable kinetic energy, since the electron energies are controlled by the electron-gun negative bias voltage, the accuracy of which is typically 0.1%. On the other hand, known target Auger lines (eg. Ne – KLL lines), even though they are known with higher accuracy than the electron-gun measurements, they are only available in certain specific energy regions. Besides, they are mostly resolved only in deceleration mode and therefore excluded from energy calibrations at low resolution mode. In addition, their small number per energy slice (four Ne – KLL lines are detected in an energy slice at F = 4) is not adequate for determining accurately quadratic energy calibration relations, applicable over a wider energy region.

Consequently, an electron gun can be primarily used for an energy calibration within an accuracy of ~0.2%. Though for the accurate determination of the spectral lines, the information on the beam energy, or the cusp energy t is indispensable (see Eq. 8). The cusp energy t can be determined by directly measuring the spectrum in the cusp region. However, the uncertainty in the energy calibration along with the uncertainty in the maximum cusp peak determination result in an overall uncertainty, which is not adequate for unambiguous KLL spectral line determination (within 1–2 eV). Instead, well-known projectile Auger lines can be used for a high accuracy energy spectrum. In fact, this is the method the beam energy was determined in the experiments presented in this work. For example, in collisions of 4.11 MeV $B^{3+} + H_2$, the energy of the doubly excited $(2s2p^2)^2D$ line, was used for determining the beam energy and the energies of the other doubly excited lines with an accuracy of 0.15% (see §9.3 and table 7).

A typical oscilloscope tube electron-gun was biased at a known set of negative voltages, measured with an accurate multimeter (5 1/2 digit model Keithly 197) and the positions (channels) of the electron peaks were recorded. The electron gun was placed at the same position as the gas-cell, in order to have the same lens focusing conditions. The gas-cell and the electron-gun were mounted in the same cube on the beam line (see Fig. 11) on micrometer rods and could be interchanged, even during

the experiment, for testing purposes.

For the set of voltages that the spectrograph was operated, the recorded relation between the electron energy and the triggered channel number proved *not* to be linear but rather a smooth quadratic function of the form of Eq. 114 (see also Eq. 103), as theory and also SIMION predicted (see §4.4.3 and Fig. 28).

$$T = a + b\,i + c\,i^2 \tag{114}$$

In order to check the validity of the theoretically predicted universal form of the energy calibration Eq. 103 ($\tau_i = A + B\,i + C\,i^2$, valid for any tuning energy W and deceleration factor F), Eq. 103 was re-written after using Eq. 32 in the following form:

$$\frac{T}{W} = \frac{A - 1 + F}{F} + \frac{B}{F}\,i + \frac{C}{F}\,i^2 \tag{115}$$

Then from Eqs. 114 and 115 the normalized universal factors A, B and C are obtained as:

$$A = \frac{a}{W}\,F - F + 1 \tag{116}$$

$$B = \frac{b}{W}\,F \tag{117}$$

$$C = \frac{c}{W}\,F \tag{118}$$

In Fig. 48, the factors A, B and C are plotted for tuning energies W ranging from 180eV to 2750 eV, for the deceleration factors of F = 1 and F = 4, while in Table 4 their mean values and uncertainties are given. It is seen that within the error bars of the individual measurements and moreover of the mean values for each deceleration case, the universality of the energy calibration relation Eq. 103 is well obeyed. It is also seen that the energy calibration should be done for a wide set of tuning energies W and probably at different deceleration factors F in order to get quite accurate A, B and C values.

Table 4: A, B and C constants for the universal energy calibration relation: $\tau_i = A + B\,i + C\,i^2$.

	A	δ_A	B	δ_B	C	δ_C
F = 1	0.840	±0.004	8.37×10^{-4}	$\pm 0.60 \times 10^{-4}$	1.30×10^{-6}	$\pm 0.20 \times 10^{-6}$
F = 4	0.845	±0.002	8.00×10^{-4}	$\pm 0.17 \times 10^{-4}$	1.35×10^{-6}	$\pm 0.06 \times 10^{-6}$

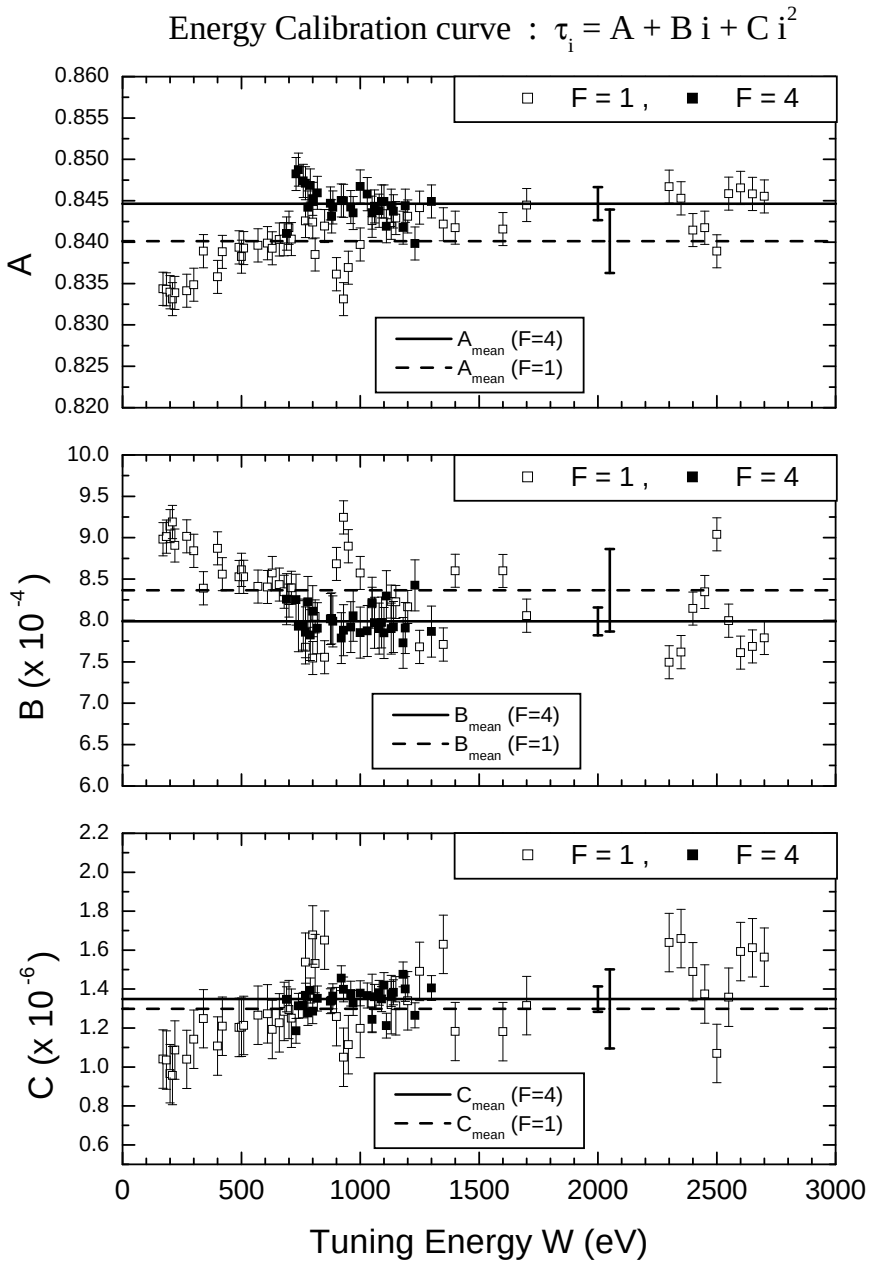

Figure 48: Plot of the A, B and C factors of the experimental universal energy calibration relation $\tau_i = A + B\,i + C\,i^2$. Electron-gun in use. Mean values for the cases of F=1 (solid line) and F=4 (dashed line) are shown along with their error bars.

7.2 Double Differential Cross-Section

The Double Differential Cross-Section (DDCS) derivation from the raw experimental data is obtained from the well known experimental formula given by Eq. 119, applied in most of the detecting systems using analysers: [13]

$$DDCS_i \equiv \frac{d^2\sigma_i}{d\Omega dE_i} = \frac{N_{e_i}\ DTC}{N_I\ L\,n\ \Delta\Omega\ \Delta E_i\ T\ \eta_i} \tag{119}$$

where i refers to the i-th channel. The symbols appearing in this equation are explained and commented as follows:

$\mathbf{N_e}$: The number of electron counts at a certain channel i, recorded during the measurement. The statistical uncertainty in this number is:[24] $\delta N_{e_i} = \sqrt{N_{e_i}}$

DTC: According to §3.7 the dead time correction (DTC) is defined as the ratio of the total number of counts recorded by a scaler over the total number of counts recorded by the ADC during the acquisition time interval. Dead time is independent of the channel number, due to the randomness of the events. In other words, DTC is the average DTC recorded for all the channels. This fact was checked experimentally by measuring a portion of the Binary Encounter electron peak in collisions of 21.7MeV F^{8+} + H_2 at different count-rates. The count-rate was controlled either by changing the ion beam current or by changing the gas-cell pressure in the case where the ion current was already maximum.

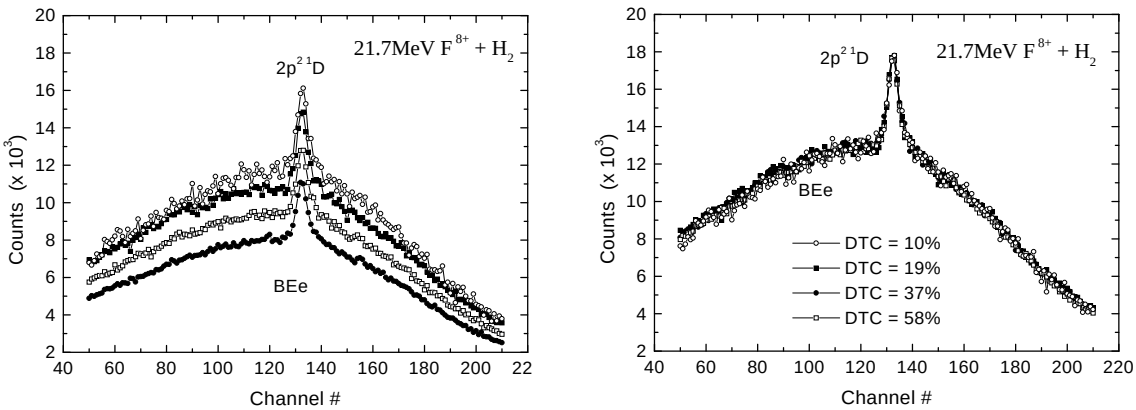

Figure 49: [*Left*] A portion of the BEe peak in collisions of 21.7MeV F^{8+} + H_2, recorded at different count rates. Raw data are shown. [*Right*] Raw data were corrected for DTC. The peak superimposed on the BEe peak is the $(2p^2)^1D$ RTE line due to the formation of $F^{7+}[(2p^2)^1D]$ state during the collision.

In Figs. 49(left) and 49(right) the raw data and the data corrected for DTC are plotted, respectively. In Fig. 19 the DTC is plotted as a function of the count-rate, indicating that the DTC linear dependence on count-rate is satisfied up to count-rates

[24]Electron counting is random events following the Poisson distribution.

of 6kHz. In most of the experiments reported in this presentation DTC was limited to 20%. DTC is assumed to be a number exactly known as it is the ratio of two numbers measured exactly.

$\mathbf{N_I}$: The number of ions collected at the last Faraday Cup of the beam line, during the measurement. This number is calculated from the total collected charge Q (measured in nC) and the ion beam charge state q as follows:

$$N_I = \frac{Q(nC)}{q \cdot 1.6 \times 10^{-10}} \tag{120}$$

The total collected charge Q is obtained through experimentally defined parameters according to the formula:

$$Q(nC) = \frac{Qcnt\, I_{FS}}{Cnts} \tag{121}$$

I_{FS} is the current integrator (CI) scale in use (measured in nA). $Cnts$ is the number of counts per second to be generated by the CI when operated to its maximum reading at a certain scale. $Qcnt$ is a number set on the data acquisition software as the upper limit of the total counts to be generated by the CI. When the number Qcnt is reached, after adding all the counts generated by the CI, the end of the measurement is signaled. In other words, $Qcnt$ defines the duration of the data acquisition.

The normalization of the measurement duration to the beam current, is based upon the fact that, the beam current is actually not affected from the target collisions. Indeed, soft and BEe electrons do not change the projectile charge and therefore do not affect the beam current. ELC part of the cusp electrons may increase the beam charge, while a decrease may come from electron capture processes. The beam reduction maybe roughly estimated, considering an ion beam current I_0 traversing a gas target of density n. Then the electron current I from a length of path L is given by: [86]

$$I = I_0\, \sigma\, n\, L \tag{122}$$

where σ is the total cross-section. For single collision conditions, I can be directly inferred to the ion beam current reduction. Assuming gas-cell length of L = 5cm, target pressure 10mTorr, which corresponds to 3×10^{14} molecules/cm^3 (see Eq. 123), and total cross-section of a maximum value of 10^{-16} cm^2, [25]the beam current reduction is $15/Z_p$ %, where Z_p is the initial beam charge. Assuming an average value of $Z_p = 5$, the uncertainty in the beam current and therefore in the number N_I is: $\delta N_I/N_I \leq 3\%$

Another uncertainty in number N_I comes from the error in parameter Cnts. For the CI mostly in use (Brookhaven Instrument Corporation model 1000) the uncertainty in Cnts was given to be 0.02% for all scales, which is well included in the aforementioned uncertainty.

[25]This is the highest value for the total cross-section of the ELC process at collisions of $\sim$ 1 MeV/u beam energy (see Fig. 42) and of the single electron capture [97]

L: The effective length of the gas-cell. For a gas-cell with actual length L_1 and openings on either side of diameters D_1 and D_2, the effective length is given by $L = L_1 + (D_1 + D_2)/2$. For the gas-cell in use (actual length = 50mm, openings diameters: $D_{entrance}$ = 1.5mm, D_{exit} = 2mm) L = 5.175cm. $(D_1 + D_2)/2$ can be accepted as the uncertainty in length determination, resulting in $\delta L/L = 3.5\%$.

n: The number of molecules per cm^3. For the gas pressures used in these experiments (i.e. up to about 50mTorr), it is a very good approximation to treat the gas-target as an ideal gas, described by the well known equation of state P V = n R T. Using the state equation, the gas density n can be written as a function of the gas pressure P (measured in mTorr), at room temperature (T = 300 °K), as:

$$n(molecules/cm^3) = 3.222 \times 10^{13}\ P(mTorr) \tag{123}$$

The assumption of single collision condition (valid for $n\,\sigma\,L << 1$) however should be checked prior to measurement, by comparing the recorded yields at different target pressures. The situation is illustrated in Fig. 50, where the yield of the BEe peak, obtained in collisions of 21.78MeV F^{9+} + He, was recorded at different target pressures. The yields shown were normalized to target pressure of 50mTorr, after correcting for DTC, revealing a linear pressure dependence up to pressures of 50mTorr. In Fig. 51 the same test took place for collisions of 4.4 MeV B^{3+} + Ar, showing a deviation from the linear pressure dependence, for pressures higher than 10mTorr.

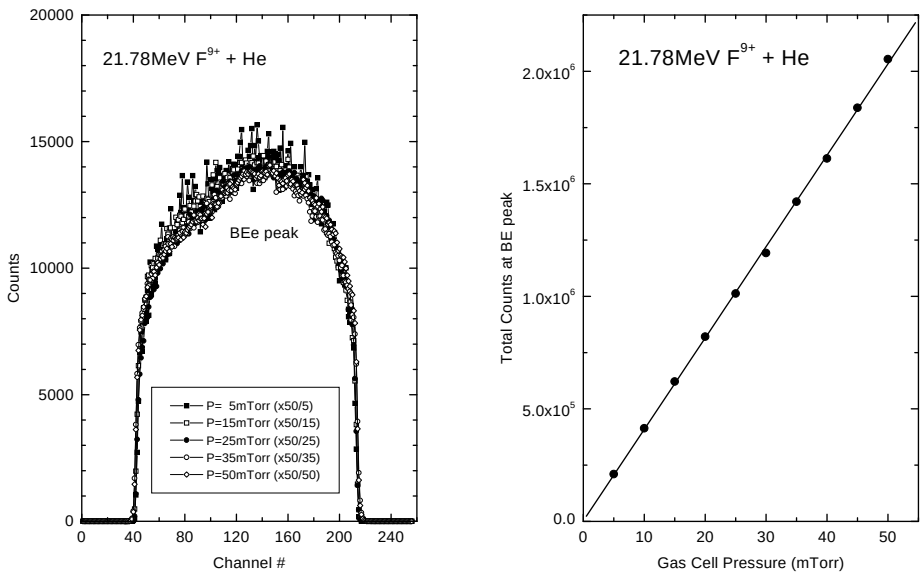

Figure 50: [*Left*] Yield of the BEe peak obtained in collisions of 21.78MeV F^{9+} + He, recorded at different target pressures. Yields were normalized to a target pressure of 50mTorr. [*Right*] Linear pressure dependence is observed for the BEe yield up to pressures of 50mTorr is observed.

According to the baratron readings during the measurement, the pressure uncertainty $\Delta P/P$ was never larger than 2.5%. Therefore, $\delta n/n \leq 2.5\%$. In this number, the variation of the temperature, coming either from the laboratory environment or by the ion beam hitting the gas-cell apertures, is also included.

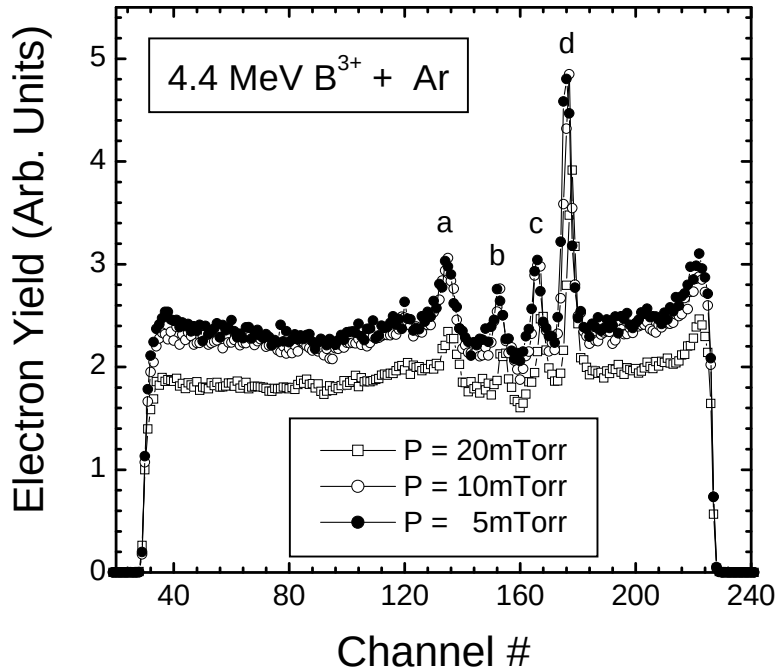

Figure 51: 4.4 MeV B^{3+} + Ar spectra recorded in target pressures of 5, 10 and 20 mTorr. Data were corrected for DTC and normalized to the same pressure. Note that for the case of 20mTorr, a deviation from the linear pressure dependence is established. The four peaks shown in the spectrum are attributed to the formation of the doubly excited B^{2+} lines: (a) $(1s2s2p)^4P$, (b) $[1s(2s2p\,^3P)]^2P_-$, (c) $[1s(2s2p\,^1P)]^2P_+$ and (d) $(1s2p^2)^2D$.

$\Delta\Omega$: The solid angle defined by the opening of the lens entrance ($d_{LE} = 4$mm) and the distance l of the lens entrance from the center of the gas-cell ($l = 264$mm).

$$\Delta\Omega = \frac{\pi d_{LE}^2}{4l^2} = 1.8 \times 10^{-4} sr \tag{124}$$

The uncertainty in $\Delta\Omega$ arises from the extended gas-cell target. Considering also the gas-cell half length in the calculation of the solid angle, (i.e. $l \pm 25$mm), the solid angle uncertainty reads: $\delta(\Delta\Omega)/\Delta\Omega = 9.5\%$.

ΔE: The energy step of the spectrum per channel. Re-writing the relation (32) as

$T = \frac{W}{F}(\tau - 1 + F)$ and identifying T with E, ΔE_i becomes:

$$\Delta E_i \equiv \Delta T = \frac{dT}{d\tau}\Delta\tau_i = \frac{W}{F}\,\Delta\tau_i \tag{125}$$

$\Delta\tau_i$ is calculated from the energy calibration formula (103) as:

$$\Delta\tau_i = \frac{W}{F}\,(B\,+\,2\,C\,i)\,\Delta i = \frac{W}{F}\,(B\,+\,2\,C\,i) \tag{126}$$

since $\Delta i = 1$. Combining relations (125) and (126), ΔE_i reads:

$$\Delta E_i = \frac{W}{F}\,(B\,+\,2\,C\,i) \tag{127}$$

The accurate knowledge of ΔE is the most sensitive and important correction to the raw data, since all the other parameters are - under most experimental conditions - numbers, whose effect on the raw data is only multiplicative. ΔE, on the contrary, also *tilts* the spectrum resulting in both the correct electron yields and the proper matching of the different tuning energy spectra slices.

In order to illustrate this correction, a simple model for simulating the ideal HDA was implemented. Electrons were generated within a disk at the center of the gas-cell region at random positions, angles and Gaussian distribution energies, and then flown to the entrance of the lens, focused in first order at the entrance of the analyser and finally energy analysed and detected at the PSD surface. Data output of x and y electron positions on the PSD surface were projected onto the dispersion axis and transformed to artificial raw data, i.e. counts vs channel number. The channel numbers were also energy calibrated using the exact theoretical relation Eq. 101. The model was programmed in FORTRAN code and 1,000,000 electrons were flown for each Gaussian peak.

The raw data (counts vs energy) for such an artificial electron peak with a Gaussian distribution in initial energies with mean energy T = 1000eV and FWHM = 150eV, as obtained from the previously described model, are shown in Fig. 52 (left). The peak was recorded in three different slices of tuning energies 900eV, 1000eV and 1100eV, as the peak width was larger than the energy window of the analyser. It is obvious that the different energy slices recorded at different tuning energies need to be corrected so as to properly match in the overlap. It is straightforward to see that, a simple multiplication of the raw data is not adequate for such a correction. In Fig. 52 (right) the raw data have been corrected for the energy width of the channel ΔE_i resulting in the electron yield (counts / ΔE_i) showing a perfect matching of the different energy slices.

The same study was also repeated for the case where the electrons were decelerated (F > 1) prior to their energy analysis. In Fig. 53 (left) the raw data of a Gaussian energy electron distribution detected at deceleration factors of F = 1 and F = 4 are shown. The initial electron peak at mean energy T = 1000eV and FWHM = 100eV is "recorded" at tuning energy W = 1000eV for the case of F = 1. When F = 4 the same

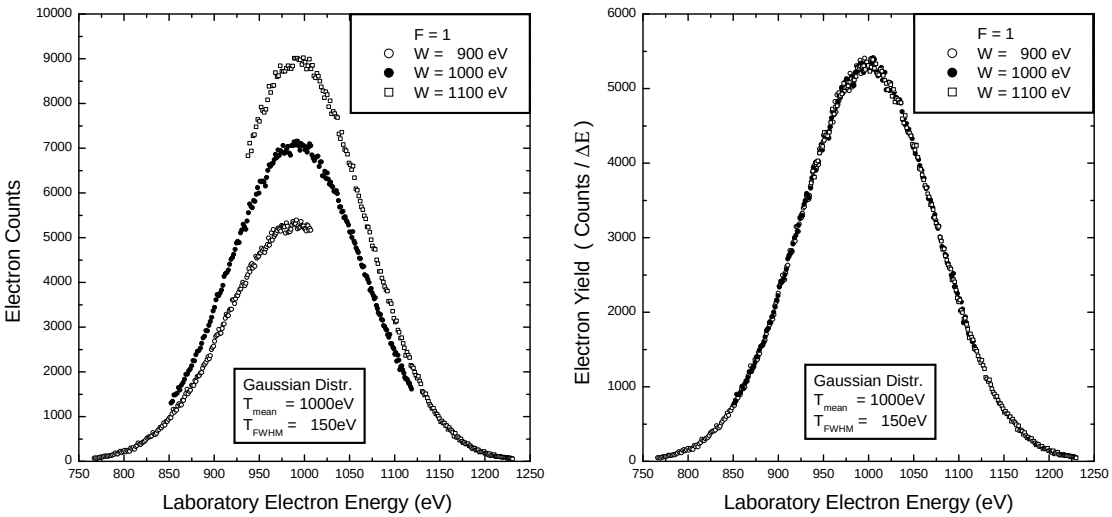

Figure 52: *[Left]* Artificial raw data (counts vs energy) for a Gaussian electron distribution over energy is obtained from the simulation of the ideal field HDA at three slices of different tuning energies. *[Right]* Artificial raw data after correction for the channel energy width ΔE. Perfect matching of the energy slices is observed. Deceleration factor F = 1.

peak is "recorded" at five different energy slices (as the energy window of the analyser is inversely proportional to the deceleration factor F) of tuning energies of W = 900, 950, 1000, 1050 and 1100eV. In Fig. 53 (right) the raw data were corrected for ΔE resulting not only in the perfect matching of the energy slices for the F = 4 case, but also in the perfect matching of the recorded spectrum for both deceleration factors. The last result shows that the electron yield is indeed independent of the deceleration factor F, as it should be, demonstrating the correctness of the suggested dispersion correction for the HDA. This demonstration was performed assuming an "ideal" 1/r potential, and using simulated data. An example of matching different energy slices for a real measurement, is shown in Fig. 57.

The previous examples illustrate the method of matching the different spectra slices in cases where the detected peaks were very broad in energy width (i.e of the order of the analyser energy window: $\Delta T_{FWHM} \geq \Delta T_{WINDOW}$). The situation is completely different when the peak width is very small ($\Delta T_{FWHM} << \Delta T_{WINDOW}$). In this case the final peak shape is governed by the spectrograph energy resolution.

In Fig. 54 an electron energy distribution consisting of two Gaussian peaks G_1 and G_2, of mean energies 1000eV and 1020eV with FWHM of 25eV and 1eV, respectively, were "recorded" at tuning energies of 1000eV and 1050eV with a deceleration factor F = 1. It is clearly seen that the spectra parts which are governed by the spectrograph resolution (i.e. the G_2 peak) do not match. The explanation is based upon the detection

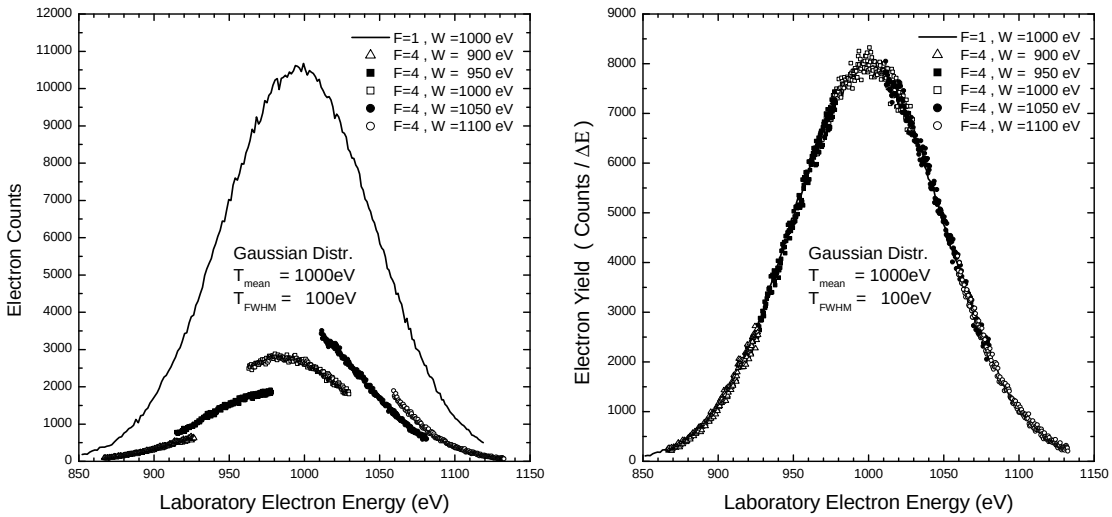

Figure 53: *[Left]* Artificial raw data (counts vs energy) for a Gaussian energy electron distribution obtained from the simulation of the ideal field HDA at deceleration factors of F = 1 and F = 4. Five energy slices were required for the F = 4 case to cover the peak energy spread. *[Right]* Artificial raw data after correction for the channel energy width ΔE. Perfect matching of both the energy slices in the case of F = 4 and the absolute electron yield obtained separately for the two deceleration factors.

procedure. The peak G_2 is detected at the beginning (low channel number) of the PSD dispersion axis in the case of W = 1050eV, and at the end (high channel number) in the case of W = 1000eV. Since the spectrograph energy resolution depends upon the detection position (see Fig. 89), the final shape of the detected peak is affected by the position at which it is detected. The spectrum parts which are not affected by the spectrograph energy resolution (i.e. the G_1 peak) show a perfect energy matching of the slices, as it is expected. Thus, the different overlapping energy slices should be matched only at regions where the spectra are continuous rather than where sharp peaks exist.

The uncertainty in ΔE can be calculated from the uncertainty of the factors B and C, shown in Fig. 48. Assuming an average uncertainty for channel number $i = 130$ and the values of Table 4, the average uncertainty in ΔE is obtained as: $\delta(\Delta E)/\Delta E = 8.5\%$.

T: The transmission of the spectrograph. Transmission is defined as the ratio of the number of particles detected by the spectrograph exit (PSD area) over the number of particles entering the spectrograph entrance (lens entrance). Therefore the only particles that are taken into account in the transmission definition are the ones that are emitted from the gas-cell through a cone defined by the distance between the gas-

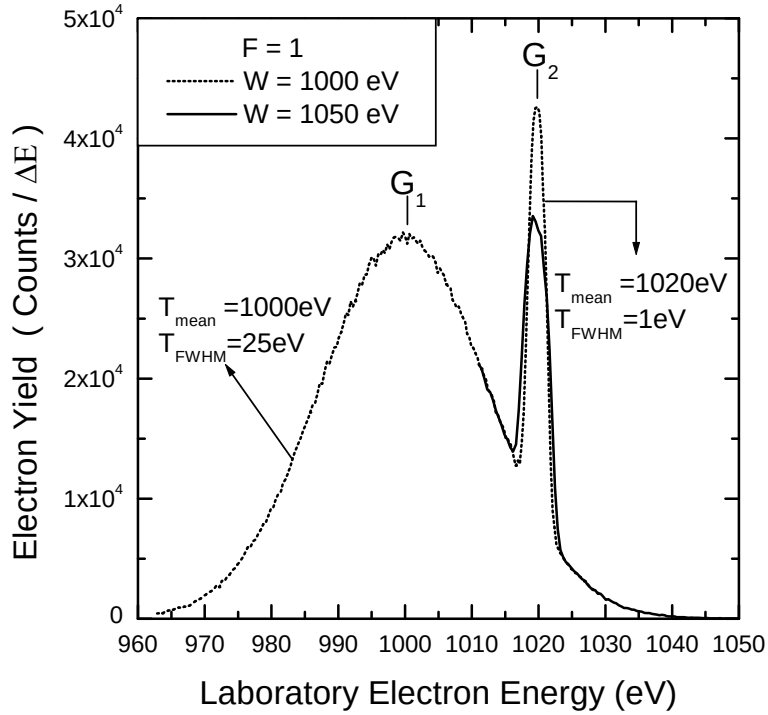

Figure 54: Artificial spectra of electron energy distribution, consisting of two Gaussian peaks G_1 and G_2, of mean energies 1000eV and 1020eV, and FWHM of 25eV and 1eV, respectively are "recorded" at tuning energies of 1000eV and 1050eV and a deceleration factor F = 1. Note that the G_2 peak parts of the spectra (for which $\Delta T_{FWHM} << \Delta T_{WINDOW}$) do not match well, due to differences in analyser resolution along the PSD. However the areas of peaks G1 and G_2 are the same for both cases of W, as expected.

cell and the lens entrance and the opening dimension of the lens entrance, i.e. the ones that are flying within the solid angle $\Delta\Omega$ defined for the spectrograph previously in this chapter.

Transmission is, in general, a function of the particle exit position. According to the theory of the ideal hemispherical analyser, the transmission function is described by a trapezoidal form. [67, 73] In principle the lens transmission can be assumed to be unity, due to the large analyser entrance opening used ($d_{AE} = 6mm$). Therefore the linear magnification can easily be limited to values of $|M_L| < d_{AE}/d_o = 6/2.5 = 2.4$, even for very high deceleration factors, when proper lens voltages are applied (see Fig. 87). Consequently the spectrograph transmission should follow the trapezoidal form of the ideal HDA.

Indeed, in Fig. 55(left) a SIMION study of the HDA transmission is shown for the case of $\xi = 1.23$, $\gamma = 1.5$ and F = 1. A group of 63 electrons generated all over the

gas-cell volume were flown at different group energies and the electrons detected at the PSD area (40mm diameter) were recorded. Lens voltages were set according to the energy resolution optimization. The trapezoidal transmission function form is evident. In Fig. 55(right) an experimental example is shown. A portion of the experimental Binary Encounter electron peak recorded at F = 1 and W = 2500eV in collisions of 21.5 MeV $F^{9+} + H_2$, is shown along with the theoretically predicted one. Experimental data were normalized to the theory. The sudden cut-off of the experimental spectrum justifies the trapezoidal form of the spectrograph transmission.

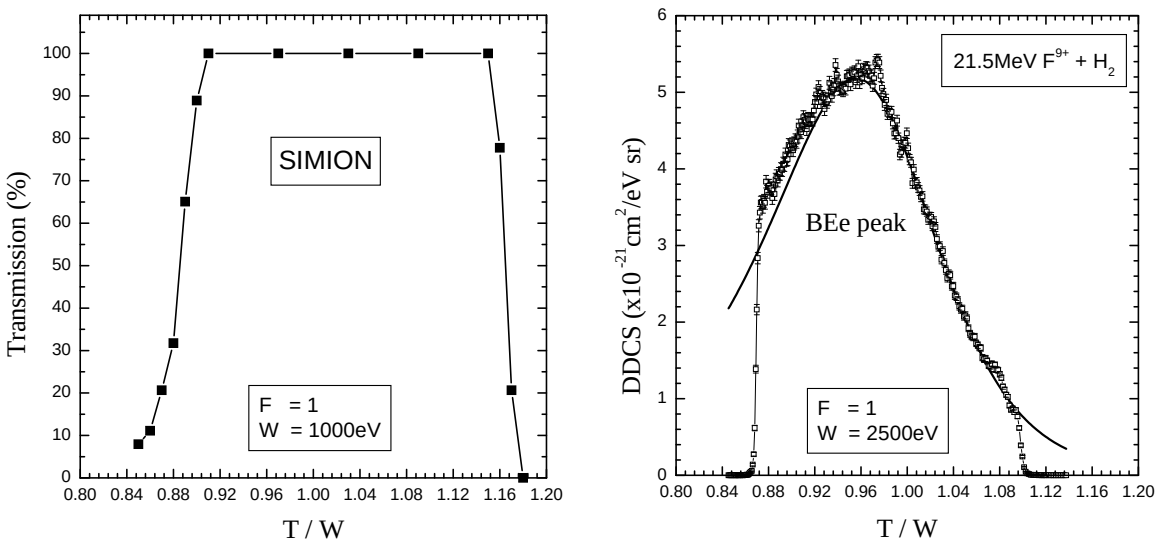

Figure 55: [*Left*]SIMION study of transmission of the hemispherical spectrograph for the case of $\xi = 1.23$ and $\gamma = 1.5$. [*Right*] Experimental spectrograph transmission visualized from the comparison between the experimental Binary Encounter electron peak recorded in collisions of 21.5 MeV $F^{9+} + H_2$ (data points), and the theoretically predicted one (solid line).

In all data analysis, only the part of the spectrum for which transmission was maximum was retained.This was true for the channel interval between 40 and 220. The maximum transmission value was then determined by the two 90% transmission grids, placed at the exit of the analyser, i.e. $T = (0.9)^2 = 0.81$. The accuracy of the transmission value is expected to be better than 0.01. Therefore $\Delta T/T \leq 1\%$

η: The MCP efficiency. η is the probability that an electron reaching the MCP surface will produce an electronically measurable signal (a pulse higher than the noise level). From a statistical point of view, the efficiency can be defined as the ratio of the average number of electrons producing measurable signals when hitting the MCP, to the total number of electrons hitting the MCP surface during the data acquisition time.

The efficiency (for a certain MCP orientation and for a certain overall MCP voltage) depends on the *active* MCP area and the electron kinetic energy. The active MCP area is defined as the actual area occupied by all the microchannels cross-sections over the total MCP area. There is a certain probability for an electron not to enter a microchannel of the MCP, but hit the surface between neighboring microchannels instead. In this case a real event is not recorded. For the MCP used in the experiments presented in this dissertation, the active area, as given by the manufacturer[26], was 55%. However, even if the electron enters the microchannel, it may not produce a measurable signal, due to the quantum character of the amplification process. This is the second case where a real event is not recorded. Therefore the absolute experimental efficiency is expected to be smaller than the value of 55%.

The amplification factor of an MCP is a function of the kinetic energy of the charged particle that is detected. For electrons, detection at energies around 300eV have the highest efficiency. For higher kinetic energies amplification drops slowly, while for lower kinetic energies it drops much faster. [98–100] The relative MCP efficiency was studied by using the $(2p^2)^1D$ RTE peak superimposed on the BEe peak in collisions of 21.7 MeV F^{8+} + H_2. The spectrum was recorded at a tuning energy W = 2500eV, for different detection energies. This was achieved by biasing the PSD at appropriate voltages. The raw data were corrected for DTC and each spectrum was integrated over the same energy area under the RTE line. The total counts for each integration were normalized to the maximum value of the integration set. The results, presented in Fig. 56, show that the maximum efficiency occurs at kinetic energies around 350eV, followed by a sudden drop at lower energies and a smooth decrease for higher energies, as already expected.

Although Fig. 56 indicates the maximum efficiency at electron energy of 350 eV, it would be a mistake to adopt this value for the measurements. As seen in Fig. 56, the efficiency function varies relatively fast around the 350 eV value. Since the analyser energy window is $\simeq$20%, a choice of a universal detection energy at 350eV would result in a measurable efficiency variation over the PSD area. To avoid this problem, an electron energy detection of 1000 eV was used instead. This means that the MCP voltages were always set in such a way (negatively biased, see Fig. 17) so that the central ray always impacted the MCP with an energy of 1000 eV.

For the low resolution mode though, where the energy window extends from 900eV to 1100eV, a further correction of the efficiency can be implemented. By fitting the detection energy region between 800 – 1200 eV in Fig. 56 to a line, the efficiency η results in the following form:

$$\eta(E_{DET}) = \bar{\eta}\,[1 - 10^{-4}\,(E_{DET} - W)] \tag{128}$$

where E_{DET} is the electron detection energy, and $\bar{\eta}$ the efficiency value for $E_{DET} = 1000eV$, which is left to be determined. For the high resolution mode, the energy window is narrow enough to allow for treating the efficiency as a number, i.e. $\eta = \bar{\eta}$.

[26]Gallileo Electro-Optics Corporation (now Burle Electro-Optical Inc.).

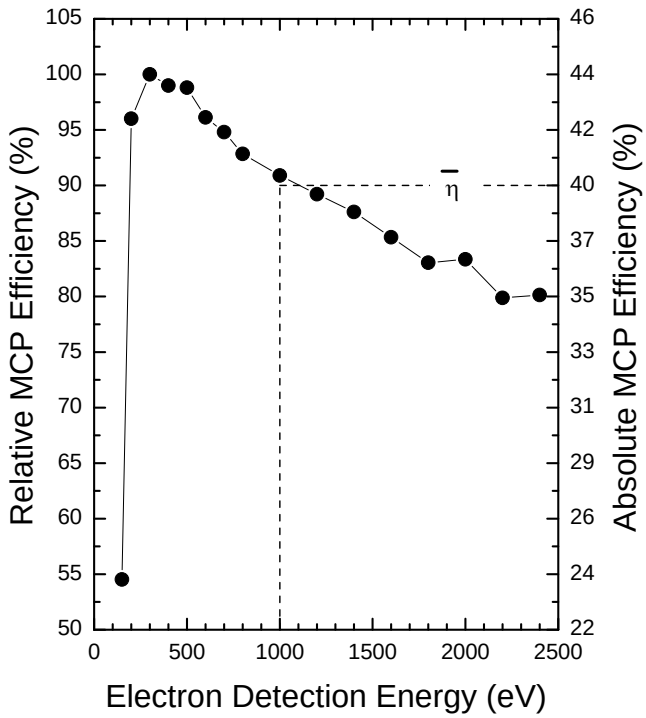

Figure 56: Experimental relative MCP efficiency η as a function of the electron energy detection. The absolute MCP efficiency (right y-axis) refers to the average absolute MCP efficiency $\bar{\eta} = 40\%$ at 1000 eV detection energy.

The overall uncertainty in the efficiency η is thus primarily due to the uncertainty in $\bar{\eta}$ and it is described next.

7.3 Absolute MCP efficiency determination: Binary Encounter electron normalization

In §2.1 the excellent agreement between experimental studies on the BEe DDCS using H_2 and He targets in collisions with bare projectiles and the Impulse Approximation (IA) model at collision energies of a few MeV/amu, was mentioned. This fact was embodied in the data analysis, in order to define the absolute MCP efficiency. On the assumption that all the parameters involved in the DDCS formula of Eq. 119 except the MCP efficiency η are well known, the BEe peak was used to determine the absolute value of $\bar{\eta}$.

The BEe peak was recorded in collisions of 21.5MeV F^{9+} + H_2 at tuning energies of 1850eV, 2100eV, 2300eV, 2500eV and 2700eV, in order to fully cover the BEe peak region (and at the same time check the matching quality of the different spectra slices)

at a deceleration factor of F = 1. The raw data were corrected for all the experimental factors except the MCP efficiency $\bar{\eta}$ which was treated as a free parameter. It was found that an agreement between theory and experiment was established for the value of $\bar{\eta} = 0.4$. The result which is shown in Fig. 57 is reasonable since the maximum value of η defined by the manufacturer, as mentioned before, is 0.55. During a set of measurements involving boron projectiles, which lasted more than a month, while experimental conditions were kept unchanged, the MCP efficiency measurements showed that the value of $\bar{\eta}$ remained well within the range of 0.4 – 0.5.

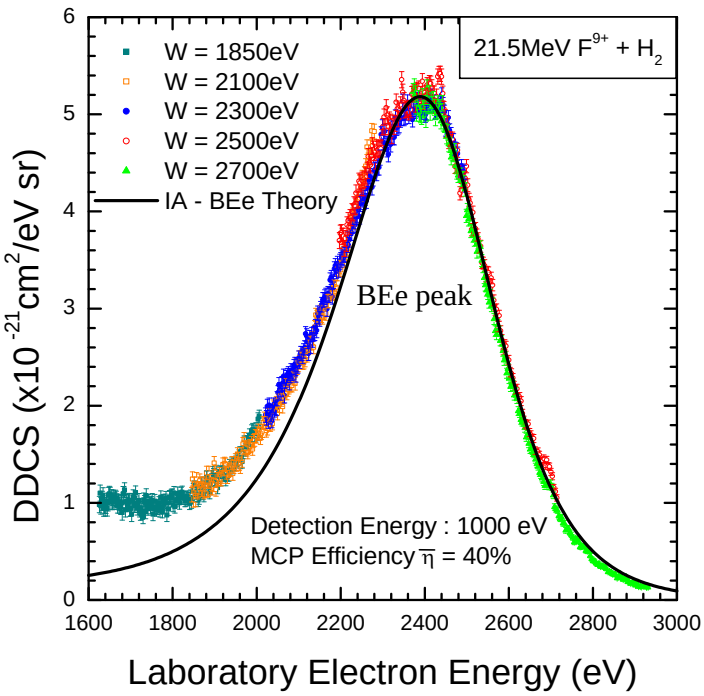

Figure 57: Absolute MCP efficiency η obtained by the normalization of the experimental data obtained in collisions of 21.5MeV $F^{9+} + H_2$, at tuning energies of 1850eV, 2100eV, 2300eV, 2500eV, 2700eV with deceleration factor F = 1, to the IA BEe theory. An intrinsic MCP efficiency $\bar{\eta} = 40\%$ for an electron detection energy of 1000eV was obtained. Note the good matching of the spectra slices.

It is well known that the high energy shoulder of the BEe peak, obtained in collision energies of a few MeV/u of highly charged ions colliding with He or H_2 targets, is described very accurately by the IA - BEe models. [46] This fact was used for the determination of the MCP absolute efficiency η as a function of the detection position (channel). The BEe spectrum of 21.5 MeV $F^{9+} + H_2$, recorded at tuning energy of W=2700 eV and deceleration factor F=1, was divided by the IA - BEe calculated one and normalized to its mean value $\bar{\eta} = 0.4$. The variation of η over the PSD

dispersion axis is illustrated in Fig. 58. It is clearly seen that the efficiency variation is $\delta\eta/\bar{\eta} < 1.25\%$, which is well accepted for the DDCS accuracy of the experiments this dissertation is involved with.

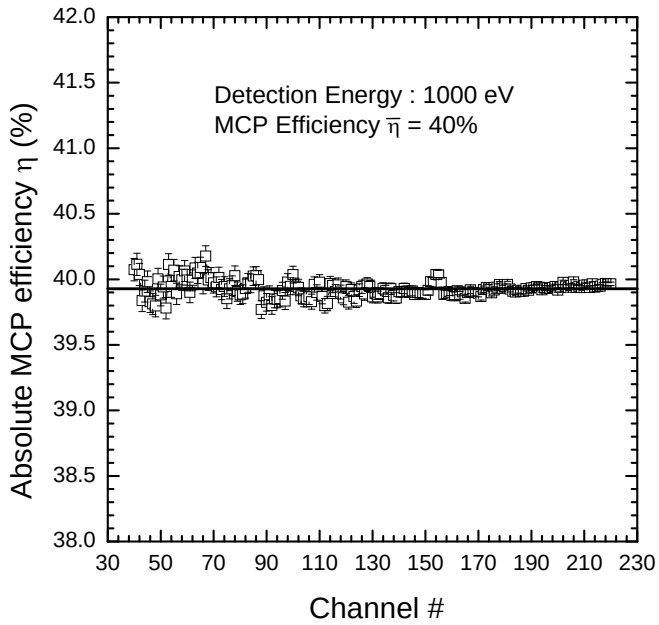

Figure 58: Absolute MCP efficiency η as a function of the PSD position - channel number.

The MCP efficiency η is the most sensitive overall parameter involved, since it can be easily affected by the PSD voltages, the vacuum quality or the threshold setting on the CFD. Therefore its frequent monitoring, through the procedure of BEe peak normalization, ensures an accurate absolute DDCS determination.

The uncertainty in the average efficiency $\bar{\eta}$ arises from the quality of the fit to the BEe peak. For the measurements presented in this work, the average efficiency could be varied within an absolute uncertainty less than 10%. Therefore this average value of $\delta\bar{\eta}/\bar{\eta} = 10\%$ can be safely assumed for the error analysis.

7.4 Error analysis

The uncertainties involved in ZAPS measurements refer to either the energy or the DDCS of the spectra. Energy uncertainties have already been treated in §7.1. The DDCS measurement involves both statistical and systematic errors. Statistical uncertainties, arising from the electron counts $N_e \pm \sqrt{N_e}$, are treated in the error analysis according to the usual method of error propagation for uncorellated variables. [101] The error bars, accompanying the experimental data in the graphs presented in this dissertation, are referred to the statistical uncertainties only.

The systematic uncertainties depend on the accurate determination of the rest of the quantities present in DDCS formula in Eq. 119. In Table 5, the typical values of the previously discussed experimental quantities along with their maximum percentage uncertainties are given. The average absolute uncertainty on the DDCS, $\delta\sigma/\sigma$, can be estimated by adding in quadrature all the estimated uncertainties for each term in Eq. 129:

$$\begin{aligned} \frac{\delta\sigma}{\sigma} &= \sqrt{\left(\frac{\delta N_I}{N_I}\right)^2 + \left(\frac{\delta L}{L}\right)^2 + \left(\frac{\delta n}{n}\right)^2 + \left(\frac{\delta(\Delta E)}{\Delta E}\right)^2 + \left(\frac{\delta(\Delta\Omega)}{\Delta\Omega}\right)^2 + \left(\frac{\delta T}{T}\right)^2 + \left(\frac{\delta\bar{\eta}}{\bar{\eta}}\right)^2} \\ &\leq 17\% \end{aligned} \tag{129}$$

The previous absolute uncertainty estimated value for DDCSs is typical for the ZAPS experiments. Furthermore, it should be mentioned that, the SDCS measurements reported in this dissertation were obtained by integrating the area of the Auger peak and the integration uncertainty was included into the statistical uncertainty. Therefore, the new SDCS measurements are accompanied also with estimated absolute uncertainty of $\delta\sigma/\sigma \leq 17\%$.

Table 5: Experimental quantities related in the determination of the absolute DDCS spectra, according to Eq. 119. Typical values are given along with their maximum percentage uncertainties.

Quantity	X	Typical Value	Error $\delta X/X$
Number of ions	N_I	10^{12} [a]	±3%
Effective gas-cell length	L	5.175 cm	±3.5%
Target density	n	3.2×10^{13}·P(mTorr)	±2.5%
Energy interval per channel	ΔE	$1.2 \cdot 10^{-3} \left(\frac{W}{F}\right)$ [b]	±8.5% [b]
Acceptance solid angle	$\Delta\Omega$	1.8×10^{-4}sr	±9.5%
Grid transmission	T	0.81	±1%
Average MCP efficiency	$\bar{\eta}$	0.4 – 0.5	±10%

[a] Refers to ∼3,000 nC of ion charge q = 3 collected at the F.C.
[b] Refers to channel $i = 128$

8 Binary Encounter electrons

8.1 Background and motivation

A very important ionization mechanism in energetic ion-atom collisions is the interaction of a target electron with the projectile in a hard binary collision. This is a two body process with maximum momentum transfer to the target electron from the projectile nucleus. The heavy nucleus is considered to be the Coulombic center, while the target is responsible only for the initial electron velocity distribution, its nucleus playing a negligible role in the ionization process itself. The emerging target electrons are referred to as Binary Encounter electrons (BEe). [102] BEe give rise to a broad energy peak, the characteristic shape of which reflects the initial electron velocity distribution corresponding to the Compton profile of the target [103].

The spectral location of the BEe peak can be calculated by classical two body kinematics, in which a bare nucleus collides with a free electron, initially at rest. Energy and momentum conservation imply that the BEe peak lies at an electron energy given by: [104]

$$\epsilon_{BE} = 4\,t\,\cos^2\theta \qquad\qquad 0^\circ \leq \theta \leq 90^\circ \tag{130}$$

where θ is the electron emission angle, and $t = 1/2\,m\,V_p^2$ is the cusp energy (Eq. 3). Thus, for zero-degree electron observation (i.e. $\theta = 0^\circ$) the BEe peak occurs at $\epsilon_{BE} = 4\,t$. As the BEe velocity is twice the initial projectile velocity, V_p, they are also referred to as $2V_p$ *electrons*. [105] However, when a *bound* target electron is considered, the free electron delta function energy peak is broadened by the initial velocity distribution, and the BEe peak appears with a broad energy distribution reflecting the target-electron Compton profile centered around $\epsilon_{BE} = 4\,t$. Furthermore, the target-electron binding energy along with a post-collision attraction of the ionized target electron to both the projectile and the target charges, reflecting two-center effects [106], are responsible for a shift in the BEe peak to lower energies (see Ref. [44] and references therein).

The detailed understanding of the BEe production is primarily useful for the dynamics of small impact parameter collisions (a binary collision is a small target-electron–projectile-ion impact parameter collision) and related projectile screening. [107–109] BEe production is also of potential importance in the study of characteristic K–Auger electron spectra in heavy ion–atom collisions, since BEe is often the dominant component of such spectra and can interfere with the coherent Auger processes, as for example the resonant transfer and excitation followed by Auger decay (RTEA). [110] Furthermore, the BEe peak is often used as a benchmark for the *in situ* electron detection efficiency normalization, since very simple models have been found adequate to predict its magnitude and position. [10, 46] Such an *in situ* normalization has been applied to the experimental data presented in this work, and details have already been presented in §7.3. Also, since BEe are normally the most energetic electrons ionized from the target in ion–atom collisions, they are the largest source of damage in collisions of ions impinging upon the atoms of a solid or biological material. Consequently, important studies on radiotherapy using heavy ions [111], on biological effects of radiation on

human tissue [112] and on stopping power of heavy ions in dense targets [113] require an accurate modeling of the BEe production mechanism.

The production of BEe is a part of electron emission in heavy ion–atom collisions and has been extensively studied the past thirty years (for recent reviews, see Refs. [47, 104]). By the late-80's the BEe formation in energetic bare-ion–atom collisions had been thought to be well understood. [46, 86, 102, 107, 114–118] The use of energetic bare projectiles established the well-known scaling of the BEe DDCS with the square of the projectile nuclear charge, Z_p^2 (Rutherford scaling). [46] Extensions of the bare projectile results to partially stripped ions, indicated also a BEe DDCS scaling with an effective (screened) projectile nuclear charge value of $Z_p^{*\,2}$, which ranged between the values of the nucleus charge Z_p^2 and the ionic charge q^2, in agreement with the static screening model. [102, 107–109, 119]

However, two experiments have dramatically illustrated that the proposed effective charge scalings were inadequate to describe the BEe DDCS's production in collisions of non–bare ions with atoms. In the first, Kelbch *et al.* [120] found that at certain angles, instead of the usual BEe peak, an unexpected double peak structure appeared when 1.4 MeV/u partially stripped uranium ions collided with noble gas targets. In the second, Richard *et al.* [2] found an *increase* in the 0° DDCS spectrum of the BEe peak with *decreasing* projectile charge state, in collisions of partially stripped fluorine ions with helium and hydrogen targets. Both these results were contrary to all static screening predictions and were termed "anomalous". The origin of the explanation for both anomalies is the fact that the target electrons are scattered by a partially stripped projectile which presents to them a strongly non-Coulombic short-range potential, unlike in the case of a bare projectile.

The theoretical investigations, following the results of Richard *et al.*, showed that the 0° BEe DDCS production from fast collisions of partially stripped ions with light targets (H_2, He) can be described within the impulse approximation (see §8.2), as the elastic scattering of quasi-free electrons in the static screened field of the projectile nucleus. [1, 121–123]. Further experimental [124, 125] and theoretical [1, 126–129] investigations showed that the electron exchange is also an important factor on the BEe production. Since that time, the projectile charge state dependence of the BEe DDCS has been measured [130–134] and calculated [110, 113, 135–138] for a variety of collision systems using H_2 and He targets, confirming the general enhancement behavior for non–bare ions. The validity of the impulse approximation method for the BEe production has also been successfully tested in measurements of energetic ions with heavier targets. [44, 139]

Non–zero-degree measurements and calculations utilizing heavy projectiles (Cu, I, Au, U) [113, 135, 140–143] were also conducted for the investigation of the "anomalous" BEe double peak structure observed by Kelbch [120], attributing the formation of these structures mainly to the diffraction of the quasi-free target electrons in the potential of the projectile. Further non–zero-degree experimental studies using lighter ions, [134, 144–150] showed that the BEe enhancement effect prevails up to a critical laboratory observation angle, beyond which BEe production approaches the normal long-range

screened scaling. In addition, more sophisticated theories treating the BEe production as a part of the electron ionization in ion-atom collisions have also been developed [151–158].

Recently, Bechthold *et al.* [159] reported on an intra–atomic double scattering of BEe in collisions of 5.9 MeV/u U^{29+} with neon, xenon and molecular targets. According to their interpretation of the findings, the target BEe electrons emitted at extreme forward laboratory angles are subsequently elastically scattered in the target nuclear potential to the large angles where they were observed. They referred to these electrons as "ternary encounter electrons" since a double scattering event is necessary to produce them. Ternary encounter electrons were earlier observed by Suarez *et al.* [160] who reported on the observation of $3V_p$ electrons in the forward direction in comparison of 20–50 keV H^+ and H^0 on He collisions. They attributed the electron peak to a projectile electron, which is first scattered in the target nuclear potential and then again in the projectile potential. Very recently, Sulik *et al.* [161] reported on the experimental evidence for consecutive projectile-target-projectile (triple) and projectile-target-projectile-target (quadruple) "ping pong" scattering of ionized target electrons in single C^+ + Xe collisions at 150 and 233 keV/u. According to the "ping pong" scattering process, the target electrons may be observed at velocities of $2V_p$, $4V_p$, $6V_p$, ..., etc, while the projectile electrons may be observed at velocities of $3V_p$, $5V_p$, $7V_p$, ..., etc. These results underline that knowledge about even fundamental ionization processes is still constantly evolving.

In this chapter, the charge dependence of the 0° BEe peak production is studied for partially stripped boron ions colliding with hydrogen targets. The study was motivated primarily by the need for an *in situ* calibration of the electron detection efficiency. [10] The lack of any measurements or calculations on BEe production for boron ions in the literature, mainly due to the weak boron beam intensity available by the tandem Van de Graaff accelerators, also added to this decision. Specifically, the BEe peak enhancement factors defined by the ratio of the non–bare to bare BEe DDCSs for the collision system $B^{(2-5)+} + H_2$, are studied at impact energies of 0.4–1.2 MeV/u, which is the energy region where the rest of the data presented in this dissertation were recorded. The Elastic Scattering Model (ESM) and Rutherford (bare nucleus) models are used within the impulse approximation in order to calculate the dependence of the enhancement factors on the projectile charge state. ESM calculations show a very good agreement with the experimental data.

8.2 Impulse Approximation

The Impulse Approximation (IA) describes the interaction of a fast projectile with a much slower target electron neglecting the collisional effect of the nucleus to which the electron is bound. The IA was initially applied in ion-atom collisions to RTE studies [162], and since then it has been successfully applied to other $e - e$ processes such as electron-electron Excitation [33], electron-electron Ionization [35, 36], Inelastic Resonant scattering [48] and Super-Elastic Scattering [163], thus providing a unified

approach for dealing with all target-electron – projectile-electron interactions [164]. In addition, the IA has been successfully utilized in BEe. [46, 165]

The basic assumption of the IA is that the collision velocity V_p is large compared to the velocity of the target electron v_t, i.e. $V_p/v_t >> 1$. [162] Thus, during the collision time, the target electron can be considered fixed. Viewing the collision process from the projectile rest frame, the electron can be treated as a quasi-free particle approaching the projectile nucleus with a velocity $\mathbf{v} = \mathbf{V_p} + \mathbf{v_t}$. Then, the quasi-free electron impact energy in the projectile frame is written as: [164]

$$\epsilon' = \frac{1}{2}\, m\, \mathbf{v}^2 = \frac{1}{2}\, m\, V_p^2 + p_z \cdot V_p + \frac{p_x^2}{2m} + \frac{p_y^2}{2m} + \frac{p_z^2}{2m} \tag{131}$$

where $p_j = m\, v_j$ is the momentum component in the $j = x, y, z$ directions and m the electron mass. Brandt [162] in his RTE - IA treatment, neglected the p_j^2 terms for small electron velocities, $v_{t_j} << V_p$. Itoh [22] *et al.* also neglected the p_j^2 terms, but subtracted the ionization energy of the active target electron E_I as a correction. Lee [46] *et al.* improved agreement between the IA model and experiment by keeping the E_I correction along with the p_z^2 term. Following Lee's IA model, Eq. 131 is written for the *i-th* target quasi-free electron as:

$$\epsilon' = \frac{1}{2}\, m\, V_p^2 + p_{z_i} \cdot V_p + \frac{p_{z_i}^2}{2m} - E_{I_i} \tag{132}$$

Thus, within the IA, the DDCS in the projectile frame for the ion-atom collision, $\frac{d^2\sigma}{d\Omega'\, d\epsilon'}$, can be related to the SDCS for the free electron-ion collision, $\frac{d\sigma}{d\Omega'}$, as follows (atomic units):

$$\frac{d^2\sigma(\epsilon', \theta')}{d\Omega'\, d\epsilon'} = \sum_i \left(\frac{d\sigma(\epsilon', \theta')}{d\Omega'}\right) \left(\frac{n_i\, J_i(Q_i)}{V_p + Q_i}\right) \tag{133}$$

where

$$Q_i \equiv p_{z_i} = \sqrt{2}\sqrt{\epsilon' + E_{I_i}} - V_p \tag{134}$$

obtained by solving Eq. 132 for p_z, and

$$J_i(Q_i) = \int\int dp_{x_i} dp_{y_i} |\psi_i(\mathbf{p}_i)|^2 \tag{135}$$

is the Compton profile which gives the probability of finding a specific target electron i with a z-momentum component Q_i , where z is the direction of the projectile velocity. $\psi_i(\mathbf{p}_i)$ is the *i-th* electron wavefunction in momentum space while n_i is the number of electrons in the *i-th* subshell. The single differential cross section $\frac{d\sigma}{d\Omega'}$ is considered to be a function of the free electron impact energy ϵ' and the scattering angle θ'. The sum index i in Eq. 133 should run over all target electrons satisfying the basic IA assumption, i.e. $V_p >> v_{t_i}$.

Calculated Hartree-Fock Compton profiles are available in the literature. [166] For H_2 and He targets, analytic expressions have been derived from fits to measurements using X-rays. [167]

8.2.1 Rutherford Scattering Model

The single differential cross-section of a free electron colliding with a bare nucleus of charge Z_p is successfully described by the Rutherford scattering model and is given in atomic units by: [168]

$$\frac{d\sigma(\epsilon', \theta')}{d\Omega'} = \left[\frac{Z_p}{4\,\epsilon' \sin^2\left(\frac{\theta'}{2}\right)}\right]^2 \tag{136}$$

where primed symbols refer to the projectile rest frame.

Substituting Eq. 136 in Eq. 133, the DDCS of a quasi-free electron scattered at 180° (zero-degree laboratory observation angle, $\theta = 0°$) from a bare nucleus is described under the IA - Rutherford treatment as:

$$\frac{d^2\sigma(\epsilon', \theta' = 180°)}{d\Omega'\, d\epsilon'} = \left[\frac{Z_p}{4\,\epsilon'}\right]^2 \sum_i \frac{n_i\, J_i(Q_i)}{V_p + Q_i} \tag{137}$$

The laboratory frame Rutherford DDCSs are obtained according to the transformations described by Eqs. 14 and 8. In Fig. 59, theoretically calculated IA - Rutherford BEe DDCSs, illustrating the dependence on the projectile energy, the nuclear charge and the Compton profile, are shown in the laboratory frame. The Compton profiles of H_2, He and Li are also shown in Fig. 60 (top) for comparison. The Rutherford SDCS, a smoothly varying function to which the Compton profiles of different target electrons are folded, resulting in the BEe peak shape usually observed, is shown in Fig. 60 (bottom) for $Z_p = 9$ and scattering angle of $\theta' = 180°$ (backscattering corresponding to zero-degree laboratory observation angle). It should be mentioned here that the Li(1s) electrons do *not* satisfy the IA basic assumption $V_p >> v_{t_i}$, and therefore were not included in the calculations.

8.2.2 Elastic electron Scattering Model

As it has already been mentioned, BEe production from fast collisions of ions with H_2 targets can be described within the IA as the elastic scattering of quasi-free electrons in the statically screened field of the projectile nucleus including electron exchange effects. This is also known as the Elastic electron Scattering Model (ESM). In the ESM calculations described by Bhalla *et al.* [129], the static potential and nonlocal exchange contributions are computed in a self-consistent Hartree-Fock atomic model. The Coulomb phase shift and the additional phase shifts due to screening and exchange effects are calculated using a partial wave treatment. The details of the calculation can be found in Refs. [123, 129, 169] The ESM code, which was used for comparison to the experimental data, was generously provided to me by Prof. C.P. Bhalla.

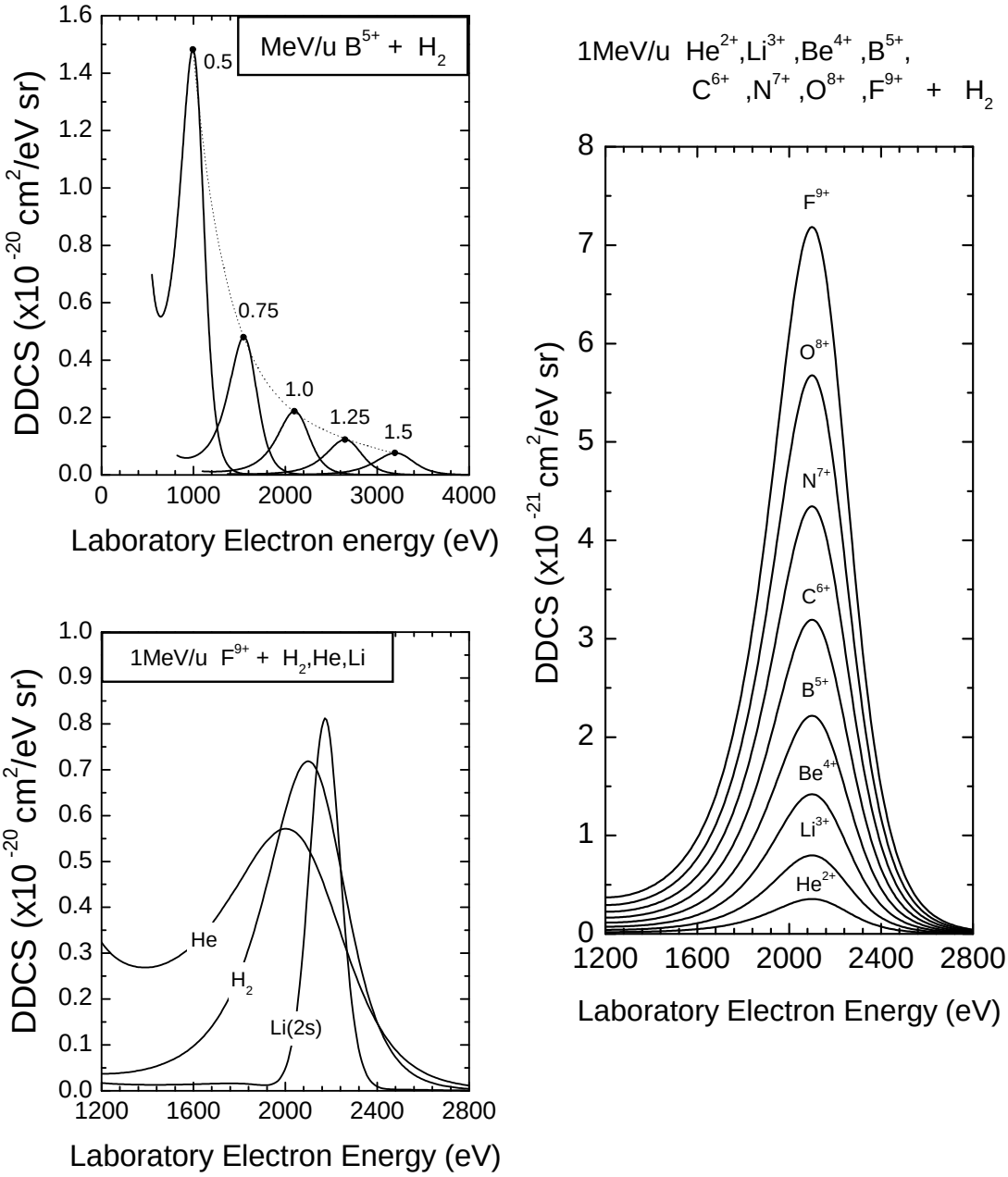

Figure 59: Theoretically calculated IA–Rutherford BEe DDCSs. [*Top-Left*]BEe DDCSs in collisions of $B^{5+} + H_2$ as a function of the projectile energy. [*Bottom-Left*] BEe DDCSs in collisions of 1 MeV/u $B^{5+} + H_2$, He and Li targets. [*Right*] BEe DDCSs in collisions of 1 MeV/u $Z_p^{Z_p+} + H_2$, where Z_p is the projectile atomic number, as a function of bare nucleus charge.

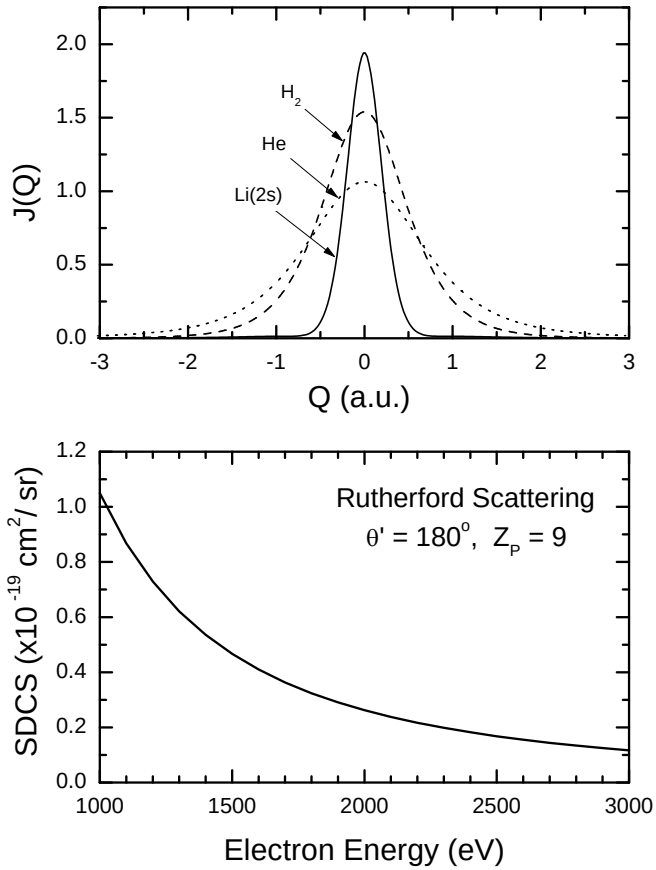

Figure 60: [*Top*] Compton profiles for H_2, He and Li. [*Bottom*] The single differential Rutherford cross section for nuclear charge $Z_p = 9$ and scattering angle of $\theta' = 180°$.

8.3 BEe peak enhancement factors for collisions of 0.4–1.2 MeV/u $B^{(2-5)+} + H_2$

In this dissertation, the BEe studies are focused on the process of the 0° BEe DDCS enhancement for partially stripped ions, i.e. for the collision system of 0.4–1.2 MeV/u $B^{(2-5)+} + H_2$. For this reason, a more detailed historical overview on this issue will be given before the presentation and discussion of the new results.

8.3.1 Historical background

Richard's results on the anomalous projectile charge dependence of BEe production were followed by a large number of theoretical and experimental investigations. Quinteros *et al.* [130] performed coincidence experiments between the binary encounter electrons and the projectile final charge state for the 0.53 MeV/u $F^{q+} + H_2$ collisional

system, showing that electron capture as a process competing with the BE process could not reduce the BEe emission by a measurable amount. They also showed that the projectile electron loss process did not contribute to the BEe peak under 0° detection. Both previous processes were candidates for the explanation of the BEe enhancement. Jagutzki *et al.* reproduced Quinteros results by performing similar experiments for the 0.53 MeV/u Cu^{q+} + He collisional system, showing in addition a significant deviation of the BEe peak spectral shape, where the emission of higher energy electrons in the laboratory forward direction was favored for less stripped projectiles.

Theoretical investigations were initiated by Olson *et al.* [121] who conducted a series of calculations on the U^{q+} + Ar system at impact energy 1.4 MeV/u, using the three-body classical trajectory Monte Carlo method, showing a BEe peak 10 times larger for the partially stripped U^{32+} ion than for the fully stripped U^{92+} ion. They attributed this behavior to the structure of the impinging non-bare projectile potential. Reinhold *et al.* [122] extended the impulse or binary encounter approximation to the non-Coulomb interaction between a clothed projectile ion and a target electron, to explain the anomalous BEe peak behavior. They qualitatively reproduced Richard's results showing that the enhancement of the elastic cross section at backward angles in the projectile frame, for the scattering of an electron from the statically screened projectile, accounts for the BEe peak enhancement. They also demonstrated by means of the classical deflection function [27] that the F^{3+} behaves like an ion with Coulomb charge equal to +3 for distant collisions and similar to 9+ for close collisions. Surprisingly though, for small impact parameters the deflection function for F^{3+} exceeds that of the bare F^{9+} ion. Shingal *et al.* [123] also performed elastic scattering calculations for fluorine projectile ions, using a statically screened projectile potential, to estimate the degree of the enhancement. Taulbjerg [1] was the first to include electron exchange in his elastic scattering model for one-electron fluorine ions, F^{8+}, predicting a 10% increase in the total BEe cross section due to the exchange term. His calculations were in excellent agreement with Richard's results.

Taulbjerg also provided a simple qualitative explanation for the BEe peak enhancement using the concepts of inner and outer screening, respectively [1], which I find quite clear and useful. Inner screening operates to reduce the effective central charge of the nucleus, while outer screening accounts for the reduction of the binding energy of the active electron. The Rutherford differential scattering cross section is proportional to the square of the central charge but inversely proportional to the square of the impact energy. Therefore, in collisions of electrons with clothed ions, inner screening of the projectile electrons tends to reduce the cross section, while outer screening has the effect that the electron is accelerated less in the clothed ion field than in the corresponding field of the bare nucleus, and accordingly tends to increase the cross section.[28] It is likely that for the case of scattering through 180° in the projectile frame, the outer screening will dominate over the inner screening explaining qualitatively the observed

[27] the impact parameter as a function of the scattering angle

[28] The concepts of outer and inner screening refer to the long-range and short-range potentials, respectively. They are also referred to as "screening" and "antiscreening" effects. [2]

enhancement. As also pointed out by Schultz and Olson [113], "the effect of the screening of the nuclear charge in the partially stripped ion case is to lower the velocity at which the electron reaches the distance of the closest approach, allowing a greater time for deflection and the possibility that much larger impact parameters can contribute to a particular range of scattering angles, especially in the backward direction".

Schultz and Olson [113] were the first to provide a systematic theoretical study of the BEe peak enhancement factors for a wide range of nuclear species (C, F, Fe, I and U) and over the range of charge states possible with these ions, as a function of the collision energy. However, their elastic scattering model does not include electron exchange effects due to the complexity of the problem when many electrons are present. They showed that the increase in the BEe peak intensity is not a constant function of the impact energy. At large impact energies BEe production scales as Z_p^2, where Z_p is the nuclear charge, while for low impact energies approaches a q^2 scaling, where q is the ion charge. It is the intermediate range of energies where the greatest enhancement occurs. They also provided a rule of thumb for collision energy at which the ratio of the partially stripped ion induced binary peak to that for the bare projectile is maximized, i.e., $E_{p_{max}} \simeq 0.75\, Z_p$.

Elastic scattering models utilizing statically screened projectile potentials which included also electron exchange terms, were developed by Chen *et al.* [126] and Bhalla *et al.* [129], indicating a better agreement with the experimental data. However, the validity of the electron exchange contribution was not yet well established, as it was strongly questioned by Salin [127] (see also Taulbjerg's answer [170]). A more detailed experimental work by Gonzalez *et al.* [124] studying simplified collisions between one electron ions of He, C, N, O and F with H_2 targets, showed a very good agreement with theoretical calculations which included electron exchange contributions. Hidmi *et al.* [125] performed also detailed experimental work colliding partially stripped carbon ions with hydrogen targets at incident energies of 0.75 MeV/u. Their results on the BEe enhancement factors compared to Bhalla's elastic scattering model [129], clearly showed a non-negligible (about 10%) electron exchange contribution, thus establishing the electron exchange process as a significant term in the elastic scattering models (see for example Ref. [138]). A more systematic experimental study on the BEe enhancement factors for a wide variety of partially stripped ions (H, C, N, O, F, Si and Cl) colliding with molecular hydrogen targets at incident energy of 1 MeV/u were also given by Hidmi *et al.* [132]. Posthumus *et al.* [133] reported on BEe peak enhancement factors for fast (6 – 8 MeV) C^{q+} and O_2^{q+} + H_2, while Liao *et al.* [134] reported for 1 MeV/u $F^{(4-9)+}$ + H_2.

Zouros *et al.* [139] explored subshell contributions and reported on the projectile charge state dependence of the 0° BEe production using 30 MeV $O^{(4-8)+}$ in collisions with O_2 targets. The use of heavy targets also showed a definite enhancement with respect to the bare projectile BEe production. Also, BEe production calculations within the impulse approximation were found to be in good overall agreement with the measured DDCSs, using only the O_2 L-shell electron contribution. Zouros *et al.* [44] extended their previous study to a variety of targets (H_2, He, O_2, Ne, and Ar) showing

that the BEe DDCSs based on the impulse approximation and independently computed elastic cross section scattering were in excellent agreement with the data for H_2 and He targets and in good agreement for the other multielectron targets, but only when outer subshells alone were included, for which $V_p/v_t >> 1$, i.e. the IA criterion was valid.

Next, the enhancement factors of the non–bare to bare BEe DDCSs of the collision system $B^{(2-5)+} + H_2$, are studied for the ion impact energies of 0.4–1.2 MeV/u. Theoretical calculations based on the Elastic Scattering Model utilized within the Impulse Approximation are compared to the experimental data, showing a very good agreement.

8.3.2 Results and discussion

The BEe enhancement factors for boron ions were determined experimentally as follows. Ions of 13 MeV B^{3+} ions were obtained from the tandem Van de Graaff accelerator, post-stripped to B^{5+} bare ions and collided with H_2 targets under single collision conditions. Electron spectra were recorded in the region of the BEe peak at different overlapping energy slices. Due to background appearance at the edges of the PSD, energy slices were recorded with an overlapping of about 50%, ensuring the expected matching of the spectra at different tuning energies. In the measurements presented in this chapter, the spectrograph focusing lens was not used, and its electrodes were grounded, resulting in an average FWHM energy resolution of about 3%, which however, did not affect the shape of the broad BEe peak. The BEe raw data obtained were background subtracted, energy calibrated, and corrected for all the experimentally determined factors of Eq. 119, except the efficiency η. They were then normalized to the bare ion BEe theory (Rutherford DDCS), thus fixing the MCP efficiency value at $\eta = 0.205$. BEe spectra for the collisions of 13 MeV $B^{(2-4)+} + H_2$ were also obtained under the same conditions as for the bare boron ions. The BEe yields were absolutely normalized using the efficiency value determined previously from the bare ions BEe peak normalization to the Rutherford scattering theory. The beam energy for these measurements was determined from the 45° analysing magnet calibration settings within an accuracy of 2%. The experimental results along with the ESM predictions and the Rutherford calculations corrected for the enhancement factor, for this collision system are shown in Fig. 61.

Comparison of the theoretical calculations to the experimental results shows an excellent agreement for the high energy wing of the BEe peak. At lower electron energies, on the lower energy wing of the BEe peak, a discrepancy appears which primarily can be attributed to the high energy tail of the cusp peak, which adds to the BEe peak enhancing its low energy part. However, at the high energy wing of the BEe peak cusp contributions are minimized arguing for the use of the high energy BEe DDCS wing in collisions of 13 MeV $B^{5+} + H_2$ for safely determining the absolute electron detection efficiency.

In order to test this result at lower impact energies, an experimental study for

the same collision system of $B^{(2-5)+} + H_2$ at projectile impact energy of 4.9 MeV was conducted, maintaining the same experimental conditions as in the study of the 13 MeV beam energy. Thus, the focusing lens was not used and the obtained BEe spectra were normalized as already described. In this experiment the PSD was physically rotated by 120° in order to improve its relatively low efficiency value of $\eta = 0.205$, which was measured previously, revealing an unused part of it to the dispersion axis of the spectrograph. In this way, the MCP efficiency was determined to be $\eta = 0.350$. Also, at the low energy wing of the BEe peak, background electrons were shown to enhance the whole spectrum recorded at a tuning energy. This behavior was absent in the high energy wing. The appearance of this kind of background has been described previously in chapter 6 and can be identified by the strong mismatch of the different energy slices spectra. In order to obtain the correct BEe peaks, energy slices were recorded with an overlapping of about 50% and the lower energy spectra were normalized to the higher energy ones in such a way that a good matching of the overlapping was achieved. The experimental results are shown in Fig. 62 in comparison to the ESM and enhancement corrected Rutherford calculations.

It is clearly seen from Fig. 62 by direct comparison of the theoretical calculations to the experimental results that an excellent agreement for the high energy wing of the BEe peak is established. The peaks appearing in the non-bare boron ions spectra are due to the formation of boron excited states which de-excite via the Auger process giving rise to the pronounced peak structures.

To further analyse the results and obtain the information on the BEe DDCSs enhancement factors, the Rutherford DDCSs for bare ions were fitted to the experimental data and to the ESM calculations by an overall scaling factor, which actually is the enhancement factor under investigation. The error bar of the fits to the experimental data was determined by the uncertainty of the fit on the BEe peak maximum. In Fig. 63 the experimentally measured BEe enhancement factors along with the ESM predictions for the boron charge states of q = 3,4 are plotted as a function of the projectile kinetic energy. The agreement between the ESM model and the experiment is well within the experimental error bars for the two boron ion charge states in this ion impact energy region.

Therefore, the ESM model can be safely utilized for the determination of the absolute electron detection efficiency by normalizing the experimental BEe spectra of $B^{(3,4)+}$ ions to the ESM calculations on BEe DDCSs. Furthermore, since the Rutherford BEe DDCS corrected for the enhancement factor provide almost the same results as the ESM model as seen in Figs. 61 and 62, it can be used instead of the ESM calculations for obtaining quick and reliable results. It should be mentioned that the IA applied to Rutherford BEe DDCS, enjoys great popularity particularly by experimentalists, since it provides a simple formula, that is convenient for calculating the BEe production. Therefore, information on the BEe DDCS enhancement factors is of potential interest in order to obtain quick and at the same time reliable results on BEe DDCSs.

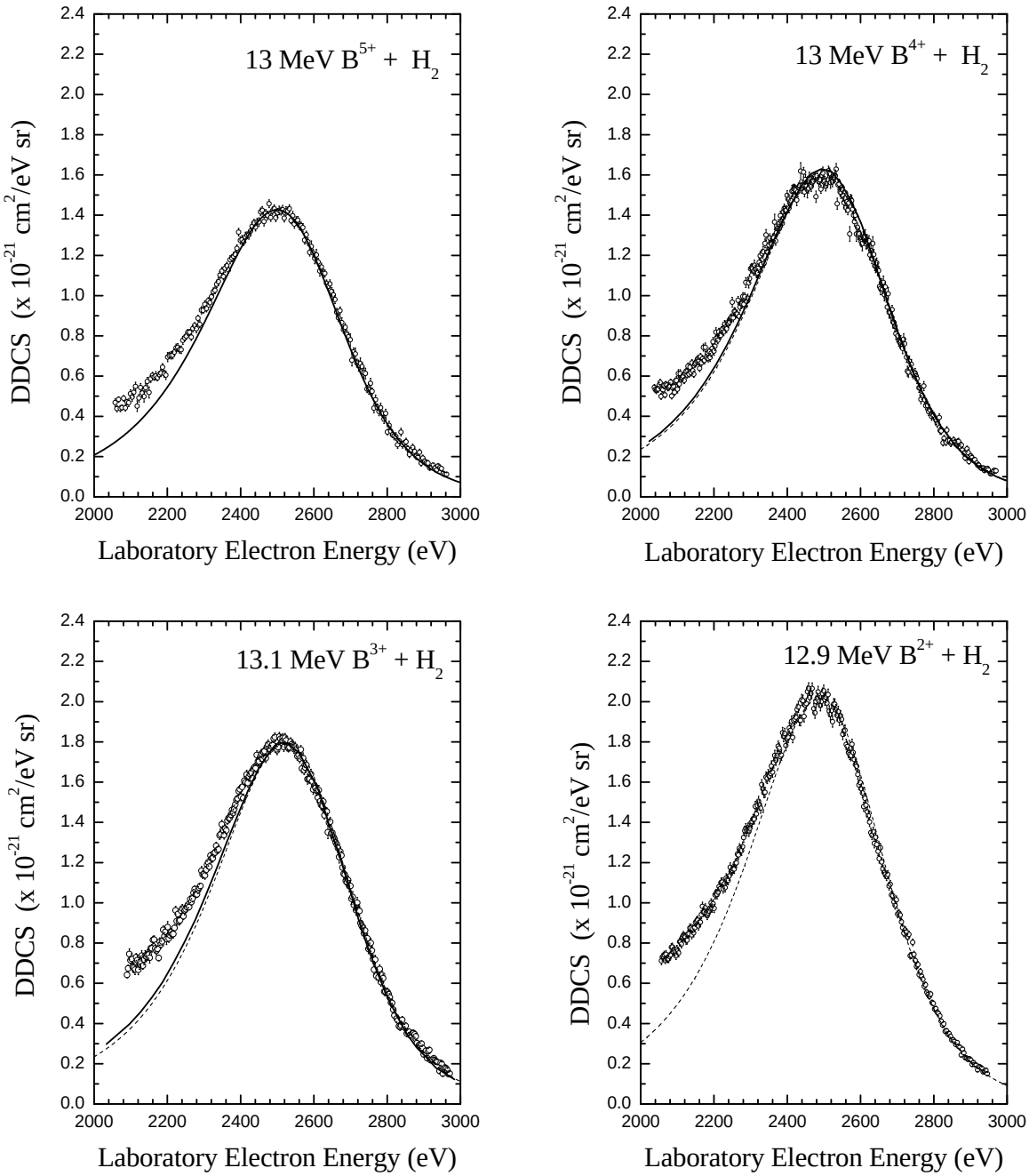

Figure 61: Experimentally measured BEe DDCSs for the collisional system of 13 MeV$B^{(2-5)+} + H_2$. Solid lines: ESM calculations. Dashed lines: Rutherford model calculations corrected for the enhancement factor. An absolute electron detection efficiency was obtained by normalizing the B^{5+} data to the BEe DDCS Rutherford theory (*Top-Left*) and used for normalizing the BEe DDCSs for $B^{(2-4)+}$ ions.

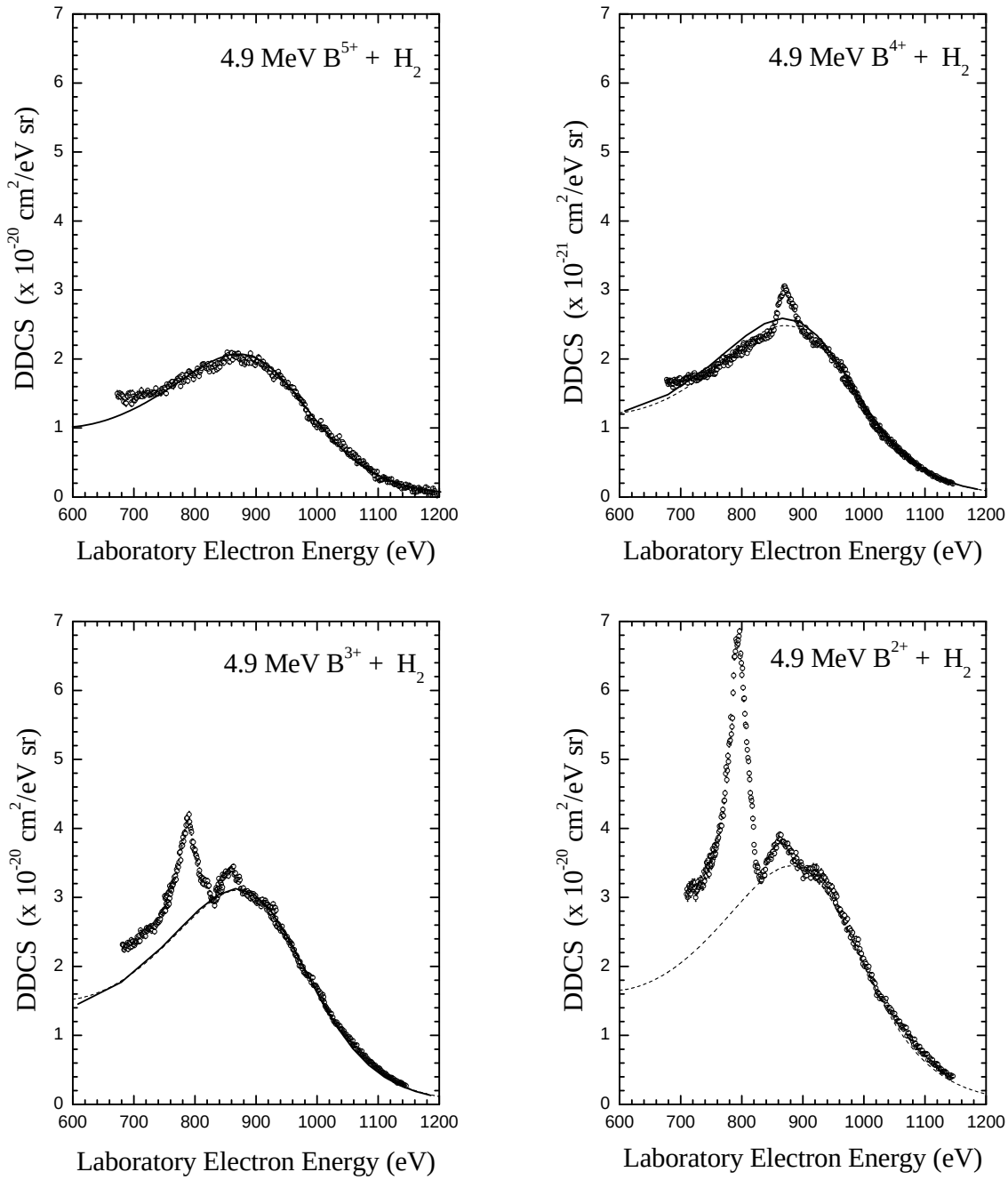

Figure 62: The same as in Fig. 61 for the collisional system of 4.9 MeV$B^{(2-5)+} + H_2$. The peaks appearing in the non-bare boron ions spectra are due to the formation of boron excited states, which de-excite via the Auger process.

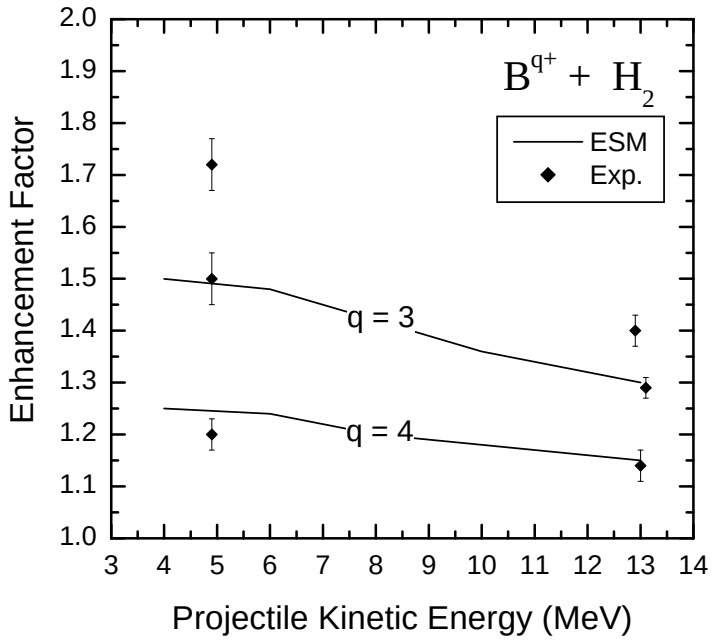

Figure 63: Experimentally measured BEe DDCS enhancement factors for the collision system of $B^{(2-5)+} + H_2$ as a function of the projectile kinetic energy. ESM calculations (solid lines) are seen to be in very good agreement to the data.

8.4 Conclusions

The need for an *in situ* calibration of the electron detection efficiency motivated the study of the BEe peak enhancement factors, defined by the ratio of the non–bare to bare 0° BEe DDCSs, for the collision system $B^{(2-5)+} + H_2$, at impact energies of 0.4–1.2 MeV/u. Experimental results showed the well known BEe DDCS to increase with decreasing ion charge state. Thus, an enhancement factor attributed to the partially stripped boron ion BEe production relative to the bare boron ion, was obtained for the charge states of 2, 3 and 4 as a function of the ion beam energy. The Elastic Scattering Model was used within the Impulse Approximation to calculate the dependence of the enhancement factors on the projectile charge state showing a very good agreement to the experimental data. This good agreement verifies the argument stated in the introduction of this chapter, that the 0° BEe DDCS production from fast collisions of partially stripped ions with light targets (H_2, He) can be described within the impulse approximation, as the elastic scattering of quasi-free electrons in the static screened field of the projectile nucleus, including also electron exchange effects. It also implies the ESM model can be used as a benchmark for the determination of the absolute electron detection efficiency by normalizing the experimental BEe spectra of $B^{(3,4)+}$ ions to the ESM calculations on BEe DDCSs. Finally, the information on the BEe

DDCS enhancement factors can be used with the Rutherford BEe DDCS instead of the ESM calculations for conveniently obtaining quick and at the same time reliable results.

9 Spectroscopy of $B^{(1-3)+}$ intermediate states

9.1 Motivation

The boron ion beams available from the KSU tandem Van de Graaff accelerator are very low intensity beams. For example, for the KLL–Auger RTE studied in this thesis, the available B^{4+} beam current for energies between 4 and 8 MeV did not exceed the value of 10 nA at the target area. In some cases, boron beams as low as 20pA were utilized. ZAPS measurements performed at tandem accelerators utilizing negative ions and conventional tandem parallel plate analysers, are practically impossible at these low beam intensities, as already mentioned in §2.3. For this reason, boron ions have not been utilized frequently in ion–atom collision studies, as opposed to C, O and F ions, which can be provided at high intensities. However, the implementation of the high-efficiency hemispherical spectrograph at the J.R. Macdonald laboratory facility, allowed for including boron ions in ion–atom collision studies. In this chapter, new results on the spectroscopy of B^{q+} (q = 1,2,3) intermediate states are presented and discussed.

The high resolution spectra for all the boron ions colliding with hydrogen targets presented here, were recorded at a deceleration factor of F = 4, corresponding to a mean instrumental energy resolution of about 0.2%. The uncertainty in the energy determination of the Auger lines is due to the FWHM of Gaussian fits applied to the peaks. The energy resolution obtained in this way differs from the mean instrumental value of 0.2%, as it is referred to the projectile rest frame and therefore is affected by the kinematic transformations, as already discussed in §2.2.1. In addition, the observed Auger spectra are presented in absolute DDCSs, primarily for illustrating the dependence of the DDCSs on the projectile collision energy, but also for further data analysis, as for example in the case of the He-like B^{3+} doubly excited states SDCSs determination, presented in chapter 10. The results from the previous study in chapter 8 on the BEe enhancement factors for partially stripped boron ions, were utilized for the absolute electron yield normalization. Finally the Auger line identification was based on previous measurements or calculations [26, 28, 29, 31, 32, 171–174], while the best known of these were used for an absolute energy calibration of the whole energy spectrum (see §7.1).

9.2 The Auger spectrum of $B^{4+} + H_2$: Production of He-like B^{3+} doubly excited states

Doubly excited states of He-like ions received considerable interest in the past (see for example C.D. Lin [175] and references therein) for the purpose of better understanding the electron spectra and the strong configuration mixing that occurs. Several attempts have been made to explain the mixing and classify the states ([171, 175] and references therein), as when the admixture of many configurations is substantial for a given state, using the LS labeling for that state becomes meaningless.

In this chapter, high resolution Auger spectra from the 4–8 MeV $B^{4+} + H_2$ collisions are reported. The spectrum, shown in Fig. 64, is dominated by the production of He-like B^{3+} doubly excited states. Calculations of doubly excited states in isoelectronic He-like ions, performed by Lipsky *et al.* [171], are compared to the experimental data. Despite the configuration mixing, the conventional single configuration scheme $2lnl'$ (or KLn for the Auger decay channel to the ground state, where n : L,M,N and O) is retained in the spectral notation as a convenience, since there is still a one-to-one correspondence between the radial quantum numbers (2 and n) and the true states. [171] The classification of the He–like Boron doubly excited states according to Lipsky *et al.* [171], along with the Auger electron energies for the decay channel to the $B^{4+}(1s)$ ground state, is reproduced in Table 6.

Doubly excited states of He-like ions are primarily produced in collisions of hydrogen-like ions with H_2 targets via the transfer and excitation process (TE) [95], in which a quasi-free target electron is captured to an excited projectile state (nl), while a projectile electron is excited to another state ($n'l'$). The TE process can be resonant, when mediated by e–e interaction, and then is referred to as resonant transfer and excitation (RTE). RTE will be examined in detail in chapter 10. The experimental signature for the production of doubly excited ionic projectile states is the detection of the electrons resulting from the Auger decay of these states.

The B^{4+} ions were obtained by post-stripping the primary B^{2+} beam with thin ($5\mu g/cm^2$) carbon foils before colliding it with the H_2 target. The beam energy was varied between the values of 4–8 MeV, as the doubly excited states are resonantly populated for projectile energies in the interval of 2–8 MeV.

The B^{4+} beams of kinetic energies lower than 3.7 MeV were too weak (less than 10 pA) to be utilized, even for the highly efficient spectrograph in use. Since TE followed by Auger decay to the ground state is considered, under the IA, as an elastic electron scattering process, the Auger spectrum lies in the BEe peak region (see Appendix J). The data were recorded in four different energy slices, matched in the overlapping regions and normalized to the BEe peak, according to the method presented in §6.4.

In Fig. 64 the recorded absolute DDCS spectra are shown in the projectile rest frame, for the energy region of 180–270eV. The KLL, KLM, KLN and KLO Auger lines produced from the decay of the TE $2lnl'$ states (n = 2,3,4 and 5, respectively) to the $B^{4+}(1s)$ ground state, are seen to be well resolved. However, the instrumental energy resolution was not adequate for resolving the Auger lines within each manifold for the $2lnl'$ ($n \geq 3$) states, as clearly seen in Fig. 64. In addition, in the $2lnl'$ manifold the $(2p^2)^1D$ and $(2s2p)^1P$ lines are also not resolved. However, RTE SDCS calculations obtained by utilizing the Auger and x-ray rates obtained from the COWAN code [176,177], showed that the intensity of the $(2s2p)^1P$ line relative to the $(2p^2)^1D$ is less than 10%, while the relative intensity of the rest of the lines is even smaller. The proof of this statement is given in §10.3. For this reason, the peak in the $2l2l'$ manifold was identified as the $(2p^2)^1D$ state and used for the accurate energy calibration of the whole spectrum. It should be mentioned that due to the dominance of the $(2p^2)^1D$ state in the KLL manifold, the contributions of the $(2pnp)^1D$ and $(2snd)^1D$ states

are expected to dominate also the other KLn manifolds too. Calculations by Lipsky *et al.* [171] on the energy limits of each isoelectronic sequence are indicated in Fig. 64 (solid lines in middle figure). They are seen to be in excellent agreement with experimental data.

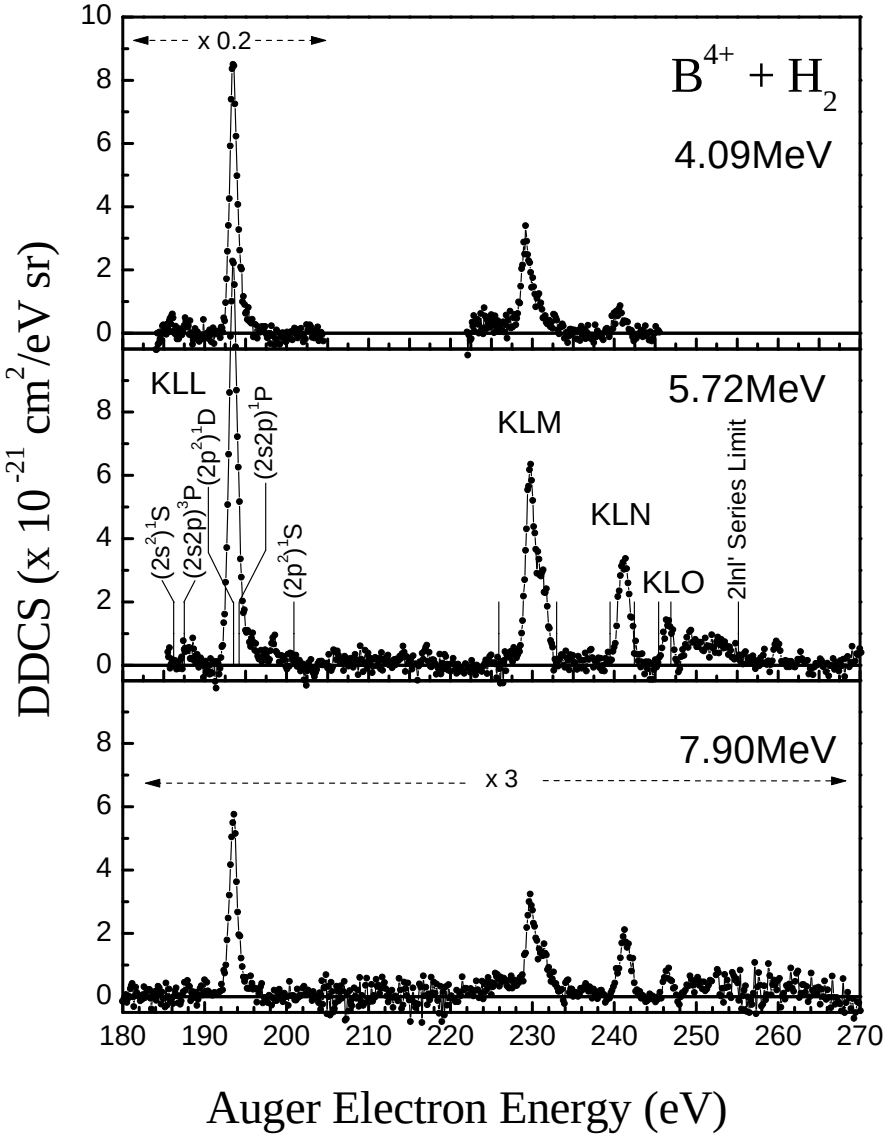

Figure 64: Absolute Auger electron DDCS spectra showing the KLn (n=2-5) series of doubly excited states of He-like $B^{3+}(2lnl')$, formed by TE in collisions of 4–8 MeV B^{4+} + H_2, and de-excited via Auger decay to the $B^{4+}(1s)$ ground state. Calculations [171] of the KLn series limits are seen to be in excellent agreement with the data. Data were scaled at occasion for improved presentation purposes as indicated. Laboratory frame data are available in Appendix J.

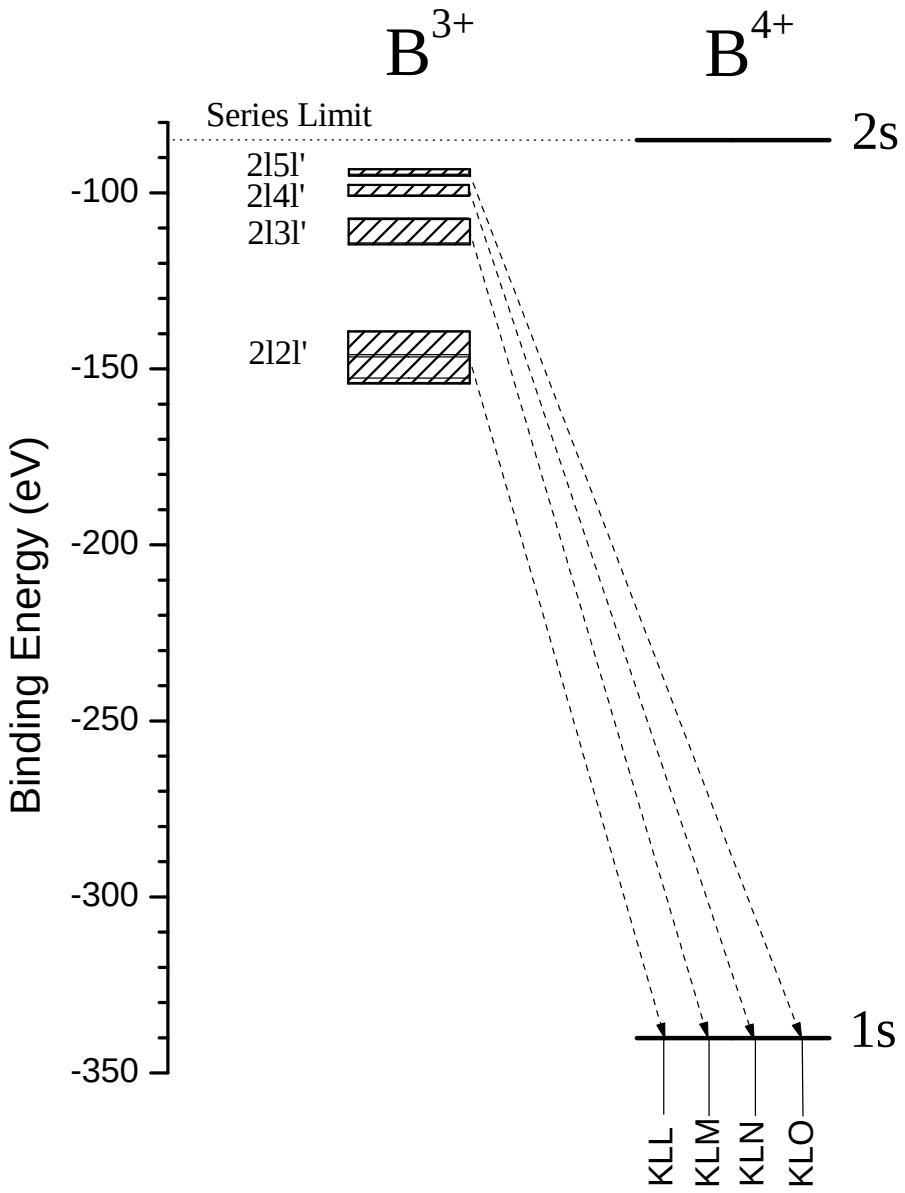

Figure 65: Energy level diagram of He-like $B^{3+}(2lnl')$ doubly excited states, de-exciting via Auger decay to the $B^{4+}(1s)$ ground state. A more complete energy level diagram is given in Appendix I.

In Table 6, the classification of $B^{3+}(2lnl')$, $n = 2$–5, doubly excited states (see Appendix G) according to Lipsky *et al.* [171] along with calculations of their binding energies (with respect to the totally stripped ions) are reproduced. In addition, the Auger electron energies, resulting from the de-excitation to the $B^{4+}(1s)$ ground state

along with the single configuration notation for the $2l2l'$ manifold are presented. Note that the Auger selection rules do not allow for the Auger decay of all the doubly excited states (see Appendix H). Furthermore, the energy level diagram of the doubly excited states decaying to the $B^{4+}(1s)$ state is illustrated in Fig. 65.

Table 6: Classification of the $B^{3+}(2lnl')$ (n = 2–5) doubly excited states ordered by their binding energies (B.E.) according to Ref. [171]. Allowed and parity forbidden (noted with a "-" sign) Auger decays to $B^{4+}(1s)$ are also shown, along with the single configuration (LS) for the $2l2l'$ manifold. The notation "&" stands for the lowest member of the series (see Appendix G).

Line No	State	Class	B.E. (a.u.)	B.E. (eV)	LS $\xrightarrow{Auger}$ 1s (eV)	LS
1	1Se&	(2,2a)	5.655930	153.907	186.22	$(2s^2)^1S$
2	3Po&	(2,2a)	5.608160	152.607	187.52	$(2s2p)^3P$
3	3Pe&	(2,2a)	5.460528	148.719	-	
4	1De&	(2,2a)	5.387168	146.594	193.53	$(2p^2)^1D$
5	1Po&	(2,2a)	5.362826	145.931	194.20	$(2s2p)^1P$
6	1Se&	(2,2b)	5.116467	139.227	200.90	$(2p^2)^1S$
7	3Se&	(2,3a)	4.197700	114.226	225.90	
8	1Po&	(2,3b)	4.179405	113.728	226.40	
9	1Se	(2,3a)	4.143029	112.738	227.39	
10	3De&	(2,3a)	4.129233	112.363	227.76	
11	3Po	(2,3a)	4.127343	112.312	227.82	
12	1Pe&	(2,3a)	4.125847	112.271	-	
13	3Po&	(2,3b)	4.118664	112.075	228.05	
14	3Fo&	(2,3a)	4.074545	110.875	229.25	
15	1Do&	(2,3a)	4.070976	110.778	-	
16	3Pe	(2,3a)	4.061908	110.531	-	
17	1De	(2,3a)	4.055001	110.343	229.78	
18	3De&	(2,3b)	4.049603	110.196	229.93	
19	3Se&	(2,3b)	4.042347	109.999	230.13	
20	3Do&	(2,3a)	4.032579	109.733	-	
21	1Po	(2,3a)	4.022184	109.450	230.68	
22	1De&	(2,3b)	3.995822	108.733	231.39	
23	3Po&	(2,3c)	3.994789	108.705	231.42	
24	1Fo&	(2,3a)	3.987691	108.511	231.62	
25	1Po&	(2,3c)	3.954675	107.613	232.51	
26	1Se	(2,3b)	3.938354	107.169	232.96	
27	3Se	(2,4a)	3.698332	100.638	239.49	

Table 6. (Continued).

Line No	State	Class	B.E. (a.u.)	B.E. (eV)	LS $\xrightarrow{Auger}$ 1s (eV)	LS
28	1Po	(2,4b)	3.689935	100.409	239.72	
29	1Se	(2,4a)	3.678711	100.104	240.02	
30	3Po	(2,4a)	3.672141	99.924	240.20	
31	3De	(2,4a)	3.667696	99.804	240.32	
32	1Pe	(2,4a)	3.665090	99.733	-	
33	3Po	(2,4b)	3.661560	99.637	240.49	
34	3Fo	(2,4a)	3.648269	99.275	240.85	
35	1Do	(2,4a)	3.645346	99.196	-	
36	3Pe	(2,4a)	3.642912	99.129	-	
37	1De	(2,4a)	3.641810	99.099	241.03	
38	3De	(2,4b)	3.637266	98.976	241.15	
39	1Fe&	(2,4a)	3.630998	99.050	-	
40	3Do	(2,4a)	3.630988	99.038	-	
41	3Fe&	(2,4a)	3.630553	98.793	-	
42	3Se	(2,4b)	3.629698	98.770	241.36	
43	3Fo&	(2,4b)	3.625445	98.654	241.47	
44	1Po	(2,4a)	3.625358	98.652	241.48	
45	1Fo&	(2,4b)	3.624813	98.637	241.49	
46	1De&	(2,4c)	3.617483	98.438	241.69	
47	3De&	(2,4c)	3.616432	98.409	241.72	
48	3Po	(2,4c)	3.615916	98.395	241.73	
49	1De	(2,4b)	3.613242	98.322	241.80	
50	1Fo	(2,4a)	3.611516	98.275	241.85	
51	1Po	(2,4a)	3.598290	97.818	242.31	
52	1Se	(2,4b)	3.589542	97.679	242.45	
53	3Se	(2,5a)	3.480992	94.723	245.40	
54	1Po	(2,5b)	3.476543	94.602	245.52	
55	1Se	(2,5a)	3.471338	94.461	245.67	
56	3Po	(2,5a)	3.467998	94.370	245.76	
57	3De	(2,5a)	3.464881	94.285	245.84	
58	1Pe	(2,5a)	3.463413	94.245	-	
59	3Po	(2,5b)	3.461459	94.191	245.94	
60	3Fo	(2,5a)	3.455628	94.033	246.09	
61	1Do	(2,5a)	3.453980	93.988	-	
62	3Pe	(2,5a)	3.452745	93.955	-	
63	1De	(2,5a)	3.452462	93.947	246.18	
64	3De	(2,5b)	3.449932	93.878	246.25	
65	1Fe	(2,5a)	3.447447	93.811	-	
66	3Fe	(2,5a)	3.447143	93.802	-	
67	3Do	(2,5a)	3.446898	93.796	-	
68	3Se	(2,5b)	3.445287	93.752	246.38	

Table 6. (Continued).

Line No	State	Class	B.E. (a.u.)	B.E. (eV)	LS $\xrightarrow{Auger}$ 1s (eV)	LS
69	3Fo	(2,5b)	3.444625	93.734	246.39	
70	1Fo	(2,5b)	3.444193	93.722	246.40	
71	1Po	(2,5a)	3.443576	93.705	246.42	
72	3Fo&	(2,5c)	3.442501	93.676	246.45	
73	1Fo&	(2,5c)	3.442470	93.675	246.45	
74	1De	(2,5c)	3.440595	93.624	246.50	
75	3De	(2,5c)	3.440095	93.610	246.52	
76	3Po	(2,5c)	3.439407	93.592	246.54	
77	1De	(2,5b)	3.437535	93.541	246.59	
78	1Fo	(2,5a)	3.436673	93.517	246.61	
79	1Po	(2,5c)	3.430187	93.341	246.79	
80	1Se	(2,5b)	3.425384	93.210	246.92	

9.3 The Auger spectrum of $B^{3+} + H_2$: I. Production of Li-like B^{2+} and He-like B^{3+} doubly excited states

Li-like doubly excited states of C^{3+}, O^{5+} and F^{6+} ions have been studied extensively over the past 15 years in ion-atom collision experiments utilizing the J. R. Macdonald laboratory (JRML) tandem ion beam facilities, as their formation is the signature of fundamental processes, such as (RTE) [29, 31, 32, 95], Non-resonant Transfer and Excitation (NTE) [95, 178], electron-electron Excitation (eeE) [33, 164] and electron-nucleus Excitation (enE) [164, 179].

As mentioned previously, boron ions were excluded from these studies due to the very low boron beam currents, inadequate for use with tandem slit spectrometers. In this chapter, first measurements using the Boron beams available from the JRML tandem accelerator, on Li-like B^{2+} and He-like B^{3+} doubly excited states are reported. Boron ion spectroscopy was systematically studied by Rødbro *et al.* using B^{2+} in collisions with carbon foils. [172] Their results (including also results from other theoretical and experimental works) are utilized here for peak identification.

In the cases of $E_p = 4.11$ MeV and $E_p = 5.71$ MeV projectile kinetic energies the B^{3+} beam was obtained after post-stripping the B^{2+} beam by thin carbon foils. In the case of $E_p = 7.79$ MeV, the B^{3+} beam was obtained directly from the tandem accelerator after gas stripping inside the accelerator terminal. In each occasion the B^{3+} beam was collided with H_2 targets. The data were recorded and normalized in the same way with the 4–8 MeV $B^{4+} + H_2$ spectra. The absolute DDCSs obtained are shown in Fig. 66. The KLL Auger lines of Li-like Boron, clearly seen at the energy region

of 150–170eV, are identified according to Ref. [172], as the $(1s2s^2)^2S$, $(1s2s2p)^4P$, $[1s(2s2p)^3P]^2P_-$, $[1s(2s2p)^1P]^2P_+$ and $(1s2p^2)^2D$ states. The aforementioned peaks were fitted with Gaussian distributions, and the FWHM obtained was identified as the overall uncertainty in their energy determination. The $(1s2p^2)^2D$ line, given at an Auger energy of 166.5 eV by Rødbro *et al.* [172], was used for the accurate energy calibration of the whole spectrum. In Table 7, the new measurements of the Auger electron energies are presented along with the data and calculations of the previous references. [172] Note that the uncertainty in the energy larger than the instrumental energy resolution, since the peak fitting was applied in the projectile rest frame. The instrumental energy resolution, defined in the laboratory frame, is about 2 times smaller according to Eq. 11.

Even though the lines are well resolved (except the $(1s2s^2)^2S$) the accuracy achieved in this work was not better than the accuracy reported by Rødbro *et al.* [172] The reason is that the spectrograph was designed for zero-degree highly efficient measurements and therefore does not utilize small slits that are adequate for very high resolution spectroscopic studies. In addition, the achieved deceleration with the focusing lens, which was implemented in the spectrograph to compensate for the use of large apertures, remained in small values (F=4), therefore not allowing for very high resolution measurements.

It is worth mentioning here, that the higher energy uncertainty of the ^4P line compared to the others, is because it is a metastable state. It is not allowed to Auger decay to the ground state according to spin considerations. Therefore it is a long lived state, which mostly decays outside the gas-cell area and therefore the optimized focusing conditions for the electrons originating from inside the gas-cell do not apply in that case, degrading the ^4P peak energy resolution. Actually, this can be a rough test for the existence of any other metastable line in the spectra.

As it will be shown in §9.5, the B^{3+} beam can have a substantial ($\leq 26\%$) $(1s2s)\,^3S$ metastable component. [180] It may also have a smaller ($\leq 8\%$) $(1s2s)\,^1S$ metastable component. Therefore, the production mechanisms of the Li-like doubly excited states involve predominantly the $B^{3+}[(1s^2)\,^1S]$ ground and $B^{3+}[(1s2s)\,^3S]$ metastable states, respectively. In Fig. 67, the dominant mechanisms (involving the $B^{3+}[(1s^2)\,^1S]$ ground state and both the $B^{3+}[(1s2s)\,^3S]$ and $B^{3+}[(1s2s)\,^1S]$ metastable states) are illustrated along with the intermediate states binding energies and the electron spin configurations.

From Fig. 67, it is clearly seen that the ground state $(1s^2)\,^1S$ can populate the doubly excited states via the RTE and NTE mechanisms. In NTE, a target electron is captured into some projectile state, while at the same time, a projectile electron is excited via an electron–target-nucleus interaction. [95] In chapter 10, the RTE process is examined in detail. The metastable $(1s2s)\,^3S$ and $(1s2s)\,^1S$ states primarily populate the Li-like doubly excited states via direct electron transfer (T) or NTE mechanisms. The electron transfer mechanism refers to the capture of the target electron to the $2p$ projectile state. It should be mentioned here that RTE is energetically not allowed for the excitation of $(1s2s)\,^3S$ or $(1s2s)\,^1S$ to the $(1s2l2l')\,^{(2S+1)}L$ states, as can be clearly seen in Fig. 67.

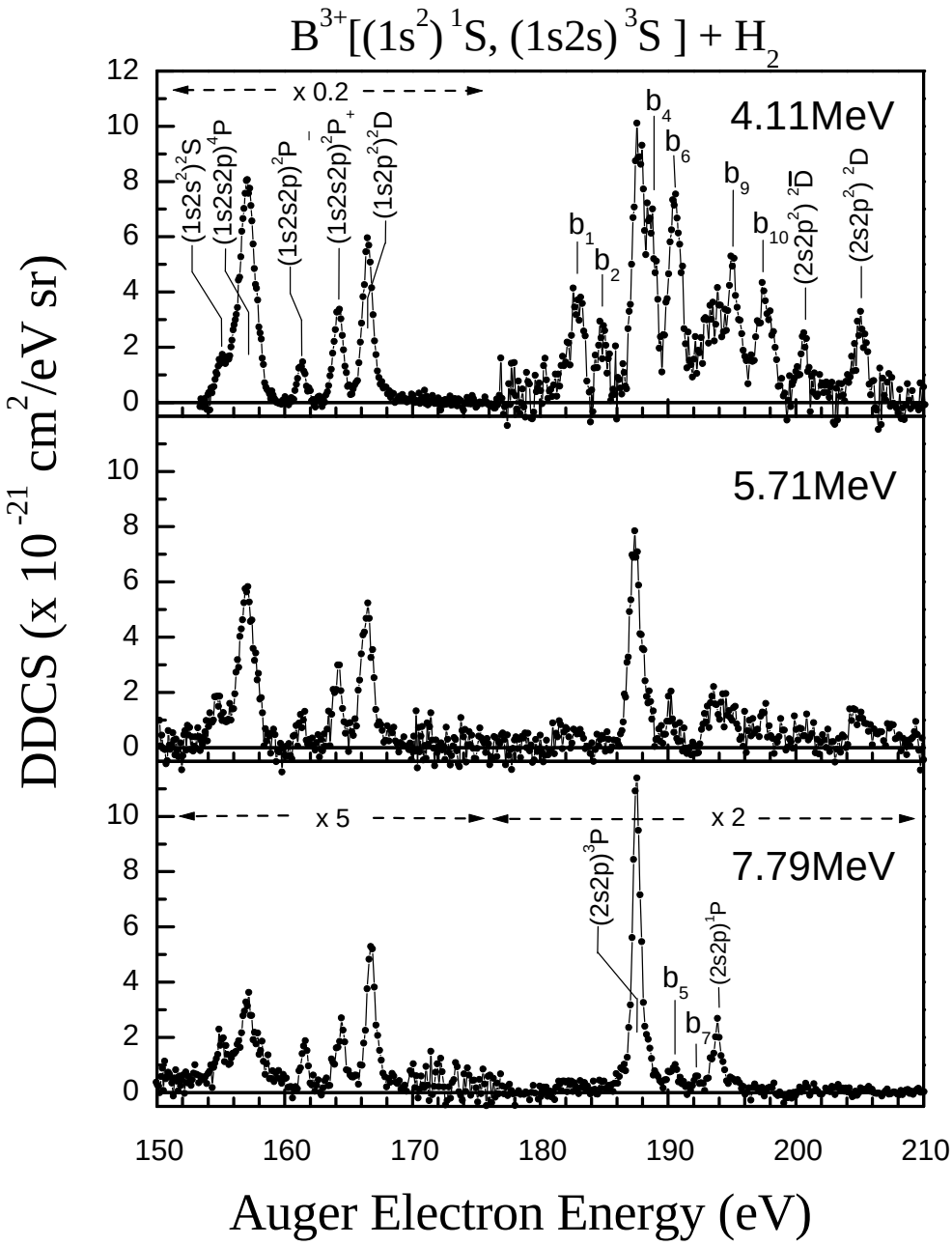

Figure 66: Absolute Auger electron DDCS spectra for the collisions of 4–8 MeV B^{3+} with H_2 targets. The production of ^2S, ^4P, $^2P_-$, $^2P_+$ and ^2D Li-like doubly excited states is dominant at low projectile energies. The He-like ^3P and ^1P doubly excited states along with the $(2s2p^2)^2\bar{D}$ and $(2s2p^2)^2D$ triply excited states are also observed. The 4.11 MeV and 5.71 MeV B^{3+} beams were obtained after post-stripping the B^{2+} beam by thin carbon foils. The 7.79 MeV B^{3+} beam was obtained directly from the tandem accelerator after gas stripping. In all cases, the B^{3+} beam has a significant $B^{3+}[(1s2s)^3S]$ metastable component (see Fig. 71). Data were scaled at occasion for improved presentation purposes as indicated. Laboratory frame data are available in Appendix J.

The production of $^2P_-$, $^2P_+$ and ^2D Li-like doubly excited states is seen to be dominant at low projectile energies but it drops rapidly with increasing collision energy. Considering that the RTE resonance for these states is about 3.2 MeV, it is evident that these states are primarily populated from the ground state via RTE. The ^4P state *cannot* be produced from the ground state, due to spin conservation considerations (see also §9.5). This can be clearly seen in Fig. 69, where the mixed and ground beam boron spectra are shown in comparison. Therefore the ^4P is mainly produced from the $(1s2s)\,^3S$ metastable state. The rapid drop of the ^4P cross section when the beam energy is increased, can be explained if the primary formation mechanism is electron transfer (to the 2p state), whose cross section is well known to decrease rapidly with increasing projectile energy. [181] Moreover, from the same Fig. 69, it is evident that the ^2S state is also produced primarily from the $(1s2s)\,^3S$ metastable state by transfer to the 2s state.

As seen in Fig. 66, the recorded spectrum extends up to electron energies of 210 eV. The formation of the He-like doubly excited $(2s2p)\,^3P$ state is well pronounced for all the projectiles energies. Its slow drop with energy is characteristic of the $1s \rightarrow 2p$ excitation which indicates that this state is primarily formed from the metastable $(1s2s)\,^3S$ part of the beam. This is also evident in Fig. 68, where spectra of the ground $B^{3+}[(1s^2)^1S]$ and the mixed $B^{3+}[(1s^2)^1S, (1s2s)^3S]$ beam states colliding with H_2 targets are compared. The absence of the $(2s2p)\,^3P$ state in the spectra of the ground state boron beam strongly indicates that the formation of the $(2s2p)\,^3P$ state proceeds from the $(1s2s)\,^3S$ metastable part of the beam.

The formation of $(2s2p)^1P$ He-like doubly excited state is also clear in the spectrum of 7.79MeV in Fig. 66. This state has been observed in the past by Lee *et al.* [31] in collisions of 33.25 MeV F^{7+} ions with H_2 and He targets. This state can be formed from the metastable $B^{3+}[(1s2s)^3S]$ state by $1s \rightarrow 2p$ excitation with simultaneous spin exchange. It may also be formed by direct $1s \rightarrow 2p$ excitation from the $B^{3+}[(1s2s)^1S]$ state. However, the fraction of this metastable state at the beam energy of E_p = 7.9 MeV is negligible ($\leq$ 2% as this beam was obtained directly from the tandem accelerator after gas stripping, see §9.5 and Fig. 71 (right)).

The $(2s2p^2)^2D$ triply excited state which Auger decays to the $(1s2s)^3S$ state or both to the $(1s2s)^1S$ and $(1s2p)^3P$ states (noted then as $(2s2p^2)^2\bar{D}$), is also visible in Fig. 66. Details on the production and decay of the triply excited states are given in §9.4.

The rest of the lines, which have not been definitely identified yet, were labeled as b_i (i = 1..10). Their energies along with the uncertainties, obtained after Gaussian fits, are given in Table 7. However, an attempt to identify these lines was made by running the COWAN code [176, 177] which primarily resulted in the electron state configuration along with the LS coupling, the binding energy of the state and the Auger rates. The results show that most of these states are three electron states decaying to the ground state $B^{3+}(1s^2)$. In Table 13, the calculated intermediate states, their absolute binding energies, the Auger electron energies resulting from their decay to the ground state, and the Auger rates are given. Only states with Auger rates higher

than 10^{11} s^{-1} were considered for the presented states. In Table 14, the proposed intermediate states corresponding to the b_i measured states are given, along with the most probable production mechanisms. According to Fig. 68, peaks which are present in both the ground and mixed beam spectrum, were considered to be formed primarily from the ground state beam.

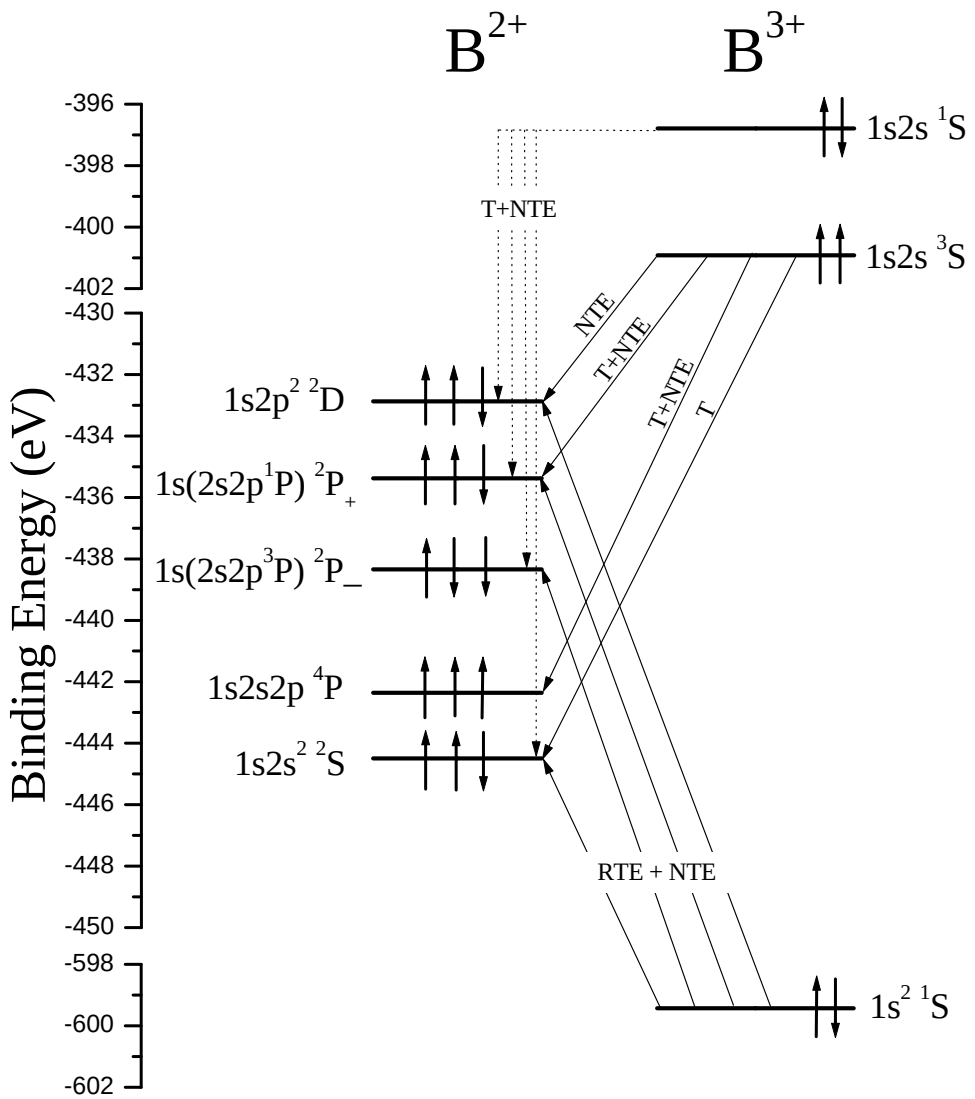

Figure 67: Energy level diagram with the dominant production mechanisms for the $(1s2l2l')^{(2S+1)}L$ doubly excited states formed in collisions of $B^{3+}[(1s^2)\,^1S]$ and $B^{3+}[(1s2s)\,^3S]$ ions with H_2 targets. Schematic spin alignment is also shown. A more complete energy level diagram is given in Appendix I.

Table 7: KLL Auger electron energies of B^{2+} excited states produced in collisions of $B^{3+}[(1s^2)^1S, (1s2s)^3S] + H_2$. An attempt to assign transitions to the observed lines b_i utilizing COWAN code calculations can be found in Table 14.

Intermediate State	Final State	Theory	Experiment (Other)	Experiment (This work)
$(1s2s^2)^2S$	$(1s^2)^1S$	154.93^a	155.1 ± 0.3^a	155.1 ± 1.1
$(1s2s2p)^4P$	$(1s^2)^1S$	157.07^a	157.0 ± 0.3^a	157.0 ± 1.5
$[1s(2s2p)^3P]^2P_-$	$(1s^2)^1S$	161.08^a	161.4 ± 0.3^a	161.3 ± 0.8
$[1s(2s2p)^1P]^2P_+$	$(1s^2)^1S$	164.05^a	164.3 ± 0.5^a	164.2 ± 0.9
$(1s2p^2)^2D$	$(1s^2)^1S$	166.55^a	166.5 ± 0.5^a	$166.5^\dagger$
b_1				182.7 ± 1.6
b_2				184.8 ± 0.9
$(2s2p)^3P$	$(1s)^2S$	187.52^b		187.5 ± 0.8
b_3				188.0 ± 0.5^e
b_4				188.8 ± 0.6^e
b_5				190.4 ± 1.1
b_6				190.8 ± 0.6^e
b_7				192.2 ± 0.8
$(2s2p)^1P$	$(1s)^2S$	194.20^b		193.8 ± 0.8
b_8				193.9 ± 0.5^e
b_9				195.3 ± 0.9^e
b_{10}				197.9 ± 1.8
$(2s2p^2)^2\bar{D}$	$(1s2p)^3P^*$	200.64^c		200.6 ± 1.1
		201.89^d		
$(2s2p^2)^2D$	$(1s2s)^3S$	205.03^c		205.0 ± 1.1
		205.23^d		

† Used for energy calibration
* It may also decay to $(1s2s)^1S$ final state with almost the same energy (200.79 eV)
^{a} From Rødbro *et al.* [172]
^{b} From Lipsky *et al.* [171]
^{c} From Safronova *et al.* [173]
^{d} From L. B. Madsen (private communications)
^{e} Energies measured from the spectrum of ground state $B^{3+}[(1s^2)^1S]$ beam, shown in Fig. 68

9.4 The Auger spectrum of $B^{3+} + H_2$: II. Production of Li-like B^{2+} triply excited states

The first experimental investigation of triply excited states was published in 1975 by Bruch *et al.* [182] They used 300-keV Li^+ ions passing through 8–$\mu g/cm^2$–thick carbon foils to populate highly excited states in neutral lithium and measured the Auger electrons emitted from the decay of the autoionizing states formed. Rødbro *et al.* [172], using projectile electron spectroscopy at 6.4°, reported on the observation of triply excited states also in Li-like Be. Although there were not many publications for a period of 20 years, recently, a new interest in this subject arose and a number of investigations on photon-induced triply excited states in atomic lithium were reported (see Ref. [183] and references therein). The photoexcitation techique allows for the population of $^2P^o$ states, starting form the $(1s^22s)^2S^e$ Li ground state, due to dipole transition selection rules. States with $^2D^e$ symmetry can be further reached only by combining a synchrotron and a laser to induce a two-photon transition. [183–185] Only one such measurement has been reported to date. [184] Thus, lithium triply excited states of different symmetry and parity can be studied using the photoexcitation method. It would be interesting though to study also the isoelectronic sequence of the Li-like triply excited states. To my knowledge, such a study does not exist in the literature.

The use of ion–atom collisions is an alternative and very efficient way to study the Li-like triply excited states. Ion–atom collisions have the advantage over the photoexcitation method of allowing the production of most of the $^{(2S+1)}L$ states in an one-step process, as the photoexcitation selection rules do not apply. However, the potential feature of the method is that it allows for the study of the isoelectronic sequence of the Li-like triply excited states. In this dissertation, the production of the $(2s2p^2)^2D$ triply excited state in collisions of 4.11 MeV B^{3+} with H_2 targets is reported. The metastable $(1s2s)^3S$ part of the B^{3+} beam is used to populate the triply excited state.

Pre-excited metastable beams have been used in the past in various electron–ion collisions for the experimental observation of superelastic scattering [186, 187], and the investigation of dielectronic recombination [188, 189]. Here, the collision of a $(1s2s)^3S$ metastable ion with a quasi-free target electron can lead to the capture of the electron into an excited state $nl\,(n \geq 2)$, while a $1s$ projectile electron can be excited into an $n'l'\,(n' \geq 2)$ state, producing a double vacancy in the K-shell, i.e., a hollow ion. An experimental signature of the production of triply excited ionic projectile states is the detection of the electrons resulting from the Auger decay of such a triply excited state. The process can be written schematically as:

$$e^- + (1s2s)^3S \longrightarrow (2snln'l')^{2S+1}L_J \longrightarrow e^-_A + (1s2s)^3S$$

which is referred to as resonance elastic electron scattering or dielectronic excitation plus Auger decay in the case of free electrons and RTE in the case of quasi-free electrons.

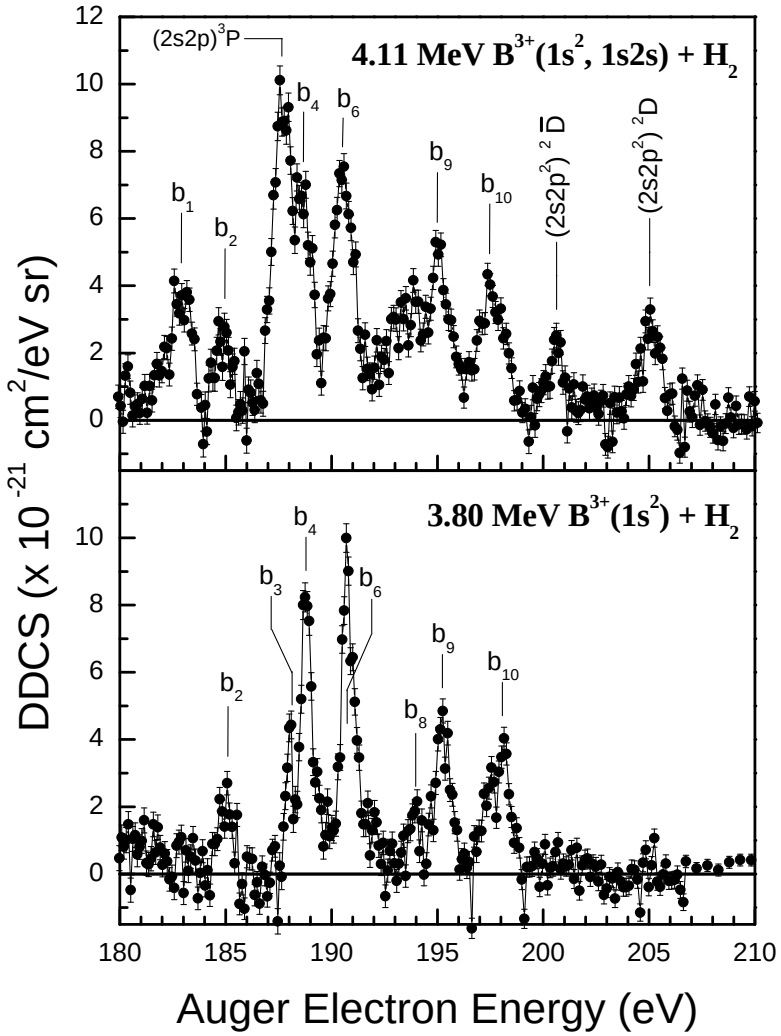

Figure 68: Experimental data for collisions of 3.80 MeV B^{3+} ground state $(1s^2)^1S$ projectiles (*bottom*) and 4.11 MeV B^{3+} mixed state $[(1s^2)^1S, (1s2s)^3S]$ (*top*) with H_2 targets. The 4.11 MeV B^{3+} mixed state data are the same as shown in Fig. 66. The formation of the triply excited states can be seen in the energy region between 200 and 210 eV. The two peaks at 200.6 eV and 205.0 eV are attributed to the formation of the $(2s2p^2)^2D$ state, which Auger decays to the $(1s2s)^3S$ state, or to the $(1s2s)^1S$ and the $(1s2p)^3P$ states, and then is denoted as $(2s2p^2)^2\bar{D}$. The Auger lines of the top spectrum are seen to be broader due to the increased uncertainty of the projectile energy due to energy straggling in the post-stripper foil. In the bottom spectrum, the accelerator gas stripper was used (see §9.5).

The 4.11 MeV B^{3+} mixed beam was obtained by post-stripping a primary B^{2+} beam by thin carbon foils, thus also producing a considerable ($\simeq$ 26%, see Fig. 71) amount of $(1s2s)^3S$ metastable component in the He-like boron beam. This beam

was collided with H_2 targets, leading to the production of the Li-like triply excited states. The same approximately energy B^{3+} beam was obtained also directly from the tandem accelerator by gas-stripping, as it was discovered that the B^{3+} beam had very little metastable fraction ($\simeq 1\%$, see Fig. 71), when it was produced by gas-stripping inside the tandem accelerator at energies close to 4 MeV. [190] A triply excited state formation directly from the ground state is either not permitted in collisions with H_2 targets (i.e. production of ^4P states), or is very improbable, since it involves a three step production mechanism. The electron energy spectrum was measured with both beam types. The absolute DDCS spectra are plotted for comparison in Fig. 68 in the projectile rest frame. The small collision energy difference is not considered important to affect the spectra structure.

It is clearly seen that the collision with the metastable component of the beam gives rise to two peaks in the energy region between 200 and 210 eV. Safronova's calculations [173] on the binding energies of the triply excited states, along with the Auger decay energies to the $(1s2s)^1S$, $(1s2s)^3S$, $(1s2p)^1P$ and $(1s2p)^3P$ states, were reproduced in the form shown in Table 8. Moreover, in Table 9, the Auger decay energies of the triply excited states to the aforementioned $(1s2l)^{(1S+1)}L$ states, which have autoionization rates higher than 10^{13} s^{-1} are given, for the easier identification of the experimental lines. Auger rates smaller than 10^{13} s^{-1} are not expected to contribute significantly to the electron spectrum. In addition, in Table 10, the binding energies of the $(1s2l)^{2S+1}L$ states, as calculated by Safronova *et al.* [173], are also given.

Table 8: Binding energies of boron Li-like triply excited states and Auger decay electron energies to the Helium-like B^{3+} $(1s2s)^1S$, $(1s2s)^3S$, $(1s2p)^1P$ and $(1s2p)^3P$ states. Calculations from Ref. [173].

Triply Excited State	Binding Energy (eV)	Auger Transition Energy (eV)			
		$(1s2s)^3S$	$(1s2s)^1S$	$(1s2p)^3P$	$(1s2p)^1P$
$(2s^22p)^2P$	201.29	199.75	195.51	195.36	192.74
$(2s2p^2)^4P$	200.67	200.37	196.13	195.98	193.36
$(2s2p^2)^2D$	196.01	205.03	200.79	200.64	198.02
$(2p^3)^4S$	193.48	207.55	203.31	203.16	200.54
$(2s2p^2)^2S$	192.24	208.80	204.56	204.41	201.79
$(2s2p^2)^2P$	192.00	209.04	204.80	204.64	202.03
$(2p^3)^2D$	191.33	209.71	205.47	205.32	202.70
$(2p^3)^2P$	187.31	213.73	209.49	209.34	206.72

Table 9: Auger electron energies of boron Li-like triply excited states de-exciting to the Helium-like B^{3+} $(1s2s)^1S$, $(1s2s)^3S$, $(1s2p)^1P$ and $(1s2p)^3P$ arranged in increasing order. Only decays with autoionization rates higher than 10^{13} s^{-1} are presented. Calculations from Ref. [173]. In bold are the observed line energies.

Triply Excited State	Final State	Auger Energy (eV)
$(2s^22p)^2P$	$(1s2p)^1P$	192.74
$(2s^22p)^2P$	$(1s2p)^3P$	195.36
$(2s^22p)^2P$	$(1s2s)^1S$	195.51
$(2s2p^2)^4P$	$(1s2p)^3P$	195.98
$(2s^22p)^2P$	$(1s2s)^3S$	199.75
$(2s2p^2)^2D$	$(1s2s)^3P$	**200.64**
$(2s2p^2)^2D$	$(1s2s)^1S$	**200.79**
$(2s2p^2)^2P$	$(1s2p)^1P$	202.02
$(2p^3)^2D$	$(1s2p)^1P$	202.70
$(2s2p^2)^2S$	$(1s2p)^3P$	204.41
$(2s2p^2)^2S$	$(1s2s)^1S$	204.56
$(2s2p^2)^2P$	$(1s2p)^3P$	204.64
$(2s2p^2)^2D$	$(1s2p)^3S$	**205.03**
$(2p^3)^2D$	$(1s2p)^3P$	205.32
$(2p^3)^2P$	$(1s2p)^1P$	206.72
$(2s2p^2)^2S$	$(1s2s)^3S$	208.80
$(2s2p^2)^2P$	$(1s2s)^3S$	209.04
$(2p^3)^2P$	$(1s2p)^3P$	209.34
$(2p^3)^2P$	$(1s2s)^1S$	209.49
$(2p^3)^2D$	$(1s2s)^3S$	209.71
$(2p^3)^2P$	$(1s2s)^3S$	213.73

From Table 9, it is clearly seen that, the experimentally identified peak at the energy of 205.0 ± 1.1 eV, can be attributed to the formation of the $(2s2p^2)^2D$ state which de-excites to the initial metastable $(1s2s)^3S$ state (elastic scattering). The primary mechanism for this process is RTE, as it may be concluded from Fig. 66, where the cross section of the state is seen to drop rapidly with the beam energy. Another candidate for this observed line, as seen in Table 9, would be the $(2p^3)^2D$ Auger decaying to the $(1s2p)^3P$ state. However, the formation of the $(2p^3)^2D$ triply excited state from

the metastable part of the beam requires at least a two step process, contrary to the $(2s2p^2)^2D$ state which can be formed in a one-step process (i.e., RTE). Therefore, it is not expected to contribute significantly to the production of the observed Auger peak.

The other experimentally identified peak at the energy of 200.6 ± 1.1 eV, can be attributed, according to Table 9, to the formation of the $(2s2p^2)^2D$ state which de-excites either to the $(1s2s)^1S$ or to the $(1s2p)^3P$ states, respectively. The experimental energy resolution was not adequate to resolve these two lines. The observed Auger line was labeled $(2s2p^2)^2\bar{D}$, following similar notation in the literature. [26]

Finally, it is interesting to note that the Auger lines of the ground state beam are seen to be narrower in Fig. 68 than the lines of the mixed beam. In the later case, a foil post-stripper was used inducing an uncertainty of the projectile energy due to energy straggling in the post-stripping foil. [49, 50]

Table 10: Binding energies of the He-like $B^{3+}[(1s2l)^{(2S+1)}L]$ states. Calculations from Ref. [173].

State	Binding Energy (eV)
$(1s2s)^3S$	401.03
$(1s2s)^1S$	396.79
$(1s2p)^3P$	396.64
$(1s2p)^1P$	394.02

9.5 The Auger spectrum of $B^{3+} + H_2$: III. Determination of B^{3+} beam metastable fraction

When negative ions are post-stripped inside the tandem Van de Graaff accelerator (either on gas or foil), then, in general, the production of two-electron ion beams results in a non-negligible metastable beam fraction. Fractions as high as 30% have been reported in the past for F^{7+} beams. [191] Metastable beams are long-lived states since they cannot de-excite to the ground state due to dipole transition selection rules. Metastable fractions in general depend on a number of parameters such as the density of the stripping gas or the thickness of the stripping foil, the atomic number of the stripper element and the energy of the ion beam when stripped. The quantitative information on the metastable beam fraction is indispensable for the absolute cross-section determination of any process specifically involving transitions from the metastable state.

The signature of the presence of the $(1s2s)^3S$ metastable component in the ion beam, is the formation, after collision with the target, of excited states that cannot be populated using the $(1s^2)^1S$ ground state beam. This case is illustrated in Fig. 69 (top). The B^{3+} beam was obtained after post-stripping the B^{2+} on thin carbon foils. The formation of the $(1s2s2p)\,^4P$ state in collisions of 4.11 MeV $B^{3+} + H_2$, de-exciting via Auger decay to the ground state $1s^2$, can be primarily attributed to the process of electron transfer to the 2p state of the metastable beam state $(1s2s)\,^3S$. An NTE process may also contribute to the formation of the $(1s2s2p)\,^4P$ state, as already mentioned in §9.3 (Fig. 67). The ground state clearly cannot populate the ^4P state, at least for two electron targets such as H_2. Indeed, a transfer and excitation (TE) process will not populate it due to spin conservation considerations, while a transfer of both target electrons to 2s and 2p states with a simultaneous loss of the 1s projectile electron (T^2L) is also excluded, as the H_2 target electrons are in a singlet spin state and therefore do not have the required spin triplet. Consequently, the presence of the $(1s2s2p)\,^4P$ line in the spectra in Fig. 69 (top) is strong evidence that the B^{3+} ion beam, produced by post-stripping the B^{2+} beam by thin carbon foils, is a mixture of both ground $(1s^2)\,^1S$ and metastable $(1s2s)\,^3S$ states, respectively.

The most clear example though would be the measurement of the same spectrum using both the ground and the mixed state beam. This case is illustrated in Fig. 69. The same energy region DDCS was recorded in collisions of 4.11 MeV $B^{3+}[(1s^2)^1S,\ (1s2s)^3S] + H_2$ (mixed state) and of 3.80 MeV $B^{3+}[(1s^2)^1S] + H_2$ (ground state). Data were normalized as described in §9.2. The mixed state beam was obtained by post-stripping the primary B^{2+} beam using thin carbon foils, while the ground state $B^{3+}[(1s^2)^1S]$ beam was obtained directly from the tandem accelerator by gas-stripping. The absence of the ^4P state in the gas-stripped B^{3+} beam spectrum is strong evidence that this type of stripping process produces little (depending on the stripping energy) if any ions in the metastable $B^{3+}[(1s2s)^3S]$ state.[29] The presence of the ^4P state in the mixed state beam spectrum must therefore arise from a significant metastable $B^{3+}[(1s2s)^3S]$ beam component.[30]

This is explained by recent results [180], summarized in Fig. 71 (left), where it is seen that at low beam energies (i.e. 4 MeV) the stripping process results in a negligible amount of metastable beam fraction when gas is used, contrary to stripping in a thin foil, where the $B^{3+}[(1s2s)^3S]$ metastable beam fraction seems to be relatively constant ($\simeq 26\%$) and independent of the beam energy. However, for sufficiently high stripping energies (> 5 MeV) the two stripping processes result in the same fraction ($\simeq 26\%$).

[29] The difference of the beam energy in the compared spectra of Fig. 69 is negligibly small, to account for the differences in the spectra.

[30] This measurement triggered interest in systematically studying the production of the metastable $B^{3+}[(1s2s)^3S]$ beam fraction as a function of the energy and the stripper in use (gas or foil).Unfortunately, at the time, I had to fulfill my military obligations in the Greek Airforce and missed the chance to follow up this observation with more measurements. These were undertaken by KSU graduate student M. Zamkov as a part of his Ph.D. thesis under the supervision of Prof. P. Richard.

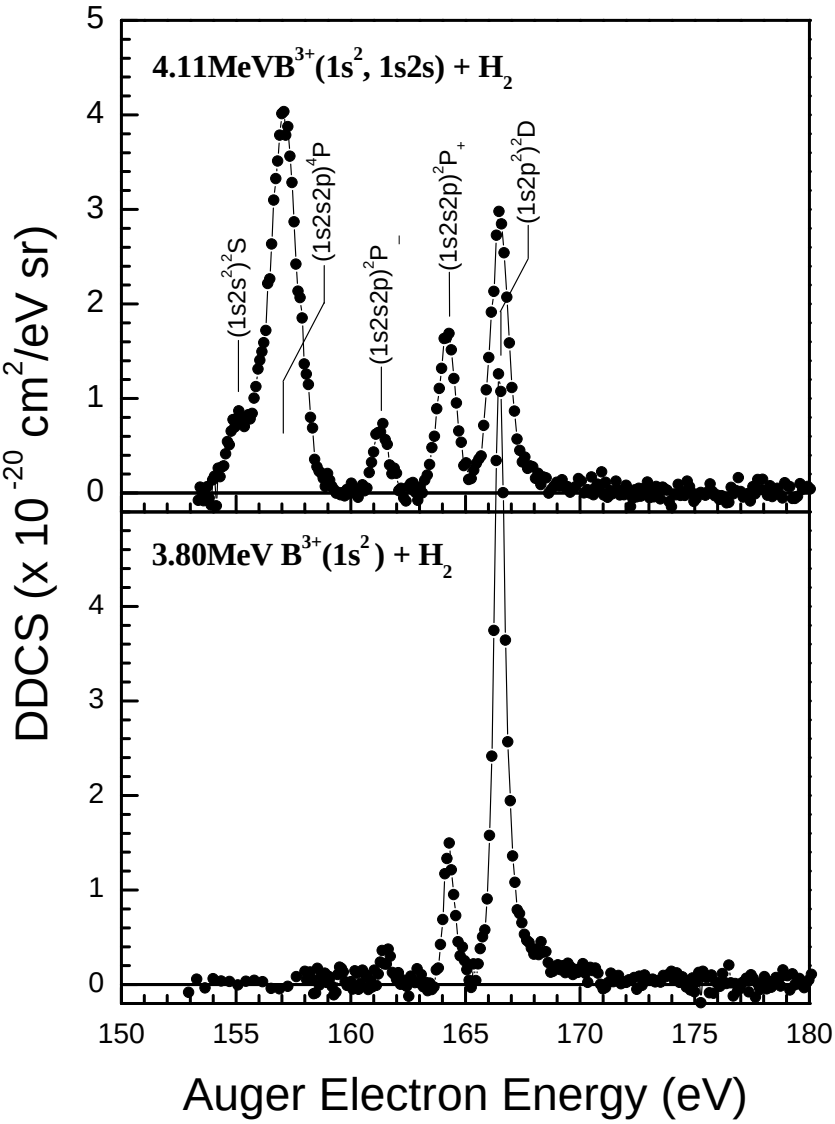

Figure 69: [*Top*] Formation of the $(1s2s2p)^4P$ state in collisions of 4.11 MeV $B^{3+} + H_2$ indicating the existence of a significant metastable $B^{3+}[(1s2s)^3S]$ beam component. The B^{3+} beam was obtained by post-stripping the B^{2+} by carbon foils, as can also be inferred by the slightly broader lines due to energy straggling of the projectile in the post stripper foil. [*Bottom*] The absence of the $(1s2s2p)^4P$ state in collisions of 3.80 MeV $B^{3+} + H_2$ is clearly observed, indicating that the beam is predominantly in the ground state. In this case the B^{3+} beam was obtained directly from the tandem accelerator using the terminal gas-stripper (no post-stripping).

The determination of the $B^{3+}[(1s2s)^3S$ metastable beam fraction is based on the ra-

tio of the electron yield of the $(1s2p^2)^2D$ and $(1s2s2p)^4P$ doubly excited states. Indeed, as mentioned already in §9.3, the formation of $(1s2s2p)^4P$ state is possible only from the $B^{3+}[(1s2s)^3S]$ metastable state via direct electron transfer or NTE, respectively. The $(1s2p^2)^2D$ state on the other hand, can be formed both from the $B^{3+}[(1s^2)^1S]$ ground state via RTE or NTE and the metastable state via NTE. However, the NTE components are expected to be much smaller than the RTE, especially for projectile energies near the RTE peak resonance or higher. Actually, it has been reported by Lee *et al.* [31] that in collisions of 0.25–2 MeV/u F^{7+} with H_2 and He targets, the formation of $(1s2p^2)^2D$ state due to NTE components was negligible for projectile energies close to or higher than the RTE peak resonance. Therefore, NTE contributions can be neglected for high enough projectile energies. As a result, the ratio of the electron yields (SDCSs) of the ^4P state to the sum of ^4P and ^2D states determines the metastable fraction of the beam. Further information on the finer details of the experimental method and the physics of the stripping processes either by gas or by foil targets, can be found in [180].

In addition, the observation of the $(1s2s)^3S$ metastable component indicates the possible existence of the $(1s2s)^1S$ metastable component. However, the ^1S component cannot populate either the ^4P state, due to spin conservation considerations, or the ^2D state, as the RTE process is not energetically allowed and the NTE is negligible as in the ground state case. Furthermore, it could be completely quenched by the magnetic field of the various analysing magnets used along the beamline. [192, 193] Therefore the ^1S metastable component can be neglected in the method used for determining the $B^{3+}[(1s2s)^3S]$ metastable fraction. Furthermore, assuming statistically populated $(1s2s)^3S$ and $(1s2s)^1S$ metastable states, during the stripping process, a population ratio $^3S/^1S = 3$ is established.

In order to estimate the amount of the metastable beam components at the target area, the lifetimes of both the $(1s2s)^3S$ and $(1s2s)^1S$ metastable states were estimated by extrapolating well known lifetime values from the C, O, N and F ions. [194,195] The results are presented in Fig. 70, while in Table 11, the data for the lifetimes are given. Including the extrapolated values for the lifetimes τ into the exponential decay law, $N = N_0 e^{-t/\tau}$, and calculating the flight time t from the ion beam velocity and the ion traveling distance[31], the metastable beam fractions at the target area were estimated. The results are shown in Fig. 71.

As it is clearly seen from Table 11 the $(1s2s)^3S$ has a very large lifetime and practically does not decay during the flight time to the target area. The $(1s2s)^3S$ state, however, has a lifetime comparable to the flight time, and can be reduced by 8 % or 42 %, depending on the flight time. Thus, for foil post-stripped beam (after the LINAC analysing magnet) and a foil stripped beam (inside the tandem accelerator),

[31]The stripping process occurred either in the tandem accelerator gas-stripper of after the LINAC analysing magnet (see Fig. 10). The corresponding distances for the above cases are 43 m and 9 m, respectively. Two more post stripping positions are located between the two 45° magnets and before the LINAC analysing magnet. The corresponding distances for these cases, which were not utilized in the experiments described in this thesis, are 30 m and 12 m, respectively.

constant fractions of 7.9% and 5%, respectively, are established, as shown in Fig. 71 (right).

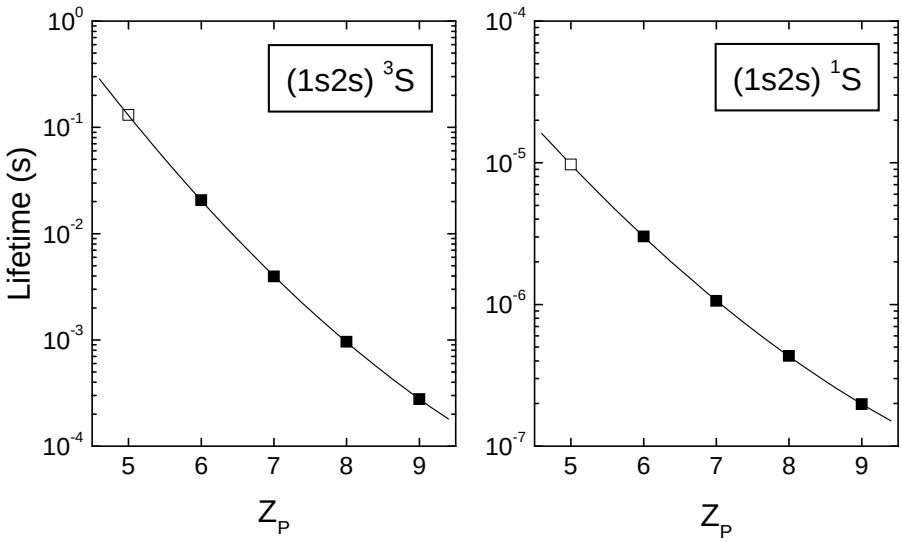

Figure 70: Lifetimes of the $(1s2s)^3S$ and $(1s2s)^1S$ metastable states as a function of the atomic number Z_p. Data from Ref. [194, 195]. Open squares correspond to the extrapolated values.

Table 11: Lifetimes of the $(1s2s)^3S$ and $(1s2s)^1S$ metastable states for different atomic numbers Z_p. Data from Ref. [194, 195] and Fig. 70.

State	Z_p	Lifetime (s)
$(1s2s)^3S$	5	1.31×10^{-1} ⋆
	6	2.06×10^{-2}
	7	3.95×10^{-3}
	8	9.62×10^{-4}
	9	2.77×10^{-4}
$(1s2s)^1S$	5	9.73×10^{-6} ⋆
	6	3.02×10^{-6}
	7	1.06×10^{-6}
	8	4.33×10^{-7}
	9	1.98×10^{-7}

⋆ Extrapolated values.

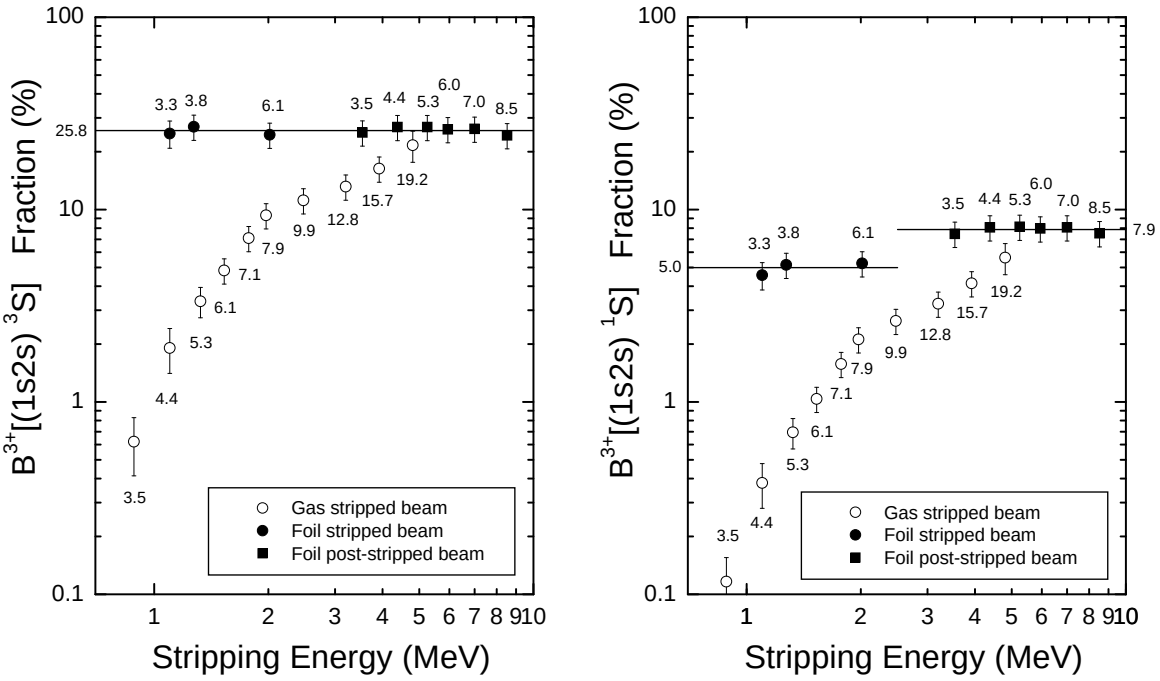

Figure 71: [*Left*] Experimentally determined $B^{3+}[(1s2s)^3S]$ metastable beam fraction as a function of the projectile stripping energy. Adapted from Refs. [180, 196]. [*Right*] Estimated $B^{3+}[(1s2s)^1S]$ metastable beam fraction, at the target area, as a function of the projectile stripping energy. Both figures include data for gas and foil stripping, as also for foil post-stripping processes. Small numbers near data points correspond to the actual collision energy.

9.6 The Auger spectrum of $B^{2+} + H_2$

B^{2+} ions produced by gas-stripping inside the tandem accelerator were collided with H_2 targets at projectile energies between 4–8 MeV, in order to obtain a supplement to B^{3+} and B^{4+} ion studies of the B^{2+} Auger spectrum. Absolute DDCS spectra were obtained similarly as in the cases of B^{3+} and B^{4+} ions, and are shown in Fig. 72. The formation of the Li-like doubly excited states of $[1s2s^2]^2S$, $[1s2s2p]^4P$, $[1s(2s2p)^3P]^2P_-$, $[1s(2s2p)^1P]^2P_+$ and $[1s2p^2]^2D$, already identified in the B^{3+} spectra previously, are seen to be prominent. The production mechanisms of these states though, are different than the ones examined in the case of the B^{3+} projectiles, and are briefly described below. The B^{2+} beam is found only in the $1s^2\,2s$ ground state, thus simplifying the excited state production mechanisms contrary to the B^{3+} beam, which has a significant metastable part. The Li-like states produced in collisions of O^{5+} and F^{6+} with H_2 and He targets, with the exception of the $(1s2p^2)^2D$, which was not identified, were also

studied by D. H. Lee in his 1990 Ph. D. thesis. [96]

The electron–nucleus excitation (enE) [164, 179], in which the projectile $1s$ electron is excited to the $2p$ state due to the interaction with the target nucleus is the most prominent mechanism which can lead to the formation of the ^2S, $^2P_-$ and $^2P_+$ states. However, it may *not* produce the ^4P due to spin conservation. The ^2S, $^2P_-$ and $^2P_+$ states also can be produced by the electron-electron excitation (eeE) [33, 164] where the $1s \rightarrow 2p$ excitation is succeeded by an interaction with the target electron rather than the target nucleus. The enE mechanism is known to contribute significantly over the entire projectile energy region, while the eeE mechanism becomes important at rather high projectile energies, above the energy threshold of the excitation. [33, 164] The projectile energy thresholds E_0^{enE} and E_0^{eeE} for enE and eeE processes, respectively, are given by T.J.M. Zouros [164] as:

$$E_0^{enE} = \frac{M_p}{M_t}\Delta E \tag{138}$$

$$E_0^{eeE} = \frac{M_p}{m}\Delta E \tag{139}$$

where M_p and M_t are the projectile and target nuclei masses, m is the electron mass and ΔE is the excitation energy for the transition $1s^2\,2s \rightarrow 1s2s2p$. Considering the transition $1s^2\,2s \rightarrow (1s2s2p)^2P_+$, which has the highest threshold ($\Delta E = 204.5eV$), the projectile energy thresholds results in: $E_0^{enE} = 2.25$ keV and $E_0^{eeE} = 4.13$ MeV. Therefore, for the range of projectile energies seen in Fig. 72, eeE mechanisms are also important in the formation of the Li-like B^{3+} doubly excited states. It is important to notice that Compton profile width considerations of the target electron allow for the eeE process to contribute at projectile energies even lower than the energy threshold $E_0^{eeE} = 4.13MeV$. [33] Finally, the eeE mechanism including also electron exchange may contribute to the production of the ^4P state, as well as for projectile energies exceeding the excitation threshold. [33, 197]

A two step process which can give rise to all the ^2S, $^2P_-$, $^2P_+$ and ^4P states is the transfer and loss (TL) mechanism, which consists of the transfer of one target electron to the $2p$ projectile state and a simultaneous loss (i.e. ionization) of one of the $1s$ projectile electrons. The TL process is known to contribute mostly at low projectile energies due to the rapid decrease of the capture cross section with increasing projectile energy. [181, 198].

The formation of the $[1s2p^2]^2D$ doubly excited state can be attributed primarily to the mechanisms of double excitation ($1s \rightarrow 2p$ and $2s \rightarrow 2p$), RTE or NTE with simultaneous $2s$ electron loss. The most likely seems to be the $2s$ electron loss with RTE in the region of 4 MeV collision energy.

In the B^{2+} spectrum of Fig. 72, the Be-like triply excited states $(1s2s2p^2)^3D$ and $(1s2s2p^2)^1D$, formed primarily by RTE as well as NTE and de-exciting via Auger decay to the $B^{2+}[(1s^2 2s)^2S]$ ground state, are also observed. The spectroscopic determination was based on their previous identification in collisions of O^{5+} + He [26] and F^{6+} + H_2/He [28, 31]. Their measured energies are given in Table 12.

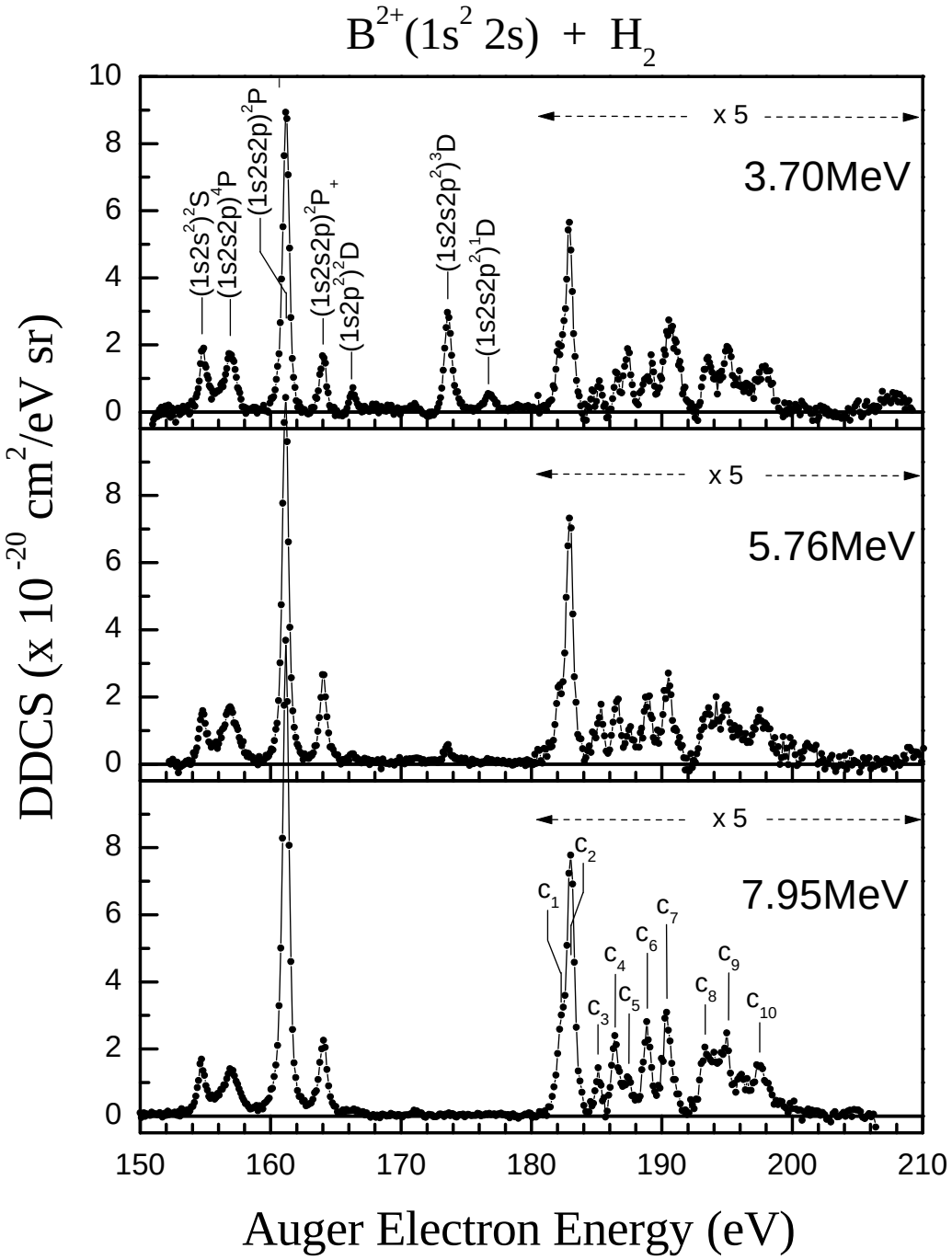

Figure 72: Absolute Auger electron DDCS spectra for the collisions of 4–8 MeV $B^{2+}(1s^2 2s)$ with H_2 targets. The production of ^2S, ^4P, $^2P_-$, $^2P_+$ and ^2D Li-like doubly excited states is prominent. The Be-like doubly excited states $(1s2s2p^2)^3D$ and $(1s2s2p^2)^1D$ are also observed. Data were scaled at occasion for improved presentation purposes as indicated. Laboratory frame data are available in Appendix J.

As in the case of the B^{3+} + H_2 spectrum, the rest of the lines, which have not been explicitly identified yet, were labeled as c_j (j =1..10). Their energies are given in Table 12. COWAN code calculations, the results of which are summarized in Table 13, show that most of these states are three electron states decaying to the ground state $B^{3+}(1s^2)$. In Table 14, the proposed intermediate states corresponding to the c_j measured states are given, along with the most probable production mechanisms.

Table 12: Auger electron energies of B^{2+} and B^+ excited states produced in collisions of of $B^{2+}[(1s^2 2s)^2 S]$ + H_2. An attempt to assign transitions for the c_j lines utilizing COWAN code calculations can be found in Table 14.

Intermediate State	Final State	Theory	Experiment (This work)
$(1s2s2p^2)^3D$	$(1s^2 2s)^2 S$	174.09*	173.6 ± 0.7
$(1s2s2p^2)^1D$	$(1s^2 2s)^2 S$		176.8 ± 1.0
c_1			182.6 ± 1.0
c_2			183.0 ± 0.7
c_3			185.1 ± 0.6
c_4			186.5 ± 0.8
c_5			187.4 ± 0.8
c_6			188.9 ± 0.8
c_7			190.4 ± 0.9
c_8			193.6 ± 0.9
c_9			195.6 ± 1.0
c_{10}			197.8 ± 1.3

* From Rødbro *et al.* [172]

Table 13: $B^{3+}[(1s2ln'l')^{(2S+1)}L_J]$ intermediate states Auger decaying to the $B^{3+}(1s^2)$ ground state. The binding energies B.E., the Auger electron energies E_A and the Auger rates A_α were obtained from calculations using the COWAN code. The Auger energies were shifted by 0.73 eV for calibration with the $(1s2p^2)^2D$ line. Only states with Auger rates higher than 10^{11} s^{-1} were considered.

Config.	$(1s2l)^{(2S'+1)}L'$	$^{(2S+1)}L$	J	B.E. (eV)	E_A (eV)	A_α ($\times 10^{12}$/s)
1s2s3s	(^{3}S)	^{2}S	1/2	418.31	181.91	17.0
	(^{1}S)	^{2}S	1/2	414.78	185.43	7.5
1s2s3p	(^{3}S)	^{2}P	1/2	417.57	182.65	0.7
	(^{3}S)	^{2}P	3/2	417.57	182.65	0.7
	(^{1}S)	^{2}P	1/2	413.67	186.55	0.2
	(^{1}S)	^{2}P	3/2	413.66	186.55	0.2
1s2s3d	(^{3}S)	^{2}D	3/2	415.65	184.57	2.1
	(^{3}S)	^{2}D	5/2	415.65	184.57	2.1
	(^{1}S)	^{2}D	3/2	411.50	188.71	9.3
	(^{1}S)	^{2}D	5/2	412.09	188.13	2.0
1s2s4s	(^{3}S)	^{2}S	1/2	410.00	190.21	3.8
	(^{1}S)	^{2}S	1/2	405.93	194.28	2.3
1s2s4p	(^{3}S)	^{2}P	1/2	409.58	190.63	2.9
	(^{3}S)	^{2}P	3/2	409.58	190.63	2.9
	(^{1}S)	^{2}P	1/2	405.12	195.10	9.3
	(^{1}S)	^{2}P	3/2	405.12	195.10	9.3
1s2s4d	(^{3}S)	^{2}D	3/2	409.26	190.96	1.2
	(^{3}S)	^{2}D	5/2	409.26	190.96	1.2
	(^{1}S)	^{2}D	3/2	404.82	195.40	1.5
	(^{1}S)	^{2}D	5/2	404.82	195.40	1.5
1s2s4f	(^{3}S)	^{2}F	5/2	409.27	190.94	0.4
	(^{3}S)	^{2}F	7/2	409.27	190.94	0.4
	(^{1}S)	^{2}F	5/2	404.43	195.78	0.2
	(^{1}S)	^{2}F	7/2	404.43	195.78	0.7

Table 13. (Continued).

Config.	$(1s2l)^{(2S'+1)}L'$	$^{(2S+1)}L$	J	B.E. (eV)	E_A (eV)	A_α ($\times 10^{12}$/s)
1s2p3s	(^{3}P)	^{2}P	1/2	412.31	187.91	13.9
	(^{3}P)	^{2}P	3/2	412.30	187.91	13.9
	(^{1}P)	^{2}P	1/2	411.28	188.93	1.4
	(^{1}P)	^{2}P	3/2	411.28	188.93	1.4
1s2p3p	(^{3}P)	^{2}S	1/2	411.24	188.98	6.3
	(^{1}P)	^{2}S	1/2	408.55	191.67	0.6
	(^{3}P)	^{2}D	3/2	412.09	188.12	2.1
	(^{3}P)	^{2}D	5/2	411.50	188.72	9.4
	(^{1}P)	^{2}D	3/2	409.68	190.53	11.5
	(^{1}P)	^{2}D	5/2	409.68	190.53	11.5
1s2p3d	(^{3}P)	^{2}P	1/2	404.48	195.74	1.6
	(^{3}P)	^{2}P	3/2	404.48	195.73	1.6
	(^{1}P)	^{2}P	1/2	401.90	198.32	0.2
	(^{1}P)	^{2}P	3/2	401.90	198.32	0.2
	(^{3}P)	^{2}F	5/2	404.76	195.45	0.2
	(^{3}P)	^{2}F	7/2	404.76	195.46	0.2
	(^{1}P)	^{2}F	5/2	402.21	198.00	2.4
	(^{1}P)	^{2}F	7/2	402.21	198.00	2.4
1s2p4s	(^{3}P)	^{2}P	1/2	405.68	194.53	1.8
	(^{3}P)	^{2}P	3/2	405.68	194.54	1.8
	(^{1}P)	^{2}P	1/2	403.15	197.07	0.6
	(^{1}P)	^{2}P	3/2	403.15	197.07	0.6
1s2p4p	(^{3}P)	^{2}S	1/2	404.16	196.06	1.9
	(^{1}P)	^{2}S	1/2	402.12	198.10	2.0
	(^{3}P)	^{2}D	3/2	405.04	195.17	9.3
	(^{3}P)	^{2}D	5/2	405.04	195.18	9.2
	(^{1}P)	^{2}D	3/2	402.65	197.56	5.0
	(^{1}P)	^{2}D	5/2	402.65	197.56	5.0
1s2p4f	(^{3}P)	^{2}D	3/2	404.71	195.51	0.2
	(^{3}P)	^{2}D	5/2	404.71	195.51	0.2

Table 14: Tentative assignments of the unidentified b_i and c_j lines observed in the spectra of B^{3+} + H_2 and B^{2+} + H_2 (see Figs. 66 and 72, respectively), according to calculations of the COWAN code. Auger energies resulting from the Auger decay of the states to the $B^{3+}(1s^2)$ ground state (unless otherwise noted) are given along with the most probable production mechanisms. Only intermediate states with Auger rates higher than 10^{11} s^{-1} were considered. Definitely identified states are also given for the sake of completeness.

Intermediate State	E_A Theory (eV)	Assign.	E_A Experiment (eV)	Production Mechanism Initial State	Production Mechanism Transition
$(1s2s^2)^2S$	154.93		155.1 ± 1.1	$(1s2s)^3S$ $1s^22s$	T(2s) E(1s→2s), T(2s)L(1s)
$(1s2s2p)^4P$	157.07		157.0 ± 1.5	$(1s2s)^3S$ $1s^22s$	T(2p) T(2p)L(1s)
$[1s(2s2p)^3P]^2P_-$	161.08		161.3 ± 0.8	$1s^2$ $(1s2s)^3S$ $1s^22s$	T(2s)E(1s→2p), T(2p) E(1s→2p), T(2p)L(1s)
$[1s(2s2p)^1P]^2P_+$	164.05		164.2 ± 0.9	$1s^2$ $(1s2s)^3S$ $1s^22s$	T(2s)E(1s→2p) T(2p) E(1s→2p), T(2p)L(1s)
$(1s2p^2)^2D$	166.55		166.5†	$1s^2$ $1s^22s$	T(2p)E(1s→2p) E(1s→2p)E(2s→2p)
$(1s2s2p^2)^3D$ ††	174.09		173.6 ± 0.7	$1s^22s$	T(2p)E(1s→2p)
$(1s2s2p^2)^1D$ ††			176.8 ± 1.0	$1s^22s$	T(2p)E(1s→2p)
$[(1s2s)^3S\ 3s]^2S_{1/2}$	181.91				
$[(1s2s)^3S\ 3p]^2P_{1/2,3/2}$	182.65	c_1 b_1 ⋆	182.6±1.0 182.7±1.6	$1s^22s$ $(1s2s)^3S$	E(1s→3p) T(3p)

† Used for energy calibration. †† Decays to $B^{2+}(1s^22s)$ ground state
⋆ Mixed B^{3+} beam containing both $(1s2s)^3S$ metastable and $1s^2$ ground states.

Table 14. (Continued).

Intermediate State	E_A Theory (eV)	Assign.		E_A Experiment (eV)	Production Mechanism Initial State	Production Mechanism Transition
$[(1s2s)^3S\ 3d]^2D_{3/2,5/2}$	184.57	b_2		184.8±0.9	$1s^2$	T(2s)E(1s→3d)
$[(1s2s)^1S\ 3s]^2S_{1/2}$	185.43		c_3	185.1±0.6	$1s^22s$	E(1s→3s)
$[(1s2s)^1S\ 3p]^2P_{1/2,3/2}$	186.55		c_4	186.5±0.8	$1s^22s$	E(1s→3p)
$(2s2p)^3P$	187.52			187.5 ± 0.8	$(1s2s)^3S$	E(1s→2p), T(2p)L(1s)
			c_5	187.4 ± 0.8	$1s^22s$	E(1s→2p)L(1s)
$[(1s2p)^3P\ 3s]^2P_{1/2,3/2}$	187.91	b_3		188.0±0.5	$1s^2$	T(2p)E(1s→3s)
$[(1s2p)^3P\ 3p]^2D_{3/2}$	188.12	b_3		188.0±0.5	$1s^2$	T(2p)E(1s→3p)
$[(1s2s)^1S\ 3d]^2D_{5/2}$	188.13	b_3		188.0±0.5	$1s^2$	T(2s)E(1s→3d)
$[(1s2s)^1S\ 3d]^2D_{3/2}$	188.71	b_4		188.8±0.6	$1s^2$	T(2s)E(1s→3d)
			c_6	188.9±0.8	$1s^22s$	E(1s→3d)
$[(1s2p)^3P\ 3p]^2D_{5/2}$	188.72	b_4		188.8±0.6	$1s^2$	T(2p)E(1s→3p)
$[(1s2p)^1P\ 3s]^2P_{1/2,3/2}$	188.93	b_4		188.8±0.6	$1s^2$	T(2p)E(1s→3s)
$[(1s2p)^3P\ 3p]^2S_{1/2}$	188.98	b_4		188.8±0.6	$1s^2$	T(2p)E(1s→3p)
$[(1s2s)^3S\ 4s]^2S_{1/2}$	190.21	b_5		190.4±1.1	$1s^2$	T(2s)E(1s→4s)
		b_5 ⋆			$(1s2s)^3$	T(4s)
			c_7	190.4±0.9	$1s^22s$	E(1s→4s)
$[(1s2p)^1P\ 3p]^2D_{3/2,5/2}$	190.53	b_5		190.4±1.1	$1s^2$	T(2p)E(1s→3p)
$[(1s2s)^3S\ 4p]^2P_{1/2,3/2}$	190.63	b_5		190.4±1.1	$1s^2$	T(2s)E(1s→4p)
		b_5 ⋆			$(1s2s)^3$	T(4p)
			c_7	190.4±0.9	$1s^22s$	E(1s→4p)
$[(1s2s)^3S\ 4f]^2F_{5/2,7/2}$	190.94	b_6		190.8±0.6	$1s^2$	T(2s)E(1s→4f)
$[(1s2s)^3S\ 4d]^2D_{3/2,5/2}$	190.96	b_6		190.8±0.6	$1s^2$	T(2s)E(1s→4d)
$[(1s2p)^1P\ 3p]^2S_{1/2}$	191.67	b_7		192.2±0.8	$1s^2$	T(2p)E(1s→3p)

⋆ Mixed B^{3+} beam containing both $(1s2s)^3S$ metastable and $1s^2$ ground states.

Table 14. (Continued).

Intermediate State	E_A Theory (eV)	Assign.		E_A Experiment (eV)	Production Mechanism Initial State	Production Mechanism Transition
$(2s2p)^1P$	194.20			193.8 ± 0.8	$(1s2s)^3S$	E(1s→2p) + Exch. T(2p)L(1s)
$[(1s2s)^1S\ 4s]^2S_{1/2}$	194.28	b_8		193.9±0.5	$1s^2$	T(2s)E(1s→4s)
$[(1s2p)^3P\ 4s]^2P_{1/2,3/2}$	194.53					
$[(1s2s)^1S\ 4p]^2P_{1/2,3/2}$	195.10	b_9		195.3±0.9	$1s^2$	T(2p)E(1s→4s)
$[(1s2p)^3P\ 4p]^2D_{3/2,5/2}$	195.17	b_9		195.3±0.9	$1s^2$	T(2s)E(1s→4p)
$[(1s2s)^1S\ 4d]^2D_{3/2,5/2}$	195.40	b_9		195.3±0.9	$1s^2$	T(2s)E(1s→4d)
			c_9	195.6±1.0	$1s^2 2s$	E(1s→4d)
$[(1s2p)^3P\ 3d]^2F_{5/2,7/2}$	195.45	b_9		195.3±0.9	$1s^2$	T(2p)E(1s→3d)
$[(1s2p)^3P\ 4f]^2D_{3/2,5/2}$	195.51	b_9		195.3±0.9	$1s^2$	T(2p)E(1s→4f)
$[(1s2p)^3P\ 3d]^2P_{1/2,3/2}$	195.74					
$[(1s2s)^1S\ 4f]^2F_{5/2,7/2}$	195.78		c_9	195.6±1.0	$1s^2 2s$	E(1s→4f)
$[(1s2p)^3P\ 4p]^2S_{1/2}$	196.06					
$[(1s2p)^1P\ 4s]^2P_{1/2,3/2}$	197.07	b_{10}		197.9±1.8	$1s^2$	T(2p)E(1s→4s)
			c_{10}	197.8±1.3	$1s^2 2s$	E(1s→2p)E(2s→4s)
$[(1s2p)^1P\ 4p]^2D_{3/2,5/2}$	197.56	b_{10}		197.9±1.8	$1s^2$	T(2p)E(1s→4p)
			c_{10}	197.8±1.3	$1s^2 2s$	E(1s→2p)E(2s→4p)
$[(1s2p)^1P\ 3d]^2F_{5/2,7/2}$	198.00	b_{10}		197.9±1.8	$1s^2$	T(2p)E(1s→3d)
			c_{10}	197.8±1.3	$1s^2 2s$	E(1s→2p)E(2s→3d)
$[(1s2p)^1P\ 4p]^2S_{1/2}$	198.10	b_{10}		197.9±1.8	$1s^2$	T(2p)E(1s→4p)
			c_{10}	197.8±1.3	$1s^2 2s$	E(1s→2p)E(2s→4p)
$[(1s2p)^1P\ 3d]^2P_{1/2,3/2}$	198.32	b_{10}		197.9±1.8	$1s^2$	T(2p)E(1s→3d)
			c_{10}	197.8±1.3	$1s^2 2s$	E(1s→2p)E(2s→3d)
$(2s2p^2)^2\bar{D}$ ‡	200.64			200.6 ±1.1	$(1s2s)^3S$	T(2p)E(1s→2p)
$(2s2p^2)^2D$ ‡‡	205.03			205.0 ±1.1	$(1s2s)^3S$	T(2p)E(1s→2p)

‡ Decays to $B^{3+}(1s2s\,^3P)$ or $B^{3+}(1s2s\,^1S)$ metastable states
‡‡ Decays to $B^{3+}(1s2s\,^3S)$ metastable state

9.7 Conclusions

First systematic measurements on the B^{q+} (q = 1,2,3) spectroscopy, obtained from collisions of 4–8 MeV $B^{(2-4)+}$ ions with H_2 targets were presented and compared to previous works. The implementation of the high-efficiency hemispherical spectrograph at the JRML facilities, allowed for including boron ions in ion–atom collision studies, as the boron ion beam is one of the lower intensity beams. The high resolution spectra for all the boron charge states were recorded with a mean instrumental energy resolution of 0.2%. The absolute experimental uncertainty of the Auger lines (projectile rest frame) was measured between 0.6–1.1 eV, depending on the statistics and the uncertainty on the projectile energy in case the beam was obtained by foil post-stripping. The observed Auger spectra were presented in absolute DDCSs, utilizing results from the previous study of BEe enhancement factors for partially stripped boron ions.

In the Auger spectrum of 4–8 MeV B^{4+}+ H_2, the KLL, KLM, KLN and KLO lines, resulted in the Auger decay of the formation of the He-like doubly excited states, were clearly observed. The calculated limits of the KLn series [171] were in excellent agreement with the data. The collisions of 4–8 MeV B^{3+}+ H_2 showed the formation of He-like B^{3+} and Li-like B^{2+} doubly excited states as well as the formation of Li-like B^{2+} triply excited states, i.e. hollow boron ions. Even though the identification of all the observed lines has not yet been completed, the results of Li-like doubly excited states from previous works [172] were reproduced well within the experimental uncertainties. Furthermore, the observation of the $(2s2p^2)^2\bar{D}$ and $(2s2p^2)^2D$ lines, the identification of which was based on theoretical calculations [173], showed the formation of Li-like B^{2+} triply excited states in a single ion–atom collision. The Auger spectrum of 4–8 MeV B^{2+}+ H_2 was also recorded showing the dominant formation of the Li-like doubly excited states, observed previously in the B^{3+}+ H_2 spectra. The dominant production mechanisms of the excited states observed in all boron spectra were briefly discussed.

An attempt to identify the rest of the lines in the B^{3+}+ H_2 and B^{2+}+ H_2 spectra, which were not explicitly determined, was made by running the COWAN code. The results have shown that most of these states are three electron states decaying to the ground $B^{3+}(1s^2)$ state. The proposed intermediate states, the Auger electron energies resulting from their decay to the ground state, and the most probable production mechanisms were summarized in Table 14.

Finally, a very important result obtained from the Auger spectrum of collisions between energetic B^{3+} ions and H_2 targets, was the quite accurate determination of the metastable $(1s2s)^3S$ component of the B^{3+} beam. This result is of potential importance for the determination of absolute cross sections in ion–atom collisions involving the B^{3+} ions. In addition, the metastable beam fraction study triggered the interest on the detailed understanding of the production mechanisms in the stripping processes involving gas or foil targets. [180]

10 Resonant transfer and excitation

10.1 Background

Resonance Transfer and Excitation (RTE) [95,162,199] is a correlated two-electron process, mediated by the electron-electron interaction, involving the transfer of a loosely bound target electron to the projectile with the simultaneous excitation of a projectile electron. The RTE process gives rise to excited projectile states which relax either by photon or Auger electron emission. The production of these excited states is investigated experimentally by low resolution coincidence measurements of the emitted x-ray and the projectile charge state [199–212], of the x-ray and a second x-ray [213, 214] or by high resolution Auger electron spectroscopy [22, 24, 26–32, 215–217]. The processes are then termed RTEX, RTEXX and RTEA, respectively.

RTEX is an ion–atom collision process analogous to the Dielectronic Recombination (DR) process, present in free-electron–ion collisions. [218–220] DR is the process of Radiationless Capture (RC) followed by photon emission. Similarly the ion–atom RTEA analogous process in free-electron–ion collisions is RC followed by Auger decay, known as Resonant Elastic Scattering (RES). [220, 221] These processes are schematically illustrated in Fig. 73. To the extent that the active target electron can be considered free, RTE can be seen as the time-reversed Auger effect.

The first RTE observation [200] and its relation to the DR process, which has been identified as a significant energy-loss mechanism in magnetically confined nuclear-fusion plasmas [222], triggered the interest in the RTE studies. DR also plays an important role in the study of astrophysical plasmas [223] and the electron cooling of heavy ion beams in storage rings [224]. In the early 80's DR cross section measurements have proven to be a formidable task since either crossed-beam or merged-beam techniques are required. [225–228] The last decade, however, much progress has been achieved in DR measurements by using electron cooling devices in Storage Rings. [229,230] RTE has been shown that it can provide accurate information on DR cross sections for velocities large compared to the target electron velocity, (see Ref. [231] for example). RTE experiments involve mainly gas targets, where the quasi-free target-electron density is many orders of magnitude larger compared to that in electron–ion experiments, thus favoring the ion–atom experiments for DR studies through the RTE measurements. In addition, RTE has been proven a fundamental process in understanding the dynamic role of the electron-electron interactions in ion–atom collisions.

Tanis *et al.* [200] were the first to observe the process of electron capture with simultaneous excitation in ion-atom collisions of 70 MeV S^{13+} + Ar by detecting coincidences between sulfur K x-rays and electron capture events. The process was identified as analogous to DR in electron-ion experiments. Very soon, Tanis *et al.* [199] showed the resonance behavior of the process by performing their previous S^{13+} + Ar experiment at projectile energies varying from 70–160 MeV. The process was termed "Resonant Transfer and Excitation" – RTE by Brandt [162], who calculated RTE cross sections by applying the Impulse Approximation (IA) to relate the RTE to the DR cross section.

In his IA model, the RTE cross section is obtained from the DR cross section after folding in the Compton profile of the target electrons. Sample calculations on the S^{13+} + Ar collision system, utilizing known DR cross sections for S^{13+} [232], were in good qualitative agreement with the measurements. Details of Brandt's IA model are given in §10.2.

Tanis *et al.* [201,204] extended their RTE studies to the collision systems of 100–360 MeV $Ca^{(16-18)+}$ + He, 180–460 MeV $V^{(19-21)+}$ + He and 100–360 MeV $Ca^{(10-12,16-19)+}$ + H_2, using the x-ray–projectile-charge coincidence technique, establishing the existence of the RTE process in ion-atom collisions. Strong resonant behavior with structure, reflecting the narrower He and H_2 Compton profiles compared to Ar, was observed for these collision systems. The measurements were in reasonable agreement with theoretical calculations based on Brandt's IA model and since then, they were often utilized for comparison with improved IA - RTE theoretical models. [231,233–235] As very clearly was pointed out by McLaughlin and Hahn in their paper in Ref. [231], where they compare various theoretical DR cross sections with the experimentally determined by RTE in collisions of Ca^{12+} + H_2, the relationship between DR and RTE was "dramatically" confirmed.

The ion–atom experiments that followed utilized the RTEX method, as also the RTEXX, provided important information on the RTE KLn (n≥1) formation for collision systems involving $Ca^{(16-19)+}$ [205], Ti^{19+} [206], S^{15+} [213,214], F^{6+} [210,213], $Nb^{(28-32)+}$ [208], U^{90+} [209], Mg^{9+} [210], $Fe^{(23-25)+}$ [211] and Kr^{34+} [212] ions in collisions with H_2 targets. RTEX experimental results on total RTE cross sections were quite well reproduced by theoretical IA - DR treatments. [233–236] However, both RTEX and RTEXX are low resolution techniques, only sufficient for resolving K_α and K_β x-rays, but not allowing for detailed experimental information on the population processes of the intermediate LS states.

Swenson *et al.* [26] were the first to use high resolution zero-degree Auger electron measurements to study the formation of $(1s2s2p^2)^3D$ and $(1s2s2p^2)^1D$ states in the collision system of 5–25 MeV O^{5+} + He. Evidence for the population of intermediate states via RTE, in zero-degree Auger electron measurements, had been proposed earlier by Itoh *et al.* [7] for the $(2p^2)^1D$ state formed in collisions of 50–500 keV He^+ + He. The resonant behavior of the $(2p^2)^1D$ state was also illustrated theoretically by Fritsch and Lin [174] in their TE studies using the close-coupling method, which showed a peak structure cross section for the $(2p^2)^1D$ state formed in collisions of the benchmark system of He^+ + H. Ever since, the most stringent tests of any RTE calculation has been supplied by state-selective studies performed using high resolution zero-degree Auger electron spectroscopy. Since the Auger yields are larger compared to the x-ray yields for low-Z projectiles, RTEA studies have been primarily involved with ions from the first row of the periodic table, including He^+ [22,24,27], $C^{3,5+}$ [32,217], O^{5+} [26,30,216] and $F^{(6-8)+}$ [28–31,215], in collisions with He and/or H_2 targets.

All the above RTEA studies were made at 0° with respect to the beam direction, except Ref. [237] which were made at 9.6°. All the x-ray measurements in RTEX experiments reviewed previously, were made at 90° with respect to the beam direction.

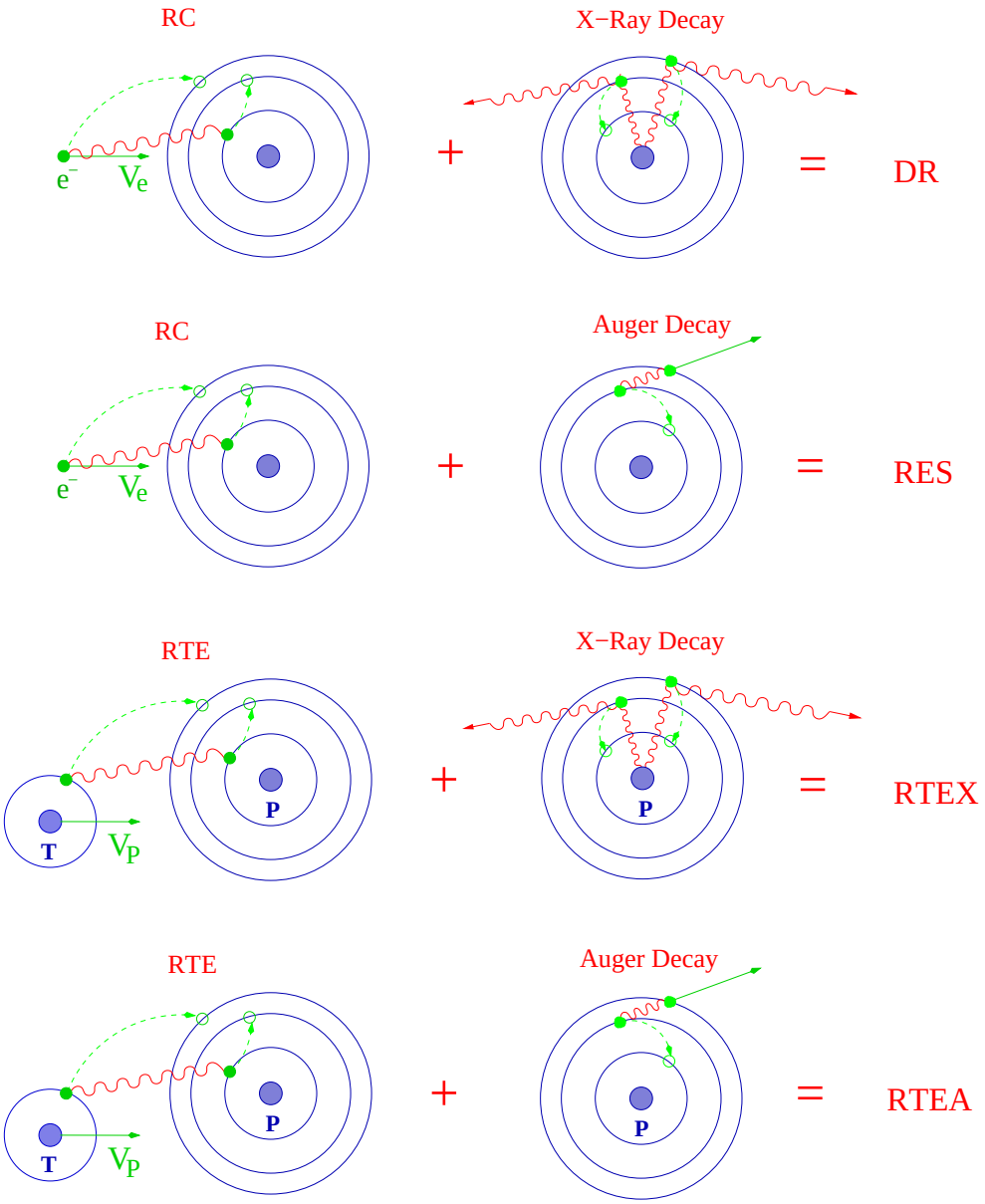

Figure 73: Simplified schematic diagram of the Dielectronic Recombination (DR), Resonant Elastic Scattering (RES), Resonance Transfer and Excitation followed by x-ray emission (RTEX), and Resonance Transfer and Excitation followed by Auger electron emission (RTEA) processes. RTEX and RTEA are the ion-atom processes analogous to the electron-ion DR and RES processes, respectively.

Bhalla [110] was the first to report calculations on the angular distribution of both the Auger electrons and the photons in RTE. His calculations were in very good agreement with the experiment. In his work, it was also indicated that RTE selectively populates the $M_L = 0$ magnetic substates, implying a strong angular dependence of the Auger

electron or x-ray yield. Furthermore, his model also treated the first time considered interference between BEe and RTE electrons, clearly present in DDCS spectra. This interference was seen to be small for ^3D states [95], but almost 50% for the $(2s2p)^1P$ states which, however, are too weak to be observed. [32]

A process which can be also attributed to simultaneous transfer and excitation, and therefore has the same signature as RTE, was reported by Pepmiller *et al.* [178, 238] The process was termed Non-resonant Transfer and Excitation – NTE and it involves an excitation of a projectile electron under the Coulomb influence of the target nucleus, while at the same time a target electron is captured to some projectile excited state under the Coulomb influence of the projectile nucleus.

Clark *et al.* [239] and Tanis *et al.* [202, 203] reported on the distinguishing features between the RTE and NTE peaks in x-ray – ions coincidence measurements, for the collision systems of 15–94 MeV Si^{11+} + He and 15–200 MeV S^{13+} + He, respectively. They showed that NTE occurs at impact energies lower than RTE, but a significant overlap in their cross section peaks exists, implying a unified RTE and NTE treatment rather than an RTE or NTE separate modeling. Such a unified theoretical treatment of simultaneous transfer and excitation was first developed by Feagin *et al.* [240] for collisions of one-electron ions with one-electron targets. Further theoretical [221, 241–244] and experimental [25, 238] studies are also available in literature.

Another non-resonant process similar to NTE termed Uncorrelated Transfer Excitation (UTE) or two electron transfer excitation (2eTE) was first reported by Schulz *et al.* [237] The only difference between NTE and UTE is that the excitation of the ion is mediated by an electron-electron interaction between the excited projectile electron and a second target electron (other than the one which is captured). UTE threshold lies at the projectile electron excitation energy and therefore is expected to occur at the upper edge of the RTE process. UTE has been the object of some controversy [29, 234, 245] and even though it was theoretically investigated [221, 237, 246], its experimental observation has not been well established yet.

In the following, Brandt's [162] and Bhalla's [110] IA - RTE treatments are briefly presented. Theoretical results are compared to the experimental data for the case of $(2p^2)^1D$ RTE state formed in collisions of 4–8 MeV B^{4+} + H_2. It is mentioned at this point, that RTE results using boron ions are reported here for the first time. Boron beams available from tandem Van de Graaff accelerators are too weak to be efficiently utilized with slit spectrometers. However, with the new hemispherical spectrograph the measurements were quite feasible.

10.2 IA - RTEA theoretical description

The basic principles of the impulse approximation have already been described in chapter 8. In the IA, the cross section σ_{RC} for the production of a particular resonance state in electron-ion collisions and the cross section σ_{RTE} for the production of the

same resonance state in ion-atom collisions are related by: [162]

$$\sigma_{RTE} = \sum_j \int_{-\infty}^{+\infty} d^3\mathbf{p}_j \, (\sigma_{RC})_p \, |\psi_j(\mathbf{p}_j)|^2 \tag{140}$$

where the index i is referred to a specific target electron which satisfies the basic IA assumption that the collision velocity is large compared to the velocity of the target electron, i.e. $V_p >> v_{t_i}$. Following Brandt's formulation [162] and using the Eqs. 132, 134 and 135 the RTE cross section is written in atomic units as:

$$\sigma_{RTE} = \sum_j \frac{J_j(Q_j)}{V_p + Q_j} \int_{E_R-\Delta\epsilon/2}^{E_R+\Delta\epsilon/2} d\epsilon \, \sigma_{RC}(\epsilon) = \sum_j \frac{J_j(Q_j)}{V_p + Q_j} \; \Delta\epsilon \, \bar{\sigma}_{RC} \tag{141}$$

where $\Delta\epsilon$ is an energy interval around the energy resonance E_R larger than the resonance width Γ_d of the intermediate state, and $\bar{\sigma}_{RC}$ the energy averaged RC cross section at the resonance. Defining the RC strength as

$$\Omega_{RC} \equiv \Delta\epsilon \, \bar{\sigma}_{RC} \tag{142}$$

and using the expression $J(Q) = \sum_i J_i(Q_i)$, for the Compton profile of target electrons in the same subshell, i.e with the same ionization energy E_I (therefore the same Q_i) the RTE cross section is written as:

$$\sigma_{RTE} = \frac{\Omega_{RC}}{\epsilon_0} \frac{J(Q)}{V_p + Q} \overset{(132)}{=} \frac{\Omega_{RC}}{\epsilon_0} \frac{J(Q)}{\sqrt{2(E_R + E_I)}} \tag{143}$$

Q, $J(Q)$ and V_p are expressed in atomic units, while $\epsilon_0 = 27.2116$ eV. The RC collision strength is given by: [229]

$$\Omega_{RC} = \frac{\pi^2\hbar^3}{2m} \cdot \frac{\omega_d}{\omega_i} \cdot \frac{A_\alpha^{d\to i}}{E_R} = 2.475 \times 10^{-30} \; \frac{\omega_d}{\omega_i} \cdot \frac{A_\alpha^{d\to i}}{E_R} \; (cm^2 \, eV) \tag{144}$$

where $A_\alpha^{d\to i}$ and E_R are the transition rate in s^{-1} and the resonance energy in eV of the time-reversed Auger transition, respectively. The statistical weights for the ground and intermediate states, ω_i and ω_d, respectively, are given by:

$$\omega_i = (2L_i + 1)(2S_i + 1) \; , \quad \omega_d = (2L_d + 1)(2S_d + 1) \tag{145}$$

The RTEA cross section is calculated by assuming that for any fast collision process, the production can be well separated from the decay part. Thus, the RTEA cross section can be related to the RTE cross section as:

$$\sigma_{RTEA} = \sigma_{RTE} \cdot \xi \tag{146}$$

where ξ is the Auger yield defined as the ratio of the Auger transition rate $A_\alpha^{d\to f}$ of the intermediate state $|d>$ to the final state $|f>$, to the sum of all the Auger and

x-ray transition rates $A_\alpha^{d\to f'}$ and $A_r^{d\to f''}$, respectively, from $|d>$ to all the possible final states, $|f'>$ and $|f''>$, i.e:

$$\xi \equiv \frac{A_\alpha^{d\to f}}{\sum_{f'} A_\alpha^{d\to f'} + \sum_{f''} A_r^{d\to f''}} \tag{147}$$

In the same way the Resonant Excitation strength Ω_{RE} is related to Ω_{RC} according to:

$$\Omega_{RE} = \Omega_{RC} \cdot \xi \tag{148}$$

The single differential RTEA cross section is written under the assumption of separation between the production and the decay part as:

$$\frac{d\sigma_{RTEA}(\theta')}{d\Omega'} = \sigma_{RTEA} \cdot \frac{\hat{W}(\theta')}{4\pi} \tag{149}$$

where $\hat{W}(\theta')$ is the angular distribution of the Auger electrons. Primed symbols are referred to the projectile rest frame, consistent with the notation followed in this work.

Special restrictions apply for Auger electron detection at zero-degree laboratory angle observation. [95] When the initial electron beam direction $\theta' = 0°$ is fixed as an axis of quantization, the spherical harmonics expansion of the initial free electron state contains components of only $m_{l_i} = 0$ magnetic quantum number. The same result applies also to the Auger electron detection at $\theta = 0°$ laboratory angle observation (i.e. $\theta' = 180°$). Therefore the RTEA process considering a quasi-free electron e^- and a H-like projectile $Z_p^{(Z_p-1)+}$ can be written as:

$$e^-(l_i, m_{l_i} = 0) \; + \; Z_p^{(Z_p-1)+}(L_i, M_{L_i} = 0) \xrightarrow{RTE} Z_p^{(Z_p-2)+}(L_d, M_{L_d})$$

$$\xrightarrow{0°\,Auger} e_A^-(l_f, m_{l_f} = 0) \; + \; Z_p^{(Z_p-1)+}(L_f, M_{L_f} = 0)$$

Applying the Auger selection rules in the LS-coupling scheme (see appendix H) for the excitation channel, results in the population of only the $M_{L_d} = 0$ substates. The same result is obtained also from the de-excitation channel. Consequently the RTE state is *collisionally aligned* and thus the non-statistical or *state-selective* population of the magnetic substates results in non-isotropic angular distribution of the emitted Auger electrons [30, 95] or photons. Cleff and Mehlhorn [247] described in general the angular distribution of Auger electrons in the functional form of:

$$\hat{W}(\theta') = 1 + \sum_{n=1} A_{2n} \cdot P_{2n}(\cos\theta') \tag{150}$$

where $P_{2n}(\cos\theta')$ are the Legendre polynomials and the coefficients A_{2n} depend on the transition. For example, the angular distribution $\hat{W}(\theta')$ for an $L_d = 2$ to an

$L_f = 0$ Auger transition, which is of interest in this study, is given in the LS-coupling scheme: [248]

$$\begin{aligned}\hat{W}(\theta') &= 1 + \frac{10}{7}\frac{\sigma_{20}+\sigma_{21}-\sigma_{22}}{\sigma_{20}+2\sigma_{21}+2\sigma_{22}}P_2(\cos\theta') + \frac{18}{7}\frac{3\sigma_{20}-4\sigma_{21}+\sigma_{22}}{\sigma_{20}+2\sigma_{21}+2\sigma_{22}}P_4(\cos\theta') \\ &= 1 + \frac{10}{7}P_2(\cos\theta') + \frac{6}{7}P_4(\cos\theta') = 4\pi|Y_{L_d 0}(\theta')|^2\end{aligned}$$

where, $\sigma_{L_d,M_{L_d}}$ are the $|i>\rightarrow|d>$ partial production cross sections, $P_2(\cos\theta')$ and $P_4(\cos\theta')$ are the usual Legendre polynomials, while $Y_{20}(\theta')$ is the usual spherical harmonic. It is interesting to note that, in general, $\hat{W}(\theta')$ depends only on $|M_{L_d}|$. In particular, for the RTE process $\sigma_{21} = \sigma_{22} = 0$, due to the strong alignment of the intermediate states.

Therefore, the single differential RTEA cross section for zero-degree ($\theta' = 180°$) observation of RTE states decaying to $L_f = 0$ can be written according to Eqs. (143), (144), (145), (146), (149) and (151) as:

$$\begin{aligned}\frac{d\sigma_{RTEA}}{d\Omega'}(\theta=0°) &= \frac{\Omega_{RC}}{\epsilon_0}\cdot\frac{J(Q)}{V_p+Q}\cdot\frac{\hat{W}(\theta'=180°)}{4\pi}\cdot\xi \quad (L_i=0, L_f=0) \\ &= \frac{2.475\times10^{-30}}{4\pi\epsilon_0}\cdot\frac{J(Q)}{\sqrt{2(E_R+E_I)}}\cdot\frac{(2L_d+1)^2(2S_d+1)}{(2L_i+1)\ \ (2S_i+1)}\cdot\frac{A_\alpha^{d\rightarrow i}}{E_R}\cdot\xi \quad (151)\end{aligned}$$

Bhalla's approach [110] treats the RTE and BEe DDCS in a unified model allowing for interference between these coherent electrons. His basic result for the $(2p^2)^1D$ intermediate state decaying to $1s$ ground state can be summarized in the following expression:

$$\frac{d^2\sigma(\theta')}{d\Omega' d\epsilon'} = \frac{d^2\sigma_{BEe}(\theta')}{d\Omega' d\epsilon'} + \frac{[C_R(\epsilon',\theta')+C_I(\epsilon',\theta')](\Gamma_d/2\pi)+A(\epsilon',\theta')(\epsilon'-E_R)}{(\epsilon'-E_R)^2+(\Gamma_d/2\pi)^2} \quad (152)$$

where the resonant part $C_R(\epsilon',\theta')$, the symmetric interference $C_I(\epsilon',\theta')$ and the anti-symmetric interference $A(\epsilon',\theta')$ parts are given by:

$$C_R(\epsilon',\theta') \equiv \frac{D}{4\pi}[1+\frac{10}{7}P_2(\cos\theta')+\frac{18}{7}P_4(\cos\theta')] \quad (153)$$

$$C_I(\epsilon',\theta') \equiv -\frac{D}{4\pi}\cdot\frac{Z_p\sin\Delta[(A_\alpha+A_r)/A_\alpha][P_2(\cos\theta')/\sin^2(\theta'/2)]}{(2\epsilon'/\epsilon_0)^{1/2}} \quad (154)$$

$$A(\epsilon',\theta') \equiv -\frac{D}{4\pi^2}\cdot\frac{Z_p\cos\Delta[(A_\alpha+A_r)/A_\alpha][P_2(\cos\theta')/\sin^2(\theta'/2)]}{(2\epsilon'/\epsilon_0)^{1/2}} \quad (155)$$

Note that the $(2p^2)^1D$ RTE state can deexcite to *only* the ground state $1s$ by Auger electron emission and to $(1s2p)^1P$ by x-ray emission, respectively. Therefore, for this case $A_\alpha^{d\rightarrow i} = A_\alpha^{d\rightarrow f} \equiv A_\alpha$ with $|i>=1s$ and $|d>=(2p^2)^1D$. Also $A_r^{d\rightarrow f} \equiv A_r$ with $|f>=(1s2p)^1P$.

The constant D, the difference in the Coulomb phase shifts Δ, the Coulomb phase shifts η_l, the Coulomb phase factor γ [249] and the total energy width of the $|d>$ intermediate state Γ_d, are given by:

$$D(\epsilon', E_p) = \frac{\pi^2\hbar^3}{2m\epsilon'} \cdot \frac{\omega_d}{\omega_g} \cdot \frac{A_\alpha^2}{A_\alpha + A_r} \cdot \frac{J(Q)}{V_p + Q} \tag{156}$$

$$\Delta = 2\eta_2 - 2(mZ_pe^2/\hbar^2k)\ln[\sin(\theta'/2)] - 2\eta_0 \tag{157}$$

$$\eta_l = \arg\Gamma(l+1+i\gamma) = \eta_0 + \sum_{s=1}^{l} \tan^{-1}\left(\frac{\gamma}{s}\right) \tag{158}$$

$$\gamma = \frac{Z_pe^2}{\hbar c}\sqrt{\frac{mc^2}{2\epsilon'}} = Z_p\sqrt{\frac{\epsilon_0}{\epsilon'}} \tag{159}$$

$$\Gamma_d \equiv \hbar(\sum_{f'} A_\alpha^{d\to f'} + \sum_{f''} A_r^{d\to f''}) = \hbar(A_\alpha + A_r) \tag{160}$$

The DDCS for the BEe part can be described by either the ESM model or by a corrected Rutherford model as was presented in chapter 8. The single differential RTEA cross section is obtained by taking an average of the second term in Eq. 152 over an energy interval which is larger than Γ_d. Neglecting the BEe term the SDCS for the RTE becomes:

$$\frac{d\sigma_{RTE}}{d\Omega'}(\theta') = C_R(\epsilon' = E_R, \theta') + C_I(\epsilon' = E_R, \theta') \tag{161}$$

Note that the resonant part $C_R(\epsilon' = E_R, \theta' = 180°)$ is identical to the one given by Eq. 151. This result will be used for comparison with the experimental data on RTE measurements with B^{4+} ions incident on H_2 targets. In addition, it is evident from Eqs. 143, 144, 148 and 156 that:

$$D(\epsilon' = E_R, E_p) = \Omega_{RE} \cdot \frac{J(Q)}{V_p + Q} = \Omega_{RE}\cdot = \frac{J(Q)}{\sqrt{2(E_R + E_I)}} \tag{162}$$

10.3 RTEA with B^{4+} ions

The absolute DDCS spectra obtained in collisions of 4–8 MeV B^{4+} + H_2, already presented from the spectroscopic point of view in chapter 9, are used here for studying the RTE process of populating the B^{3+} He-like doubly excited states. Similar spectra, obtained in collisions of F^{8+} + H_2 and C^{5+} + H_2, were observed in the past by DePaola *et al.* and by Parameswaran *et al.* [32], respectively. The KLL Auger decay lines are the only well resolved lines in the B^{4+} + H_2 spectrum, as seen in Fig. 64, except for the $(2p^2)^1D$ and $(2s2p)^1P$ states.

The explanation for the absence of the $(2s^2)^1S$, $(2s2p)^3P$ and $(2p^2)^1S$ intermediate states which are Auger decaying to the $B^{4+}(1s)$ ground state, was attempted by calculating the relative RTEA intensities of these lines compared to the most prominent $(2p^2)^1D$. The COWAN program was used to obtain the Auger and x-ray rates

of these transitions and calculate, according to Eq. 151, the absolute SDCSs. In Table 15, the Auger energies E_R, the Auger rates A_α, the x-ray rates A_r, the Resonant Excitation strength Ω_{RE} and the angular distribution term for zero-degree observation $\hat{W}(\theta = 0°) = 2L_d + 1$, are given for the KLL intermediate states. The x-ray rates A_r are summed over all the possible radiative decay channels.

It is very interesting to notice in Table 15, that the high Auger rate is not the only important factor for the observation of a transition. A very significant quantity for the RTE process, is the statistical weighting factor $\omega_d = (2L_d + 1)(2S_d + 1)$. Due to this factor, although the $(2s^2)^1S$ and $(2s2p)^3P$ states have Auger rates which are different by an order of magnitude, they have similar Resonant Excitation strengths. Moreover the $2L_d + 1$ term of the statistical weight ω_d turns out to be the most sensitive term in the RTEA SDCS calculation, as it appears to be on the second power in the final RTEA SDCS equation (Eq. 151), due to the multiplication of the Resonant Excitation term with the angular distribution term of the Auger electrons. Thus, as it is seen from Table 15, the relative intensity of the $(2s^2)^1S$ state is predicted lower than the $(2s2p)^3P$ state, even though its Auger rate is higher by an order of magnitude.

Table 15: The Auger energies E_R, the Auger rates A_α, the x-ray rates A_r (referring to the sum of all possible radiative decay channels), the Resonant Excitation strengths Ω_{RE} and the angular distribution term for zero-degree observation $\hat{W}(\theta = 0°)/4\pi$ are given for the KLL intermediate states. The last column is the the ratio of the SDCSs of the states to the SDCS of the $(2p^2)^1D$ state.

Intermediate State	E_R(d $\rightarrow$ 1s) (eV)	A_α ($\times 10^{13}$/s)	A_r ($\times 10^{13}$/s)	Ω_{RE} ($\times 10^{-18}$) (eV·cm^2)	$\hat{W}(\theta = 0°)$ $(2L_d + 1)$	Relative Intensity (%)
$(2s^2)^1S$	186.22	29.88	0.033	1.984	1	4.3
$(2s2p)^3P$	187.52	2.02	0.197	1.093	3	7.2
$(2p^2)^1D$	193.53	28.60	0.120	9.106	5	100
$(2s2p)^1P$	194.20	15.91	0.065	3.029	3	20
$(2p^2)^1S$	200.90	1.10	0.086	0.063	1	0.14

According to the calculations of Table 15, the intensity ratio of the $(2s2p)^1P$ state to the $(2p^2)^1D$ should be 1/5. However, in these calculations the interference between binary encounter and RTE Auger electrons is not included. Parameswaran *et al.* reported on the observation of the doubly excited He-like states in collisions of C^{4+} + H_2. In their theoretical calculations they included also the interference terms which show that only the $(2p^2)^1D$ state is enhanced while the other states are lowered. They

predict a lowering factor of about 2 for the $(2p^2)^1D$ state. Thus, applying their predictions to the boron case, it results in a ratio for the $(2s2p)^1P$ state to the $(2p^2)^1D$ smaller than 1/10.

The experimental data on the RTEA SDCS for the $(2p^2)^1D$ state were obtained from the absolute DDCS spectra recorded in projectile energies of 3.70, 4.09, 5.20, 5.72, 6.50 and 7.90 MeV. The absolute SDCS experimental values were obtained from DDCS spectra after summing over an energy region larger than the base width of the $(2p^2)^1D$ RTE peak. The results are plotted in Fig. 74 as a function of the projectile energy. The error bars shown are the statistical uncertainties. The absolute uncertainty is about 20% (see §7.4). Theoretical calculations, incorporating interference with the BEe, according to Bhalla's model are also shown for comparison to the experimental data. The Auger and x-ray rates A_α and A_r, respectively, for the $(2p^2)^1D$ RTE transition, needed for the theoretical calculations, were obtained by extrapolating known calculated rates for the ions of C^{4+}, N^{5+}, O^{6+} and F^{7+}. [250] The obtained value for the Auger rate was later found to be in agreement with COWAN calculations. In Fig. 75 the quadratic fits, on the theoretical data of the Auger and X-ray rates of the $(2p^2)^1D$ state, utilized for the extrapolation, are plotted.

In order to qualitatively test the agreement between the theory and the experiment, the ratio of the experimental data to the corresponding theoretical values was calculated resulting in an average value of 0.84 ± 0.06. The results are plotted in Fig. 74 (top).

The $B^{3+}(2p^2)^1D$ SDCS experimental data along with the $F^{7+}(2p^2)^1D$ data (see §6.4), were used to obtain the Resonant Excitation strength Ω_{RE} according to Eq. 151. The results are presented in Table 16 including previous Ω_{RE} measurements for the ions of C^{4+}, N^{5+}, O^{6+} and F^{7+}, as also the corresponding Ω_{RE} theoretical calculations. In addition, the resonant energies and the Auger and x-ray rates values of the $(2p^2)^1D$ state for the previous ions are given along with the new extrapolated values for B^{3+}. In Fig. 76 the experimental and theoretical Resonant Excitation strengths Ω_{RE} of the $(2p^2)^1D$ RTE state are plotted as a function of the atomic number Z_p.

From Fig. 74 it is seen that the IA - RTEA calculations, agree with the experimental data within a scaling factor of 0.84 ± 0.06. This fact indicates that the NTE process is indeed negligible in this case, at least for the projectile energies reported here. At lower impact energies NTE is expected to contribute, however, as it was mentioned previously, B^{4+} ions at energies lower than 3.7 MeV were of extremely low intensity (<10pA) to be utilized even with the new highly efficient spectrograph. The extrapolated values for the Auger and x-ray rates are seen to be reasonable, and their incorporation into the IA - RTEA model shows good agreement with the measurement. As mentioned before, Auger rates calculations using the COWAN code are in agreement with the extrapolated value. Furthermore, comparison between IA - RTEA calculations including or not interference with BEe, show that the interference term is much smaller than the resonance term at this detection angle, in agreement to Bhalla's IA - RTEA predictions. [110]

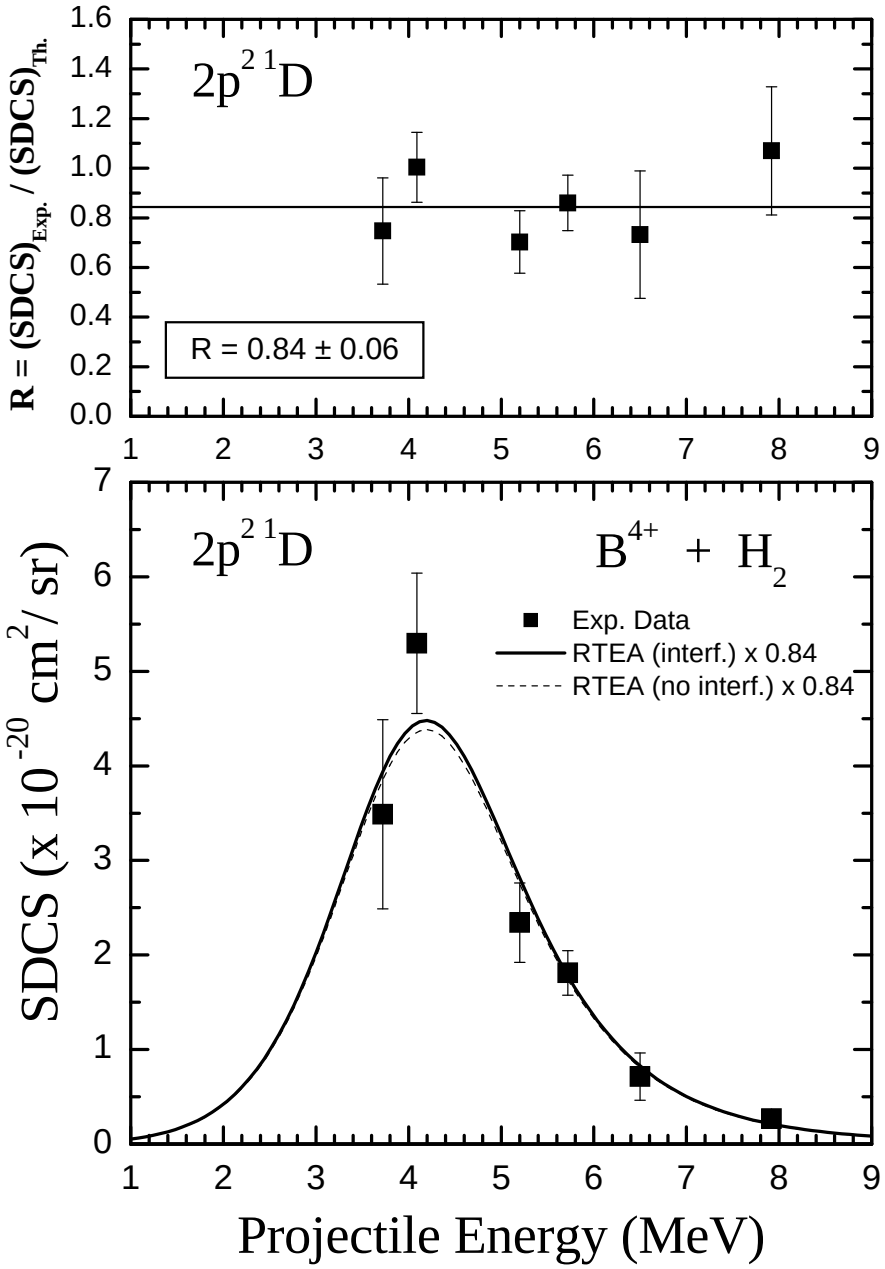

Figure 74: [*Top*] Ratio of the absolute SDCS $(2p^2)^1D$ RTE state experimental data to the corresponding theoretical values as a function of the projectile energy. [*Bottom*]SDCS of the aforementioned $(2p^2)^1D$ RTE state as a function of the projectile energy. Solid line: IA - RTEA calculations including interference with BEe. Dashed line: IA - RTEA calculations without BEe interference. Theory was multiplied by a factor of 0.84 to best fit the data.

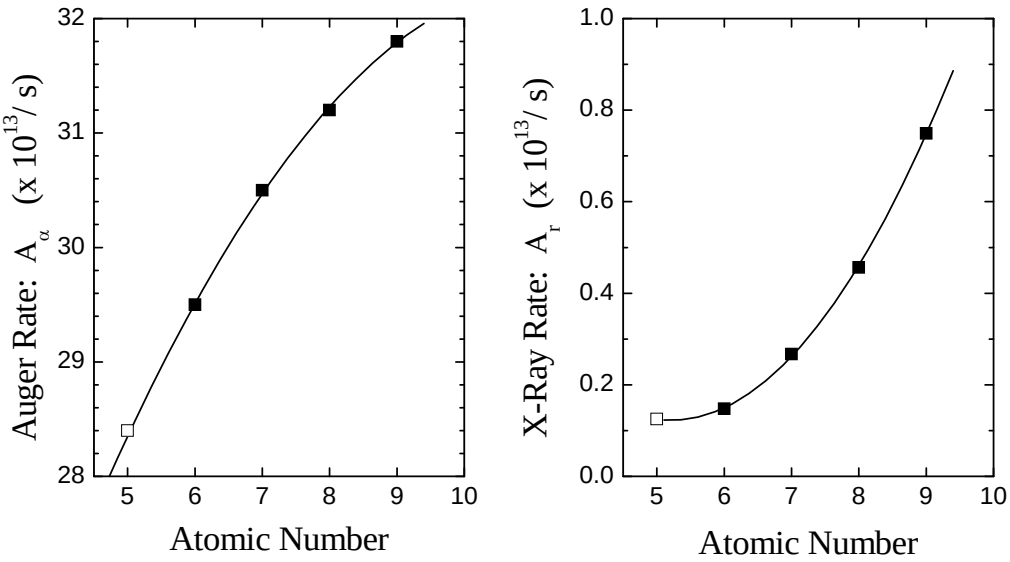

Figure 75: Quadratic fits on the theoretical data of the Auger and X-ray rates A_α and A_r, respectively, of the $(2p^2)^1D$ state of He-like doubly excited ions. Data from Ref. [250] Open squares are the new extrapolated points. COWAN code calculations for the rates of B^{3+} are also in agreement with these values.

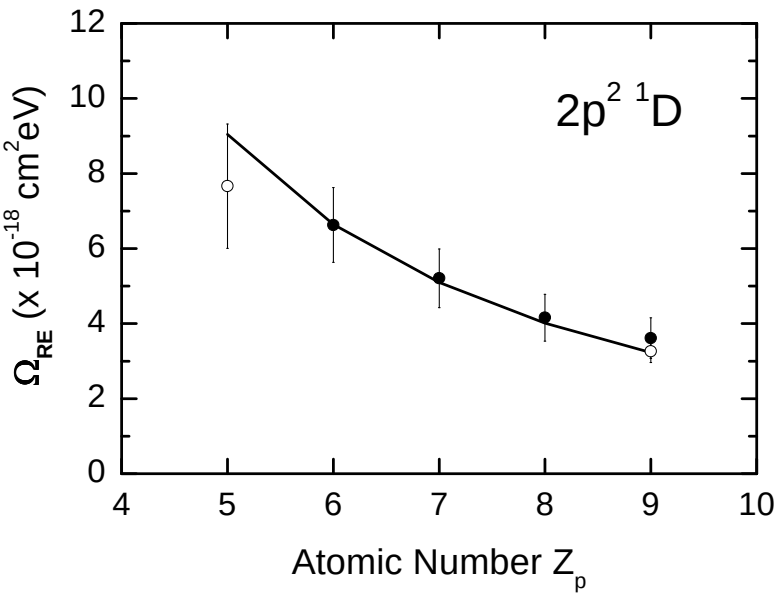

Figure 76: Resonant Excitation strengths Ω_{RE} of the $(2p^2)^1D$ RTE state as a function of the atomic number Z_p. Solid line: Theory; solid circles: From Ref. [251]; open circles: this work.

Table 16: Resonance parameters for the $(2p^2)^1D$ doubly excited state resulting from the collisions of H-like ions with H_2 targets. E_R is the Auger line energy, Z_p is the atomic number, A_α is the Auger decay rate, A_r is the radiative decay rate, ξ is the Auger yield and Ω_{RE} is the resonant excitation strength.

Ion	Z_p	E_R (eV)	A_α ($\times 10^{13}$/s)	A_r ($\times 10^{13}$/s)	ξ	Ω_{RE}(Th.) ($\times 10^{-18}$) (eV·cm^2)	Ω_{RE}(Exp.) ($\times 10^{-18}$) (eV·cm^2) Other work	Ω_{RE}(Exp.) ($\times 10^{-18}$) (eV·cm^2) This work
B^{3+}	5	193.5[a]	28.4⋆	0.125⋆	0.9956	9.041		7.7 ± 1.6
C^{4+}	6	273.3[b]	29.5[b]	0.148[b]	0.9950	6.645	6.6 ± 1.0[c]	
N^{5+}	7	366.9[b]	30.5[b]	0.267[b]	0.9913	5.100	5.2 ± 0.8[c]	
O^{6+}	8	474.2[b]	31.2[b]	0.456[b]	0.9856	4.012	4.2 ± 0.6[c]	
F^{7+}	9	595.0[b]	31.8[b]	0.749[b]	0.9770	3.231	3.6 ± 0.5[c]	3.3 ± 0.3

[a] From Ref. [171], [b] From Ref. [250], [c] From Ref. [251], ⋆ Extrapolated values (also from COWAN code calculations).

As was mentioned before, the spectrograph resolution was not adequate for resolving the KLM and KLN manifolds. However, a total RTEA SDCS was obtained for these states, according to the method applied to the SDCS determination of $(2p^2)^1D$ RTE state. The results are summarized in Fig. 77. Unfortunately, I am not aware of any calculations on Auger and/or x-ray yields for the $2l3l'$ and $2l4l'$ states in order to incorporated them in the IA - RTEA model and compare them with the experimental data. However, assuming the mean energy values 230 and 241 eV of the KLM and KLN Auger lines, respectively, as the resonance energies, IA - RTEA calculations were performed assuming unity Auger yields (i.e. $\xi = 1$) and treating the Auger rates as free parameters. The results are also shown in Fig. 77. It is clearly seen that, the resonance structures, peaked at impact energies higher than the peak energy of the $(2p^2)^1D$ state, strongly indicate the presence of the RTEA process for the states included in the $2l3l'$ and $2l4l'$ manifolds.

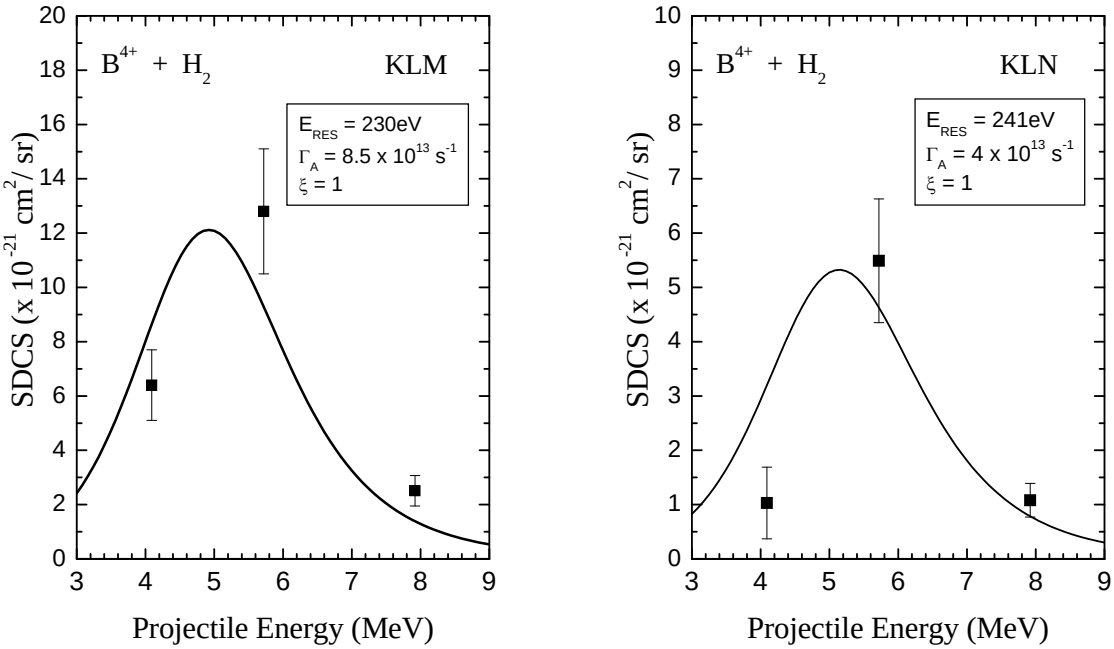

Figure 77: SDCSs of the $2l3l'$ (left) and $2l4l'$ (right) intermediate states formed in collisions of 4–8 MeV $B^{4+} + H_2$ and decaying to the $B^{4+}(1s)$ ground state, as a function of the projectile energy. IA - RTEA calculations assuming unity Auger yields are also plotted (solid lines). The resonance structure strongly indicates the presence of the RTEA process for the states included in the $2l3l'$ and $2l4l'$ manifolds.

10.4 RTEA with B^{3+} ions

The experimental data on the RTEA SDCS for the $(1s2p^2)^2D$ state were obtained from the absolute DDCS spectra recorded in projectile energies of 4.11, 5.71, 7.79 MeV, which were presented in §9.3 (see Fig. 66) from the spectroscopic point of view. The absolute SDCS experimental values were obtained from DDCS spectra after fitting the $(1s2p^2)^2D$ peak with Gaussians and correcting this result for the B^{3+} ground state beam fraction, according to the data presented in §9.5. The results are plotted in Fig. 78 (bottom) as a function of the projectile energy. The error bars shown are the statistical uncertainties. The absolute uncertainty is about 20% (see §7.4). Theoretical RTE calculations, which do not include interference with the binary encounter electrons, are also shown for comparison to the experimental data. The Auger rate A_α for the decay of the ^2D state to the $1s^2$ ground state, needed for the theoretical calculations, was obtained by running the COWAN code. The Auger yield ξ was assumed to be 1, as the rates for the radiative transitions are much smaller than the Auger rates. The overall error from these assumptions is not expected to be higher than 5%.

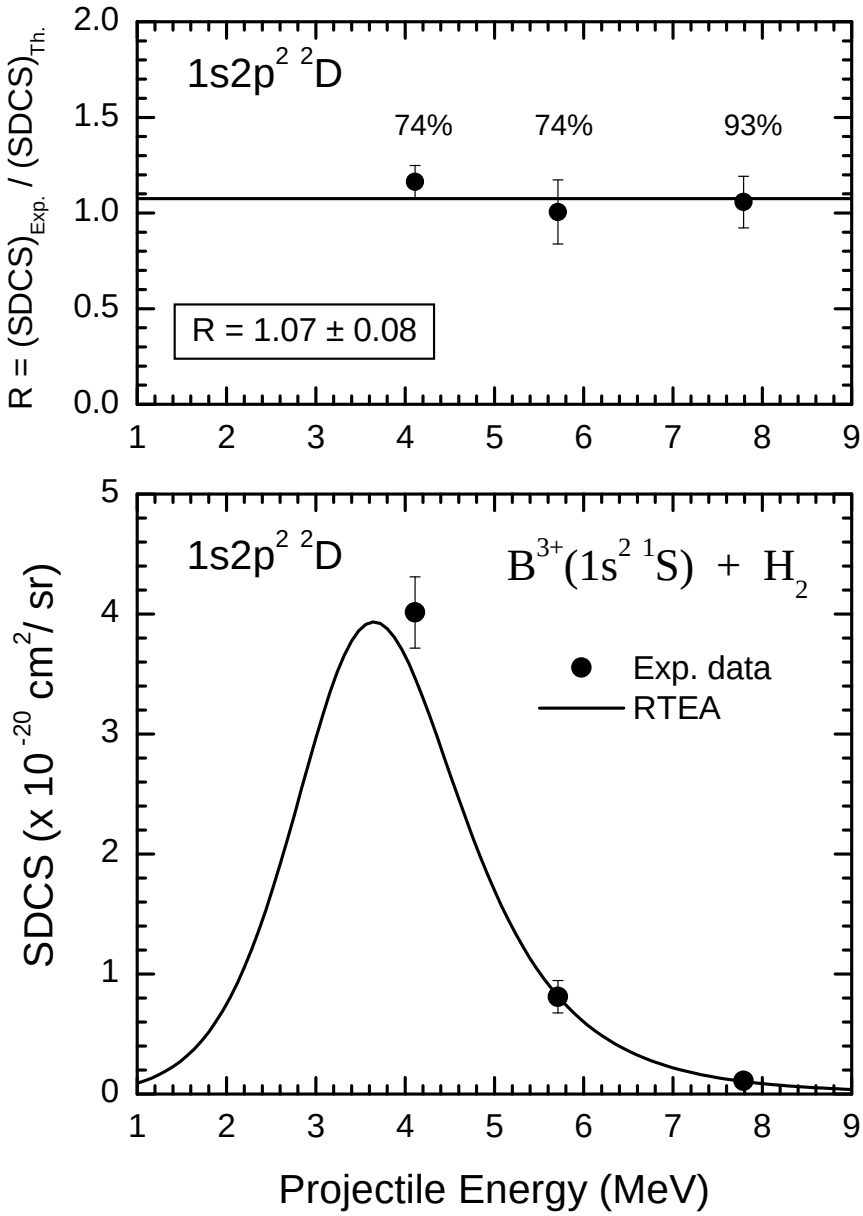

Figure 78: [*Top*] Ratio of the absolute SDCS $(1s2p^2)^1D$ RTE state experimental data to the corresponding theoretical values as a function of the projectile energy. The numbers in percent above the data points are the B^{3+} ground state beam fractions. [*Bottom*] SDCS of the aforementioned $(1s2p^2)^1D$ RTE state as a function of the projectile energy. Solid line: IA - RTEA calculations (assuming $\xi = 1$ and not including BEe interference).

In order to qualitatively test the agreement between the theory and the experiment, the ratio of the experimental data to the corresponding theoretical values was calculated

resulting in an average value of 1.07 ± 0.08. The results are plotted in Fig. 78 (top). The $B^{3+}(1s2p^2)^2D$ SDCS experimental data were used to obtain the Resonant Excitation strength Ω_{RE} according to Eq. 151. The results are presented in Table 17 along with the theoretical predictions.

Resonant Excitation strengths Ω_{RE} of the $(1s2s2p^2)^3D$ and $(1s2s2p^2)^1D$ RTE states, produced in collisions of 3.70 MeV B^{2+} + H_2 are also given in Table 17. The data were obtained after fitting with Gaussians the peaks shown in Fig. 72. In Table 18, all the experimentally obtained RTE SDCS and Ω_{RE} data are summarized.

Table 17: Resonance Excitation strengths Ω_{RE} along with the the corresponding Auger energies E_R and the Auger decay rates A_α. An Auger yield $\xi = 1$ was assumed for all the transitions.

Intermediate State	Final State	E_R (eV)	A_α ($\times 10^{13}$/s)	Ω_{RE}(Th.) ($\times 10^{-18}$) (eV·cm^2)	Ω_{RE}(Exp.) ($\times 10^{-18}$) (eV·cm^2)
$(1s2p^2)^2D$	$1s^2$	166.5±0.7	8.6	6.39	6.8±0.5
$(1s2s2p^2)^3D$	$1s^22s$	173.6±0.7			3.8 ± 0.6
$(1s2s2p^2)^1D$	$1s^22s$	176.8±1.0			1.0 ± 0.4

Table 18: Summary of RTEA SDCS and Ω_{RE} measred in this work.

Ion	Intermediate State	Final State	E_p (MeV)	SDCS ($\times 10^{-20}$ cm^2/sr)	Ω_{RE} ($\times 10^{-18}$ eV·cm^2)
B^{4+}	$(2p^2)^1D$	$1s^2$	3.70	3.5 ± 1.0	
			4.09	5.3 ± 0.7	
			5.20	2.3 ± 0.4	7.7±1.6
			5.72	1.8 ± 0.2	
			6.50	0.7 ± 0.2	
			7.90	0.27 ± 0.06	
	KLM	$1s^2$	4.09	0.64 ± 0.13	
			5.72	1.28 ± 0.23	
			7.92	0.25 ± 0.06	
	KLN	$1s^2$	4.09	0.10 ± 0.06	
			5.72	0.55 ± 0.11	
			7.92	0.11 ± 0.03	
F^{7+}	$(2p^2)^1D$	$1s^2$	21.60	1.09 ± 0.1	3.3±0.3
B^{3+}	$(1s2p^2)^2D$	$1s^2$	4.11	4.0 ± 0.3	
			5.71	0.81 ± 0.13	6.8±0.5
			7.79	0.11 ± 0.01	
B^{2+}	$(1s2s2p^2)^3D$	$1s^22s$	3.70	2.31 ± 0.36	3.8 ± 0.6
B^{2+}	$(1s2s2p^2)^1D$	$1s^22s$	3.70	0.60 ± 0.25	1.0 ± 0.4

10.5 Conclusions

In summary, the experimental data of the Auger spectra of the collision system 4–8 MeV $B^{(3-4)+}$ + H_2 were used to obtain the first measurements on the SDCS of the boron $(2p^2)^1D$ and $(1s2p^2)^2D$ RTE states, which Auger decay to the $1s$ and $1s^2$ ground states, respectively. IA - RTEA calculations, utilizing Auger rate calculations from the COWAN code are seen to be in good agreement with the measurements, especially for the $(1s2p^2)^2D$ state. This indicates the validity of the Impulse Approximation for the RTE process in this collision system. Also, it indicates that the competing NTE process is negligible at the reported impact energies.

IA - RTEA calculations on the $(2p^2)^1D$ RTE state, including also interference with binary encounter electrons showed that for zero-degree measurements the interference effects for this state are very small and could be neglected.

First measurements on the SDCS of the boron KLM and KLN lines, corresponding to the $2l3l'$ and $2l4l'$ manifolds, respectively, which Auger decay to the $1s^2$ ground state, were also obtained from the collision system 4–8 MeV B^{4+} + H_2. The results showed also a resonance structure, similarly as for the $(2p^2)^1D$ state, indicating that the $2l3l'$ and $2l4l'$ states are also RTE states.

Absolute SDCS data for the $F^{7+}[(2p^2)^1D]$ RTE state formed in collisions of 21.6 MeV F^{8+} + H_2, along with the $B^{3+}[(1s2s2p^2)^3D]$ and $B^{3+}[(1s2s2p^2)^1D]$ RTE states formed in collisions of 3.70 MeV B^{2+} + H_2 were also reported. IA - RTEA theory is in very good agreement with the $F^{7+}[(2p^2)^1D]$ data.

Finally, the Resonant Excitation strengths Ω_{RE} were obtained for each of the above cases.

11 Summary and conclusions

The basic purpose of this work was to describe in detail the implementation of a high efficiency hemispherical spectrograph using 2D-PSD into the ZAPS technique, making in this way the method even more applicable as a standard investigation tool, and to utilize its high efficiency to provide new measurements with weak intensity beams and/or low cross section processes. A secondary task was the investigation of the spectrograph focusing and dispersive properties independently of the experimental technique, due to the novel non-conventional *paracentric* entry of the HDA in combination with the 2D-PSD and the focusing/decelerating lens system in use. The results were already discussed in detail at the end of each chapter. Here, the most important conclusions as also some future prospects are summarized as follows:

- Implementation of a novel highly efficient hemispherical spectrograph into ZAPS, utilizing a large hemispherical analyser, a 2D-PSD and a focusing/decelerating lens system. The potential feature of the spectrograph is the huge gain in spectra acquisition time which allows for including low intensity beams in ion-atom collision studies as well as low cross section processes. An efficiency factor of about 300–1000 compared to the KSU tandem PPA slit spectrometer has been established for low intensity beams. It is the first time that a single-stage spectrograph with PSD is successfully utilized in ZAPS. The implementation of the spectrograph is expected to make the ZAPS method even more applicable as a standard investigation tool.

- A novel feature of the hemispherical spectrograph is its *paracentric* entry, i.e., an entry radius R_0 smaller than the conventional central entry at mean radius $\bar{R} \equiv (R_1 + R_2)/2$, where R_1 and R_2 are the inner and outer radii of the analyser, respectively. It has been explicitly shown in this work that the paracentric entry improves the analyser focusing properties.

- The problem of the electron trajectories followed inside the ideal electrostatic potential 1/r of a hemispherical deflector analyser was solved for the first time for the most general case of arbitrary charged particle entry R_0 and arbitrary entry potential $V(R_0) \equiv V_0$. The HDA focusing and dispersive properties were also studied in detail.

- Study of the BEe peak enhancement factors for the collision system $B^{(2-5)+} + H_2$, at impact energies of 0.4–1.2 MeV/u. These results are primarily used for the *in situ* calibration of the electron detection efficiency. The very good agreement of the Impulse Approximation Elastic Scattering Model calculations with the experimental data verified, in addition, the argument that the 0° BEe DDCS production from fast collisions of partially stripped ions with light targets (H_2, He) can be described within the impulse approximation, as the elastic scattering of quasi-free electrons in the static screened field of the projectile nucleus, including also electron exchange effects.

- First systematic measurements on the B^{q+} (q = 1,2,3) spectroscopy, obtained from collisions of 4–8 MeV $B^{(2-4)+}$ ions with H_2 targets. The implementation of the high efficiency hemispherical spectrograph at the JRML facilities, allowed for including boron ions in state-selective ion–atom collision studies, as the boron ion beam is one of the lower intensity beams available by tandem Van de Graff accelerators in general.

- First time observation of the $(2s2p^2)^2\bar{D}$ and $(2s2p^2)^2D$ lines, showed the formation of Li-like B^{2+} triply excited states in a single ion–atom collision.

- Determination of the metastable $(1s2s)^3S$ component of the B^{3+} beam. This result is of potential importance for the determination of absolute cross sections in ion–atom collisions involving the B^{3+} ions. In addition, the metastable beam fraction study, triggered the interest on the detailed understanding of the production mechanisms in the stripping processes involving gas or foil targets. Also, production of almost pure ground state He-like $B^{3+}(1s^2)$ beam was accomplished by gas-stripping in the accelerator at low energies.

- First measurements on the SDCS of the $B^{3+}(2p^2)^1D$ and $B^{3+}(1s2p^2)^1D$ RTE states. IA - RTEA calculations are seen to be in good agreement with the measurements, indicating the validity of the Impulse Approximation for this collisional system at the reported impact energies. Also, the competing NTE process is seen to be negligible.

Future Prospects

- Replacement of the RAE CAMAC-based data acquisition system with a PC-based control system for increased portability of the ZAPS setup.

- Implementation of a fast (1MHz) readout Delay Line Anode detector for eliminating count rate limitations of the data acquisition system due to dead time.

- Possibility of developing a two stage hemispherical spectrograph. The main reason is that, despite the very nice results obtained for KLn Auger electrons, any attempt to measure lower energy projectile LMM Auger electrons was not successful due to the very high background signal, resulting from the cusp electrons hitting inside the spectrograph producing a background, which dominated the spectra, especially when operated in deceleration mode.

- Study of basic ion-atom collision processes such as RTE, NTE, TE, eeE, etc., utilizing energetic highly charged but weak intensity beams of higher Z ions (Si, Mn), available from the JRML tandem Van de Graaff – Linear Accelerator facilities.

- Utilize Li vapor targets as also Li vapor laser-excited targets with much narrower Compton profiles to probe the BEe and RTE processes.

APPENDIX

A Kinematic Broadening

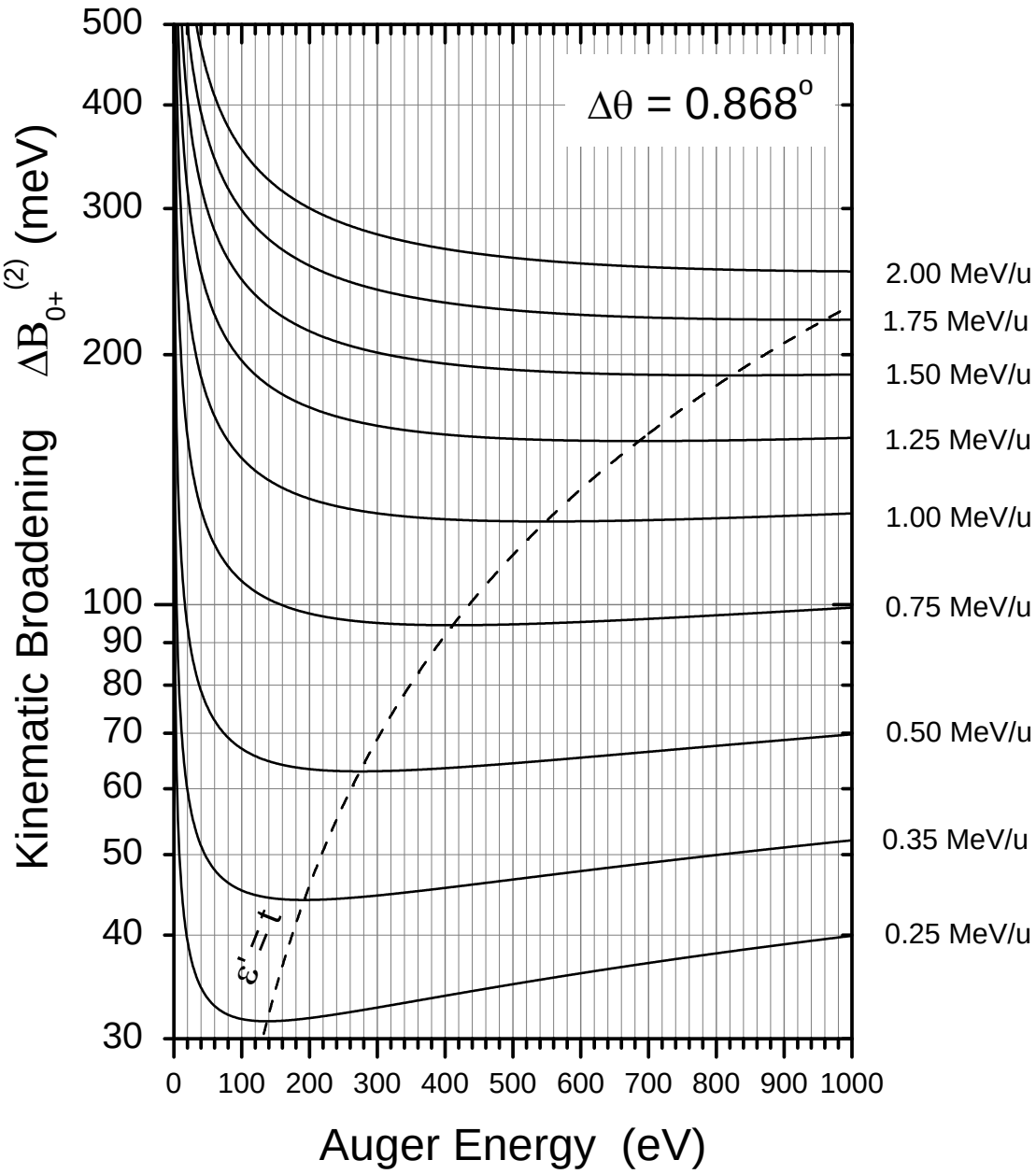

Figure 79: Second order broadening coefficient $\Delta B^{(2)}$ as function of the Auger electron energy ϵ' for $\theta' = 0°$ and $\theta = 0°$ (Eq. 22). The spectrometer full acceptance angle is $\Delta\theta$=0.868°.

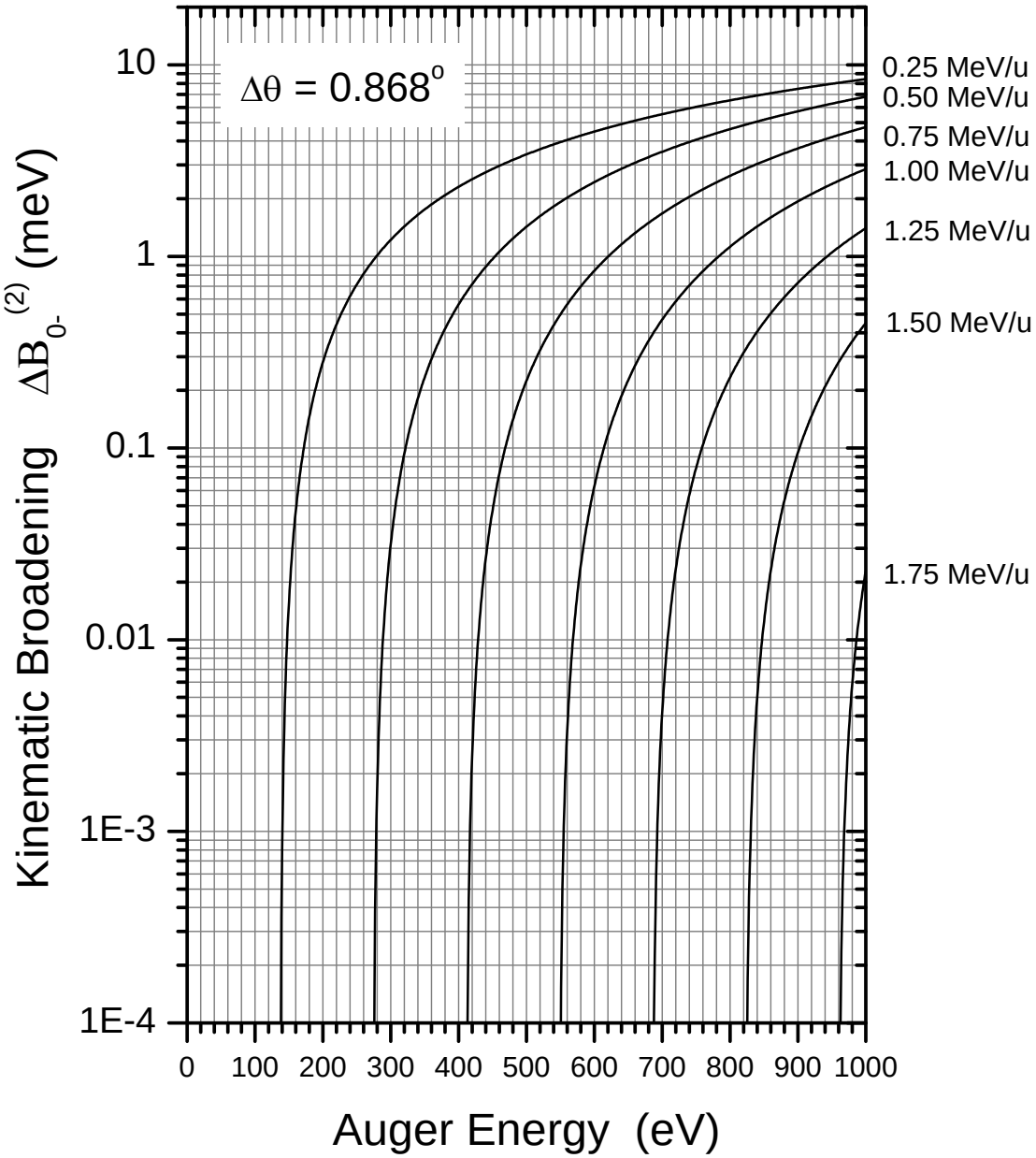

Figure 80: Second order broadening coefficient $\Delta B^{(2)}$ as function of the Auger electron energy ϵ' for $\theta' = 180°$ and $\theta = 0°$ (Eq. 23). The spectrometer full acceptance angle is $\Delta\theta$=0.868°.

B Ion Beam Production and Manipulation

Singly-charged negative ions are produced by the sputter ion source. These ions are extracted from the source at the energy of about 70 keV and are mass-analysed by a 20° analysing magnet. Then they are injected into the tandem Van de Graaff accelerator to be accelerated at the terminal voltage, +V. For the KSU tandem $V_{max} \simeq 7\,MV$. The accelerated negative ions reach the tandem tank half way, where the maximum positive terminal voltage, +V, occurs, where they collide with a thin carbon foil or a low density gas (usually N_2). Negative ions are stripped from their electrons and the positive ions produced by the collision are furthermore accelerated to the end of the tandem tank. Thus, the final energy gain for a ion of initial and final mass m_i and m_f, respectively, and final charge q is $E = (q + m_f/m_i)V$. Usually $m_f = m_i$ (i.e. F^{q+} ions are obtained from F^-) and then the energy gain is $E = (q + 1)$ V. Energy is measured in MeV when the terminal voltage is measured in MV.

The stripping process inside the accelerator produces a distribution of charge states at different intensities and energies. In an experiment the beam charge-state and energy are pre-determined so the final goal is to get the desired ion beam at the highest intensity – at least for the experiments that this dissertation is involved with.

The charge q-distribution of the foil-stripping process can be estimated using *Marrion and Young* [252] nuclear reaction analysis table. Though in JRM laboratory, a very useful program for computing the q-distribution of the stripping process of both foil-stripping and gas-stripping was available and used most of the times. The program called TANDEM [32] could predict within the order of magnitude the expected current of all charge states.

The charge-state selection is obtained in the first 45° analysing magnet (see Fig. 10). The magnet was calibrated with an NMR device which is much more accurate than the meter of the terminal voltage. For this reason, the analysing magnet is set at the Hall Probe Voltage value (HPV) determined by the NMR frequency and the terminal voltage is tuned in order to maximize the beam current in the meter (Faraday Cup) after the analysing magnet. A feed back system in the terminal voltage, using the difference of the beam current measured at a pair of slits placed in between the two 45° analysing magnets, automatically adjusts the beam energy to the one set by the magnet. Therefore the beam energy along with the beam current are kept constant through the measurement. A energy uncertainty of $\Delta E/E = 7 \times 10^{-4}$ is characteristic for the J. R. M. tandem Van de Graaff accelerator.

After the first 45° analysing magnet the ion beam is transfered through a second 45° magnet in order to enter the Linear Accelerator (LINAC). The LINAC can be used to further accelerate or decelerate the ions. In the experiments presented in this dissertation the LINAC was not used but rather treated, during the beam transportation, as a common beam pipe. After the LINAC the beam is bent through a 90° magnet to the direction of the beamline in use. It passes at 0° from the first switching magnet

[32] The TANDEM and the CHARGE codes were based on semi empirical laws obtained from experimental data tables

and then bent at 15° left with respect to the beam direction, by the second switching magnet to the experimental setup.

The ion beam transportation requires the control of magnets, magnetic and electrostatic deflectors, focusing lenses, valves, Faraday cups and Beam Profile Monitors. It should be noted that the operation of the tandem accelerator and the transportation of the ion beam to the target region are done by the experimenters in the main control room.

In case that the beam current of a charge state q is predicted to be too low for the experimental requirements by the TANDEM program (i.e. less than ~50nA for the tandem spectrometer or less than ~1nA for the hemispherical spectrograph), a technique called *post-stripping* is applied. In this technique a lower charge state, where the beam is more intense, is selected from the first 45° analysing magnet. The lower charge state is further stripped away (post-stripped) on a thin carbon foil (10μ g/cm^3) which is placed, via a movable rod, perpendicular to the ion beam direction. Such movable rods exist in the regions between the two 45° magnets and before the LINAC analysing magnet. The new charge distribution has a maximum current at higher q-values resulting in more intense beams for higher charge states. The desired charge state for the experiment is then selected from the LINAC analysing magnet and is driven up to the experimental region.

In the J.R.M. laboratory, a program called CHARGE was available for calculating the charge distribution resulting from the collisions of an ion beam of charge q and kinetic energy E, with a thin carbon foil. Therefore, combination of the TANDEM and CHARGE codes could provide the information on the final post-stripped charge distributions for all the initial charge states. Although the absolute current values were not reproduced in reality, the relative current values of the beams of different charge states were quite reliable and were very helpful both in the beam transport and the planning of the experiment.

Table 19: Table of measured B^{q+} electrical currents at the target.

q	E_p (MeV)	I (nA)	Stripping Process
4	4	0.07	foil post stripping
	6	0.2	foil post stripping
	8	3	foil post stripping
3	4	2	foil post stripping
		0.5	terminal gas stripping
	6	3	foil post stripping
	8	4	terminal gas stripping
2	4	0.5	terminal gas stripping
	6	3	terminal gas stripping
	8	3	terminal gas stripping

C Vacuum considerations

The mass rate of flow through a vacuum system is proportional to the throughput, defined as: [91]

$$Q \equiv P\,S \tag{163}$$

where P and S are the pressure and the pumping speed, respectively, measured at the same point. The throughput of a vacuum system with one gas source is the same at every point. It can be shown [91], that the throughput of a tube depends on the pressure drop $P_1 - P_2$ across the tube and the conductance C of the tube as:

$$Q = (P_1 - P_2)\,C \tag{164}$$

Considering a vacuum system with a one gas source at pressure $P_1 = P$ (i.e. the gas-cell's pressure in the real experiment) and a point x for measuring the pressure (i.e. the ion gauge location), Eq. 164 can be written as:

$$Q = P\,C \tag{165}$$

since $P_1 >> P_2$ (P_1 is usually a few mTorr, while P_2 is less than 1 μTorr). Therefore the pressure at the point x can be written according to Eqs. 163 and 165 as:

$$P(x) = \frac{Q}{S(x)} = \frac{C\,P}{S(x)} \tag{166}$$

The master equation that relates the effective pumping speed $S(x)$ of the vacuum system measured at a point x, to the pump's (constant) pumping speed S_p and the conductance $C(x)$ of the tube manifold from the gas source to the measurement point x, is described by:

$$S(x) = \frac{S_p}{1 + \dfrac{S_p}{C(x)}} \tag{167}$$

The conductance of a tube manifold depends on geometrical parameters but also on the gas under pumping. In other words, for the same tube manifold, the conductance depends solely on the pumped gas. It is known that the conductance of H_2 is higher than the conductance of He, i.e. $C_{H_2} > C_{He}$, since the conductance is proportional to the mean molecular velocity. [253] Then form Eq. 167 it is straightforward to see that the effective pumping speed of H_2 is higher than the effective pumping speed of He, i.e. $S_{H_2}(x) > S_{He}(x)$. This result may be erroneously interpreted as for predicting that the pressure at the point x is lower for H_2 than for He. Eq. 166 indicates that for the same gas source pressure (i.e. the same gas-cell pressure) the throughput is different depending on the different gas conductance. Taking the ratio of the pressure measured at the point x for H_2 and He, $P_{H_2}(x)$ and $P_{He}(x)$ respectively, and using the Eqs. 166 and 167, it is obtained:

$$
\begin{aligned}
\frac{P_{H_2}}{P_{He}} &= \frac{C_{H_2}}{C_{He}} \cdot \frac{S_{H_2}}{S_{He}} = \frac{C_{H_2}}{C_{He}} \cdot \frac{\dfrac{S_p}{1+\frac{S_p}{C_{H_2}}}}{\dfrac{S_p}{1+\frac{S_p}{C_{He}}}} \\
&= \left(\frac{C_{H_2}}{C_{He}}\right)^2 \cdot \frac{C_{He}+S_p}{C_{H_2}+S_p} \simeq \left(\frac{C_{H_2}}{C_{He}}\right)^2
\end{aligned} \tag{168}
$$

Therefore, since $C_{H_2} > C_{He} \Rightarrow P_{H_2} > P_{He}$.

For example, at 300°K, $C_{H_2} = 46.04$ lt/(s cm^2) and $C_{He} = 32.55$ lt/(s cm^2) and the measured pressure for hydrogen would be twice the measured pressure for helium.

D Electronics Calibration

Calibrating the electronics means that all the four signal lines starting from the PSD up to the ADC should give rise to pulses with the same height for the same input signal. In other words, all lines should result in the same number (channel) in the pulse height distribution for the same input signal. Any deviation from the previous statement leads to deformation of the correct PSD circular image (see Fig. 18(f)) and therefore in erroneous results.

The first step of the calibration is to use the oscilloscope for adjusting the amplification for every one of the four signals, so that the height of the positive peak of each pulse is the same for the same input signal. Usually the preamplifiers have an input called "test" in order to apply an input signal there and proceed to the calibration. However, in order to simulate as much as possible the experimental conditions, it is preferable to use a capacitor to feed the signal exactly from the entrance of the preamplifier. The second step in the calibration is a method of fine tuning after the previous rough calibration using the oscilloscope. The electronic diagram for this method is shown in Fig. 81. The values that are written in the diagram for the positive pulse height (H), the rise time (T_r), the fall time (T_f) and the total pulse time duration (T) are typical of an ordinary amplifier calibration. Typical signal frequencies that were used are of the order of 1 kHz.

A 1pF capacitor was used along with input signals of the order of 100mV, the height of which could be varied in a known way through a signal attenuator. For each line the height was varied and the channel at the pulse height distribution was recorded. In this way a linear relation of the form $V_i = a_i + b_i \times$ channel, between the input voltage height V and the channel was obtained for each line i, (i = 1 - 4).

The constant a_i terms were used as offsets in the part of the software responsible for the pulse height distribution, but they were neglected since their absolute values depend on the real experimental input voltage height. The information of the four b_i factors on the other hand is the main reason of the calibration. Choosing one of them as the relative unit (i.e. b_2=1) and dividing the rest of b_i's ($i \neq 2$) by this, the gain factors used in the data acquisition program for the pulse height distribution were obtained. If the first step of the calibration is done with enough care, the second step is an optimization in the gain factors which does not amount to more than a 2% correction.

After the electronics were calibrated the shape of the PSD area should be circular if plotted in equidistant x and y axes. An accurate way to determine the center of the PSD circular area is to rotate it (using software) and check any possible changes in the values of the pre-recorded (x,y) center. If this is so, then repeating the same process, after small changes in the amplification factors, leads to an accurate determination of the center of the PSD circular area. Finally, the PSD image may need an overall rotation (for example to make it coincide with possible preferred experimental axis or to project along a special axis). This is also done via software programming.

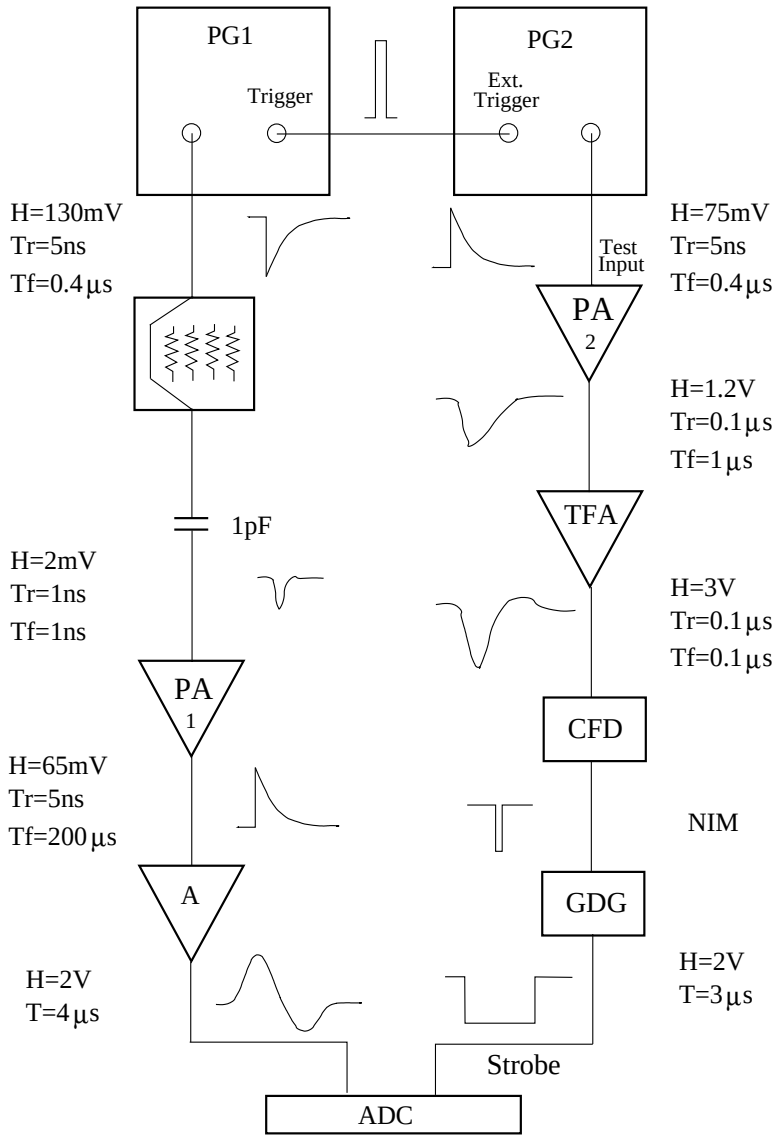

Figure 81: Electronics Calibration Diagram. Notation as in Fig. 17, except A: Amplifier.

E The paracentric HDA: I. Ideal 1/r potential - Theory

E.1 Energy conservation across potential boundary

The region outside the analyser (Fig. 82 region I) is supposed to be at constant potential (free motion), while the region inside the analyser (Fig. 82 region II) to be at a potential given by Eq.28. In other words, the fringing field effects have been assumed to be negligible. Thus, the potential is seen to have a sharp step going across the boundary of the two regions. This can is represented mathematically by a potential with step at $\theta = 0$: [85]

$$V(r,\theta) = V(r)\,u(\theta) + V_p\,u(-\theta) \tag{169}$$

with $V(r)$ given by Eq. 28 and

$$u(\theta) = \begin{cases} 0 & \text{for} \quad -\pi < \theta < 0 \qquad \text{Region I} \\ 1 & \text{for} \quad \pi \geq \theta \geq 0 \qquad \text{Region II} \end{cases} \tag{170}$$

Next, it is shown that energy is conserved across the potential boundary by direct calculation of the work along an arbitrary closed path $abcdefa$ (see Fig. 82) made up of two arcs of constant radius (r_1 and r_2) and two straight sections along the radial directions of constant θ ($\theta = \pm\theta_0$). The sharp boundary separating region I and II is at $\theta = 0$. Since the force in region I is zero the work along path $abcd$ must also be zero. Thus, the work along the path $defa$ needs to be calculated:

$$W_{defa} = \int_d^e + \int_e^f + \int_f^a \mathbf{F}\cdot d\mathbf{s} \tag{171}$$

$$\begin{aligned} W_{de} &= \int_d^e F_\theta\, r_1\, d\theta && (172)\\ &= -q\int_0^{\theta_0} \frac{\partial}{\partial\theta} V(r,\theta) d\theta && (173)\\ &= -q\,[V(r_1) - V_p]\int_0^{\theta_0} \delta(\theta) d\theta && (174)\\ &= -q\,\tilde{V}(r_1) && (175) \end{aligned}$$

similarly

$$W_{fa} = q\,\tilde{V}(r_2) \tag{176}$$

and finally

$$W_{ef} = \int_e^f F_r dr \tag{177}$$

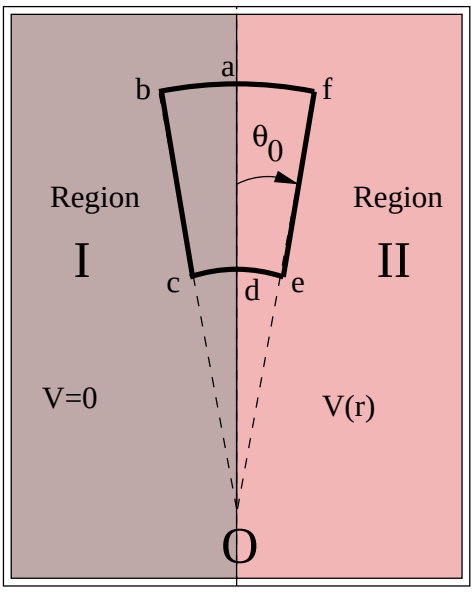

Figure 82: Integration path (bold line) $abcdefa$ used to show energy conservation across the potential step at $\theta_0 = 0$ (see text). The total work performed to go around the closed path $abcdefa$ is zero. In Region I the potential is constant, while in Region II it is given by $V(r)$ of the analyser.

$$= -q \int_{r_1}^{r_2} \frac{\partial}{\partial r} V(r,\theta) dr \tag{178}$$

$$= -q \int_{r_1}^{r_2} \frac{\partial}{\partial r} V(r) dr \tag{179}$$

$$= -q\,[V(r_2) - V(r_1)] = -q\,[\tilde{V}(r_2) - \tilde{V}(r_1)] \tag{180}$$

which when added up give $W_{abcdefa} = 0$, i.e. the work along the closed path abcdefa is zero. Any closed path joining regions I and II can always be represented by integrals of this type which cancel out. Thus, total energy is conserved even across the boundary.

In the region I (outside the analyser), the particle has a total energy T, equal to its kinetic energy $t = \frac{1}{2} m\, v^2$ plus the potential energy $q\, V_p$ due to the decelerating potential V_p, while inside the analyser it has a total energy equal to the sum of its kinetic and potential energies, K and $q\, V$. The conservation of energy on either side of the boundary gives:

$$\begin{aligned}
\text{Total energy outside analyser} &= \text{Total energy in } \tfrac{1}{r} \text{ field in analyser} \\
T = t + qV_p &= K(r) + qV(r) = \frac{1}{2} m v^2 + qV(r) \overset{(39)}{=} \\
&= \frac{1}{2} m \dot{r}^2 + \frac{1}{2} \frac{L^2}{m r^2} - q \frac{k}{r} + q\, c + q\, V_p \overset{(44)}{=} \\
&= E' + q\, c + q\, V_p
\end{aligned} \tag{181}$$

and thus,

$$E' = t - qc = T - qc - qV_p \tag{182}$$

where E' is the total energy inside the analyser found to be conserved in Eq. 44.

E.2 Particle refraction across potential boundary

In region I the potential is constant and the particle thus feels zero force, its velocity remains constant and therefore so does its angular momentum $L^\star$.[33] In region II, the force is central and therefore the angular momentum L must also be conserved. However, due to the finite step potential at the boundary the two angular momenta are in general *not* equal. This follows directly from the integration of motion in the θ direction in the plane of the orbit. [85]

Using the Lagrangian along with the potential $V(r,\theta)$ which has already been defined in Eq. 169, the equation of motion in the orbital plane for the θ coordinate is given by:

$$\begin{aligned}
\frac{d}{dt}\left(m\,r^2\,\dot{\theta}\right) = \frac{dL}{dt} &= -q\,\tilde{V}(r)\delta(\theta) \Rightarrow \\
\frac{d}{dt}(L^2) &= -2\,L\,q\,\tilde{V}(r)\delta(\theta) \Rightarrow \\
\dot{\theta}\,\frac{d}{d\theta}(L^2) &= -2\,m\,r^2\,\dot{\theta}\,q\,\tilde{V}(r)\delta(\theta) \Rightarrow \\
\frac{d}{d\theta}(L^2) &= -2\,m\,r^2\,q\,\tilde{V}(r)\delta(\theta)
\end{aligned} \tag{183}$$

which can be directly integrated across the boundary $\theta = 0$ along a path of constant $r = r_0$ to yield: [85]

$$L^2 - L^{\star 2} = -2\,m\,r_0^2\,q\,\tilde{V}(r_0) \tag{184}$$

At the entry radius $r = r_0$ the angular momenta must clearly be given by:

$$L^\star = m\,r_0\,v_0^\star\,\sin(\frac{\pi}{2} + \alpha^\star) = r_0\,\sqrt{2\,m\,t}\,\cos\alpha^\star \tag{185}$$

and

$$L = m\,r_0\,v_0\sin(\frac{\pi}{2} + \alpha) \overset{(181)}{=} r_0\,\sqrt{2\,m\,[t - q\,\tilde{V}(r_0)]}\cos\alpha \tag{186}$$

where v_0, $v_0^\star$ and α, $\alpha^\star$ are the entry velocities and angles inside (region II) and outside (region I) of the analyser.

Using Eqs. 184 and 185 the angular momentum L can be expressed in terms of the entry angle $\alpha^\star$ (instead of α) and the potential $\tilde{V}(r_0)$.

$$L^2 = 2\,m\,r_o^2\,[\,t\,\cos^2\alpha^\star - q\,\tilde{V}(r_0)] = L^{\star\,2}\left[1 - \frac{q\,\tilde{V}(r_0)}{t\,\cos^2\alpha^\star}\right] \tag{187}$$

[33] The symbol $\star$ is reserved for marking quantities inside region I of potential V_p to distinguish from quantities inside region II of potential V(r)

Defining $K = \frac{1}{2}\, m\, v^2 = \frac{1}{2}\, m\, (v_r^2 + v_\theta^2)$ and $t \equiv K^\star = \frac{1}{2}\, m\, v^{\star 2}$ the change in the kinetic energy $\Delta K^\star$, when crossing the boundary at r_0 can be written as:

$$\Delta K^\star \equiv K - K^\star = -q\, \tilde{V}(r_0) \tag{188}$$

Combining Eqs. 184-188 it is straightforward to show that: [85]

$$v \sin\alpha = v^\star \sin\alpha^\star \tag{189}$$

or

$$v_r = v_r^\star \tag{190}$$

and

$$v_\theta^2 - v_\theta^{\star 2} = -\frac{2q\, \tilde{V}(r_0)}{m} \tag{191}$$

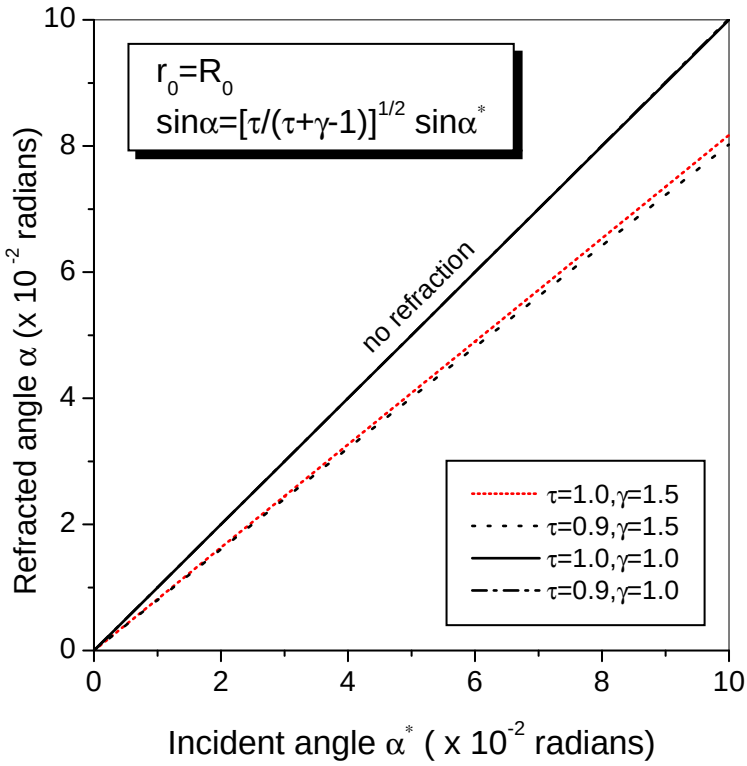

Figure 83: Relation between the entry angle $\alpha^\star$ prior to refraction (angle of incidence) and angle α after refraction (angle of refraction) for two cases: (a) $\gamma = 1$ ($\tilde{V}_0 = 0$), $R_0 = \bar{R}$ (conventional case), (b) $\gamma = 1.5$ ($\tilde{V}_0 = 0.5w$, $R_0 = 0.8125\bar{R}$ (paracentric entry used in this thesis). In both cases $q = -1$ (electrons), $t = w = 1000$ eV, $r_0 = R_0$ and $R_\pi = \bar{R}$. Clearly, the effect of refraction is non-negligible for paracentric entry and $\tilde{V}_0 \neq 0$ ($\gamma \neq 1$).

From Eq. 190 it is seen that the radial velocity, $v_r = \dot{r}$, is continuous across the boundary [67], as opposed to the angular velocity, $v_\theta = r\,\dot{\theta} = \frac{L}{m\,r}$ which is not. Eq. 189 is thus seen to be the charged-particle analog of Snell's law of refraction in optics. [91]

The relations between α and $\alpha^\star$ are summarized as follows: [85]

$$\sin\alpha = \frac{\sin\alpha^\star}{\sqrt{1-\frac{q\,\tilde{V}(r_0)}{t}}} \tag{192}$$

$$\cos\alpha = \sqrt{\frac{1-\frac{q\,\tilde{V}(r_0)}{t\,\cos^2\alpha^\star}}{1-\frac{q\,\tilde{V}(r_0)}{t}}}\,\cos\alpha^\star \tag{193}$$

$$\tan\alpha = \frac{\tan\alpha^\star}{\sqrt{1-\frac{q\,\tilde{V}(r_0)}{t\,\cos^2\alpha^\star}}} \tag{194}$$

Note that when $\tilde{V}(r_0) = 0$, for that entry position, $\alpha = \alpha^\star$. The relation between $\alpha^\star$ and α is shown for in Fig. 83 for the case of paracentric entry with $\gamma = 1.5$ and for conventional entry with $\gamma = 1$. In both cases $r_0 = R_0$.

E.3 General form of the elliptical trajectory

Using Eqs. 42, 185, 187 and 194 the trajectory equation (56) is written in terms of the entry point r_0, the entry angle $\alpha^\star$ and the initial kinetic energy t (reduced by the retarding potential V_p):

$$\frac{r_0}{r_\theta} = \frac{q\,k}{2\,t\,r_0}\frac{(1-\cos\theta)}{(1-\frac{q\,\tilde{V}(r_0)}{t\,\cos^2\alpha^\star})\cos^2\alpha^\star} + \cos\theta - \frac{\tan\alpha^\star\,\sin\theta}{\sqrt{1-\frac{q\,\tilde{V}(r_0)}{t\,\cos^2\alpha^\star}}} \tag{195}$$

Eq. 195 may also be expressed in terms of the applied potential constants k and c appearing in Eq. 28. The applied potential is determined in a straightforward way through the central ray. Thus, replacing the values of $r_0 = R_0$, $r_\theta = R_\pi$, $\theta = \pi$, $\alpha = 0$, $t = w$ into Eq. 195 and using the potential equation (28) at $r = R_0$, the trajectory equation becomes:

$$\frac{R_0}{R_\pi} = \frac{q\,k}{R_0(w - q\,c) + q\,k} \tag{196}$$

Also from the definition of γ (Eq.33)

$$q\,\tilde{V}_0 \equiv q\,\tilde{V}(R_0) = -\frac{q\,k}{R_0} + q\,c = (1-\gamma)\,w \tag{197}$$

Eqs. 196 and 197 are solved, introducing also the parameter ξ defined in Eq. 34, yielding for the constants k and c: [85]

$$q\,k = \gamma\,w\,R_0(1+\frac{R_0}{R_\pi}) = w\,R_0(1+\xi)\frac{\gamma}{\xi} \tag{198}$$

$$q\,c = w(1+\gamma\frac{R_0}{R_\pi}) = w(1+\frac{\gamma}{\xi}) \tag{199}$$

$q\,\tilde{V}_0$ can also be expressed in terms of the parameters γ, ξ and the tuning energy w as

$$q\,\tilde{V}(r_0) = -\frac{q\,k}{r_0} + q\,c = w\left(1 + \gamma\left[\frac{1}{\xi} - (\frac{1}{\xi} + 1)\frac{R_0}{r_0}\right]\right) \tag{200}$$

Replacing $q\,k$, $q\,c$ and $q\,\tilde{V}(r_0)$ from the Eqs. 198, 199 and 200, respectively into Eq. 195 and using the definition for $\tau = t/w$ introduced in Eq. 32, the final trajectory equation in terms of the parameters γ, ξ, the reduced tuning energy τ and the entry angle $\alpha^\star$ is obtained: [34]

$$\frac{r_0}{r_\theta} = \frac{1}{2}\frac{\gamma}{\tau}\frac{R_0}{r_0}\frac{(1+\frac{1}{\xi})}{\left[1 - \frac{1+\gamma\,[\frac{1}{\xi} - \frac{R_0}{r_0}(1+\frac{1}{\xi})]}{\tau\,\cos^2\alpha^\star}\right]}\frac{(1-\cos\theta)}{\cos^2\alpha^\star} + \cos\theta - \frac{\tan\alpha^\star}{\sqrt{1 - \frac{1+\gamma\,[\frac{1}{\xi} - \frac{R_0}{r_0}(1+\frac{1}{\xi})]}{\tau\,\cos^2\alpha^\star}}}\sin\theta \tag{202}$$

E.4 HDA dispersion

For a fixed energy τ the dispersion increases with increasing ξ and decreases for increasing γ. Changes in ξ and γ imply electrostatic field changes, which do not affect the initial charged particle kinetic energy but change - through the field changes - the conserved energy E' (Eq. 182), i.e. the sum of the kinetic and the potential energy inside the analyser, a quantity which characterizes the orbit type and size. In order to understand how these changes affect the dispersion, the dependence of the particle elliptical trajectory semi-major axis on γ and ξ will be studied. The semi-major axis value involves changes in both the field strength and the conserved energy E'. For this reason the problem is simplified by applying the initial conditions $\alpha = 0$ and $r_0 = R_0$. Then substituting Eqs. 182,198,199 and 32 into Eq. 46 the semi-major axis can be written as:

$$a = -\frac{qk}{2E'} = \frac{\gamma\,(1+\xi)}{\frac{\gamma}{\xi} + 1 - \tau}\left(\frac{\bar{R}}{2}\right) \tag{203}$$

The numerator refers to the changes of the field while the denominator to the changes in the conserved energy E'. The dependence of a on parameters ξ and γ will be examined separately by keeping one of the two variables at the constant value of 1, which refers

[34] This may be compared to the trajectory equation written in terms of α:

$$\frac{r_0}{r_\theta} = \frac{1}{2}\frac{\gamma}{\tau}\frac{R_0}{r_0}\frac{(1+\frac{1}{\xi})}{\left[1 - \frac{1+\gamma\,[\frac{1}{\xi} - \frac{R_0}{r_0}(1+\frac{1}{\xi})]}{\tau}\right]}\frac{(1-\cos\theta)}{\cos^2\alpha} + \cos\theta - \tan\alpha\sin\theta \tag{201}$$

to the conventional HDAs. Eq. 203 is then gives:

$$a(\xi = 1) = \frac{2\,\gamma}{\gamma\,+\,1\,-\,\tau}\,\left(\frac{\bar{R}}{2}\right) \tag{204}$$

$$a(\gamma = 1) = \frac{1+\xi}{\frac{1}{\xi}\,+\,1\,-\,\tau}\,\left(\frac{\bar{R}}{2}\right) \tag{205}$$

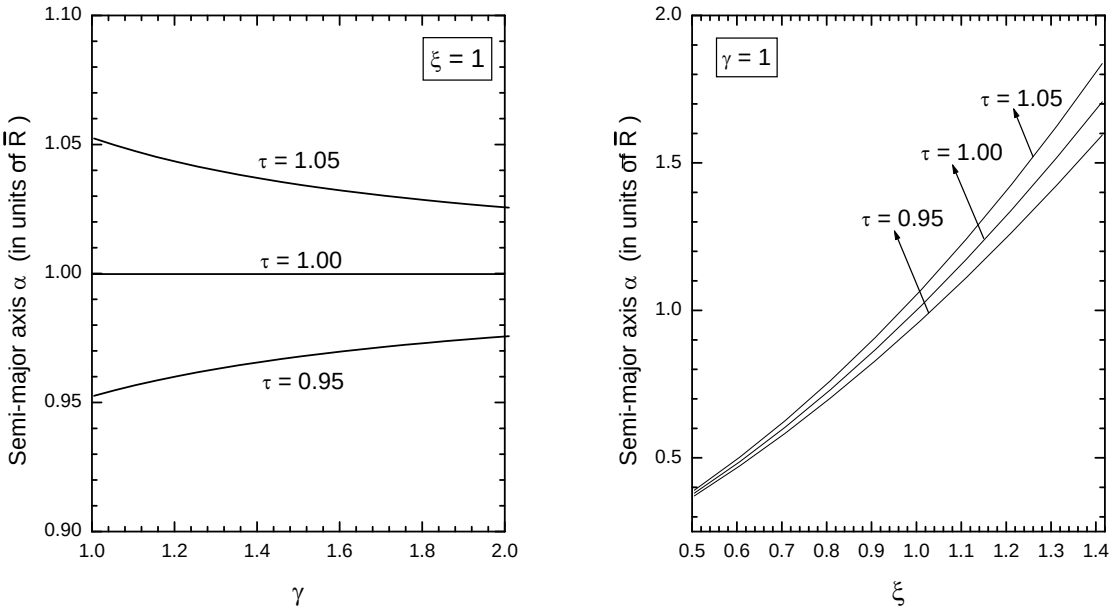

Figure 84: Plot of the semi-major axis as a function of γ (Eq. 205)[*Left*] and as a function of ξ (Eq. 204)[*Right*] for reduced pass-energies $\tau = 0.95$, $\tau = 1$ and $\tau = 1.05$

In Fig. 84(Left) the semi-major axis is plotted as a function of γ (Eq. 204) for reduced pass energies $\tau = 0.95$, $\tau = 1$ and $\tau = 1.05$. It is seen that, as γ increases, the two semi major axis of $\tau = 0.95$ and $\tau = 1.05$ converge equally around the value of $2\bar{R}$, i.e. the value of the central ray ($\xi = 1, \tau = 1$). The result of the above example for the two pass energies can be generalized to the case where the two pass energies actually differ by a small amount of Δt around the mean value t_0 ($t_0 \neq w$). Then it becomes obvious that the density of energies in the same spatial region increases. Therefore according to the dispersion definition (Eq. 86) the dispersion must decrease. A further insight into the problem shows that the increase in γ, starting at the initial value of 1, actually leads to an increase in field strength qk by a factor of γ (Eq. 198), a fact which in turn leads to an increase in the absolute value of energy E by the quantity of $w(\gamma - 1)$ (Eqs. 182,199). Note that the the equipotential surfaces change in such a way that the field becomes more intense at the same region. The ratio of the two changes actually defines the new semi-major axis of the elliptical orbit and therefore the new exit point.

The interpretation of the dispersion dependence on ξ is obtained in the same way as in the case of γ. In Fig. 84(Right) the the semi-major axis is plotted as a function of ξ (Eq. 205) for the cases of reduced pass energies of $\tau = 0.95$ and $\tau = 1.05$. It is seen that, as ξ increases, the two semi-major axis of $\tau = 0.95$ and $\tau = 1.05$ diverge. It is easy to understand that the density of energies in the same spatial region in this case decreases, and according to the dispersion definition (Eq. 86) dispersion increases. As in the case of γ, the increase in ξ actually led to a decrease [35] in field strength qk by the quantity $2 - ((1+\xi)/\xi^2)\bar{R}$, a fact which in turn led to a decrease in the absolute value of energy E' by the quantity of w/ξ. Note that the equipotential surfaces change so that the field becomes less intense at the same region, but the entrance point is now moved to regions of more intense field. The ratio of the two changes again defines the new semi-major axis of the elliptical orbit and therefore the new exit point.

E.5 HDA resolution

A mean overall base-resolution $\overline{\Re_b}$ can be defined through Eq. 94 (case of $\tau = 1$), introducing also the mean dispersion $\bar{D} = D(\tau = 1)$, as:

$$\overline{\Re_b} \equiv \Re_b(\tau = 1) = \frac{(\frac{1}{2}|M_L|d_o + \Delta r_\pi)}{\bar{D}\,F} + \frac{1}{4}(\frac{d_{LE}}{M_L\,l})^2 \tag{206}$$

$$= \frac{(\frac{1}{2}|M_L|d_o + \Delta r_\pi)}{(1+\xi)R_\pi}\left(\frac{\gamma}{F}\right) + \frac{1}{4}(\frac{d_{LE}}{M_L\,l})^2 \tag{207}$$

In Fig. 85 the mean overall base-resolution $\overline{\Re_b}$ as a function of M_L for different F values is plotted. It is seen that for each deceleration factor F there is an optimum linear magnification factor M_L that minimizes the energy resolution. As the deceleration factor F increases, the value of $|M_L|$, for which the resolution is minimized, slowly increases. In order to obtain the optimal value of $|M_L|$ for which the energy resolution in Eq. 206 is minimized, the first derivative of $\overline{\Re_b}$ is set to zero.

$$\frac{\partial\overline{\Re_b}}{\partial|M_L|} = 0 \tag{208}$$

After some algebra, the optimum M_L value is found.

$$|M_{Lopt}| = \left[\left(\frac{d_{LE}}{l}\right)^2\left(\frac{\bar{D}}{d_o}\right)\,F\right]^{\frac{1}{3}} \tag{209}$$

In the spectrograph mode (fixed voltages) the optimum magnification $|M_{Lopt}|$ can only be defined for the mean dispersion $\bar{D}$. This is because D depends on the initial kinetic energy of the charged particles under detection, while $\bar{D}$ depends on the tuning

[35] It should be kept in mind that the entrance point R_0 displacement ($\xi \neq 1$) is done while maintaining $\gamma = 1$ i.e. $V(R_0) = 0V$

energy of the spectrograph. $|M_L|$ is set through the voltages applied to the lens, which are kept constant for a measurement of the spectrum part that corresponds on the PSD area, and therefore should not depend on the initial kinetic energy of the charged particle but on the tuning energy of the spectrograph. A plot of the optimum linear magnification factor as a function of the deceleration factor F can be seen in Fig. 87(left). For the paracentric analyser under study: $|M_{Lopt}| = 0.24\,F^{\frac{1}{3}}$.

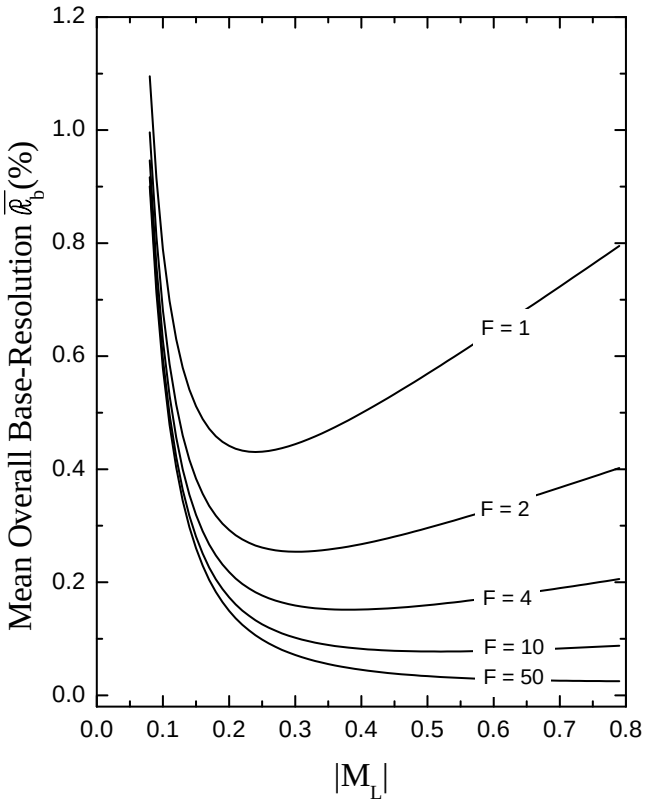

Figure 85: Mean overall base-resolution $\overline{\Re_b} = \overline{\Delta T}/T$ plotted as a function of the lens linear magnification $|M_L|$ for different deceleration factors F.

Upon substituting $|M_{Lopt}|$ back into Eq. 94 the overall optimum (minimized) base-resolution reads

$$\Re_{bopt} = \frac{1}{D}\left[\Delta r_\pi + \frac{\left(\bar{D}\,F\right)^{\frac{1}{3}}}{2}\left(\frac{d_o\,d_{LE}}{l}\right)^{\frac{2}{3}}\right]\left(\frac{t}{T}\right) + \frac{1}{4}\left(\frac{d_o\,d_{LE}}{l\,\bar{D}\,F}\right)^{\frac{2}{3}} \tag{210}$$

Substituting $|M_{Lopt}|$ back into Eq. 206 or replacing D with $\bar{D}$ and t/T with $1/F$ in Eq. 210, the mean overall optimum (minimized) base-resolution reads

$$\overline{\Re}_{bopt} = \frac{\Delta r_\pi}{F\,\bar{D}} + \frac{3}{4}\left(\frac{1}{F}\right)^{\frac{2}{3}}\left[\left(\frac{d_o}{\bar{D}}\right)\left(\frac{d_{LE}}{l}\right)\right]^{\frac{2}{3}} \tag{211}$$

In Fig. 86(left) the optimum overall base resolution is plotted as a function of the reduced pass energy τ for different deceleration factors, while in Fig. 86(right) a plot of the mean overall base resolution as a function of the deceleration factor F is shown for the cases of $|M_L| = 1$,$|M_L| = 0.5$,$|M_L| = 0.75$ and $|M_L| = |M_{Lopt}|$. A comparison between these three cases, indicates the importance of achieving initially small magnifications $|M_L|$ for no deceleration $F = 1$. In other words, the energy resolution should be minimized by a good lens focusing system, prior to applying deceleration.

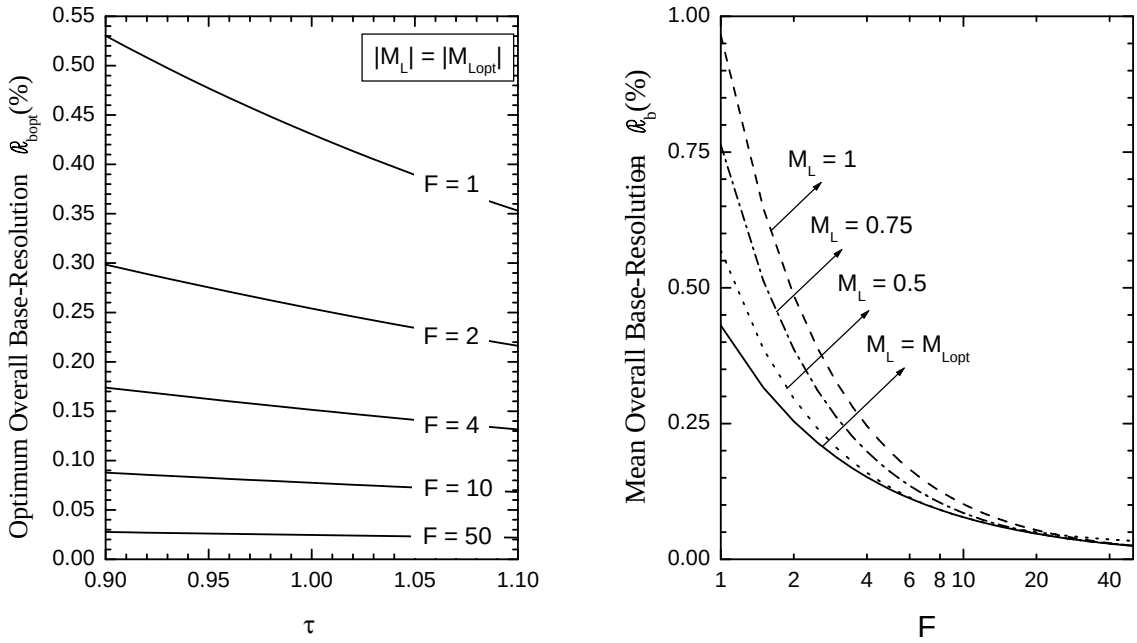

Figure 86: [*Left*] Plot of the optimum overall base-resolution as a function of the reduced pass-energy τ for different deceleration factors. [*Right*] Plot of the mean overall base-resolution as a function of the deceleration factor for $|M_L| = 1$, $|M_L| = 0.5$, $|M_L| = 0.75$ and $|M_L| = |M_{Lopt}| = 0.24\,F^{\frac{1}{3}}$. The importance of achieving small values of magnification factors $|M_L|$ at small values of deceleration the factor F is obvious.

It is seen from Eq. 210 that the angular aberration term in the optimum overall base-resolution $\Re_{bopt}$ *does* depend on the deceleration factor F, through the optimal magnification factor $|M_{Lopt}|$ dependence on F (Eq. 209) - a fact that was not obvious in Eq. 94. This indicates that the energy resolution may keep improving with increasing F (see Fig. 86). However, when the image size d_i becomes larger than the analyser entrance aperture d_{AE}, electron transmission losses through the lens begin to occur, thus putting a limit to the maximum useful value of M_L, and therefore to the minimum possible resolution.

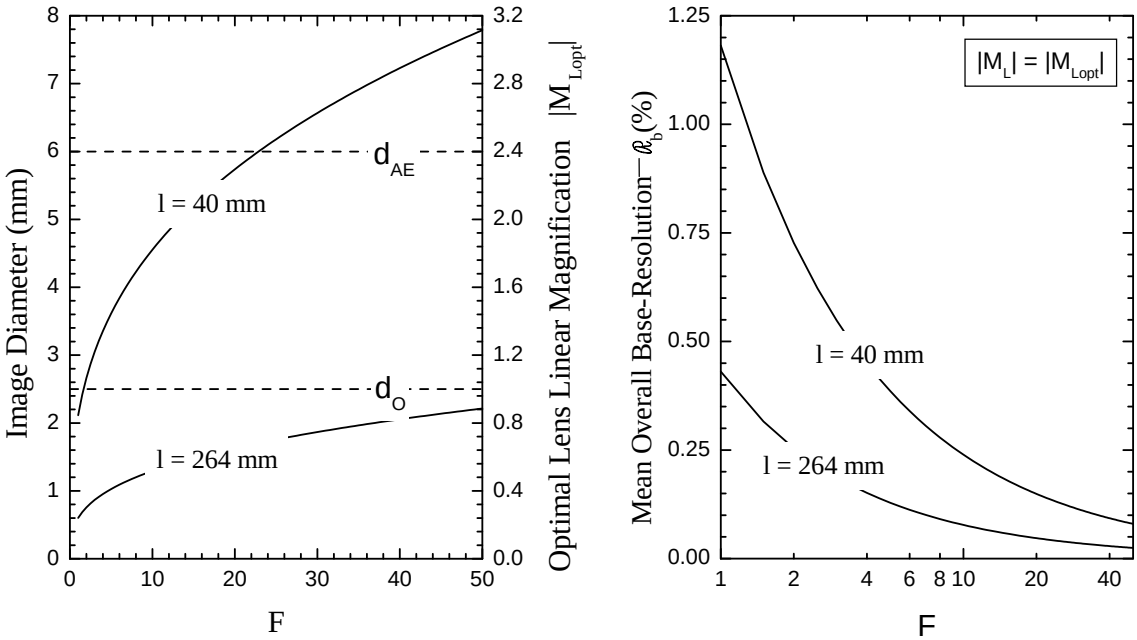

Figure 87: [*Left*] Plot of the image distance d_i (left y-axis) and the lens optimal linear magnification factor $|M_{Lopt}|$ (right y-axis) as a function of the deceleration factor F for the cases of object distances $l = 264mm$ and $l = 40mm$. [*Right*] Same as (left) but for the mean overall base-resolution.

This can be clearly seen in Fig. 87(left) where the image distance occupied at the entrance of the HDA (left y-axis) is plotted as a function of the deceleration factor F. It can also be seen that the distance between the target (object) and the lens entrance l plays a crucial role on the resolution value, since it defines the object half angle α. Thus for the experimental value of $l = 264$mm the optimum ($M_L = |M_{Lopt}|$) image diameter d_i is smaller than the analyser entrance $d_{AE} = 6$mm for a very wide range of deceleration factors, setting practically no limit on the energy resolution. Though for a hypothetical position very close to the lens $l = 40$mm, the optimum image diameter becomes larger than the analyser entrance d_{AE} at $F = 20$ setting a lower limit in the resolution with 10% transmission. The resolution dependence on the distance l is more clearly seen in Fig. 87 (right) where, the mean overall base-resolution is plotted as a function of the deceleration factor F.

An important feature in designing a spectrograph in general, is the contribution of the angular term to the energy resolution (Eq. 95). An estimate of this quantity can be obtained by defining the ratio χ of the angular term to the dispersion term for the average base-resolution.

$$\chi = \frac{\alpha^2}{\mathcal{R}_b} = \frac{\alpha^2\, D}{\Delta r_\pi + \Delta r_0} = \frac{\frac{1}{4}\left(\frac{d_{LE}}{M_L\, l}\right)^2}{\frac{\left(\frac{1}{2}|M_L|d_o + \Delta r_\pi\right)}{(1+\xi)R_\pi} \cdot \frac{\gamma[1+\frac{\xi}{\gamma}(1-\tau)]^2}{(\tau+F-1)}} \tag{212}$$

In literature a $\chi_{crit} = 0.25$ is a value accepted as adequate for any type of spectrometer using slits while operating in low-resolution mode (no deceleration applied). [254] In Fig. 88(left) the average ratio $\overline{\chi} \equiv \chi(\tau = 1)$ is plotted as a function of the deceleration factor F at different magnifications $|M_L|$. As can be clearly seen, in cases where the spectrograph utilizes a lens focusing system, the resolution is not necessarily minimized by minimizing just the angular term but rather by minimizing the sum of the angular and dispersion terms (see also Fig. 86(right)), since the dispersion and angular terms are no longer independent, but related through their dependence on $|M_L|$. For $|M_L| = |M_{Lopt}|$, $\overline{\chi}$ is kept at an almost constant value (~ 0.35) for deceleration factors F up to 50, as seen in Fig. 88(left). This means that the angular aberration contribution to the resolution is not a limiting factor.[36] Therefore $|M_L| = |M_{Lopt}|$ can be introduced as new criterion for designing spectrographs with lens focusing elements. From Fig .86(right) it is seen that at small deceleration factors ($F < 10$) the criterion is very important, since the mean overall base-resolution can be improved even by a factor of 2.

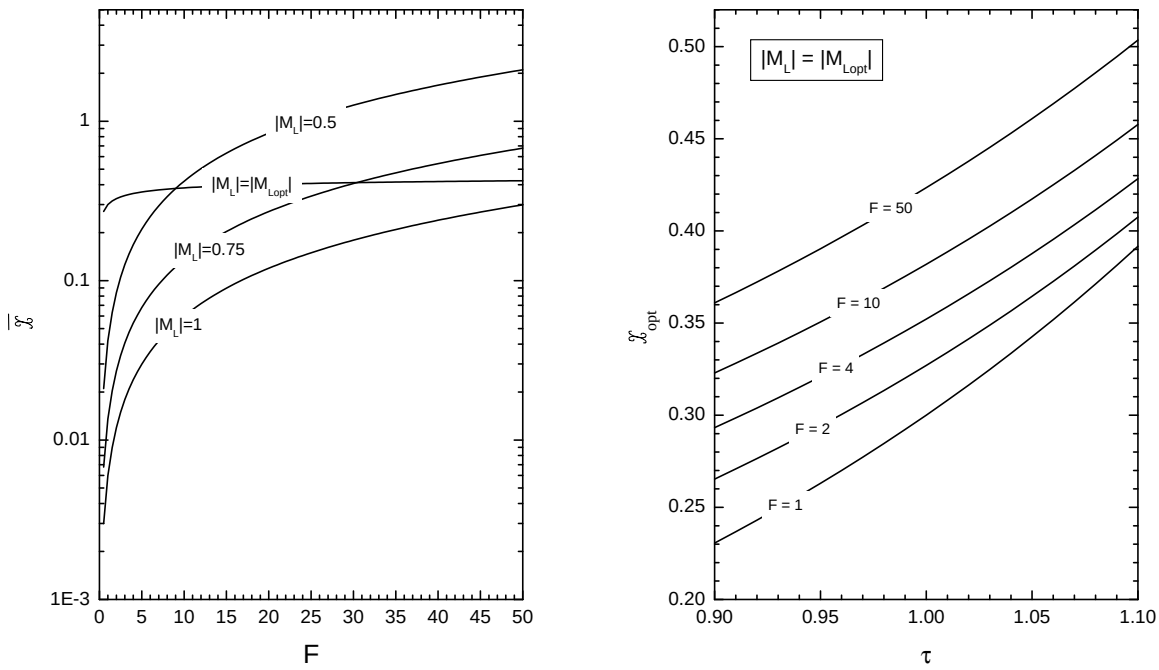

Figure 88: [*Left*] Average ratio $\overline{\chi} \equiv \chi(\tau = 1)$ (Eq. 211) for different magnifications $|M_L|$, as a function of the deceleration factor F. [*Right*] Ratio χ_{opt} of the angular contribution to the dispersion term of the energy resolution (Eq. 94) for the *optimal* magnification factor, as a function of the reduced energy τ.

[36] Operating the spectrograph with deceleration factors $F > 20$ implies far more important problems than the angular aberration contribution to the resolution, like the power supplies output accuracy.

Finally, in Fig. 88(right) $\chi_{opt} \equiv \chi(|M_L| = |M_{Lopt}|)$ is plotted as a function of τ for various values of F. χ_{opt} (χ in general) increases with increasing τ due to the increase of the dispersion D.

A very interesting feature of the HDA is the the energy resolution dependence over the dispersion axis on the PSD surface. The study took place both experimentally and by SIMION simulation. The lens voltages used in the experiment were determined according to §6.2.2. A similar study took place also for SIMION in order to get the focusing lens voltages. (The study was performed for $\xi = 1.23$ and $\gamma = 1.5$). The results are shown in Fig. 89 where the overall base resolution $\Re_b$ is plotted as a function of τ. Qualitative agreement between SIMION and experiment seems to be good. SIMION results were scaled by a factor of 0.54. In the same figure, theoretical results for different magnification factors are plotted in order to have an estimation of the value of this quantity as the experimental value of M_L can only be indirectly inferred from the width of the image on the PSD (see §6.2).

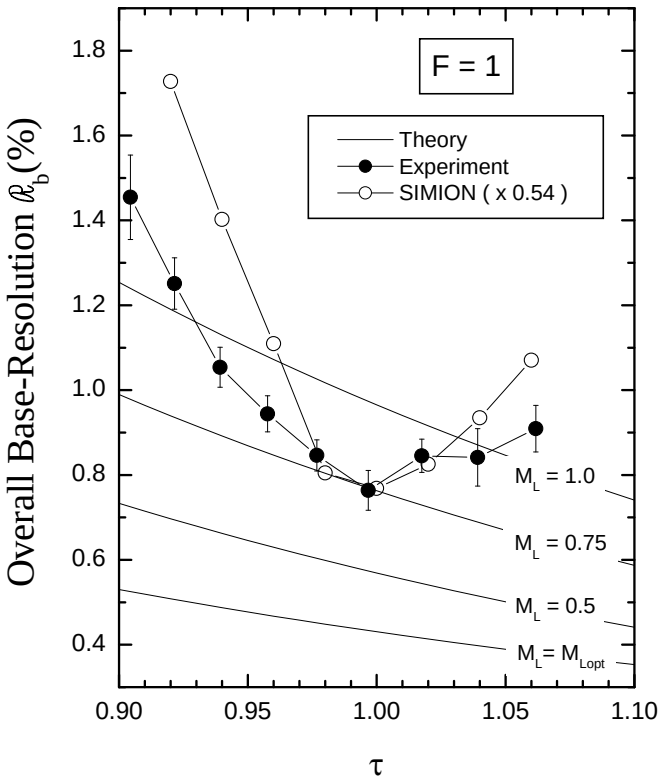

Figure 89: Overall base-resolution $\Re_b = \frac{\Delta T}{T}$ as a function of the reduced pass-energy τ. Comparison between theory (ideal $1/r$ potential), SIMION simulation and experiment. Deceleration factor was set to unity (F=1).

F SIMION3D basics

The first step in treating a problem in SIMION is to define the geometry of the 3-dimensional space where all the different elements will be confined. It is not necessary to define the space where the fields are zero. SIMION discretizes the space, transforming it to a 3-dimensional grid, and calculates the potential at each grid point of the volume, for every element, using a relaxation method. [93] The relaxation method, which actually approximates the Laplace Equation solutions, uses the 6 nearest neighbor points in the 3-dimensional space, to obtain the average new estimates for each point (except electrode points). For example, the average potential value of the grid point P_{0new} is estimated from its 6 nearest neighbor points P_i $(i = 1..6)$ as $P_{0new} = (P_1 + P_2 + P_3 + P_4 + P_5 + P_6)/6$. After certain amount of iterations the desired accuracy is obtained.

The solutions are stored in different files for each element. The final Laplace solution of the defined volume is obtained by linearly combining all the single element solutions multiplied by the potential value required for each element. The result is stored in another file in RAM. The accessibility of the Laplace solution in RAM memory has the advantage of obtaining the ion trajectories and in general any information relative to the ion flying conditions, in a very short time. Since each point of the volume requires 10 bytes of memory, it becomes clear that SIMION uses a lot of RAM memory. For example, for a volume of 100×100×100 (grid units) 10 MB of RAM memory are required.

A very important feature is that if there are any symmetries in the setup geometry (i.e. spherical or cylindrical), then only the part of the setup that can reproduce the rest of the geometry by a rotation along an axis, need to be constructed. SIMION calculates the Laplace solution at the undefined part by simply mirroring the solution of the defined part on it, during the ions flying execution. In this way a lot of RAM memory space is saved. SIMION is based upon a set of interacting files, the most important of which are listed, according to their extension names, below:

- .GEM The *Geometry files* where the electrode geometry is build using the internal SIMION commands. One can also build easily the electrode geometry using SIMION interactive environment (*modify* environment). Though this method is not recommended for complicated geometries. In either way SIMION compiles these files and the results can be seen and checked on the screen in a 3-dimensional picture (*modify* or *view* environment).

- .PA The *Potential Arrays files*. These are the files where the geometry compilation (.PA#), the Laplace solution for each element (.PA1,..., .PA5 for 5 elements) and the total Laplace solution (.PA0) are stored.

- .IOB The *Ion Optical Bench files* where many different geometries (i.e. different parts of the setup) can be combined into one. The information of the transformation factor of the grid units to mm or inches, the extension of the volume to larger areas where the potential is zero and the values of the voltages on the electrodes, are also stored in this file.

There is also another set of files less important, where information about flying conditions of the charged particles is stored. In addition SIMION can be programmed to run and save information automatically when a large number of ions are needed to be flown under different conditions.

G Classification of He-like doubly excited states

Following Lipsky's report [171], the doubly excited He-like states are classified according to the notation:

$$^{2S+1}L^{\pi} \quad (N, n\alpha)$$

where

- π is the parity values, e for even and o for odd
- N is the inner electron principal quantum number
- n is the outer electron principal quantum number
- $^{2S+1}L^{\pi}$& is the notation for the lowest energy member of series
- α is a,b,c which are obtained according to the following procedure. The obtained eigenvalues of the Hamiltonian for a given atomic system with L, S and π below N = 2 are ordered by energy. The lowest-lying state is termed a-state. The other a-states are identified from their quantum defects and from the configurations of the wavefunctions. When all of the a-states are determined, the lowest remaining state is assigned to the b-states. The procedure is repeated to the c-series.

H The Auger selection rules

- j-j coupling: $\Delta J = 0, \Delta M_J = 0$, and $\Delta\Pi = 0$
- LS-coupling: $\Delta L = 0, \Delta S = 0, \Delta M_L = 0, \Delta M_L = 0$, and $\Delta\Pi = 0$

where L is the orbital angular momentum, S is the spin, J is the total angular momentum, M_J, M_L, and M_S are the z-components of J, L, and S, respectively and Π is the parity (with values e for even and o for odd).

For example, the Auger decay of the He-like doubly excited B^{3+} states to the B^{4+} ground state, i.e.

$$^{2S+1}L^{\Pi} \rightarrow (1s)\,^2S^e + e_A(L)$$

results in the general Auger selection rule:

$$\Pi = (-1)^L$$

Therefore, states such as P^e, D^o and F^e are not permitted to Auger decay.

I The boron energy level diagram

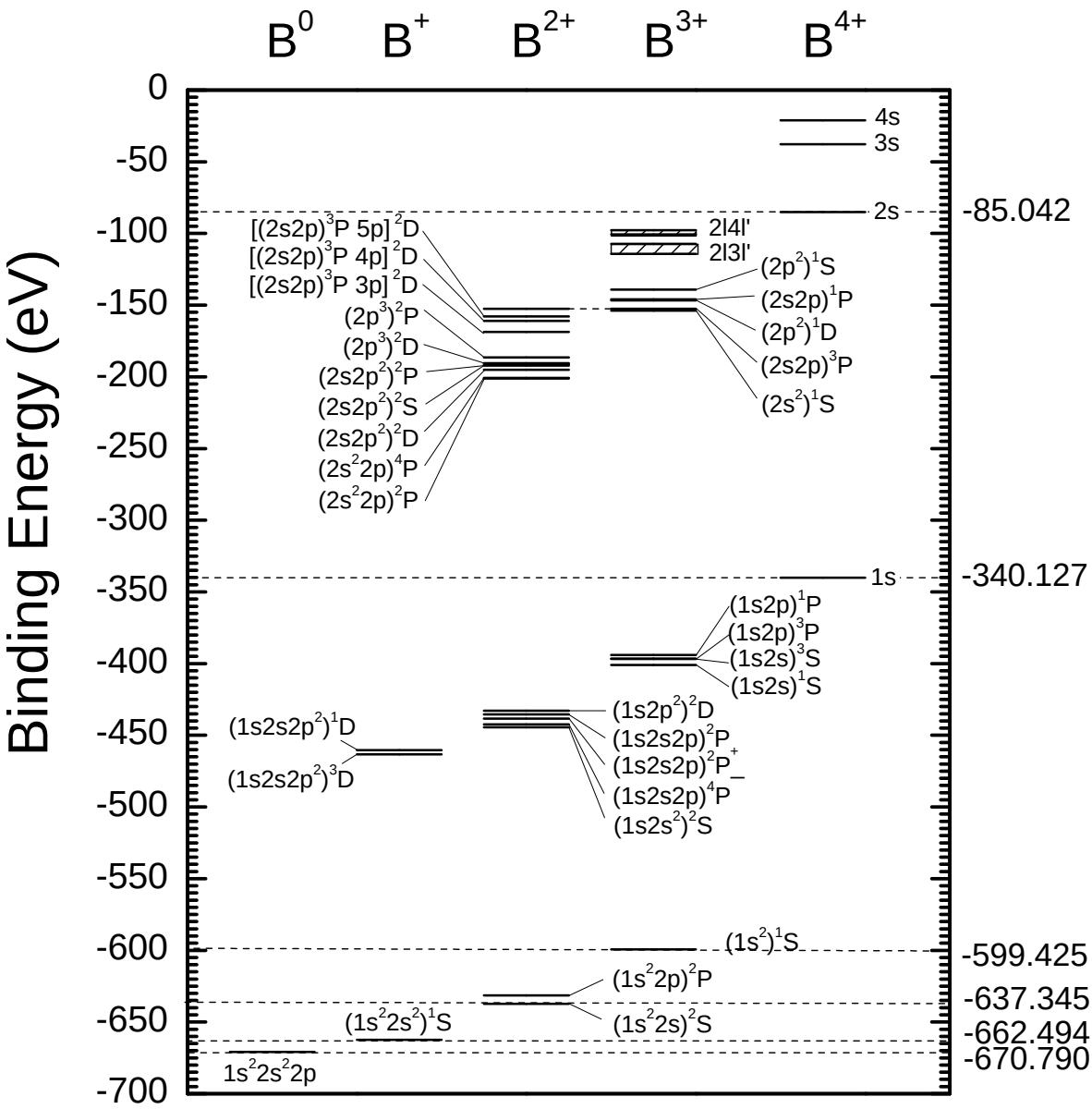

J Laboratory frame $B^{(2-4)+}$ + H_2 spectra

Laboratory frame low resolution (left graphs) and high resolution (right graphs) absolute DDCS spectra for the collisions of $B^{(2-4)+}$ ions with H_2 targets. Solid lines are the ESM calculations except in the case of B^{2+} which are the scaled Rutherford calculations. Dashed lines, wherever present, refer to the polynomial background fit of the high resolution experimental data. Different data notations (open and filled circles) refer to different energy slices.

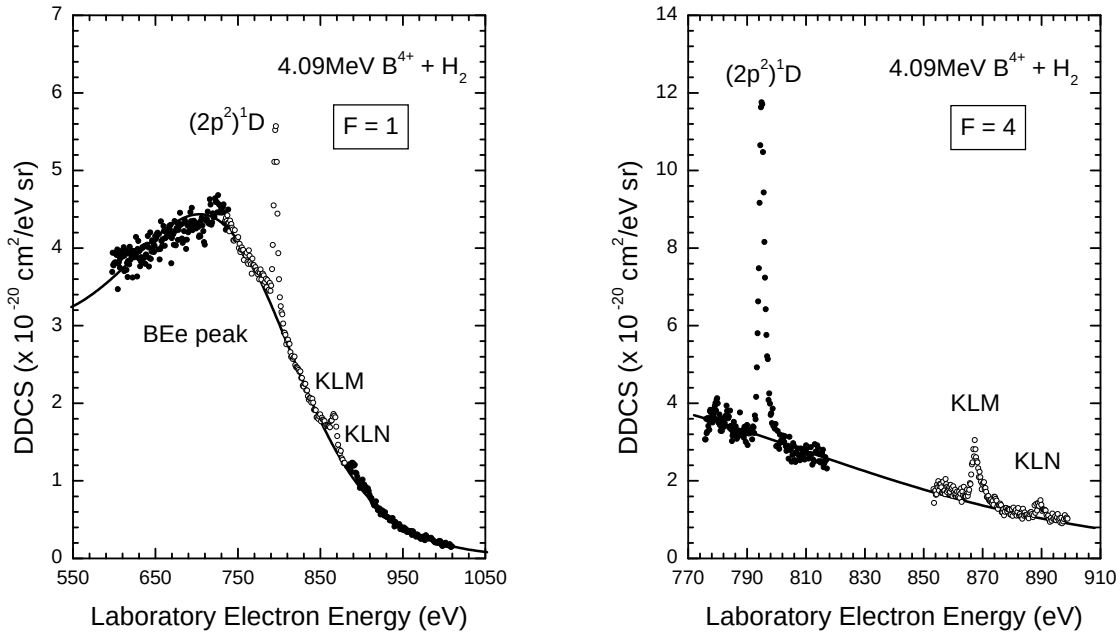

Laboratory frame data correspond to projectile rest frame data of Fig. 64 (top).

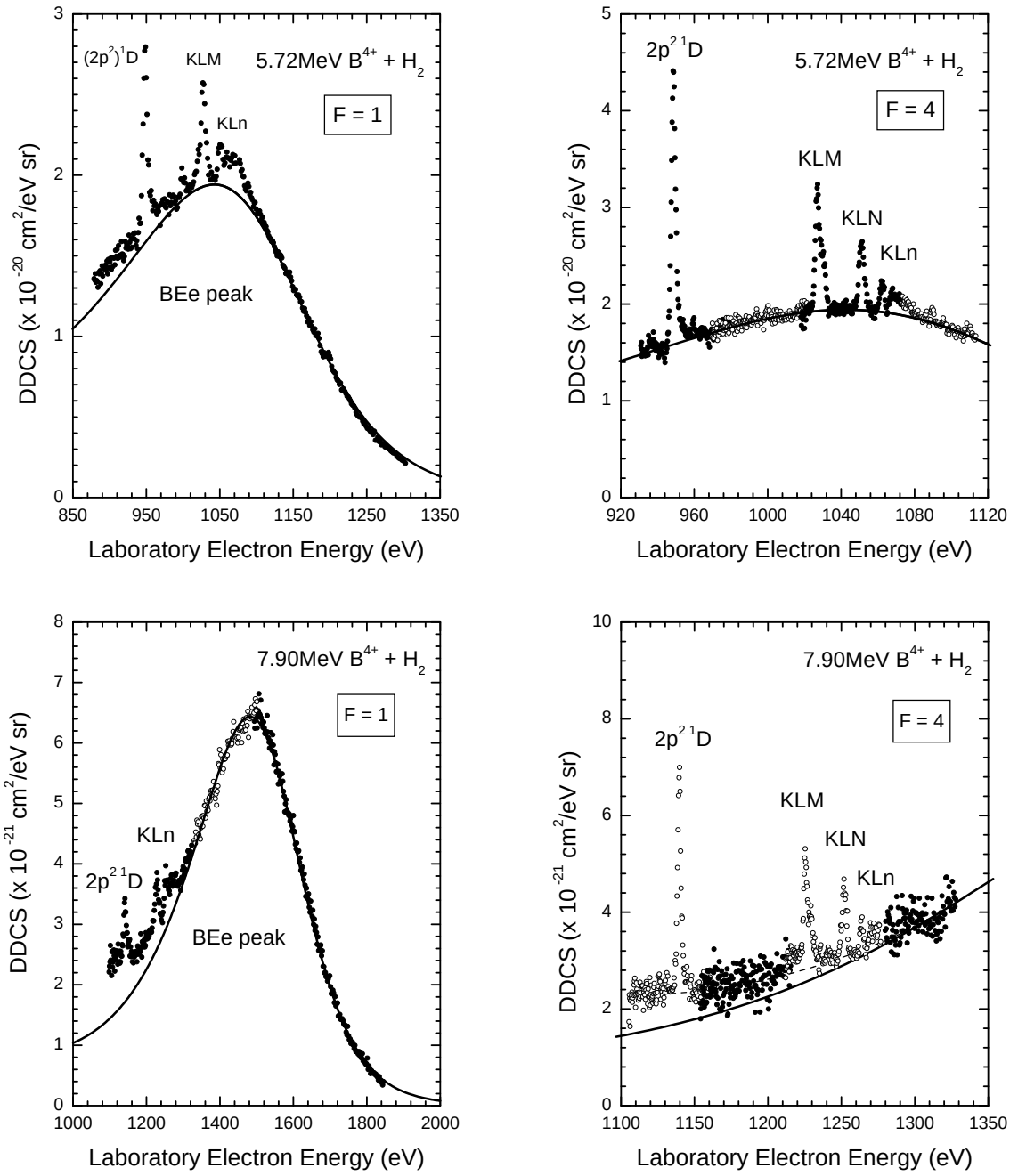

[*Top*] Laboratory frame data correspond to projectile rest frame data of Fig. 64 (middle). [*Bottom*] Laboratory frame data correspond to projectile rest frame data of Fig. 64 (bottom).

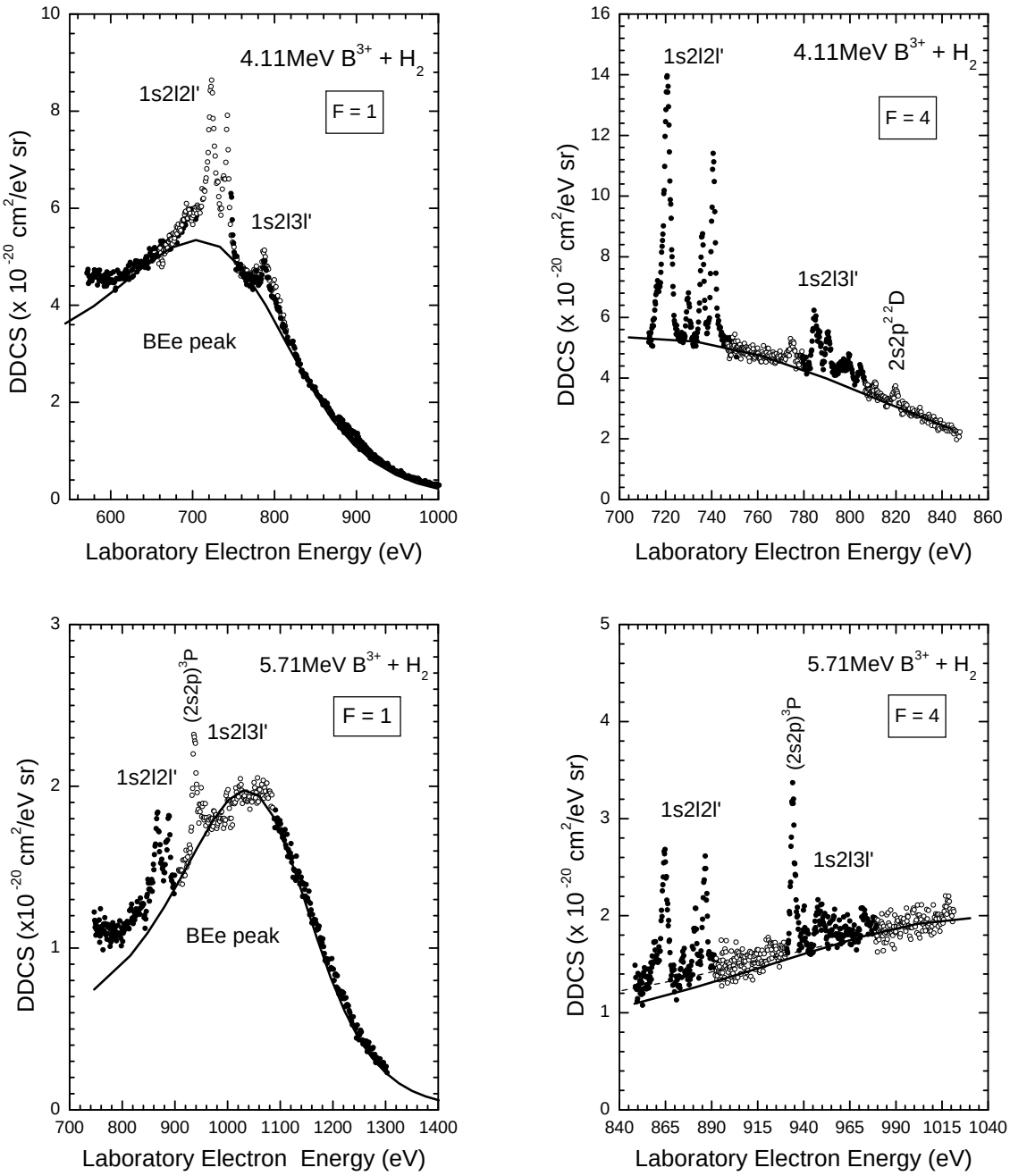

[*Top*] Laboratory frame data correspond to projectile rest frame data of Fig. 66 (top). [*Bottom*] Laboratory frame data correspond to projectile rest frame data of Fig. 66 (middle).

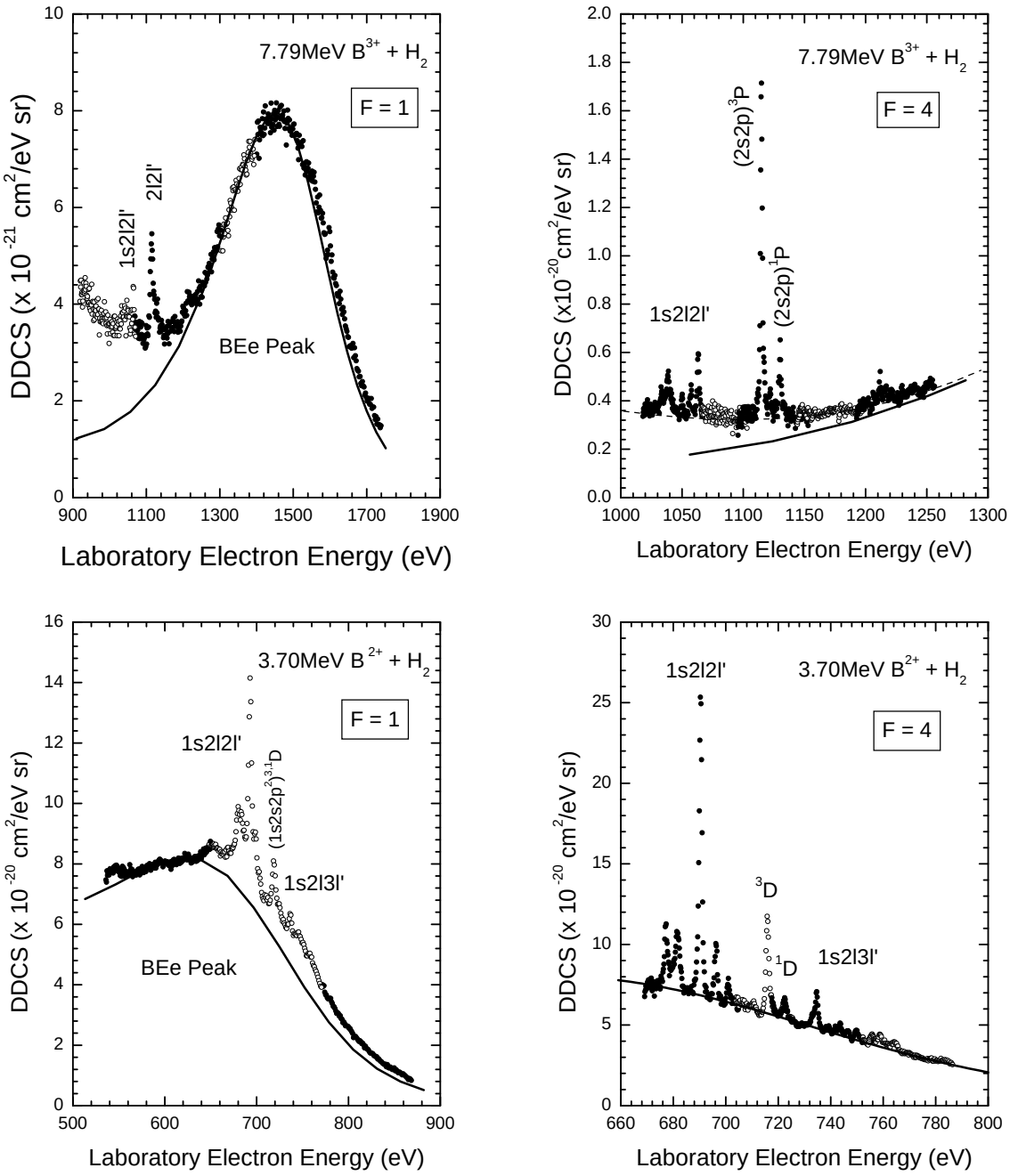

[*Top*] Laboratory frame data correspond to projectile rest frame data of Fig. 66 (bottom). [*Bottom*] Laboratory frame data correspond to projectile rest frame data of Fig. 72 (top).

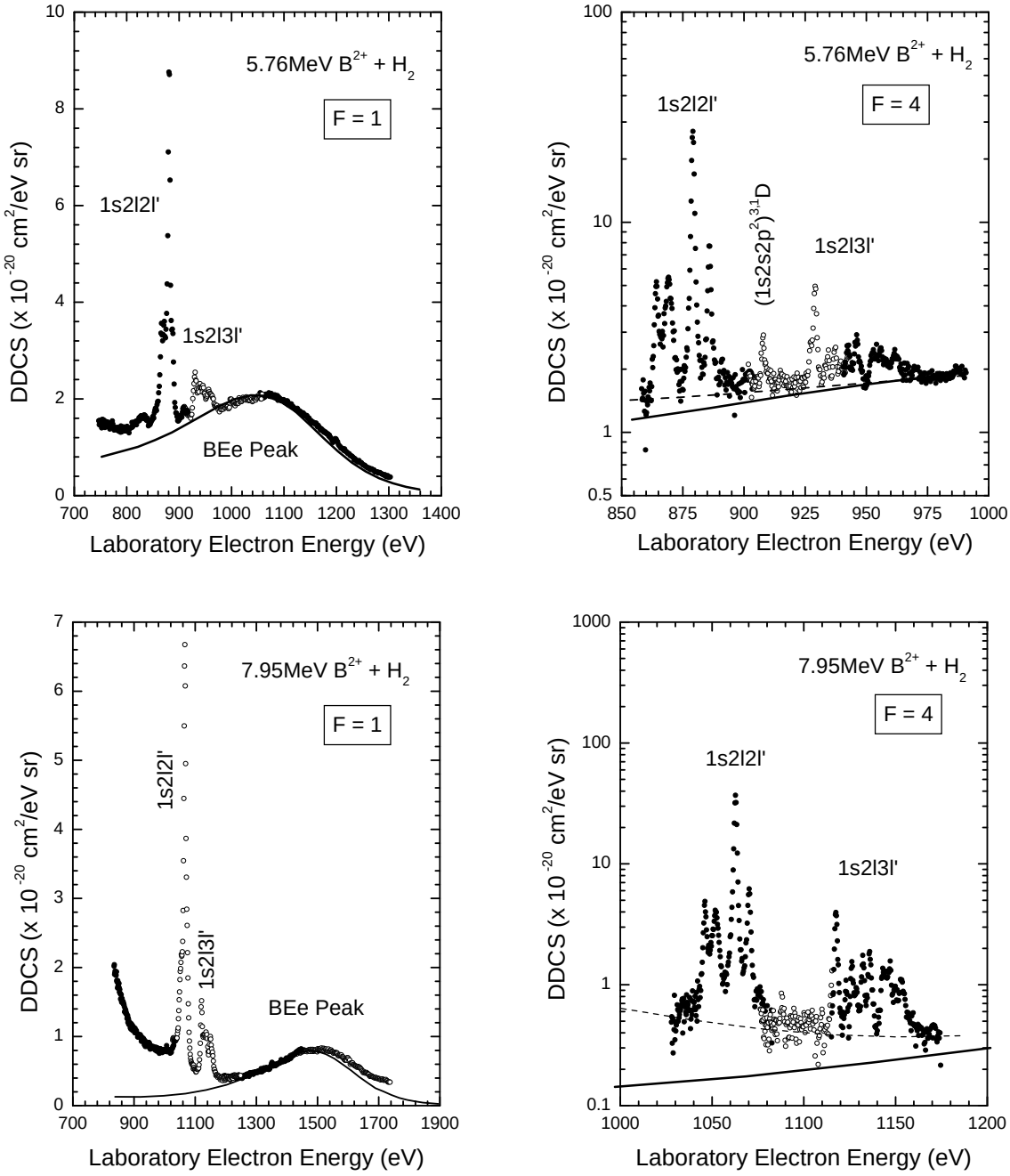

[*Top*] Laboratory frame data correspond to projectile rest frame data of Fig. 72 (middle). [*Bottom*] Laboratory frame data correspond to projectile rest frame data of Fig. 72 (bottom).

References

[1] K. Taulbjerg, J. Phys. B **23**, L761 (1990).

[2] P. Richard *et al.*, J. Phys. B **23**, L213 (1990).

[3] E. Rutherford, Phil. Mag. **21**, 669 (1911).

[4] N. F. Mott and H. S. W. Massey, *The Theory of Atomic Collisions* (Oxford University Press, London, 1965).

[5] K.-O. Groeneveld, E. Shopper, and S. Schumann, in *Solid State Nuclear Track Detectors*, edited by H. Francois (Oxford and New York, p. 81, 1980).

[6] A. Itoh *et al.*, J. Phys. B **16**, 3965 (1983).

[7] A. Itoh *et al.*, Phys. Rev. A **31**, 684 (1985).

[8] N. Stolterfoht, Phys. Rep. **146**, 315 (1987).

[9] N. Stolterfoht *et al.*, Nucl. Instrum. Methods in Phys. Res. B **24/25**, 168 (1987).

[10] T. J. M. Zouros and D. H. Lee, in *Accelerator-based atomic physics techniques and applications*, edited by S. M. Shafroth and J. C. Austin (American Institute of Physics Conference Series, New York, 1997), pp. 426–79.

[11] I. A. Sellin, in *Topics in Current Physics*, edited by S. Bashkin (Springer, Heidelberg, 1976), Vol. 1, p. 265.

[12] N. Stolterfoht, J. Electr. Spectr. and Rel. Phenom. **67**, 309 (1994).

[13] N. Stolterfoht, in *Fundamental Processes in Energetic Atomic Collisions*, edited by H. O. Lutz, J. S. Briggs, and H. Kleinpoppen (Plenum, New York, 1983), Vol. 103, pp. 295–318.

[14] J. Ullrich *et al.*, J. Phys. B **30**, 2917 (1997).

[15] K. Siegbahn *et al.*, Nova Acta Regiae Soc. Sci. Upsaliensis ser. IV **20**, (1967).

[16] W. Ho, J. Vac. Sci. Technol. **A3**, 1432 (1984).

[17] E. P. Benis and T. J. M. Zouros, Nucl. Instrum. Methods in Phys. Res. A **440**, 462 (2000).

[18] J. K. Swenson and D. Brandt, IEEE Trans. Nucl. Sci. Vol. **NS-30**, 1584 (1983).

[19] R. Morgenstern, A. Niehaus, and U. Thielmann, Phys. Rev. Lett. **37**, 199 (1976).

[20] R. Morgenstern, A. Niehaus, and U. Thielmann, J. Phys. B **10**, 1039 (1977).

[21] R. Morgenstern, A. Niehaus, and G. Zimmermann, J. Phys. B **13**, 4811 (1980).

[22] A. Itoh *et al.*, J. Phys. B **18**, 4581 (1985).

[23] T. J. M. Zouros, D. Schneider, A. Itoh, and N. Stolterfoht, Phys. Rev. A **35**, 1963 (1987).

[24] T. J. M. Zouros, D. Schneider, and N. Stolterfoht, Nucl. Instrum. Methods in Phys. Res. B **31**, 349 (1988).

[25] M. L. A. Raphaelian, H. G. Berry, and N. B. Mansour, Phys. Rev. A **43**, 4071 (1991).

[26] J. K. Swenson *et al.*, Phys. Rev. Lett. **57**, 3042 (1986).

[27] T. J. M. Zouros, D. Schneider, and N. Stolterfoht, J. Phys. B **21**, L671 (1988).

[28] T. J. M. Zouros *et al.*, Phys. Rev. A **40**, 6246 (1989).

[29] B. D. DePaola, R. Parameswaran, and W. J. Axmann, Phys. Rev. A **41**, 6533 (1990).

[30] T. J. M. Zouros, C. P. Bhalla, D. H. Lee, and P. Richard, Phys. Rev. A **42**, 678 (1990).

[31] D. H. Lee *et al.*, Phys. Rev. A **44**, 1636 (1991).

[32] R. C. Parameswaran, C. P. Bhalla, B. P. Walch, and B. D. DePaola, Phys. Rev. A **43**, 5929 (1991).

[33] T. J. M. Zouros, D. H. Lee, and P. Richard, Phys. Rev. Lett. **62**, 2261 (1989).

[34] B. Sulik *et al.*, Phys. Rev. A **52**, 387 (1995).

[35] H. P. Hülskötter, W. E. Meyerhof, E. Dillard, and N. Guardala, Phys. Rev. Lett. **63**, 1938 (1990).

[36] T. J. M. Zouros, D. H. Lee, P. Richard, and J. M. Sanders, Nucl. Instrum. Methods in Phys. Res. B **56/57**, 107 (1991).

[37] D. H. Lee *et al.*, Phys. Rev. A **46**, 1374 (1992).

[38] N. Stolterfoht *et al.*, Phys. Rev. Lett. **57**, 74 (1987).

[39] R. Mann, Phys. Rev. A **35**, 4988 (1987).

[40] H. A. Sakaue *et al.*, J. Phys. B **23**, L401 (1990).

[41] H. A. Sakaue *et al.*, J. Phys. B **24**, 3787 (1991).

[42] M. Breinig *et al.*, Phys. Rev. A **25**, 3015 (1982).

[43] H. I. Hidmi, P. Richard, and I. Ben-Itzhak, Nucl. Instrum. Methods in Phys. Res. B **88**, 313 (1994).

[44] T. J. M. Zouros *et al.*, Phys. Rev. A **53**, 2272 (1996).

[45] R. Mann, S. Hagmann, and L. Weitzel, Nucl. Instrum. Methods in Phys. Res. B **34**, 403 (1988).

[46] D. H. Lee *et al.*, Phys. Rev. A **41**, 4816 (1990).

[47] N. Stolterfoht, R. D. Dubois, and R. D. Rivarola, *Electron emission in heavy ion-atom collisions* (Springer Series on Atoms and Plasmas, Heidelberg, 1997).

[48] P. Závodszky *et al.*, J. Phys. B **32**, 4425 (1999).

[49] E. Bonderup and P. Hvelplund, Phys. Rev. A **4**, 562 (1971).

[50] P. Sigmund, Phys. Rev. A **14**, 996 (1976).

[51] N. L. S. Martin and A. von Engel, J. Phys. D **10**, 863 (1977).

[52] W. Colson, J. McPherson, and F. King, Rev. Sci. Instrum. **44**, 1694 (1973).

[53] J. Adams and B. Manley, IEEE Transactions on Nuclear Science **NS-13**, 88 (1966).

[54] J. Wiza, Nucl. Instrum. & Methods **162**, 587 (1979).

[55] M. Lampton and C. Carlson, Rev. Sci. Instrum. **50**, 1093 (1979).

[56] E. Purcell, Phys. Rev. **54**, 818 (1938).

[57] C. Kuyatt and J. A. Simpson, Rev. Sci. Instrum. **38**, 103 (1967).

[58] F. Paolini and G. Theodoridis, Rev. Sci. Instrum. **38**, 579 (1967).

[59] P. Kemeny *et al.*, Rev. Sci. Instrum. **44**, 1197 (1973).

[60] D. Roy and J.-D. Carette, Applied Physics Letters **16**, 413 (1970).

[61] D. Roy and J.-D. Carette, Can. J. Phys. **49**, 2138 (1971).

[62] D. Heddle, J. Phys. E: Sci. Instrum. **4**, 589 (1971).

[63] H. Polaschegg, Applied Physics **4**, 63 (1974).

[64] H. Polaschegg, Applied Physics **9**, 223 (1976).

[65] R. E. Imhof, A. Adams, and G. King, J. Phys. E: Sci. Instrum. **9**, 138 (1976).

[66] S. Kevan, Rev. Sci. Instrum. **54**, 1441 (1983).

[67] F. Hadjarab and J. Erskine, J. Electr. Spectr. and Rel. Phenom. **36**, 227 (1985).

[68] A. Mann and F. Linder, J. Phys. E: Sci. Instrum. **21**, 805 (1988).

[69] A. Baraldi and V. R. Dhanak, J. Electr. Spectr. and Rel. Phenom. **67**, 211 (1994).

[70] S. C. Page and F. H. Read, Nucl. Instrum. Methods Phys. Res. Sect. A **363**, 249 (1995).

[71] V. P. Afanas'ev and S. Y. Yavor, Sov. Phys. Tech. Phys. **20**, 715 (1976), [Translation of Zh. Tekh. Fiz. **45**, 1137-70 (1975)].

[72] D. Roy and D. Tremblay, Rep. Prog. Phys. **53**, 1621 (1990).

[73] M. E. Rudd, in *Low Energy Electron Spectrometry*, edited by K. D. Sevier (Wiley, New York, 1972), pp. 17–34.

[74] R. Herzog, Z. Phys. **97**, 596 (1935).

[75] F. Mariani, Rev. Sci. Instrum. **41**, 807 (1970).

[76] M. Minkov, Sov. Phys. Tech. Phys. **5**, 1285 (1971).

[77] K. Jost, J. Phys. E: Sci. Instrum. **12**, 1001 (1979).

[78] A. Baraldi, V. R. Dhanak, and G. C. King, Meas. Sci. Technol. **3**, 778 (1992).

[79] D. Hu and K. Leung, Rev. Sci. Instrum. **66**, 2865 (1995).

[80] V. D. Belov and M. I. Yavor, Rev. Sci. Instrum. **71**, 1651 (2000).

[81] E. P. Benis *et al.*, Nucl. Instrum. Methods in Phys. Res. B **146**, 120 (1998).

[82] E. P. Benis, T. J. M. Zouros, and P. Richard, Nucl. Instrum. Methods in Phys. Res. B **154**, 276 (1999).

[83] E. P. Benis, T. J. M. Zouros, H. Aliabadi, and P. Richard, Physica Scripta **T80**, 529 (1999).

[84] H. Goldstein, *Classical Mechanics* (Addison-Wesley, Reading, Massachussets, 1965).

[85] T. J. M. Zouros, E. P. Benis, and J. E. Schauer, AIP (in press) (2001).

[86] M. E. Rudd and J. H. Macek, in *Case Studies in Atomic Physics*, edited by E. W. McDaniels and M. C. McDowell (North–Holland, Amsterdam, 1972), Vol. 3, pp. 47–136.

[87] P. Louette *et al.*, J. Electr. Spectr. and Rel. Phenom. **52**, 867 (1990).

[88] A. Poulin and D. Roy, J. Phys. E: Sci. Instrum. **11**, 35 (1978).

[89] D. H. Lee *et al.*, Nucl. Instrum. Methods in Phys. Res. B **40/41**, 1229 (1989).

[90] B. Sulik and N. Stolterfoht, in *Accelerator-based atomic physics techniques and applications*, edited by S. M. Shafroth and J. C. Austin (American Institute of Physics Conference Series, New York, 1997), pp. 377–425.

[91] J. H. Moore, C. C. Davis, and M. A. Coplan, *Building Scientific Apparatus* (Addison-Wesley, London, 1983).

[92] V. Schmidt, *Electron Spectrometry of Atoms using Synchrotron Radiation* (Cambridge University Press, Cambridge UK, 1997).

[93] D. A. Dahl, *SIMION 3D v6.0* (Idaho National Engineering Laboratory, Idaho Falls, 1996).

[94] K. D. Sevier, *Low Energy Electron Spectrometry* (Wiley, New York, 1972).

[95] T. J. M. Zouros, in *Recombination of Atomic Ions*, NATO Advanced Study Institute Series B: Physics, edited by W. G. Graham, W. Fritsch, Y. Hahn, and J. Tanis (Plenum Publishing Corporation, New York, 1992), Vol. 296, pp. 271–300.

[96] D. H. Lee, Ph.D. dissertation, Kansas State University, 1990, (unpublished).

[97] J. R. Macdonald and F. W. Martin, Phys. Rev. A **4**, 1965 (1971).

[98] F. Bordoni, Nucl. Instrum. & Methods **97**, 405 (1971).

[99] R. Goruganthu and W. Wilson, Rev. Sci. Instrum. **55**, 2030 (1984).

[100] A. Müller, N. Djurić, G. Dunn, and D. Belić, Rev. Sci. Instrum. **57**, 349 (1985).

[101] P. R. Bevington, *Data Reduction and Error Analysis for the Physical Sciences* (McGraw-Hill Inc, New York, 1969).

[102] N. Stolterfoht *et al.*, Phys. Rev. Lett. **33**, 59 (1974).

[103] J. W. M. DuMond, Rev. Mod. Phys. **5**, 1 (1933).

[104] M. E. Rudd, Y. K. Kim, D. H. Madison, and T. J. Gay, Rev. Mod. Phys. **64**, 441 (1992).

[105] P. Richard, in *Two-Center Effects In Ion-Atom Collisions*, edited by T. J. Gay and A. F. Starace (American Institute of Physics Conference Series, New York, 1996), Vol. 362, p. 69.

[106] P. D. Fainstein, V. H. Ponce, and R. D. Rivarola, J. Phys. B **24**, 3091 (1991).

[107] N. Stolterfoht, in *Topics in Current Physics, Vol. 5: Structure and Collisions of Ions and Atoms*, edited by I. A. Sellin (Springer Verlag, Berlin, 1978), p. 155.

[108] J. H. McGuire, N. Stolterfoht, and P. R. Simony, Phys. Rev. A **24**, 97 (1981).

[109] L. H. Toburen, N. Stolterfoht, P. Ziem, and D. Schneider, Phys. Rev. A **24**, 1741 (1981).

[110] C. P. Bhalla, Phys. Rev. Lett. **64**, 1103 (1990).

[111] L. H. Toburen, N. F. Meeting, and L. A. Brandy, Nucl. Instrum. Methods in Phys. Res. B **40/41**, 1275 (1989).

[112] K. Katz, *Quantitative Mathematical Models in Radiation Biology* (Springer, Berlin, 1988).

[113] D. R. Schultz and R. E. Olson, J. Phys. B **24**, 3409 (1991).

[114] M. E. Rudd and T. Jorgensen, Phys. Rev. **131**, 666 (1963).

[115] M. E. Rudd, C. A. Sauter, and C. L. Bailey, Phys. Rev. **151**, 20 (1966).

[116] T. F. M. Bonsen and L. Vriens, Physica **47**, 307 (1970).

[117] S. T. Manson, L. H. Toburen, D. H. Madison, and N. Stolterfoht, Phys. Rev. A **12**, 60 (1975).

[118] L. H. Toburen and W. E. Wilson, Phys. Rev. A **19**, 2214 (1979).

[119] L. H. Toburen, Radiat. Res. **82**, 29 (1979).

[120] C. Kelbch *et al.*, Phys. Lett. **139A**, 304 (1989).

[121] R. E. Olson, C. O. Reinhold, and D. R. Schultz, J. Phys. B **23**, L455 (1990).

[122] C. O. Reinhold, D. R. Schultz, and R. E. Olson, J. Phys. B **23**, L591 (1990).

[123] R. Shingal *et al.*, J. Phys. B **23**, L637 (1990).

[124] A. D. González, P. Hvelplund, A. G. Petersen, and K. Taulbjerg, J. Phys. B **25**, L57 (1992).

[125] H. I. Hidmi *et al.*, Phys. Rev. A **47**, 2398 (1993).

[126] Z. Chen, D. Madison, and C. D. Lin, J. Phys. B **24**, 3203 (1991).

[127] A. Salin, J. Phys. B **24**, L611 (1991).

[128] K. Taulbjerg, J. Phys. B **24**, 1125 (1991).

[129] C. P. Bhalla and R. Shingal, J. Phys. B **24**, 3187 (1991).

[130] T. B. Quinteros *et al.*, J. Phys. B **24**, 1377 (1991).

[131] O. Jagutzki *et al.*, J. Phys. B **24**, 2579 (1991).

[132] H. I. Hidmi, P. Richard, J. M. Sanders, and T. J. M. Zouros, in *VIth International Conference on Physics of Highly Charged Ions*, edited by P. Richard, M. Stöckli, C. L. Cocke, and C. D. Lin (AIP, New York, 1993), Vol. 274, p. 319.

[133] J. H. Posthumus *et al.*, J. Phys. B **27**, L97 (1994).

[134] C. Liao *et al.*, Phys. Rev. A **50**, 1328 (1994).

[135] C. O. Reinhold *et al.*, Phys. Rev. Lett. **66**, 1842 (1991).

[136] C. O. Reinhold, D. R. Schultz, and R. E. Olson, Nucl. Instrum. Methods in Phys. Res. B **56/57**, 271 (1991).

[137] T. Quinteros and J. F. Reading, Nucl. Instrum. Methods in Phys. Res. B **53**, 363 (1991).

[138] V. H. Ponce, P. D. Fainstein, and R. D. Rivarola, J. Phys. B **26**, 1343 (1993).

[139] T. J. M. Zouros *et al.*, Phys. Rev. A **49**, 3155 (1994).

[140] S. Hagmann *et al.*, J. Phys. B **25**, L287 (1992).

[141] W. Wolff *et al.*, J. Phys. B **25**, 3683 (1992).

[142] W. Wolff *et al.*, J. Phys. B **26**, L65 (1993).

[143] W. Wolff *et al.*, J. Phys. B **28**, 1265 (1995).

[144] A. D. González, P. Dahl, P. Hvelplund, and K. Taulbjerg, J. Phys. B **25**, L573 (1992).

[145] D. H. Schneider *et al.*, Phys. Rev. A **46**, 1296 (1992).

[146] J. L. Shinpaugh *et al.*, J. Phys. B **26**, 2869 (1993).

[147] M. Kuzel *et al.*, J. Phys. B **27**, 1993 (1994).

[148] R. D. Dubois, L. H. Toburen, M. E. Middendorf, and O. Jagutzki, Phys. Rev. A **49**, 350 (1994).

[149] U. Ramm *et al.*, Nucl. Instrum. Methods in Phys. Res. B **146**, 39 (1998).

[150] C. Liao *et al.*, Phys. Rev. A **59**, 2773 (1999).

[151] J. Miraglia and J. Macek, Phys. Rev. A **43**, 5919 (1991).

[152] P. D. Fainstein, V. H. Ponce, and R. D. Rivarola, Phys. Rev. A **45**, 6417 (1992).

[153] D. H. Jakubaßa-Amundsen, Phys. Rev. A **49**, 2634 (1994).

[154] P. D. Fainstein, L. Gulyás, and A. Salin, J. Phys. B **27**, L259 (1994).

[155] J. N. Madsen and K. Taulbjerg, J. Phys. B **27**, 2239 (1994).

[156] L. Gulyás, P. D. Fainstein, and A. Salin, J. Phys. B **28**, 245 (1995).

[157] D. H. Jakubaßa-Amundsen and P. Küprik, Phys. Rev. A **56**, 395 (1997).

[158] T. Jalowy, D. H. Jakubaßa-Amundsen, M. W. Lucas, and K. O. Groeneveld, Phys. Rev. A **61**, 022714 (2000).

[159] U. Bechthold *et al.*, Phys. Rev. Lett. **79**, 2034 (1997).

[160] S. Suárez, R. O. Barrachina, and W. Meckbach, prl **77**, 474 (1996).

[161] B. Sulik *et al.*, Phys. Rev. Lett. (2001).

[162] D. Brandt, Phys. Rev. A **27**, 1314 (1983).

[163] P. Richard, C. Bhalla, S. Hagmann, and P. Zavodsky, Physica Scripta **T80**, 87 (1999).

[164] T. J. M. Zouros, Comments At. & Mol. Phys. **32**, 291 (1996).

[165] C. P. Bhalla, in *Recombination of Atomic Ions*, NATO Advanced Study Institute Series B: Physics, edited by W. G. Graham, W. Fritsch, Y. Hahn, and J. Tanis (Plenum Publishing Corp, New York, 1992), Vol. 296, pp. 87–97.

[166] F. Biggs, L. B. Mendelsohn, and J. B. Mann, At. Data & Nucl. Data Tables **16**, 201 (1975).

[167] J. S. Lee, J. Chem. Phys. **66**, 4906 (1977).

[168] B. H. Bransden, *Atomic Collision Theory* (W. A. Benjamin, New York, 1970).

[169] S. R. Grabbe, Ph.D. dissertation, Kansas State University, 1997 (unpublished).

[170] K. Taulbjerg, J. Phys. B **24**, L617 (1991).

[171] L. Lipsky, R. Anania, and M. J. Conneely, At. Data & Nucl. Data Tables **20**, 127 (1977).

[172] M. Rødbro, R. Bruch, and P. Bisgaard, J. Phys. B **12**, 2413 (1979).

[173] U. I. Safronova, A. S. Shlyaptseva, and R. Bruch, Physica Scripta **57**, 519 (1998).

[174] W. Fritsch and C. D. Lin, Phys. Rev. Lett. **61**, 690 (1988).

[175] C. D. Lin, in *Advances in atomic and molecular physics*, edited by S. D. Bates and B. Bederson (Academic Press, New York, 1986), pp. 77–142.

[176] R. D. Cowan, *The theory of atomic structure and spectra* (University of California Press, Berkeley, CA, 1981).

[177] S. E. Schippers, KVI internal report no. KVI-189i **Version 6.1**, 1 (2000).

[178] P. L. Pepmiller *et al.*, IEEE Trans. Nucl. Sci. **NS-30**, 1002 (1983).

[179] P. Richard, in *Atomic Inner–Shell Processes*, edited by B. Crasemann (Academic Press, New York, 1975), Vol. 1, pp. 73–158.

[180] M. Zamkov *et al.*, Phys. Rev. A to be published (2001).

[181] A. S. Schlachter *et al.*, Phys. Rev. A **27**, 3372 (1983).

[182] R. Bruch, G. Paul, J. Andrä, and L. Lipsky, Phys. Rev. A **12**, 1808 (1975).

[183] J. N. Madsen, P. Schlagheck, and P. Lambropoulos, Phys. Rev. Lett. **85**, 42 (2000).

[184] Y. Azuma *et al.*, Phys. Rev. Lett. **79**, 2419 (1997).

[185] J. N. Madsen, P. Schlagheck, and P. Lambropoulos, Phys. Rev. A **62**, 062719 (2000).

[186] I. D. Williams, J. B. Greenwodd, and P. McGuiness, J. Phys. B **28**, L555 (1995).

[187] P. Závodszky *et al.*, Phys. Rev. Lett. to be published (2001).

[188] P. Závodszky *et al.*, Phys. Rev. A **58**, 2001 (1998).

[189] A. A. Saghiri *et al.*, Phys. Rev. A **60**, R3350 (1999).

[190] E. P. Benis *et al.*, Production of triply excited states in Li-like boron XXI ICPEAC, Sendai, Japan (1999).

[191] M. Terasawa *et al.*, Phys. Rev. A **27**, 2868 (1983).

[192] C. Y. Fan, M. Garcia-Munoz, and I. A. Sellin, prl **15**, 15 (1965).

[193] G. P. Lawrence, C. Y. Fan, and S. Bashkin, Phys. Rev. Lett. **25**, 1612 (1972).

[194] T. R. Dillingham, Ph.D. dissertation, Kansas State University, (1983).

[195] T. W. Tunnell, C. Can, and C. P. Bhalla, IEEE Trans. Nucl. Sci. **NS-26**, 1124 (1979).

[196] M. Zamkov *et al.*, Stripping energy dependence of $B^{3+}(1s2s^3S)$ metastable beam fraction produced in a tandem accelerator 16th International Conference on the Application of Accelerators in Research and Industry (2000).

[197] G. Toth *et al.*, Nucl. Instrum. Methods in Phys. Res. B **124**, 413 (1997).

[198] B. Sulik, T. J. M. Zouros, A. Orbán, and L. Gulyás, J. Electr. Spectr. and Rel. Phenom. **114-116**, 191 (2001).

[199] J. A. Tanis *et al.*, Phys. Rev. Lett. **49**, 1325 (1982).

[200] J. A. Tanis *et al.*, Phys. Rev. Lett. **47**, 828 (1981).

[201] J. A. Tanis *et al.*, Phys. Rev. Lett. **53**, 2551 (1984).

[202] J. A. Tanis *et al.*, Nucl. Instrum. Methods in Phys. Res. B **10/11**, 128 (1985).

[203] J. A. Tanis *et al.*, Phys. Rev. A **31**, 4040 (1985).

[204] J. A. Tanis *et al.*, Phys. Rev. A **34**, 2543 (1986).

[205] W. G. Graham *et al.*, Phys. Rev. A **33**, 3591 (1986).

[206] S. Reusch *et al.*, Nucl. Instrum. Methods in Phys. Res. B **B23**, 137 (1987).

[207] M. Schulz *et al.*, Phys. Rev. A **38**, 5454 (1988).

[208] E. M. Bernstein *et al.*, Phys. Rev. A **40**, 4085 (1989).

[209] W. G. Graham *et al.*, Phys. Rev. Lett. **65**, 2773 (1990).

[210] E. M. Bernstein *et al.*, Phys. Rev. A **44**, 4210 (1991).

[211] M. W. Clark *et al.*, Phys. Rev. A **45**, 7846 (1992).

[212] K. Zaharakis *et al.*, Phys. Rev. A **52**, 2910 (1995).

[213] M. Schulz *et al.*, Phys. Rev. Lett. **58**, 1734 (1987).

[214] R. Schuch *et al.*, Phys. Rev. A **43**, 5180 (1991).

[215] T. J. M. Zouros *et al.*, Nucl. Instrum. Methods in Phys. Res. B **40/41**, 17 (1989).

[216] M. Benhenni *et al.*, Phys. Rev. Lett. **65**, 1849 (1990).

[217] R. Parameswaran *et al.*, Phys. Rev. A **47**, 3801 (1993).

[218] A. Burgess, Astrophys. J. **139**, 776 (1964).

[219] A. Burgess, Astrophys. J. **141**, 1588 (1965).

[220] Y. Hahn, Comments At. & Mol. Phys. **19**, 99 (1987).

[221] Y. Hahn, Phys. Rev. A **40**, 2950 (1989).

[222] Y. Hahn and K. J. LaGattuta, Phys. Rep. **166**, 195 (1988).

[223] J. Dubau and S. Volonté, Rep. Prog. Phys. **43**, 199 (1980).

[224] R. Schuch *et al.*, Nucl. Instrum. Methods in Phys. Res. B **23**, 140 (1987).

[225] D. S. Belic *et al.*, Phys. Rev. Lett. **50**, 339 (1983).

[226] P. F. Dittner *et al.*, Phys. Rev. Lett. **51**, 31 (1983).

[227] J. B. A. Mitchell *et al.*, Phys. Rev. Lett. **50**, 335 (1983).

[228] P. F. Dittner *et al.*, Phys. Rev. A **36**, 33 (1987).

[229] G. Kilgus *et al.*, Phys. Rev. Lett. **64**, 737 (1990).

[230] A. Müller, Comments At. & Mol. Phys. **32**, 143 (1996).

[231] D. J. McLaughlin and Y. Hahn, Phys. Rev. A **112**, 389 (1985).

[232] D. J. McLaughlin and Y. Hahn, Phys. Lett. **88A**, 394 (1982).

[233] N. R. Badnell, Phys. Rev. A **40**, 3579 (1989).

[234] C. P. Bhalla and K. R. Karim, Phys. Rev. A **39**, 6060 (1989).

[235] M. H. Chen, Phys. Rev. A **42**, 5228 (1990).

[236] D. J. McLaughlin and Y. Hahn, Phys. Rev. A **37**, 3587 (1988).

[237] M. Schulz *et al.*, Phys. Rev. Lett. **62**, 1738 (1989).

[238] P. L. Pepmiller *et al.*, Phys. Rev. A **31**, 734 (1985).

[239] M. Clark, D. Brandt, J. K. Swenson, and S. M. Shafroth, Phys. Rev. Lett. **54**, 544 (1985).

[240] J. M. Feagin, J. S. Briggs, and T. M. Reeves, J. Phys. B **17**, 1057 (1984).

[241] D. Brandt, Nucl. Instrum. & Methods **214**, 93 (1983).

[242] A. Jain, R. Shingal, and T. J. M. Zouros, Phys. Rev. A **43**, 1621 (1991).

[243] R. Gayet and J. Hanssen, J. Phys. B **25**, 825 (1992).

[244] H. Bachau, R. Gayet, J. Hanssen, and A. Zerarka, J. Phys. B **25**, 839 (1992).

[245] N. R. Badnell, Phys. Rev. A **41**, 3555 (1990).

[246] Y. Hahn and H. Ramadan, Phys. Rev. A **40**, 6206 (1989).

[247] B. Cleff and W. Mehlhorn, J. Phys. B **7**, 593 (1974).

[248] W. Mehlhorn, *Electron spectrometry of Auger and autoionizing states: Experiment and Theory*, Univ. of Aarhus summer lecture notes (unpublished) (1978).

[249] A. Messiah, *Quantum Mechanics* (North Holland, Amsterdam, 1970), Vol. II.

[250] H. I. Hidmi, Ph.D. dissertation, Kansas State University, 1993 (unpublished).

[251] G. Toth *et al.*, Physica Scripta to be published (2001).

[252] J. B. Marrion and F. C. Young, *Nuclear Reaction Analysis* (North-Holland Publishing Co., Amsterdam, 1968).

[253] J. F. O′Hanlon, *A user's guide to vacuum technology* (John Wiley & Sons, New York, 1980).

[254] C. E. Kuyatt and T. Jorgensen, Phys. Rev. **130**, 1444 (1963).

PUBLICATIONS

1. T.J.M. Zouros, C. Liao, S. Hagmann, E.C. Montenegro, G. Toth, P. Richard and **E.P. Benis**, *Search for inelastic electrons scattered off ions in energetic ion-atom collisions,* Nucl. Instr. & Meth. in Phys. Res. B**98**, 371-4 (1995)

2. **E.P. Benis**, K. Zaharakis, M.M. Voultsidou and T.J.M. Zouros, *A new hemispherical analyser with 2-D PSD and focusing lens for use in* 0° *electron spectroscopy*, Nucl. Instr. & Meth. in Phys. Res. B **146**, 120-5 (1998)

3. **E.P. Benis**, T.J.M. Zouros and P. Richard, *High Resolution RTE Measurements at zero degrees using a Hemispherical Analyser with Lens and 2-D PSD*, Nucl. Instr. & Meth. in Phys. Res. B **154**, 276-80 (1999)

4. **E.P. Benis**, T.J.M. Zouros, H. Aliabadi and P. Richard, *Hemispherical analyser with 2-D PSD for zero-degree Auger projectile spectroscopy*, Physica Scripta **T80B**, 529-31 (1999)

5. **E.P. Benis** and T. J. M. Zouros, *Improving the Energy Resolution of a Hemispherical spectrograph using a Paracentric Entry at a Non-Zero Potential*, Nuclear Instrum. & Meth. A., Letter to the editor **440**, 462-5 (2000)

PAPERS IN PRESS

6. T. J. M. Zouros, **E.P. Benis** and J.E. Schauer, *Charge particle trajectories in an ideal paracentric hemispherical deflection analyser*, AIP Press (2001)

PAPERS SUBMITTED

7. M. Zamkov, H. Aliabadi, **E. P. Benis**, P. Richard, H. Tawara, T. J. M. Zouros, *Energy dependence of the metastable fraction in* $B^{3+}(1s^2\,{}^1S, 1s2s\,{}^3S)$ *beams produced in collisions with solid and gas targets.*, Phys. Rev. A (2001)

8. M. Zamkov, H. Aliabadi, **E. P. Benis**, P. Richard, H. Tawara, T. J. M. Zouros, *Absolute cross section formation of the triply excited* $B^{2+}(2s2p^2\,{}^2D)$ *resonance in electron-metastable ion collisions*, Phys. Rev. A (2001)

9. T.J.M. Zouros, M. Zamkov, **E.P. Benis**, P. Richard, H. Tawara, P. Zavodszky, *Production of Li-like* $B^{2+}(2s2p^2\,{}^2D^e)$ *hollow ionic states by resonance transfer and excitation (RTE) in collisions of 2-7 MeV metastable* $B^{3+}(1s2s\,{}^3S)$ *with* H_2, Phys. Rev. Lett. (2001)

INTERNATIONAL CONFERENCES

A. With abstract and/or poster contributions

1. T.J.M. Zouros, C. Liao, S. Hagmann, E.C. Montenegro, G. Toth, P. Richard and **E.P. Benis**, *Search for inelastic electrons scattered off ions in energetic ion-atom collisions,*, VIIth International Conference on the Physics of Highly Charged Ions, HCI94, Technische Universität Wien, Vienna, Austria, September 19-23, (1994)

2. M.M. Voultsidou,**E.P. Benis**, T.J.M. Zouros, P.Richard, *SIMION3D electron optics studies of zero-degree Auger projectile electron spectrometers*, APS Meeting, Washington DC, April (1997)

3. **E.P. Benis**, M.M. Voultsidou, T.J.M. Zouros, P. Richard and S. Hagmann, *A zero-degree Hemispherical electron spectrometer with 2-Dimensional position-sensitive detector*, APS Meeting, Washington DC, April (1997)

4. **E.P. Benis**, T.J.M. Zouros, M.M. Voultsidou, P. Richard and M. Stöckli, *A hemispherical analyzer with 2-D PSD for use in zero-degree Auger projectile spectroscopy*, XX ICPEAC, Vienna, July 23-29, (1997)

5. **E.P. Benis**, K. Zaharakis, M.M. Voultsidou and T.J.M. Zouros, *A Hemispherical electron spectrometer with 2-Dimensional position sensitive detector for use in zero-degree Auger projectile spectroscopy*, ISIAC XV, Budapest, Aug 1-2, (1997)

6. **E.P. Benis**, T.J.M. Zouros, K. Zaharakis, and P. Richard, *A Hemispherical Analyzer with 2-D PSD for Use in Zero-Degree Auger Projectile Electron Spectroscopy*, Symposium on Radiation Measurements and Applications, Ann Arbor, Michigan, USA, May 11-14, (1998)

7. **E.P. Benis**, T.J.M. Zouros, K. Zaharakis, and P. Richard, *Measurement of 0° binary encounter electron production using a hemispherical analyzer with 2-D PSD and focusing lens*, Fourth International Symposium on Swift Heavy Ions in Matter (SHIM98), Berlin, Germany, May 11-15, (1998)

8. **E.P. Benis**, T.J.M. Zouros, K. Zaharakis and P. Richard, *Focusing properties of a hemispherical analyzer with 2-D PSD for electrons entering along a non-central path.* DAMOP98 meeting of The American Physical Society, Santa Fe New Mexico, May 27-30, (1998)

9. **E.P. Benis**, T.J.M. Zouros and P. Richard, *High Resolution RTE Measurements at zero degrees using a Hemispherical Analyser with Lens and 2-D PSD.* 7th Workshop on Fast Ion-Atom Collisions, Debrecen, September 9-11, (1998)

10. **E.P. Benis**, T.J.M. Zouros, H. Aliabadi and P. Richard. *Hemispherical analyser with 2-D PSD for 0° Auger projectile spectroscopy.* IX International Conference on the Physics of Highly Charged Ions, HCI98, GSI, Bensheim, Germany, September 14-18 (1998)

11. **E.P. Benis** and T.J.M. Zouros, *A Large Hemispherical Analyzer with 2D-PSD and an Asymmetrical Entrance at Non-Zero Potential for Improved Energy Resolution*, International conference on coincidence spectroscopy, Brest, France, September 23-26, (1998)

12. C. Verzani, **E.P. Benis**, T.J.M. Zouros and B.D. DePaola, *Binary Encounter of ground state and laser excited states of Lithium*, XXI ICPEAC, Sendai, Japan July 22-27, (1999)

13. **E.P. Benis**, T.J.M. Zouros, P.A. Zavodszky, H. Aliabadi and P. Richard, *Production of triply excited states in Boron and Fluorine*, XXI ICPEAC, Sendai, Japan July 22-27, (1999)

14. **E.P. Benis** and T.J.M. Zouros, *Hemispherical analyser with 2-D PSD for 0° Auger projectile spectroscopy*, Low-energy Ion beam facilities (LEIF), Annual meeting, Berlin, Germany, Oct. 20-21, (2000)

15. M. Zamkov, H. Aliabadi, T. Gray, H. Tawara, P. Richard, **E.P. Benis** and T.J.M. Zouros, *Stripping energy dependence of* $B^{3+}(1s2s\ ^3S)$ *metastable beam fraction produced in a tandem accelerator*, 16th International Conference on the Application of Accelerators in Research and Industry, Denton, Texas, November 1-4, (2000)

16. **E.P. Benis**, T.J.M. Zouros, M. Zamkov, H. Aliabadi and P. Richard *Charge state dependence of* 0° *binary encounter electron production in* B^{q+} *(q=2-5) in collisions with* H_2, DAMOP01 meeting of The American Physical Society, London, Ontario, Canada, May 15-19, (2001)

17. T.J.M. Zouros, **E.P. Benis**, M. Zamkov, H. Aliabadi and P. Richard $B^{3+}(2p^2)^1D$ *doubly-excited state formed in energetic collisions of* B^{4+} + H_2 *by resonant transfer and excitation*, DAMOP01 meeting of The American Physical Society, London, Ontario, Canada, May 15-19, (2001)

18. M. Zamkov, P. Richard, H Tawara, **E.P. Benis** and T.J.M. Zouros, *Triply excited states formed in metastable ion-atom collisions*, DAMOP01 meeting of The American Physical Society, London, Ontario, Canada, May 15-19, (2001)

19. **E.P. Benis**, T.J.M. Zouros and P. Richard *Production of doubly excited states in He-like Boron*, XXII International Conference on Photonic, Electronic and Atomic Collisions, Santa Fe, New Mexico, USA, 18-24 July (2001)

20. M. Zamkov, **E.P. Benis**, P. Richard, H. Tawara and T.J.M. Zouros, *Study of processes contributing to the production of the metastable 1s2s* ^3S *state in He-like beams*, XXII International Conference on Photonic, Electronic and Atomic Collisions, Santa Fe, New Mexico, USA, 18-24 July (2001)

21. T.J.M. Zouros, **E.P. Benis**, O. Jagutzki, K. Ullmann-Pfleger and H. Schmidt-Böcking, *PC-based fast position delay-line detection technology for high count-rate high-resolution measurements using a hemispherical electron spectrometer*, XXII International Conference on Photonic, Electronic and Atomic Collisions, Santa Fe, New Mexico, USA, 18-24 July (2001)

22. T.J.M. Zouros, **E.P. Benis**, M. Zamkov, H. Aliabadi, H. Tawara and P. Richard, *Observation of two-electron transfer-excitation in 4.5 MeV collisions of* $B^{3+}(1s^2)$ *ions with Ar*, XXII International Conference on Photonic, Electronic and Atomic Collisions, Santa Fe, New Mexico, USA, 18-24 July (2001)

23. T.J.M. Zouros, M. Zamkov, **E.P. Benis**, P. Richard, H. Tawara, P. Zavodszky, *Production of Li-like* $B^{2+}(2s2p^2\,{}^2D^e)$ *hollow ionic states by resonance transfer and excitation (RTE) in collisions of 2-7 MeV metastable* $B^{3+}(1s2s\,{}^3S)$ *with* H_2, XVII ISIAC, 26-27 July, Ensenada, Mexico, (2001)

B. Talks

1. "Charge state dependence of 0° binary encounter electron production in B^{q+} (q=2-5) in collisions with H_2", DAMOP01 meeting of The American Physical Society, London, Ontario, Canada, May 15-19, (2001)

2. "$B^{3+}(2p^2)^1D$ doubly-excited state formed in energetic collisions of B^{4+} + H_2 by resonant transfer and excitation", DAMOP01 meeting of The American Physical Society, London, Ontario, Canada, May 15-19, (2001)

C. Attendance without contributions

1. 1st Euroconference on Atomic Physics with Stored Highly Charge Ions, Heidelberg, 20-24 March (1995)

2. Network meeting on Ion-surface interactions, Les Houches, France, March 11-16, (1996)

3. 6th Workshop on Fast Ion-Atom Collisions, Debrecen, September 4-6, (1996)